

Image-based Analysis of Biological Network Structures using Machine Learning and Continuum Mechanics

Von der Fakultät Bau- und Umweltingenieurwissenschaften und
dem Stuttgart Research Centre for Simulation Technology
der Universität Stuttgart zur Erlangung der Würde
eines Doktor-Ingenieurs (Dr.-Ing.)
genehmigte Abhandlung

von

Pouyan Asgharzadeh, M.S.

aus

Teheran

Hauptberichter: Prof. Oliver Röhrle, PhD

1. Mitberichter: Prof. Dr.-Ing. Flix Fritzen

2. Mitberichter: Prof. Bettina Willie, PhD

Tag der mündlichen Prüfung: 07. Mai 2020

Institut für Modellierung und Simulation Biomechanischer Systeme
der Universität Stuttgart

2020

Report No.: CBM-06 (2020)
Institute for Modelling and Simulation of Biomechanical Systems
Department of Continuum Biomechanics and Mechanobiology
University of Stuttgart, Germany, 2020

Editor:

Prof. O. Röhrle, PhD

© Pouyan Asgharzadeh
Institute for Modelling and Simulation of Biomechanical Systems
Department of Continuum Biomechanics and Mechanobiology
University of Stuttgart
Pfaffenwaldring 5a
70569 Stuttgart, Germany

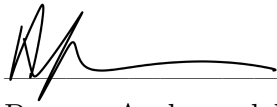
All rights reserved. No part of this publication may be reproduced, stored in a retrieval system, or transmitted, in any form or by any means, electronic, mechanical, photocopying, recording, scanning or otherwise, without the permission in writing of the author.

ISBN 978-3-946412-05-2

Declaration of originality

I hereby declare that this thesis and the work reported herein was composed by and originated entirely from me. Information derived from the published and unpublished work of others has been acknowledged in the text and references are given in the list of sources.

Stuttgart, August 27th, 2020

A handwritten signature in black ink, consisting of a stylized 'P' followed by a series of loops and a long horizontal stroke.

Pouyan Asgharzadeh

تقدیم به پدر و مادرم برای همه فداکاری‌ها، مهربانی‌ها و بزرگواری‌ها

Acknowledgements

The research presented in this thesis was carried out from years 2015-2019 at the Institute for Modeling and Simulation of Biomechanical Systems and Institute of Applied Mechanics of University of Stuttgart, Stuttgart, Germany and Department of Pediatric Surgery, Faculty of Medicine at McGill University, Montreal, Canada.

The presented work would not have been possible without the help of several people to whom I am gratefully indebted, First, I would like to express my deepest gratitude to my doctoral advisor Professor Oliver Röhrle for his limitless support. He has motivated me to pursue new ideas and face the accompanying challenges. Professor Röhrle was not only my mentor in the scientific field but was also a very invaluable support when facing challenges outside the work environment. Second, I would like to thank Professor Ralf Reski for introducing me to the world of proteins and helping me to form this work. Moreover, I would like to thank Professor Bettina Willie, who made it possible for me to experience working in direct collaboration with physicians and patients at the research department of Shriners Hospital. This gave me the hope that my scientific contribution might one day be used to improve the life quality of a patient.

I would also like to thank all the people who contributed in one way or the other to this work. First of all, I would like to thank Dr. Annette Birkhold for guiding me through this research. She gave me the confidence to and helped me to create this work independently. Throughout our many passionate discussions, I learned about fundamentals of science, the essence of creating a novel work and many things about life itself. Moreover, I would like to thank thank Bugra Özdemir, with whom I had a very close collaboration. He helped me to understand the deeply interesting biochemistry that comes into play in creating what I have used in a big portion of this thesis. I would also like to mention Dr. Said Jamai, who helped me understand fundamentals of continuum mechanics. Further special thanks to Christian Dietz who consulted me many times on machine learning and specifically helped me understand the potentials of deep learning.

I would like to thank all my students that helped me during their master thesis, bachelor thesis or working as a student assistant. Specifically, I would like to thank Prateen Kumar, Sandra Hieber, Beriet Kuhn and Zubin Trivedi for their contributions to this work. Moreover, I would like to thank all my colleagues at IMSB for all the scientific and other activities that we did together.

Finally, I would like to express my deepest gratitude to my parents and my sister for their unconditional support, care and love.

Stuttgart, August 2020
Pouyan Asgharzadeh

Contents

Deutsche Zusammenfassung	v
Abstract	viii
1 Introduction	1
1.1 Motivation	1
1.2 Outline and the Structure of the Thesis	4
1.3 Data Source	5
1.4 List of Publications	7
2 General Background on Biological Network Structure and Functionality	9
2.1 Cytoskeletal Protein as an Example of a Network structure: a Brief Overview	10
2.2 Cytoskeletal Structural Blocks	10
2.3 State of the Art in Modelling Cytoskeletal Protein Network Structure . . .	12
2.3.1 Nonlinear Continuum Mechanics of Cells and Protein Networks . .	13
2.3.2 Mechanical Models of Cytoskeletal Protein Networks	14
3 Quantitative Imaging and Machine Learning	19
3.1 Biomedical Imaging	19
3.1.1 Imaging on the Nano-scale: Quantitative Imaging of Cytoskeletal Protein Networks	19
3.1.2 Imaging on the Micro- and Macro-scale: Bone	22
3.2 Machine Learning-based Image processing	25
3.2.1 State of the Art	26
3.2.2 ML-based Image Classification	26
3.2.3 Decision Trees	27
3.2.4 Support Vector Machine (SVM)	29
3.2.5 Convolutional Neural Networks	30
4 Analyzing Structure-function Relationship at the Nano Scale: Protein Networks	35
4.1 FtsZ Protein Network Structure and Functionality	35
4.1.1 State of the Art in Analyzing the Structure of Protein Networks . .	37
4.2 A Method to Describe and Learn the Structure of Protein Networks	39
4.2.1 Protein Labeling and Confocal Laser Scanning Microscopy	41
4.3 Designing a Protein Network Structure Descriptor Method	41
4.3.1 Validation of Feature Extraction Algorithm for PNs	49
4.3.2 Structural Feature Extraction for the FtsZ1-2 Isoform	51
4.3.3 Distinguishing FtsZ isoforms: a Statistical Approach	55
4.3.4 Protein Network Classification: a Machine Learning Approach . . .	60

4.3.5	Discussion	63
4.4	Simulating the Mechanical Behaviour of Protein Networks	68
4.4.1	Mechanical Nano FE Modeling	70
4.4.2	Continuum Mechanical Analysis of FtsZ1-2 and FtsZ2-1 isoforms	73
4.4.3	From Small to Large Deformations	74
4.4.4	Discussion	77
4.5	Combining Machine Learning and Simulations to Investigate Protein Network Functionality	78
4.5.1	Machine Learning Surrogate Mechanical Model	79
4.5.2	Mechanical Behaviour Prediction	81
4.5.3	Discussion	81
4.6	Summary	83
5	Analyzing Structure-function Relationship at the Micro/Macro Scale: Bone	85
5.1	General Background on Bone	86
5.1.1	Bone Biology	86
5.1.2	Aging and Bone Loss	89
5.1.3	Models of Age-related Bone Loss and Osteoporosis	90
5.1.4	Osteogenesis Imperfecta	91
5.2	A Deep Learning Approach for Bone Age Assessment from μ CT Images	91
5.2.1	In vivo Monitoring of Tissue Maturation and Adaptation	94
5.2.2	Deep Bone Age Assessment Model (BAAM)	96
5.2.3	Analysis of Key Skeletal Maturation Regions and Features	97
5.2.4	Results: Bone Age Assessment	98
5.2.5	Results: Decoding Bone Tissue Maturation Process	101
5.2.6	Discussion	105
5.3	Analyzing Effects of in vivo Loading Treatment on Skeletal Age	106
5.3.1	In vivo Mechanical Loading	107
5.3.2	Decoding Effects of in vivo Loading using BAAM	107
5.3.3	In Vivo Loading and 3D Bone Volume Changes	107
5.3.4	Results: Rejuvenation Effects of in vivo Loading	108
5.3.5	Results: Localized Rejuvenating Manifestation of in vivo Loading	110
5.3.6	Results: Rejuvenation and Bone Volumetric Changes	112
5.3.7	Discussion	113
5.4	A Deep Learning Approach for Analyzing Osteogenesis Imperfecta (OI)	116
5.4.1	HR-pQCT Image Acquisition	117
5.4.2	Deep Bone Quality Assessment Model (BQAM)	120
5.4.3	A Random Forest Model for Morphometric Parameters Analysis	123
5.4.4	Results: BQAM Analysis of OI	123
5.4.5	Results: OI-corresponding Structural Features	129
5.4.6	Discussion	129
5.5	Summary	132
6	Conclusion	133
6.1	Summary and Main Contribution	133
6.2	Future Basic Research and Clinical Perspectives	135

Bibliography	139
Curriculum Vitae	169

Deutsche Zusammenfassung

Biologische Netzwerke existieren in den strukturellen Elementen biologischer Umgebungen: vom Zytoskelett in Zellen bis zum Fasernetzwerke in Muskeln und vom Osteozytennetzwerk bis zur Knochentrabekelstruktur. Diese Netzwerkstrukturen sind evolutionär entworfen, um eine Vielzahl von Aufgaben zu erfüllen. Sie sind robust genug die Dynamik biologischer Prozesse zu bewältigen und erfordern zugleich minimale Ressourcen. Aufgrund des evolutionären Konstruktionsprinzips des Designs dieser Netzwerkstrukturen existiert eine starke Wechselwirkung zwischen den strukturellen Eigenschaften und der Funktionalität. Diese biologische Struktur-Funktions-Beziehung besteht in mehreren Skalen der Umgebung mit diversen physikalischen Eigenschaften, was einerseits die Untersuchung und das Verständnis ihrer Details erschwert. Diese Beziehung ermöglicht es andererseits jedoch, anhand der Struktur, die Funktionalität zu untersuchen und umgekehrt.

Heutzutage ermöglichen „Rich-Content“ 3D-Bildaufnahmetechnologien die Darstellung der Struktur dieser Netzwerke mit einer beispiellosen Auflösung, die eine detaillierte Analyse dergleichen ermöglicht. Bildgebende Verfahren werden nicht nur in Forschungslabors, sondern auch in Kliniken immer häufiger eingesetzt. Dies hat dazu geführt, dass 1) große Menge an Daten (Big Data) von biologischen Netzwerkstrukturen verfügbar sind und 2) datengetriebene Modelle direkt in die Praxis umgesetzt werden können. Um dies zu tun, sind datengetriebene Modelle erforderlich, die automatisch die Struktur einer biologischen Umgebung untersuchen und diese mit ihrer Funktionalität oder Dysfunktionalität korrelieren können.

Mit der Verfügbarkeit von Big Data biologischer Strukturen besteht der Bedarf an Methoden, diese Informationsmenge nutzbar zu machen. Klassische Untersuchungsmethoden biologischer Strukturen besteht darin, repräsentative Parameter wie Materialparameter (z. B. Steifigkeit), mechanische Konstitutionsgesetze (z. B. lineare Elastizität), geometriebeschreibende Parameter (z. B. Krümmung von Filamenten in Proteinnetzwerken) und Mikroarchitekturparameter (z. B. trabekuläres Knochenvolumen) mit bestimmten Funktionen zu korrelieren (z. B. Belastbarkeit von Zytoskelettnetzwerken) oder Dysfunktionalität (z. B. Erhöhung des Frakturrisikos durch Osteoporose). Theoretisch erlaubt dieser Ansatz einen hohen Automatisierungsgrad und damit eine schnelle Diagnose von Krankheiten oder Untersuchung biologischer Strukturen gestattet, verhindert diese voreingenommen Analyse, die nicht sämtliche in den Daten vorhandene Information verwendet, die Nutzung des vollständigen Potenzials des verfügbaren Big Data zu nutzen. Daher besteht ein Bedarf an Algorithmen, die die gesamten in Bildern verfügbaren Informationen nutzen können, um eine automatische Merkmalsextraktion und eine Korrelation der Struktur mit der Funktion von Interesse durchzuführen. Dieser Ansatz spiegelt sich im Konzept der Algorithmen des Maschinellen Lernens wieder.

Diese Dissertation befasst sich mit der Entwicklung, Anwendung und Validierung einer Reihe solcher Methoden zur automatischen Analyse der Struktur-Funktions-Beziehung auf zwei verschiedenen Skalen in biologischer Umgebungen mit einem starken Wechselspiel

zwischen Struktur und Funktion: Proteinnetzwerke auf der Nanoskala und Knochen auf der Mikro- und Makroskala.

Proteinnetzwerke erfüllen in biologischen Umgebungen viele Funktionen, z. B. Tragfähigkeit, Skelettformbildung, Mobilität, Material- und Informationstransport. Die Struktur der zytoskelettalen Proteinnetzwerke als formbestimmende Proteine der Zelle wird von interne und externe mechanische Anregungen beeinflusst. Diese Struktur wird Änderungen unterworfen, etwa um Aufgaben wie die Zellteilung zu erfüllen oder als Reaktion auf äußere mechanische Belastungen oder Krankheiten wie Krebs. Wenn man die Struktur der Proteinnetzwerke und ihre evolutionären Entwurfsprinzipien, die zur Erfüllung der mechanischen Aufgaben führen, versteht, kann man 1) den Zustand des Proteinnetzwerks als Prognosemittel analysieren, um zwischen gesunden und kranken oder beladenen und nicht beladenen Zuständen zu unterscheiden, 2) unterscheidende funktionelle Eigenschaften verschiedener Proteinnetzwerke finden und 3) die Mechanismen verstehen, die in der Struktur entwickelt wurden, um die untersuchte mechanische Funktionalität bereitzustellen.

Der erste Teil dieser Dissertation befasst sich mit der quantitativen und automatischen Analyse der Struktur von Proteinnetzwerken anhand von 3D-Mikroskopiebildern. Im Gegensatz zu den gründlich untersuchten biochemischen Aspekten von Proteinnetzwerken fehlte ein Rahmenwerk zur quantitativen Beschreibung und Untersuchung der Struktur von Proteinnetzwerken. Daher wurde in Rahmen dieser Dissertation zunächst eine Bildverarbeitungsmethode entwickelt, die die Struktur des Netzwerks automatisch extrahiert und in eine Reihe von Strukturmerkmalen auflöst, die es ermöglichen, den Zustand eines Proteinnetzwerks quantitativ zu beschreiben. Anschließend wird das entwickelte mathematische Rahmenwerk für die Proteinnetzwerkanalyse verwendet, um Modelle des Maschinellen Lernens zu erstellen, die automatisch die strukturellen Aspekte von Proteinnetzwerken lernen und die Struktur mit ihrer Funktionalität in Beziehung setzen können. Diese Modelle werden dann auf Filamentous temperature sensitive Z Proteine angewandt. Filamentous Temperature Sensitive Z (FtsZ) ist ein prokaryotisches Homolog des eukaryotischen Zytoskelettproteins Tubulin, das während der Zellteilung ins Spiel kommt. Als erste Anwendung führen die entwickelten Modelle des Maschinellen Lernens eine End-to-End Klassifizierung der Isoformen dieses Proteinnetzwerks mit 7 von 8 korrekten Vorhersagen durch. Anschließend wird durch Kombination einer Reihe von Mikro-Finite-Elemente-Simulationen und Ensemble-Methoden gezeigt, dass diese Proteinnetzwerke eine tragende Funktion in Plastiden von Chloroplasten ausüben; daher wirken sie als Plastoskelett. Darüber hinaus erreichen die entwickelten Maschinen Lernenmodelle eine Korrelation von $R^2 = 0,98$ für die Vorhersage des mechanischen Verhaltens bei kleinen und großen Deformationen. Schließlich wird das Modell verwendet, um die vorher definierten Strukturmerkmale zu extrahieren, die es dem Proteinnetzwerk ermöglichen, große Deformationen zu ertragen, ohne ihre Stabilität zu verlieren (adaptive Stabilität der Netzwerke). Die Robustheit der Modelle wird gründlich validiert, indem eine Kreuzvalidierung sowie ein Vergleich zwischen den Ergebnissen des Modells und einer manuellen Segmentierung, Merkmalsextraktion und Klassifizierung durchgeführt werden.

Die Knochenstruktur, als ein biologisches Netzwerk im Mikro- und Makromaßstab, ist ebenfalls eng mit seiner mechanischen und biologischen Funktionalität verbunden. Ähnlich wie das Proteinnetzwerk des Zytoskeletts übernimmt der Knochen die Funktion der Lastaufnahme. Die Knochenstruktur wird von internem Prozesse wie Alterung und

genetische Erkrankungen, z.B. Osteogenesis Imperfecta, sowie äußere Anregungen wie mechanische Belastung beeinflusst. Die mechanische Belastung ist die Hauptantriebskraft der Organisation der Knochenstruktur. Darüber hinaus findet im Knochen ein ständiger Prozess der Knochenneubildung und Knochenresorption statt, der als Architekt der Knochenstruktur wirkt. Alterung wirkt sich auf diese (Re-)Modellierung des Knochens aus. Daher manifestiert sich das Altern tief in der Knochenstruktur. Bis heute sind die Auswirkungen des Alterns auf die Knochenstruktur und die (Re)Modellierung nicht vollständig bekannt. Die Mikrocomputertomographie ist in den letzten Jahren zur primären bildgebenden Technik zur Abbildung der Mehrskalenstruktur des Knochens geworden. Der gängige Ansatz der Bestimmung einer Anzahl von Knochenstrukturparametern wie der mittleren Dicke der Kortikalis oder einzelner Trabekel oder der Dichte der Knochenmasse im gesamten Gewebe anhand von Mikrocomputertomographieaufnahmen war jedoch bis heute nicht vollständig erfolgreich bei der Lösung der Frage nach den Ursachen und genauen Auswirkungen der alterungsbedingter Veränderungen der Knochenstruktur. Darüber hinaus war dieser Ansatz nicht in der Lage, die Auswirkungen von Krankheiten wie Osteoporose oder Osteogenesis Imperfecta auf die Knochenstruktur und die Knochenmaterialeigenschaften vollständig zu erfassen und zu analysieren.

Der zweite Teil dieser Arbeit befasst sich daher mit der Entwicklung einer Reihe von Deep-Learning-basierten Modellen, die hochauflösende 3D-Mikrocomputertomographiebilder von Knochen automatisch mit drei strukturverändernden Prozessen korrelieren: 1) interne Reize: Alterung und 2) Osteogenesis Imperfecta-Krankheit und 3) äußere Reize: Regeneration durch äußere mechanische Belastung des Knochens. Dazu wird zunächst ein tiefes neuronales Netzwerk entworfen, das in der Lage ist, in einer präklinischen Studie eine Kurzzeitalterungsvorhersage mit einer Genauigkeit von 95% durchzuführen. Dieses Modell wird dann verwendet, um die lokalisierte Manifestation des Alterns in Knochen zu untersuchen. Zweitens wird das Altersbewertungsmodell verwendet, um zu zeigen, dass eine in-vivo Belastung nach 15 Tagen zu einem um 5 Tagen verjüngten Erscheinungsbild des Knochen führt. Darüber hinaus wurde in einer klinischen Studie ein weiteres Deep-Learning-basiertes Modell entwickelt, das zum ersten Mal automatisch eine End-to-End-Erkennung verschiedener Arten von Osteogenesis Imperfecta anhand von hochauflösenden peripheren quantitativen Computertomographiebildern von Rädien bei Patienten im Alter zwischen 25 und 75 Jahre durchführt. Das Modell erreicht eine Genauigkeit von 99% bei der Erkennung von Krankheitstypen und wird verwendet, um die Auswirkungen des OI-Typs auf die Knochenmakro- und mikroarchitektur zu verstehen. Die entwickelten Deep-Learning-Modelle sind kreuzvalidiert und weisen eine hohe Robustheit in Bezug auf Alter, Geschlecht und Bildgebung auf.

Insgesamt konnte in dieser Dissertation gezeigt werden, dass eine datengetriebene automatische Analyse biologischer Netzwerkstrukturen Aufschluss über die tief verwurzelte Struktur-Funktions-Beziehung geben kann. Dies ist möglich, indem modernste Algorithmen für Maschinelles Lernen mit neu entwickelten Strukturmerkmalen kombiniert werden, die anhand quantitativer Bildgebung und kontinuumsmechanischer Modellierung abgeleitet wurden. Um so Methoden zur Analyse von Bilddaten mit hohem Inhalt zu entwickeln, mit denen biologische Netzwerkstrukturen auf der Grundlage ihrer untersuchten Funktionalität aufgelöst werden können.

Abstract

Biological networks are the structural units of biological environments from cytoskeleton in cells to fibre networks in muscles and from osteocyte network to bone trabecular structure. These network structure are evolutionary designed to perform a multitude of tasks while being robust enough to handle the dynamic nature of the biological processes and requiring as little resources as necessary. Due to the evolutionary construction principle behind the design of these network structures, there exists a strong interplay between the structural characteristics and the functionality. This structure-function relationship holds across a multi-scale and multi-physics environment which makes it burdensome to investigate and understand its details. However, this relationship enables us to study functionality through investigating the structure and vice versa.

Recently, rich-content 3D imaging technologies enable resolving the structure of these networks with unprecedented resolution allowing a detailed analysis of them. Additionally, imaging facilities have become more and more available not only in research laboratories, but also in clinics. This has resulted in 1) availability of big data on biological network structures and 2) feasibility of utilizing data-driven models directly in practice. However, to do so, one requires data-driven models that automatically investigate the structure of a biological environment and correlate it to its functionality or dysfunctionality.

With the availability of such big data on biological structure, the need for methods that can take advantage of this amount of information is imminent. The traditional technique in investigating biological structures is through extracting representative parameters such as material parameters (e.g. stiffness), mechanical constitutive laws (e.g. linear elasticity), geometry describing parameters (e.g. curvature of filaments in protein networks) and micro-architecture parameters (e.g. trabecular bone volume) and correlating these to certain functionality (e.g. load bearing characteristic of cytoskeletal networks) or dysfunctionality (e.g. increase of fracture risk in bone due to osteoporosis). Although this approach creates a high level of automatizing and therefore faster disease prognosis or investigation of biological structures, its bias and negligence of the remaining information present in images hinders it from progressing and completely utilizing the potentials of the available big datasets. Therefore, there exist the need for algorithms that can use the entirety of the information available in images while performing an automatic feature extraction and correlation of the structure to the function of interest. This matches greatly with purpose in development of machine learning-based algorithms.

This thesis is devoted to the development, application and validation of a series of such methods for automatic analysis of the structure-function relationship on two different scales of biological environments with strong interplay between the structure and function naming protein networks on the nano scale and bone on the micro and macro scale.

Protein networks carry out many functionalities in biological environments such as load bearing, skeletal shape forming, mobility, transportation of material and information. The structure of cytoskeletal protein networks as the shape defining protein of cell are affected

by internal and external mechanical stimuli. The structure undergoes changes to carry out tasks such as cell division or in response to external mechanical loads and due to diseases such as cancer. By understanding the structure of the protein networks and the evolutionary design principles leading to their performance in the mechanical tasks, one can 1) analyze the state of the protein network as a prognostic tool to distinguish between healthy/unhealthy or loaded/non-loaded states, 2) find distinguishing functional characteristics of different protein networks and 3) understand the mechanisms developed in the structure to execute the investigated mechanical functionality.

The first part of this dissertation is devoted to quantitatively and automatically analyzing the structure of protein networks using 3D microscopy images. Unlike the biochemical aspects of protein networks which has been thoroughly studied, there existed the lack of a framework to quantitatively describe and investigate the structure of protein networks. Therefore, one focus of this dissertation is in developing an image processing method that automatically extracts and resolves the structure of the network into a series of structural features allowing to quantitatively describe the state of a protein network. Afterwards, the designed mathematical framework for protein network analysis is utilized to create machine learning models that automatically learn the structural aspects of protein networks and can relate the structure to their functionality. These models are then applied on Filamentous temperature sensitive Z proteins, a prokaryotic homolog of the eukaryotic cytoskeletal protein tubulin, which comes into play during cell division. As a first application, the developed machine learning models perform an end-to-end classification of isoforms of this protein networks with 7 out of 8 correct predictions. Afterwards, by combining a series of micro finite element simulations and ensemble methods, it is shown that these protein networks carry out a load bearing functionality in plastids of host chloroplasts; hence they act as a plastoskeleton. Moreover, the developed regression machine learning models achieve a $R^2 = 0.98$ in predicting mechanical behaviour in case of small and large deformations. At last, the model is utilized to extract developed structural features that enables the protein network to undergo large deformations without losing their stability (adaptive stability of the networks). The robustness of the models are thoroughly validated by performing cross-validation as well as comparison between the results of the model and unbiased manual segmentation, feature extraction and classification.

Bone structure, a biological network of micro and macro scale, is also deeply connected to its mechanical and biological functionality. Similar to a cytoskeletal protein networks, bone carries out load bearing and skeletal functionality as well as transportation of nutrition. The bone structure is dictated by its internal processes such as maturation, aging and genetic diseases e.g. Osteogenesis Imperfecta as well as external stimuli such as mechanical loading. Mechanical loading is the main driving force in organization of the bone structure. Moreover, a constant process of bone formation and bone resorption is taking place in bone that acts as the architect of the bone structure. Aging also affects this (re)modeling of the bone. Therefore, aging is deeply manifested in the bone structure. Micro computed tomography has recently become the go to imaging technique in recent years for acquisition of images containing the multi scale structure of the bone. Up to this day, the effects of aging on bone structure and (re)modeling is not fully understood. The usual approach of determination of a set of bone parameters such as thickness of the structure in different bone compartments or the density of the bone matter in the whole tissue has not been fully successful in resolving aging related changes in bone structure.

Moreover, this approach has also not been fully capable of detecting and analyzing the effects of bone structure- and material properties-modifying diseases such as Osteoporosis or Osteogenesis Imperfect.

The second part of this thesis is devoted to designing a set of deep learning-based models that automatically correlate 3D high resolution micro computed tomography images of bones to three structure altering processes naming 1) internal stimuli for: aging and 2) Osteogenesis Imperfect disease and 3) external stimuli: regeneration by external mechanical perturbations. To do so, first a deep neural network is designed which is capable of performing short-term age prediction in a preclinical study with 95% accuracy. This model is used to investigate localized manifestation of aging in bones. Second, the age assessment model is utilized to show that in vivo loading leads to a 5 days rejuvenated appearance of bones after 15 days of loading. Moreover, in a clinical study, another deep learning-based model is designed to automatically perform, for the first time, an end-to-end detection of different types of Osteogenesis Imperfect from high resolution peripheral quantitative computed tomography images of radii in patients between 25 and 75 years. The model reaches 99% accuracy in disease type detection and is used to understand the effects of OI type on bone macro/micro-architecture. The designed deep learning models are cross validated and show high robustness to age, gender and imaging setup.

In summary, this dissertation, demonstrates that data-driven automatic analysis of biological network structures can shed light on the deeply embodied structure-function relationship. This is only possible by combining the state of the art machine learning algorithms with novel designed structural features derived from quantitative imaging and continuum-mechanical modeling to develop methodologies for analyzing rich-content image data to resolve the biological network structures based on their investigated functionality.

This dissertation was supported by the Deutsche Forschungsgemeinschaft (DFG, German Research Foundation) under Germany's Excellence Strategy – Cluster of Excellence EXC 2075 “Data-Integrated Simulation Science (SimTech)” and Transregio/SFB TRR141.

1 Introduction

1.1 Motivation

The evolutionary procedure behind the design of biological processes [70] has often led to investigations involving multiple scales and physics. This complexity lies under the purpose-oriented strategy of optimizing multiple parameters e.g. material and energy consumption, while maximizing the capability in pursuing the desired goal. Additionally, the dynamic nature of biological processes where the structure, mechanism and goals of the system simultaneously vary, contribute to the complications involved in understanding them. The traditional approach of investigating biological processes is based upon the fact that one can understand the overall mechanism of a biological system by separately studying smaller subsystems in addition to exploring the corporation of each of them. The span of success of this approach decreases with the increase in the complexity of the system due to the accumulation of errors originating from neglecting the concurrency of sub-mechanisms and the multilayer nature of the system. This makes such traditional approaches limited in comprehending biological systems.

There exists a strong connection between the structure and the function in biological processes. This relationship is grounded on the evolutionary process fueling the development of these two aspects of a biological process hand in hand [158]. Therefore, it is often observed that intricate biological processes such as multifunctionality of protein networks (PN) in cells [100] or load-induced (re)modeling of bone [364] is carried out by multifarious structural entities. It is important to note that the definition of structure in biological environments exceeds way beyond the classical mechanical load bearing assemblies. As in biological environments structure and function are not two clearly separated entities. In the context of this thesis, a structure is as described by Oxford dictionary: "an arrangement and organization of interrelated elements in a material object or system, or the object or system so organized" [315]. Structural analysis of biological networks across different scales has the potential to shed light on the dynamics of biological processes. Although, the structure-function relation in most biological environments is evident, the intricacy of this relation and the complexity of the structures involved has encumbered the analysis of biological processes by understanding the structures involved. In this thesis, the link between mechanical function and structure of some biological systems naming cytoskeletal protein networks and bone are investigated.

The emergence of computer modeling since 1950s has opened new doors for structural analysis of biological systems. The most straight forward use case of this approach has been to put new theories of governing mechanism in biological environments to test. This enables extracting new concepts such as development of constitutive law though computer models e.g. models of muscle contraction [132]. These concepts can be further validated by or developed from experimental data. Regardless of the revolutionary capabilities made possible by traditional computational modeling, the models are often either too generic

or are built specifically upon a single subject which leads to them being too specific. This results in lack of robustness in models representing the dynamics of a complete biological process. Moreover, manual production of models from each biological sample is often too time consuming to be used for building a database of computer models for a specific biological system.

In the past decade the amount of acquired data has exponentially increased [217]. Meanwhile, the data analysis hardware has improved drastically. Recent advances in data acquisition technologies in the field of biomedicine allow unprecedented insight in biological processes across different scales. In addition, the increase in parallel computation power with the newest multi-thousands core graphic cards, enables to process this enormous amount of data in sufficient time. Data-driven structural analysis with specifically-designed automatic model generator algorithms overcome the aforementioned problems regarding the mass analysis of structures without the manual labor costs.

Biomedical imaging has been adopted as one of the main prognostic as well as investigatory means by physicians and researchers. Recent advance in acquiring 3D and 4D (time resolved) images, make them even more suitable to study biological processes. The flexibility and variety of capturing images at several resolutions in different imaging methods makes them a suitable building ground for creating computer models. Through biomedical imaging, not only the relatively realistic geometry of the structure is captured, but also the multiscale and multilayered nature of biological systems are recorded. This makes biomedical images a well suited input for data-driven methods for analyzing biological structures. Moreover, the accumulation of data and the presence of suitable hardware call for objective oriented end-to-end algorithms that are designed to answer specific biomedical research questions of "how are biological structures related to their functionality?" (Fig 1.1).

Machine learning (ML)-based methods has proven to be capable of producing such end-to-end algorithms based on image data. Machine learning (ML) as prominent facade of artificial intelligence (AI) has been increasingly utilized to speed up and automate methods for computational biomedical image analysis [111]. ML-based methods consume the entirety of information recorded in an image and has the potential to automatically correlate the information in the image to the biological process of interest. This may permit an automatic inclusion of the interplay of different parameters in contrast to selectively extracting specific structural features to study. Moreover, when needed, ML methods allow consideration of the hierarchical nature of the biological structures. In contrast to the primary approach of using ML as a black box for analyzing biological systems [356], recent advances in quantitative analysis of the learning processes permit a deeper understanding of mechanisms under investigation. This makes ML a great candidate for researching dynamic biological processes.

This work focuses on a data-driven approach to analyze the structure-function relationship in two different biological environments/scales: 1) Protein networks built from nanobiopolymers and 2) metaphyseal bone containing cortical shell and trabecular structure using 3D image data. Despite basic differences between these biological settings, their mechanisms and the implications of pixel intensities, the acquired rich-content data (3D images) represent the structure-function relationship of interest in both biological network structures. Therefore, the same fundamental approach for developing methods using image processing and machine learning for investigating the biological mechanism

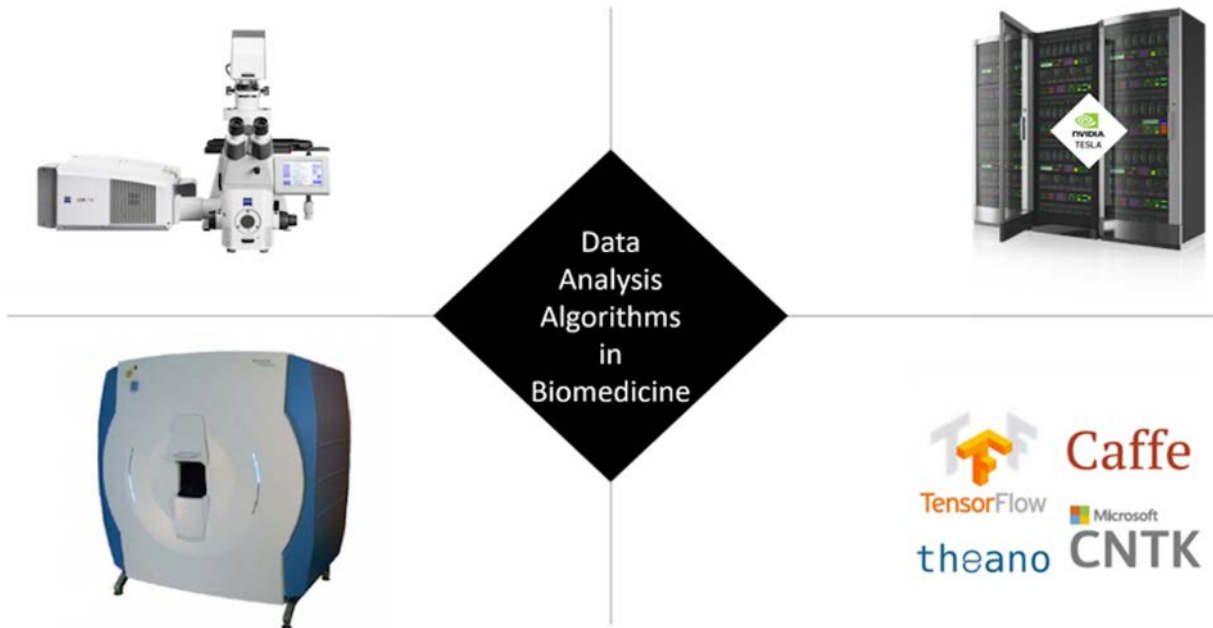


Figure 1.1: *Investigating structure-function relationship in biological environments is possible through purpose oriented data acquisition and data analysis algorithms using newly available data acquisition machines such as confocal microscopes and HR-pQCT scanners, parallel computing hardware e.g. GPU clusters and big data analysis platforms such machine learning libraries.*

has been utilized. Needless to say, each of these problems present their specific challenges in data analysis. Therefore, various algorithms and method of machine learning and image processing for decoding each of them has been selected.

At the nano scale of protein networks, I aimed at developing a series of methods for an automatic and fast assessment of cytoskeletal protein networks based on 3D microscopy images. The approach can be broken down into: 1) designing an image processing algorithm that quantitatively describes the structure of a PN allowing not only distinction between different PNs but also between different states of the same PN, 2) creating an in-silico experimental setup permitting a quantitative representation of the mechanical responses of the PN and 3) using feature-based ML algorithms (e.g. random forest) to correlate the extracted structural features to the mechanical behavior of the PN. Creating such ML models allows an end-to-end application of PN state assessment from microscopy images as well as determination of the structural features developed in the network to create such mechanical characteristic.

In contrast, at the micro/macro scale, many research has been devoted to establishing this relationship. However, for many tissues no precise link has been found between the structure and function. Specially, bone as a load bearing tissue, has been investigated extensively. The load bearing functionality provided by the bone's structure is effected by certain physiological and patho-physiological processes. Therefore, these perturbations are utilized in this thesis to study the structure-function relationship in bone. To do so, I developed machine learning models that link the structure of bone encoded in images to the effects these perturbations on the bone structure. The chosen perturbations are: 1) maturation-related changes in bone structure, 2) mechanical loading aiming at reversing

the aging-related changes and 3) alterations in bone structure due to diseases. In order to do this, in a preclinical study, which allows inducing controlled structural adaptations, I designed a deep neural network (DNN) capable of predicting the skeletal age of the subject based on X-ray images and a tool to analyze the learned structural features corresponding to the maturation stages. Furthermore, this DNN is applied on images of bone treated with in vivo loading to study the rejuvenation effects of this mechanical treatment. Afterwards, in a clinical study, the DNN was modified to investigate manifestation of bone-structure-altering Osteogenesis Imperfecta disease in patients in order to automatically identify specific disease types. This overall approach allowed an unbiased automatic investigation of bone structural changes induced by the aforementioned mechanical function-altering perturbations. Despite the considerable recent progress, there are yet many unanswered questions about the structure-function relationship in bone tissue and how functionality/dysfunctionality of bone can be studied through its structure. In micro/macro-scale focused part of this thesis, this relationship is investigated by developing and applying a series of bone quality assessment models utilizing ML.

1.2 Outline and the Structure of the Thesis

This thesis is divided into six chapters and is structured in the following way. In the first chapter, a general introduction to biological networks, their structure-function relationship and the ML-based approach developed in this thesis is provided. Further, the investigated biological environments i.e. protein networks at the nano scale and bone at the micro/macro scale are introduced here. Chapter 2 contains the biological and mathematical background of a network representation of the mentioned biological structures. This chapter further consists of an overview about the functionality of protein networks and state of the art mechanical modeling approaches for describing this functionality. Chapter 3 demonstrates how quantitative imaging is utilized to study the structure of biological networks by taking advantage of rich-data containing detailed structural information. It is further demonstrated how machine learning-based algorithms could be used to analyze such big data to automatically resolve the image data and the network structure.

In chapter four, the developed methodologies for investigating structure-function relationship at the nano scale of protein networks is presented. This chapter consist of three sections:

1. The first section contains the developed imaging and ML methods for resolving and automatically classifying protein network structures from 3D confocal laser scanning microscopy images. As a first application, how this is used to extract structural features that quantitatively describe the assembly of Filamentous temperature sensitive Z (FtsZ) proteins is demonstrated. As the second application, the capability of the method to highlight structural similarities and differences of two isoforms of this protein network is showcased. The third presented application highlights the designed ML classifier of protein network structure and its performance in an end-to-end classification of two protein isoforms.
2. The second section includes a finite element simulation framework designed to extract the mechanical behaviour of a protein network from 3D confocal microscopy

data. The designed setup allows to investigate the response of the networks in small and large deformations and extract the failure scenarios of the networks.

3. The third section contains the developed machine learning-based method that correlates the structural features of the network (extracted in the first section) with the mechanical characteristics (extracted in the second section) which allows to determine the structural features corresponding to the specific mechanical characteristics of the protein networks e.g. adaptive stability.

In Chapter five, the developed methods to study structure-function relationship on the micro and macro scale for bone tissue is demonstrated. This is done by studying the effects of three different internal and external perturbations (aging, mechanical loading and osteogenesis imperfecta disease) on bone tissue. This chapter includes three sections:

1. The first section contains my developed deep learning model for studying the manifestation of aging in bone structure. In this section, an end-to-end bone age assessment model from μ CT images is presented, which is utilized to further investigate the localization of aging information in bone.
2. The second section includes the utilization of the model introduced in the first section to analyze the effects of in vivo loading on appeared age in bones and show that this treatment leads to younger appearing bones.
3. The third section showcases the modified deep neural network from the first section to perform a bone quality assessment task. This model is utilized to detect different types of osteogenesis imperfecta disease in bone. Furthermore, it is demonstrated how this deep neural network, for the first time, can detect the osteogenesis imperfecta type automatically from high resolution peripheral quantitative tomography scans.

The last chapter is a conclusion of the work presented in this thesis. Moreover, the future possibilities with respect to basic research and clinical studies are provided in chapter six.

1.3 Data Source

The image data utilized in this work is categorized and acquired from three different sources:

1. 3D confocal laser scanning microscopy images of FtsZ protein networks, used in Chapter 4, were acquired at the Plant Biotech Lab, University of Freiburg, by Bugra Özdemir under supervision of Dr. Steffanie Müller and Prof. Ralf Reski.
2. μ CT images of mice (female C57Bl/6J) tibiae and fibulae, used in Chapter 5, were acquired by Dr. Annette Birkhold and Prof. Bettina Willie at Julius Wolf Institute, Charité Universitätsmedizin Berlin.

3. HR-pQCT images of adult human radii, used in Chapter 5, were acquired under the supervision of Prof. Bettina Willie at Shriners Hospital for Children - Canada, Department of Pediatric Surgery, McGill University in a study funded by Mereo BioPharma Group PLC.

1.4 List of Publications

The work leading to what is presented in this thesis has been previously published in the following publications.

Book Chapters

- R. Reski, B. Özdemir, **P. Asgharzadeh**, A. I. Birkhold & O. Röhrle. The plastid skeleton: a source of ideas in the nano range. In *Biomimetics for Architecture. Learning from Nature*. Birkhäuser Verlag GmbH, Basel. 2019. pp 163-166
- B. Özdemir, **P. Asgharzadeh**, Birkhold A. I., O. Röhrle & R. Reski. Das Plastidenskelett: ein Ideengeber im nano-Bereich. J. Knippers, U Schmid, T. Speck (Eds.): *Baubionik - Biologie beflügelt Architektur*, Stuttgarter Beiträge zur Naturkunde 82, Naturkundemuseum Stuttgart. 2017.
- **P. Asgharzadeh**, B. Özdemir, S. J. Müller, O. Röhrle & R. Reski. Analysis of *Physcomitrella* Chloroplasts to Reveal Adaptation Principles Leading to Structural Stability at the Nano-Scale. In *Biomimetic Research for Architecture and Building Construction*, Springer International Publishing. 2016 pp. 261-275.

Peer-Reviewed Articles

- **P. Asgharzadeh**, O. Röhrle, B. Willie & A. I. Birkhold. Decoding the Rejuvenation Effects of Mechanical Loading on Skeletal Maturation using in Vivo Imaging and Deep Learning. *Acta Biomaterialia*, 2020, 106, 193-207.
- **P. Asgharzadeh**, B. Özdemir, R. Reski, O. Röhrle & A. I. Birkhold. Computational 3D Imaging to Quantify Structural Components and Assembly of Protein Networks. *Acta Biomaterialia*, 2018, 69, 206-217.
- B. Özdemir*, **P. Asgharzadeh***, A. I. Birkhold, S. J. Müller, O. Röhrle & R. Reski. Cytological Analysis and Structural Quantification of FtsZ1-2 and FtsZ2-1 Network Characteristics in *Physcomitrella patens*. *Scientific Reports*, 2018, 8(1), 11165. [*Shared first authorship]

Conference Proceedings

- **P. Asgharzadeh**, B. Willie, A. I. Birkhold & O. Röhrle. Analyzing the Effect of Load-induced (Re)modeling on Bone Tissue Age using a Deep Neural Network. 25th Congress of the European Society of Biomechanics, July 7 - 11, 2019, Vienna, Austria.
- **P. Asgharzadeh**, B. Özdemir, R. Reski, A. I. Birkhold & O. Röhrle. Feature-based Classification of Protein Networks using Confocal Microscopy Imaging and Machine Learning. *PAMM*, 2018, 18(1), 1-2.

- **P. Asgharzadeh**, B. Özdemir, R. Reski, O. Röhrle & A. I. Birkhold. A Feature-based Deep Learning Approach for Classification of Protein Networks using 3D Live Microscopic Data. World Congress of Biomechanics, July 8 -13, 2018, Dublin, Ireland.
- **P. Asgharzadeh**, B. Özdemir, R. Reski, O. Röhrle & A. I. Birkhold. An Image Processing Framework to Quantify the Structure of Protein Networks. 23rd Congress of the European Society of Biomechanics, July 2 - 5, 2017, Seville, Spain.
- **P. Asgharzadeh**, A. I. Birkhold, M. Caliaro, O. Speck & O. Röhrle. Hydraulics of Vascular Fluid Transport in Herbaceous Plants using Theory of Porous Media. 23rd Congress of the European Society of Biomechanics, July 2 - 5, 2017, Seville, Spain.
- **P. Asgharzadeh**, B. Özdemir, S. J. Müller, R. Reski & O. Röhrle. Analysis of Confocal Microscopy Image Data of Physcomitrella Chloroplasts to Reveal Adaptation Principles Leading to Structural Stability at the Nano-scale. PAMM, 2016, 16(1), 69-70.
- S. Jamei, **P. Asgharzadeh** & W. Ehlers. Partitioned Treatment of Surface-Coupled Problems with Application to the Fluid-Porous-Media Interaction. PAMM, 2016. 16(1), 507-508.

2 General Background on Biological Network Structure and Functionality

If one considers the evolution as the architect of biological systems, it is much more realistic to imagine evolution as a experiencing entity rather than an engineer as suggested by Francois Jacob [158]. This means that instead of drafting a plan before creation (as an engineer would do), evolution assembles possibilities till meeting the needs of the system. This makes the convergence of to a solution found by evolution and engineering approach hardly possible. In this chapter, the concept of biological network structures and how this concept facilitates understanding structure-function relationship through an engineering point of view is briefly represented.

Biological networks depict biological systems in an abstract manner by apprehending essential attributes of them. The reader should be aware that in the context of this thesis, a biological network structure is not exactly the same classical/mathematical representation of a biological network, e.g. , graphs of protein signaling [41] although they have a certain share of similarities. In this regard, a biological network structure, is a modular, hierarchical and robust structure whose functionality is deeply entangled in every aspect of its structure. The concept of modularity, which is usually mentioned as a principle of biological networks [130, 153], is often what leads to the hierarchy observed in not only the structure, but also the functionality of the system as well. This modularity is similar in engineered systems where one uses modules, e.g., subroutines of code to perform specific tasks (functions) for performing a more complex task. Therefore, in the context of biological network structures, a module could be defined as: A set of connections (nodes) between simpler structural elements (points, segments) which have great interactions with each other to perform a sub-task of the system. A module has a strong interplay with other modules where this interactions allows performing complicated tasks as the goals of the evolutionary design. The next feature of the biological network structures is the robustness to tolerance. Since the structure should function in any realistic scenario, independent of severeness of inference or insult, which the system undergoes, to a great degree. These interference could contain a multitude of possibilities such as *Escherichia coli* undergoing tens of degrees fluctuations of surrounding temperature [295]. However, the structural and mechanical robustness is dominantly present in biological network structures; hence, this characteristic is investigated in this thesis.

In this work, the introduced concept of biological network structures as a platform to investigate structure-function relationship through the scales in two biological environments naming cytoskeletal protein networks and bone tissue is utilized. Exploring this relationship requires a basic understanding of the characteristics of these structures as well as their functionality. Here, these biological network structures are introduced and an overview of their functionality is provided.

2.1 Cytoskeletal Protein as an Example of a Network structure: a Brief Overview

The renowned developmental biologist, Paul A. Weiss, describes cells as a whole system "lest our necessary and highly successful preoccupation with cell fragments and fractions obscure the fact that the cell is not just an inert playground for a few almighty masterminding molecules, but is a system, a hierarchically ordered *system*, of mutually interdependent species of molecules, molecular groupings, and supramolecular entities; and that life, through cell life, depends on the order of their interactions" [7].

At any instance multiple processes are taking place inside this system (cell). The cytoskeleton, as a network of interconnected filamentous biopolymers, provides the cell the ability to transfer packages of material and information between cells, move and undergo deformations while maintaining the structural integrity. It has been recently shown that internal and external physical stimuli in form of forces can effect the mechanical and biological behaviour of the cell [161, 338]. The three main functionalities of the cytoskeleton are: to spatially arrange the content of the cell, to connect the cell to the surrounding environment and to manage the dynamics of force generation in the cell resulting in movement as well as change of morphology [100]. This is achieved by the interplay of a multitude of cytoplasmic proteins and organelles.

The modular structural elements of the cytoskeleton have been thoroughly investigated *in vitro*. The advancements in light microscopy, recently, has enabled the investigation of spatial and temporal characteristics of cytoskeleton structure. For instance, it has been shown that there exists up to 150 proteins which contain binding domains for the actin protein, as one of the major cytoskeletal biopolymers [79]. Wave complex, a molecular formation of actin regulators [225], has been demonstrated to create travelling waves correlating to cell protrusion using high resolution light microscopy [355]. This and many similar observations point towards the idea of a strong bond between the structure of the cytoskeletal biopolymers and the structural functionality of not only the cytoskeleton but also the whole cell. Despite the ever growing list of the proteins interacting with cytoskeleton, the three cytoskeletal protein networks associated with the structural functionality of eukaryotic cells are microtubules, actin and intermediate filaments [297]. In the context of this thesis, a protein network is defined as a modular network structure with biopolymer molecules as building blocks.

2.2 Cytoskeletal Structural Blocks

As introduced before, there exists a high level of modularity in the cytoskeleton. The proteins of the cytoskeleton consists of multiple copies of small protein blocks forming a relatively large structure. Therefore, depending on the assembly of these pieces, many structural formations are possible. The three cytoskeletal protein networks control the morphology and mechanics of the cytoskeleton structure. All these proteins types form networks that have specific mechanical behaviour, can undergo deformation and can re-assemble themselves to respond to external stimuli such as forces. The force is produced in cytoskeleton through a combination of polymerization and depolymerization of actin filaments and microtubules. This also leads to dynamic changes of cell shape. Moreover,

molecular units (motors) moving along the protein filaments enable transportation of material as well as organization of organelles. The overall structure of these protein networks are regulated by multiple classes of proteins: filament forming nucleation-promoting factors, growth terminating capping proteins, growth promoting polymerases and stabilizing protein such as crosslinkers. The distinguishing characteristic of these protein networks are the mechanical resistance to deformation (stiffness), the rate of assembly and their associated molecular motors [100].

Microtubule, the cytoskeletal protein network exhibits the highest stiffness and possess the most complex assembly/disassembly behaviour of the cytoskeletal protein networks. Proteins of microtubules have a extremely high persistence length (5 mm), which is the measure used for describing the stiffness of biopolymers. Microtubules have a hollow polymeric structure with 25 and 17 nm external and internal diameters made from two isoforms of tubulin [293]. Filaments of microtubules are prone to buckling under compression [40]. This stiffness comes into play in the interphase part of the cell cycle where chromosomes of the cell are separated into two.

Actin filaments show considerably less rigidity in comparison to microtubules, due to having many crosslinkers binded to their network. The network structure is highly organized and can undergo relatively high mechanical forces [100]. The filaments have a double helical form made from two spiraling strands. The actin protein networks consist of groups of aligned filaments which enables filopodial protrusions which is a key factor in communications between cells. Moreover, the actin filament network is involved in force generation required for active changes of cell shape, e.g., the process of phagocytosis. They dynamic behaviour of actin filament network is caused by constant elongation of the filaments which makes it suitable for creation of the tension forces required for cell movement (migration) [269]. Another distinguishing aspect of actin protein network is that, unlike microtubule, as a response to the local signals transmitted in cell, it is constantly being assembled and disassembled. This behaviour is for example seen in migration processes such as crawling leukocytes where the actin proteins are steadily assembled in the frontier edge of the cell and enable the cell to move by providing forward tension forces [257].

Intermediate filaments exhibit the least stiffness in cytoskeletal protein networks and can mainly withstand tensile forces. In the network of intermediate filaments, crosslinking amongst themselves as well as to other biopolymers of the cytoskeleton has been reported [358]. It has been shown that cells form intermediate filament networks in case of experiencing mechanical stress [101]. furthermore, intermediate filament network contributes in the structural integrity of the eukaryotic nucleus. However, due to not being polarized, it does not play a role in the dynamic/active mechanical behaviour of the cytoskeleton.

The above mentioned mechanical functionality of the major cytoskeletal protein networks is only a few examples from a long list. To study the structure-function relationship in the protein networks creating the cytoskeleton, the next logical step would be to understand their mechanics. In the next section a summary of mechanical models developed for representing the behaviour of these protein networks is provided.

2.3 State of the Art in Modelling Cytoskeletal Protein Network Structure

The cytoskeleton is the main player in cellular mechanics. Analyzing the mechanical behaviour of the cytoskeleton is a common approach for understanding the mechanics of cells. There exist two main goals for mechanical activities of cells naming maintenance and transportation of intercellular signals as well as materials. At first glance, it is observed that cells exhibit a viscoelastic behaviour [350]. This means that after experiencing a deformation, cells tend to recover their original shape. This is of course dependant on the magnitude of deformation as well as its duration. The recovery takes place in a viscoelastic manner. This is due to the fact that cells are capable of storing elastic energy and they can dissipate this energy by viscous friction, which is based on the rate of deformation being applied to them. It is a common practice to consider cells as incompressible entities [84]. The most simple viscous behaviour can be expressed in terms of a one-dimensional combination of linear springs and dampeners. From this, the elementary viscous solid model can be build by having a spring in parallel to a series of a spring and a dampener. This model considers cells as a homogeneous entity and absolutely ignores the details of structural elements inside the cell. The mathematical representation of such model can be described by:

$$\sigma(t) = \int_{t_0}^t G(t - t_0) \delta \epsilon, \quad (2.1)$$

where σ , $G(t)$, t_0 , t and ϵ represent the stress, relaxation module, starting time, end time and strain respectively. Although this models provides a good basis for understanding the mechanical cell behaviour as a whole, it is not at all efficient in explaining different mechanical functionality of structural elements of cell.

Another simplistic approach to model the cytoskeletal mechanics is the concept of tensegrity structures developed by Donald Ingber [154]. The tensegrity concept is based on the idea of "tensional integrity rather than compressional continuity" in the structural elements of the cytoskeleton (Fig. 2.1).

A tensegrity model, similar to a rheological model, tries to represent the whole cytoskeleton as a modular structure consisting of continuous tension elements (cables) and discontinuous compression elements (rods). Originating from a class of architectural designs, this model can explain the process of adaptive integrity of cytoskeletal network structure. The concept is created to study force distribution in geodesic domes. Such a model is fundamentally different to the approach of this work which aims to analyze the structure to understand it relationship to function. Nevertheless, the tensegrity model is the first of its kind to try to relate the mechanical characteristics of the cytoskeleton to its architecture/structure rather than its material characteristics. It is worth mentioning that regardless of its simplicity, this model is to some extent capable of providing clarification on "how can these structure undergo deformations while maintaining their structural integrity?". This is done by creating a rather complex network of two aforementioned elements, which can regulate the forces in the structure by deforming the continuous tensional elements and adapting the non-deformable compressional elements. Although the concept of tensegrity structure is quite helpful in understanding the approach of cytoskeletal networks in dealing with deformations, it is clear that to find better insight on the mechanics of the networks, one requires more sophisticated/detailed models. Con-

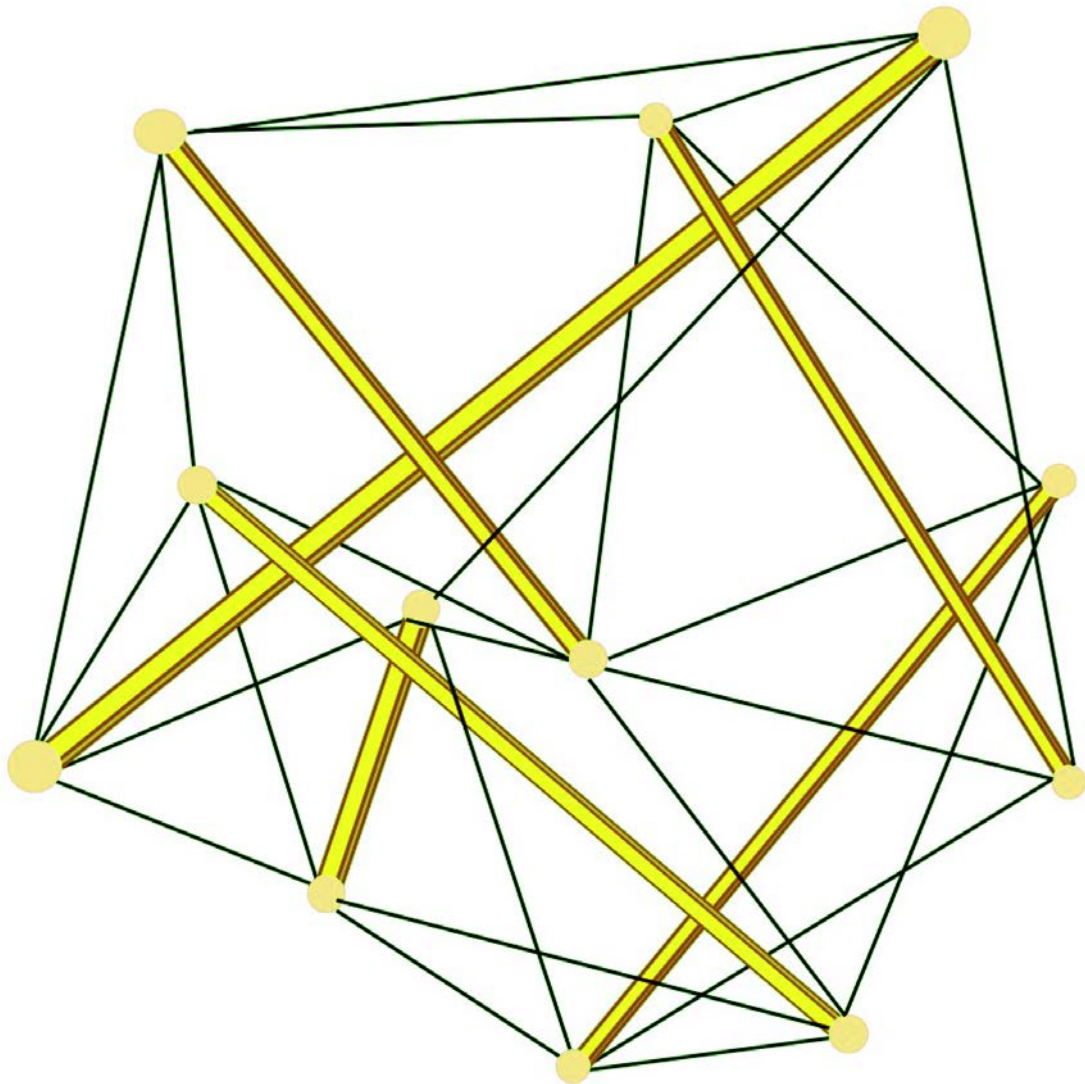


Figure 2.1: *Schematic of representation of a tensegrity structure with a continuous tensional element (green cable) and multiple rigid compressional elements (yellow rods).*

tinuum mechanics has been the prevailing playground for creating mechanical models of biological environments in the last half century and can provide the tools needed to create such models for cells and cytoskeletal protein networks. A series of such models for cells as a bulk are introduced and then more specific models for cytoskeletal protein networks are provided.

2.3.1 Nonlinear Continuum Mechanics of Cells and Protein Networks

In the context of cell mechanics, continuum mechanics models pursuit to represent the mechanical behaviour of a cell as a homogenized bulk rather than including the details of interaction of different elements inside the cell [113, 267, 330]. Continuum mechanics is based on a series of conservation principles naming conservation of mass, linear mo-

mentum, angular momentum, energy and entropy. The first three conservation principles can be shown as:

$$\frac{d}{dt} \int_V \rho dV = 0, \quad (2.2)$$

$$\frac{d}{dt} \int_V \rho \dot{\mathbf{x}} dV = \int_{S=\partial V} \mathbf{T} \mathbf{n} dS + \int_V \rho \mathbf{b} dV, \quad (2.3)$$

$$\frac{d}{dt} \int_V (\mathbf{x} \times \rho \dot{\mathbf{x}}) dV = \int_S (\mathbf{x} \times \mathbf{T}) \mathbf{n} dS + \int_V (\mathbf{x} \times \rho \mathbf{b}) dV, \quad (2.4)$$

with ρ and V representing the density and volume of the body undergoing deformation, $\dot{\mathbf{x}}$ denoting the velocity, \mathbf{t} representing traction, \mathbf{T} as the Cauchy stress tensor, \mathbf{n} as the unit vector perpendicular to surface element dS , \mathbf{b} as the body force, t as time and x as the distance of each point on the body from the reference point of the angular momentum. Eq. 2.4 implies the symmetry of the stress tensor i.e. $\mathbf{T} = \mathbf{T}^T$ and Eq. 2.2 could be considered as the preservation of volume. The nonlinearity of the system arises from Eq. 2.3. Finding an analytical solution for this complex system of equations is very cumbersome, if not impossible. This calls for numerical methods for finding an approximate solution to the system of equations. Recently, finite element (FE) method has been the go to discretisation approach for carrying out a numerical solutions of such systems of equations [382].

The elastic/viscoelastic behaviour of the cell is represented in Eqs. 2.2 and 2.3. It is common to consider quasi-static condition for modeling the behaviour of the cell. This means that the velocity and acceleration terms in these equations will vanish. Furthermore, it is also a common practice to neglect the inertia terms due to the very small mass of the cell [275]. However, one can consider the drag force of intercellular elements by introducing a viscous component to the momentum equation. Moreover, continuum mechanics is utilized to represent the mechanical behaviour of cell in multi-physics setup as a smeared out porous body where the protein networks are considered a homogeneous porous structure, saturated with a viscous interstitial fluid [317, 327].

The continuum mechanics concept would implement regional variation in the model's mechanical response to describe the inhomogeneity of the body. This is performed by specifically developing a constitutive equation for the overall cell behaviour. Such constitutive equations are derived in a two step process: 1) performing experiments to identify a mechanical behaviour of the subject (cells, biopolymer network or a protein filament) and 2) finetuning and validating the model in an observatory manner with experimental approaches. In chap. 3 a comprehensive detail of such methods and the analysis process is provided. Although this approach to modeling the mechanical behaviour of biological network structures seems highly intuitive, the main disadvantages lie in practicality of performing the aforementioned steps. With this concept at hand, more detailed mechanical models for each of cytoskeletal components has been developed. An overview of these models are provided in the next section.

2.3.2 Mechanical Models of Cytoskeletal Protein Networks

Schaap et al. showed that microtubule filaments exhibit a linear stress-strain relationship [293]. This relationship is obtained using atomic force microscopy (AFM) experiments

where a cantilever beam is pushed against the object and its deflection is measured using a laser beam. Afterwards, by using contact mechanics knowing the mechanical properties of the cantilever beam, it is possible to extract the stress-strain relationship of the object [290]. Furthermore, it is shown that up to a strain value of 0.15, the microtubule filaments behave elastically and then exhibit plastic behaviour [131]. A classical Euler-Bernoulli beam can be a suitable surrogate model for microtubule filaments based on a very high effective length relative to their thickness. This provides directly the mechanical framework to investigate the buckling of these filaments [62]. Such an approach enables investigating the vibrations in filaments as well. Although it was shown that microtubule plays a significant role in the overall morphology of the cytoskeleton as well as in its dynamics, a lack of developed mechanical models for microtubule is evident. Particle dynamics has been used by Allain et al. [6] to create a dynamic model of microtubule network. Moreover, Buxton et al. [50] further developed a microtubule protein network model based on the Bernoulli beam concept.

Actin is the most investigated cytoskeletal protein network in terms of mechanical behaviour. An increase in length as well as density of the filaments in the actin network results in an increase in stiffness [110, 160]. The length and density are both regulated by biochemical and mechanical signals; hence, such signals can dictate the shape of the cytoskeleton according to the functional requirement. Various mathematical models have been developed to represent the mechanics of these networks with regard to their functionality. For instance, coarse-grained Brownian dynamic models are capable of representing a portion of the networks features. Utilizing such models provide insight to interactions between different components of the cytoskeleton which might be impossible to observe by methods such as live cell microscopy imaging [178]. The bending of filaments and stretching of the proteins is the approach of the networks for absorbing the energy from the external force. Moreover, the actin filaments dictate the shape of cytoskeleton mostly through disassembly rather than unfolding [178]. Brownian dynamics have been used by Lou et al. [221] to study cytoskeletal reorganization of actin protein networks during micropipette aspiration. This process was shown to be successful by utilizing microscopy imaging of green fluorescent protein (GFP) fusion proteins. This led to understanding the distribution of myosin II and crosslinkers at the membrane [221]. A direct result of this model is that the response of crosslinkers of the actin protein network to certain deformations are different among them. Although this finding was validated by imaging techniques, it was only possible through mechanical modeling of the network.

The most recent computational model of mechanical behaviour of cytoskeletal protein networks is based on non-local elastic theory developed by Eringen [91]. In this model, one can consider the nonlocal Euler-Bernoulli beam model by Civalel et al. [61] to investigate the bending of microtubule filaments. In this approach, as mentioned before, a microtubule filament is considered a classical Euler-Bernoulli beam from which one would be able to calculate bending value based on forces being applied to it. The nonlocal elasticity deviates from the classical elasticity theory by considering the atomic forces that arise when different parts of small structure (protein network) get close to each other. This is due to the fact the classical elasticity runs into conflicts with atomic theory of lattice dynamics. Nonlocal elasticity provides a set of differential equations which describe the deformation of a homogeneous isotropic body. By considering a series of simplifying assumptions, one can transform them into a set of partial equations for which analytical solutions can be

determined. The nonlocal elasticity theory assumes that strain values at all points in a body influence the stress value at each point of the body (in contrast to classical elasticity where stress of a point is only dependant on the stress of that point, [91]).

The impact of all the points in the body on the stress value of one point comes into play by introducing a scale effect in the constitutive equation. In nonlocal elasticity, the underlying equations have spatial integrals depicting the weighted averages of influence of strain values at all the points on the point of interest in the body. Therefore, in the constitutive equations of nonlocal elasticity a length factor is present. In case of a homogeneous, isotropic elastic material, the theory is presented in the following formulation:

$$\operatorname{div} \boldsymbol{\sigma} + \rho(\mathbf{b} - \frac{\partial^2 \mathbf{u}}{\partial t^2}) = 0, \quad (2.5)$$

$$\boldsymbol{\sigma}(\mathbf{x}) = \int_V \alpha(|\mathbf{x} - \mathbf{x}'|, \chi) \boldsymbol{\tau}(\mathbf{x}') \, dV(\mathbf{x}'), \quad (2.6)$$

$$\boldsymbol{\tau}(\mathbf{x}') = \lambda \boldsymbol{\varepsilon}(\mathbf{x}') \boldsymbol{\delta} + 2\mu \boldsymbol{\varepsilon}(\mathbf{x}'), \quad (2.7)$$

$$\boldsymbol{\varepsilon}(\mathbf{x}') = \frac{1}{2} \left(\frac{\partial \mathbf{u}(\mathbf{x}')}{\partial \mathbf{x}'} + \frac{\partial \mathbf{u}(\mathbf{x}')}{\partial \mathbf{x}'} \right), \quad (2.8)$$

with \mathbf{x}' as the velocity vector, $\boldsymbol{\sigma}$ as the nonlocal stress tensor, \mathbf{u} as the displacement, $\boldsymbol{\tau}$ as the Cauchy stress tensor, \mathbf{x} being the position vector of the point in reference configuration, \mathbf{x} as the position vector of the point in actual configuration, $\boldsymbol{\varepsilon}$ as the strain tensor, $\alpha(|\mathbf{x} - \mathbf{x}'|)$ denotes the Euclidean distance, χ as material constant and λ and μ are the Lamé constants. The nonlocality comes with $\alpha(|\mathbf{x} - \mathbf{x}'|)$ where the distance to other points influences the strain at the point of interest. The atomic characteristics of the material such as lattice parameter and granular distance dictates the value of α .

As for the case of nonlocal elasticity, these equations could be transformed into a weak form and solved using numerical methods. Although, nonlocal elasticity introduces a meaningful depth to the mechanics of cytoskeletal protein networks, its practicality is restrained to analyzing the behaviour of single filaments. This is mostly due to the fact that in case of having a complex network of filaments, the distance kernel ($\alpha(|\mathbf{x} - \mathbf{x}'|)$) needs to be precisely considered. Moreover, the computational costs of numerical solutions of the nonlocal elasticity equations often outweighs the precision gains in mechanical representations. Furthermore, the required material parameters requirer extensive experiments which up to this point have not been carried out for all of the cytoskeletal protein networks.

Utilizing more comprehensive mechanical models to describe cytoskeletal protein networks specific lead to knowledge with respect to its behaviour. However, one should consider the level of precision required for the specific problem. In our case, which concerns with the structure-function relationship of the network as a whole, the atomic behaviour of the proteins is not the key. Therefore, choosing a linear elastic material law to model the behaviour of the protein network is sufficient [118, 205]. This is due to the fact that the errors introduced by this choice are negligible when it comes to analysing the mechanical behaviour of the whole network; hence, linear elasticity is up to this point the go to model for the analysis of whole network structures.

The introduced cytoskeletal protein networks are extremely complicated structures and many questions can not be answered. Since the main goal of this research is to present a

completely new methodology to analyze structure-feature relationship in biological networks, a simpler network structure was needed to be able to develop ideas and validate the results of the developed algorithms. This validation process is mostly performed by utilizing manually made gold standards. Therefore, a simpler protein network structure with same polymer characteristics and similar structural functionality was needed for this work. Such network can be found in Filamentous Temperature Sensitive Z (FtsZ) proteins. In the next section, a brief introduction to FtsZ protein network and what makes it a great playground for the development of our methodologies is provided.

3 Quantitative Imaging and Machine Learning

3.1 Biomedical Imaging

Images, are one of the main components in a data-driven analysis of the structure-functional relationship in biological networks. This means that images are either directly analyzed or indirectly after being put through an image processing framework. Imaging techniques depends mostly on the scale of the structure of interest. This includes various forms of microscopy modalities, e.g., light microscopy at nano- and micro-scale structures and X-ray tomography at macro-scale structures. In this chapter, the imaging processes and the ML method utilized to acquire and analyze the data in this thesis are introduced.

3.1.1 Imaging on the Nano-scale: Quantitative Imaging of Cytoskeletal Protein Networks

Processes such as organelle organization, adaptive structural deformation and cytokinesis can be visualized and studied using live-cell light confocal microscopy. In a perfect setting for imaging cytoskeleton, the environment is non-toxic and far-red emissions and excitation wavelengths are present [220]. Confocal imaging of cytoskeletal protein networks such as microtubules and actin is possible through connecting fluorophores to taxanes and phalloidines that can bind to microtubules and F-actin filaments, respectively [19, 365]. At the moment, one can find many repertoire of genetically encoded fluorescent proteins that allow visualization of cytoskeletal protein networks [283]. Through the development of methods such as CRISPR/Cas9, biochemists can now perform more effective fusion of the fluorescent proteins to the proteins of interest [76, 253]. At this point, confocal microscopy can acquire subcellular resolution. More advanced microscopy techniques such as light-sheet microscopy allow demonstration of the embryonic development with great resolution [173]. This requires new algorithms that are capable of handling the large amount of produced image data. Moreover, the possibility of having large image datasets on specific protein structures, calls for computational techniques that can quantitatively analyze the structural information embedded in images. Quantitative imaging approaches are being used not only in case of cytoskeleton research, but also in many other fields of developmental biology.

As discussed in chapter 2, the structure of cytoskeletal proteins is a result of an evolutionary design process base upon a structure-function relationship. During their development, cytoskeletal protein networks undergo dynamic assembly and disassembly based on internal and external stimuli. One possible approach to investigate the applied forces on the cytoskeletal protein networks is by determining the orientation in these networks [379]. If many filaments of the network are aligned, one could use a 1D Fourier transform

along an axis perpendicular to the filament direction to determine the frequency pattern of the network [58]. To scale up to 2D quantitative description of protein networks, edge detection methods can be utilized to calculate the orientation of fibers from the 2D microscopy images. For instance, using edge detection methods, Wirsching and Cram showed the dependency of the mechanical response of the cytoskeleton in case of stretch to myosin II activity [363].

Conventional edge detection techniques aim to determine the alignment of filaments through pixel coordinates. In the past few years, a series of new algorithms have been developed to look more closely into the structure of protein networks through quantitative imaging algorithms. For example Xu et al. [370], introduced SOAX as a tool to quantify 3D connectivity of protein networks and analyze the curvature of the network structures. SOAX has been used to determine the coordination and connectivity of actin filaments in yeas [368]. Such algorithms work based on the idea of active contours [56]. The underlying idea of such algorithms is to combine classical edge detection methods with a growth model that aims to let filaments grow on the image based along their calculated curvature.

The process of filament tracking could be extremely difficult in presence of high noise or complex networks. Moreover, the first required step for such methods is always segmentation of the image, which could be very cumbersome on its own. Therefore, researcher have used a coarse grain orientation of the filaments of the cytoskeletal protein networks to assess the orientation changes due to mechanical forces [37, 55]. This approach utilizes a 2D Fourier transform on moving 2D image window to capture the orientation of the filaments. Other approaches are based on creating a shape matrix (structural tensor) from local intensity gradients, which are obtained from a moving window across the image [273]. In such methods, the eigenvectors of the shape matrix provide information about the orientation of the network. In case of the local 2D window on the image, the first eigenvector shows the orientation of the filaments in that window. One could estimate the homogeneity of orientation in the network by analysing the similarity of the orientations in different windows across the network. Such analysis has been used to analyze the filaments of microtubule in *Arabidopsis* [216]. Such quantitative analysis of filament orientation in cytoskeletal protein networks is mainly performed to see the effects of mechanical forces on the cell.

Despite the recent interest in quantitatively analyzing the structure of cytoskeletal protein networks, there are still many aspects that cannot be described with existing methods. For example, details of connectivity of filaments such as number of meeting filaments in connections, the angles between them, the local changes in properties of the filaments such as their thickness and many more cannot be extracted using the aforementioned methods. Therefore, to proceed with correlating the structure to functionality of biopolymer network, a method is developed that would extract a set of structural features with which one could quantitatively describe the network structure. Details of the developed method, its validation and applications is presented in [4.2].

Confocal Laser Scanning Microscopy

As far as the biopolymer protein networks, the CLSM data was obtained in a joint project within SFB TRR141 project. The acquisition was carried out by Bugra Özdemir and Ralf Reski. In the last two decades, many different imaging techniques such as CLSM [137],

atomic force microscopy [135], cryo-electron tomography [162] and stimulated emission depletion (STED) nanoscopy [81] has been used to visualize cytoskeletal protein networks in 2D and 3D images. However, CLSM is the most common imaging technique in the most recent protein network analysis research. Since the main source of images used in this thesis is CLSM imaging, in this section, a short overview of this imaging technique, its advantages and its shortcomings is provided.

CLSM has been the most used imaging instrument to examine subcellular structures. This holds specially in case fluorescent microscopy. The most important advantage of CLSM over older generation fluorescent microscopy methods is its ability to decrease out-of-focus flare and therefore increase the sharpness of images and increasing resolution in z direction (perpendicular to imaging plane) [138]. CLSM has been specifically useful in the field of plant cell research where smaller size cells were proven to be more difficult to image and analyze.

During the past decades, fluorescence microscopy has been increasingly used to investigate dynamics of plant cells [214]. Immunofluorescence, made fluorescence microscopy an extremely powerful tool to portray live cells. Moreover, the possibility of tagging proteins with fluorescent agents made a breakthrough in visualizing these building blocks of life. Nowadays, GFP-tagged protein can be imaged by CLSM technique at resolution higher than light microscopy [138].

There exist a series of important restrictions for CLSM imaging. For instance, acquiring sharp images along the z -axis of imaging was proven to be particularly difficult. This is due to emanation of light from different directions towards the specimen at the vicinity of the focal plane resulting in confusion of the focusing signal [360]. In case of the investigated plastids, this could be specially troublesome where the chloroplast could have a substantial thickness in the direction of imaging; whereas, in animal cells cultured for imaging, this might not be the case. To overcome this difficulty, different approaches such as fixing and embedding the cells [45] or compressing the cell [359] has been used. However, such techniques are obsolete for the case of quantitative analysis of protein structures and further correlating the structure to its dynamic functionality.

For a comprehensive explanation of principles of CLSM, the reader is referred to the book of White et al. [357]. Here a short overview of the technique is provided. In wide-field epifluorescence microscopy, an excitatory light converges to an expanding from the focal plane when it hits the entirety of the subject placed at field of view. All the excited regions emit the fluorescent signal, which together form the captured image. This results in a great contamination of signals from other planes that are not being imaged yet emitting fluorescent. As a result, the signal-to-noise ratio decreases drastically. In CLSM, only a minimal portion of the subject is illuminated rather than the whole body. The lenses used in light microscopy require a point spread function (PSF) since they can not focus on an specific point. PSF describes the diffracted shape of the volume of interest. The laser beam passing through a optical fiber is converged when passing through an objective lens after exciting the specimen. Afterwards, the focused fluorescent emission goes toward another small aperture objective, behind which the image is created. This is done by means of a photomultiplier tube.

This complex process of CLSM microscopy enables visualizing the cytoskeletal protein networks. Moreover, this technique is used to collect the images used for quantitative analysis of FtsZ networks. In 4.2 a more detailed process of CLSM imaging FtsZ including

the performed biochemistry is presented.

As the CLSM of fluorescence-labelled FtsZ in *Physcomitrella patens* reveals complex geometrical patterns and as chloroplasts in loss-of-function mutants show distinct shape defects, polymers of FtsZ might provide scaffolds ensuring the stability and structural integrity of plastids [277]. This hints to a clear skeletal functionality of FtsZ isoforms; Thus, the term plastoskeleton was coined for FtsZ polymers in *P. patens* plastids [277]. These FtsZ networks are reminiscent of geodesic domes in architecture [10]. Similar FtsZ networks are not described for chloroplasts from other land plants, which might be due to the fact that *P. patens* chloroplasts are evolutionary intermediate between free-living bacteria and fully domesticated plastids of higher plants [279]. Because of this intermediate position and its many experimental advantages, *P. patens* chloroplasts are suitable objects for live-cell visualization and subsequent modelling [157].

3.1.2 Imaging on the Micro- and Macro-scale: Bone

In this section, an overview of the most common and advanced techniques in imaging the structure of bone is provided, its micro-/macro-architecture, morphology and (re)modeling. The classical technique to study bones is by means of histology. Current state of the art imaging techniques such as μ CT and HR-pQCT imaging enable visualization of the 3D structure of the bone in a relatively noninvasive manner.

High-resolution X-ray Tomography

μ CT permits the visualization of high-resolution 3D structure of bone. It became standard method of quantitatively describing bone tissue level. μ CT utilizes X-rays to create a 3D portrayal of the internal structure of the bone. To do so, the X-ray attenuation distribution of the imaged bone is captured as a 3D image. This process is possible by an X-ray beam traversing through the bone and being attenuated by projection of internal structure of the bone along its way. After capturing and converting the altered X-ray beam to electric signal, a 3D matrix where each cell can correlate to bone structure is created.

Although Bohemian mathematician Radon developed the main idea of tomography in 1917, it wasn't until 1960 when the computer technology drastically progressed that the X-ray tomography became feasible. In 1963, Allan M. Cormack, who calculated radiation absorption distributions of tissues in a body, used this technology for the first time in biomedical imaging [65]. The first CT scanner was built in the 1970s, which led to its creator Godfrey Hounsfield receiving the noble prize for Physiology and Medicine together with Allan M. Cormack. In the 1980s, researchers started using CTs and by imaging with longer exposure and higher resolutions. In 1989, Feldkamp et al. [95] was the first to use μ CT to image trabecular bone. Since 1994 commercial μ CT scanners are available and increasingly used by researchers to study bone micro-structure.

The bone imaging technology has improved drastically in recent years, which has led to improvement in visualization and knowledge of bone micro/macro-architecture. In research, HR-pQCT has become one of the prevailing bone imaging technique in the recent years. HR-pQCT utilizes computational analysis of X-ray attenuation to acquire sectional images [108]. HR-pQCT is commonly mistaken with μ CT, but in fact these terms are not inter changeable. This is due to the great difference of image resolution in the two techniques (μ CT up to a fracture of μ m and HR-pQCT 30 – 273 μ m nominal isotropic

pixel size). The resolution of HR-pQCT is marginally higher than structural details of trabecular bone compartment [108]; therefore, it allows resolving the trabecular bone structure. At the moment, two commercial HR-pQCT machines are available for acquiring 3D scans of human bones allowing to resolve bone micro-architecture (XtremeCT, SCANCO Medical AG, Brüttisellen, Switzerland). However, two different generations of these scanners are available (Xtreme CT I and II).

Bone Structural Parameters

From the acquired CT image, one can calculate a series of structural parameters to quantitatively track the structure of the bone. These parameters can then be used to quantitatively characterize the structural changes taking place in bone as a result of mechanical loading, disease, or effects of treatments.

CT images enable a 3D visual interpretation of bone micro-structure containing its multi-scale nature. However, the amount of information embedded in these images is too high to be evaluated manually. Therefore, the first and most common approach up to now has been to reduce the dimensionality of the image data by to deduce predefined bone parameters. This allows a more feasible assessment of bone quality. Morphometric indices [39] extracted from binary images are introduced to carry out this dimension reductions. It is important to notice that, morphometric indices are commonly calculated based on the segmented image of the bone, since the determining algorithm can not differentiate between bone and surrounding tissue. This segmentation is usually performed by a global threshold. The fundamental structural, material properties and dynamics difference between cortical and trabecular compartments of the bone calls for a separate analysis of them. This is done by defining a region of interest (ROI) in which only one of these bone compartments is present, before calculating the indices in the selected ROI. Table 3.1 shows a series of most commonly determined trabecular and cortical indices which usually can be automatically calculated in commercial softwares. It is clear that these indices provide an description of the static state of the bone. Only very recently, researchers have been focusing on time-resolved analysis of bone structures. For instance, Birkhold et al. [28] have looked at aging/loading-induced (re)modeling of bones by developing a 4D imaging framework to quantitatively analyze bone structure dynamics [32].

Although these parameters are currently the go-to measurements for describing bone quality, weather in terms of setting thresholds to calculate fracture possibility [169] or to measure skeletal aging [280], there exists two main restrictions to the use of such parameters:

1. The simplicity of their definition can not always express the complex manifestation of bone structural multi-scale alterations due to aging or bone diseases such as osteoporosis.
2. The attempt in finding correlations between the state of the bone (healthy/diseased, young/old and immature/mature) and the morphometric indices could be sometimes obsolete as the interplay of different bone structure modifications from any internal and external stimuli on bone could be not present in these indices.

However, since structure of the bone, down to its smallest structural block, is already

Variable	Sign	Description
Bone volume fraction	BT/TV	Ratio of bone volume present in ROI to total volume
Trabecular thickness	Tb.Th	Mean thickness of trabeculae
Total area	Tt.Ar	Total cross-sectional area of the periosteal envelope
Cortical thickness	Ct.Th	Mean cortical thickness
Trabecular number	TB.N	Mean number of trabeculae per unit length
Cortical area	Ct.Ar	cortical volume (Ct.V) / ROI height
Trabecular separation	Tb.Sp	Mean distance between trabeculae
Cortical area fraction	Ct.Ar/Tt.Ar	Cortical area / Total area

Table 3.1: Common calculated morphometric indices.

captured with the high-resolution image data, if one could automatically correlate the structure/image to the interested state, it would be possible to avoid calculating such parameters. Moreover, this might allow an automatic extraction of any structural features related to these functionality/dysfunctionality states. However, it is mentioned that the huge dimensions of these data was the initial reason to introduce these indices. The solution might be found in automatic data analysis; hence artificial intelligence and machine learning. ML methods and specifically deep learning enable correlating structured data to structural concepts in an automatic manner. It is very clear that such correlation can be made only in case of a real manifestation of the concept in the data available.

3.2 Machine Learning-based Image processing

The main goal of machine learning (ML) is to find a solution for a problem by creating self improving computer models. At the time of writing this thesis, ML is one of the most active fields of research and a great number of researchers have decided to investigate development of ML models to answer scientific questions in almost any field of research that can gain knowledge by mass production and analysis of data. ML as the intersection of mathematics, statistics and data science has seen a great success in recent years due to development of new training/learning algorithms as well as exponential growth in availability of data. ML models are currently being used not only in scientific research, but also in manufacturing, finances, marketing and health care industries [166].

On its core, ML aims at answering two deeply connected questions: 1. How can models improve their functionality/usability through learning from the consequences of their actions? and 2. What are the underlying laws that holds for any learning system including humans and machines? Although most of researchers focus at answering the first question, one should not forget that without investigating the second question, finding a solution to the first one is not possible.

ML started as an abstract concept and improved drastically over the last three decades to achieve a state in which it has a practical use in our every day life. ML as one of the dominant aspects of ML as proven to become the go to approach for creating computer models in fields of computer vision, natural language processing, speech recognition, robotics and maybe the most prominent of all, image processing. The desired approach of creating ML models in almost all of the fields is to train them on examples of possible decisions-consequences. This is fundamentally different than the classical creation of computer models where a set of rules is defined and created for to meet decisions in different scenarios. Basically, ML models learn to automatically come up with any possible set of rules to map the input information domain to the output domain.

Learning, can be described as the progression of performance in execution a task e.g. improving decision making, measurements or predictions based on a training experience. For instance, in the case of detecting lung nodules from chest X-ray scans [150], a model is trained based on observing the scans and the location of nodules and is asked to find them in a scan. Afterwards the model will be informed of the correctness of its decision and this process is repeated to achieve higher performance in lung nodules detection task.

Various ML models has been developed to handle the wide variety of data as well as problem types [46, 71]. In an abstract form, ML models can be seen as an automatic search for a mathematical function that provides the desired output. The key concept here is that the function is not dictated to the model. It rather will be found by the model itself, hence, artificially intelligence. There exist a wide variety of approaches for the search process and optimizing the desired function. The function approximation in case of detecting lung nodules will be as follow: image as the input, a vector containing the coordinates of the nodule as output (0 output in absence of nodules).

Regardless of the training model, a major challenge in terms of practicality as well as scientific validity of the model is characterization of the capability of the model; hence, measurement of its performance. In this regard following questions need to be answered:

1. What is the accuracy of the learning process during training?
2. To which level is the model capable of handling the errors in its learning process as

well as errors present in the training data?

3. Is it actually possible to map the learning data to the desired output? Or in other words, is there actually a set of underlying correlations to be learned?
4. Can the ML model be used to extrapolate results from its learning data? How far can this extrapolation be considered truth worthy?

These questions need to be very carefully considered when choosing ML models. Specifically, in case of biomedical engineering, where mistakes may have drastic influences on diagnosis and therapy of patients.

3.2.1 State of the Art

The widely utilized ML-based models follow the concept of supervised learning [185]. Supervised learning is currently used for applications such as face recognition and medical image analysis. In supervised learning, the model is trained to produce specific outcomes about which the model knows. This is in contrast to unsupervised learning, in which the model is responsible for finding a possible pattern in the data without knowing what the model designer expects from it [20]. This makes supervised learning for tasks such as biomedical image analysis e.g. disease detection, image classification and image segmentation an ideal case. Supervised learning models usually learn a function $f(\mathbf{x})$ which maps the input \mathbf{x} to a probability distribution to the possible outcomes of \mathbf{y} . There are various possibilities for creation and optimization of $f(\mathbf{x})$ e.g. ensemble methods [77], logistic regression [33], support vector machines (SVM) [336], convolutional neural networks (CNN) [117] and Bayesian classifiers [33].

Here, the source of information on biological network structure is image data. ML could potentially enable us to correlate the structure captured in images to the desired functionality. This desired functionality is a specific mechanical response of biopolymers which will be, for example aging/loading-induced (re)modeling and manifestation of OI diseases in bone, respectively. The ML-based models developed herein are either partially or entirely created as image classifiers.

3.2.2 ML-based Image Classification

ML image classifiers aim to automatically extract relevant features correlating images to a certain class. The features are extracted based on texture, morphology, pixel intensities, color channels and a combination of any other information stored in the images. Such classification task may in certain cases be trivial for humans, but the concept of automatic extraction of related features makes classification a challenging task for machines; hence, a great playground of ML. The difficulty is introduced by heterogeneity of the structures in images.

State of the art ML-based image classification models rely on a comprehensive learning stage. During learning a process of feature extraction takes place [24]. Features of an image can be categorized into color, texture and dimension. Mapping the image to the feature space can be considered the task of a feature extractor algorithm. Extracting features describing an image, or more specifically, a structure present in an image has proven to be a challenging task [125]. Features could be considered a representation of

visual content present in an image. Therefore, a classifier would be able to separate content from irrelevant information. Texture detection is usually performed by applying filters on images to separate the content from semantic information. For example, using 2D Gabor functions, one can achieve segmentation close to human precision [306]. ML models can be trained on these features or be utilized to extract them. The three ML models that are most prominently used for the task of image classification are decision trees, SVMs and CNNs. In this thesis, random forest models are used which are a part of decision trees (4.5) and CNNs (5.2, 5.3 and 5.4). Although, at these chapters a detailed descriptions of models used is provided, a short overview of these models can be useful for the comprehension in understanding the role of ML in image classification.

3.2.3 Decision Trees

Decision tree (ensemble) methods are one of the most capable forms of ML models. These models are suitable for analyzing unstructured datasets which makes them advantages for training on features that are already extracted from images. These models utilize a voting system and combine the decision from many simultaneously created model; hence the term decision tree as these models create a set of highly randomized decision trees [177]. Afterwards an induction algorithm is used to grow a tree. At each level of the created tree (nodes) the induction algorithm tries to minimize the decision error on the test dataset (a dataset which is not seen by the model during training). The elements of a decision tree can be described as follow:

1. Root node: the entirety of the dataset.
2. Data Split: dividing a node into sub-datasets.
3. Decision node: further splitting of a sub-node.
4. Leaf: end nodes where no splitting takes place.
5. Pruning: converging nodes (opposite of splitting).
6. Branch: A sub-tree (part) of a decision tree

A decision tree segregates the data based on the corresponding classes while identifying the parameters corresponding to the most homogeneous sub-dataset (Fig. 3.1).

Decision trees are greedy algorithms i.e. they do not always find the best fitting trees [291]. Moreover, these models are prone to overfitting i.e. learning the training data by heart so that extrapolation to test data is not possible. To tackle these shortcomings, more advanced ML models based on decision trees are developed e.g. random forest and gradient boosting models.

Random Forest

A random forest model (RF) is created by training multiple (millions) of trees (T_r) on random subsets (S_r) of the training data (\vec{x}) for the sake of predicting the state y [42].

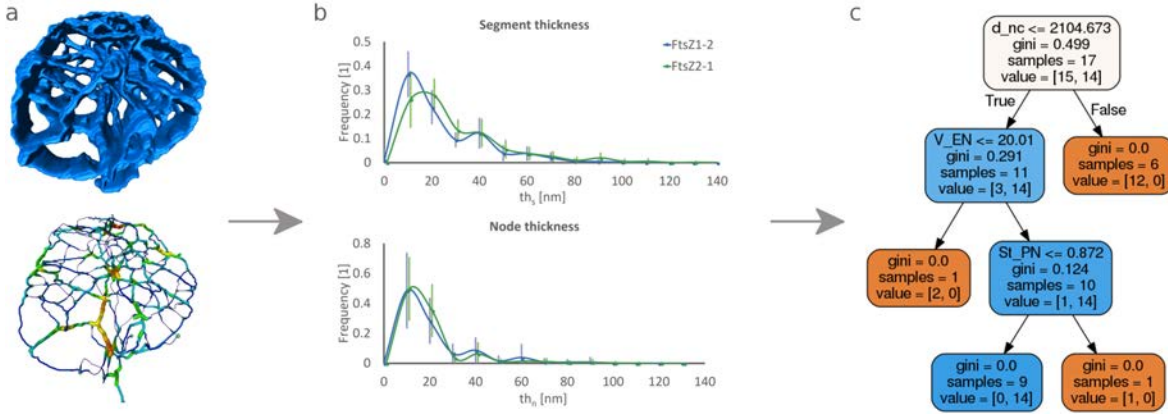


Figure 3.1: Using a decision tree in protein Classification. a) Quantitative imaging. b) Feature extraction. c) Creating a decision tree.

For each S_r an entropy value describing the amount of information spent on each decision making per (branching on nodes) is calculated as:

$$H(S_r) = -P_{(\text{left})} \log_2 P_{(\text{left})} - P_{(\text{right})} \log_2 P_{(\text{right})}, \quad (3.1)$$

with $P_{(\text{left})}$ and $P_{(\text{right})}$ denoting the probability distribution for the attribute branching to left or right branch at each node. This allows determining the amount of information gained at each node for the decision making process of the tree as on subset S_r for each attribute A as:

$$\text{Gain}(S_r, A) = H(S_r) - \sum_{V \in \mathbf{A}} \frac{|S_{rV}|}{|S_r|} H(S_{rV}), \quad (3.2)$$

with S_{rV} denoting the sub-subset. By calculating the information gain value for each attribute on each subset, one can pick the attribute with highest information gain to create nodes on. Employing the concept of entropy and gain, one can determine the importance of each node in grown trees on the decision making task as:

$$I_n = \frac{|S_{rV}|}{|S_r|} H(S_{r_n}) - \frac{|S_{rV}^{\text{right}}|}{|S_r^{\text{right}}|} H(S_{r_n}^{\text{right}}) - \frac{|S_{rV}^{\text{left}}|}{|S_r^{\text{left}}|} H(S_{r_n}^{\text{left}}). \quad (3.3)$$

At last, I_n is utilized to calculate the importance of each attribute in the dataset by summing up the normalized importance of the nodes, on which that specific feature is used.

After training multiple trees on subsets of the data, a voting is carried out on all trained trees to map the dataset to the desired state:

$$RF(\vec{x}) = \sum_{i=1}^n T_r^i(\vec{x}). \quad (3.4)$$

Gradient Boosting

Similar to random forest, gradient boosting models aim at performing a mapping of unstructured data to a certain target:

$$f^*(\vec{x}) = y, \quad (3.5)$$

Here, a prediction model (f^*) is produced in the form of an ensemble of weak prediction models to map the set of features:

$$\vec{x} = [x_1, x_2, \dots], \quad (3.6)$$

to a state (y). During learning, new models are consecutively fitted to provide a more accurate prediction [104], to construct the new models to be maximally correlated with the negative gradient of the loss function Ψ , associated with how wrong the prediction is. Given N_n training examples: $\{(\vec{x}_1, y_1), \dots, (\vec{x}_N, y_N)\}$, where $\vec{x}_i \in \vec{x}$ and $y_i \in y$, the gradient boosting decision tree model estimates the function f of future \vec{x} by the linear combination of individual decision trees

$$f_M(\vec{x}) = \sum_{m=1}^M T(\vec{x}; \theta_m), \quad (3.7)$$

where $T(\vec{x}; \theta_m)$ denotes the i -th decision tree, θ_m is its parameter set, M is the number of decision trees. The final estimation is determined in a forward stage-wise fashion, i.e. based on an initial model $f_0(\vec{x})$ of \vec{x} , the model of step m is determined as:

$$f_m(\vec{x}) = f_{m-1}(\vec{x}) + T(\vec{x}; \theta_m), \quad (3.8)$$

where $f_{m-1}(\vec{x})$ is the model in step $m - 1$. θ_m is learned by empirical loss minimization as

$$\theta_m = \arg \min_{\theta_m} \sum_{i=1}^M \Psi(y_i, f_{m-1}(\vec{x}) + T(\vec{x}; \theta_m)), \quad (3.9)$$

with the loss function Ψ . The assumption of linear additivity of the base function, leads to the estimation of θ_m for best fitting the residual $\Psi(y - f_{m-1}(\vec{x}))$. To this end, the negative gradient of the loss function at f_{m-1} is used to approximate the residual R :

$$R_{m,i} = - \left[\frac{\partial \Psi(y, f(x_i))}{\partial f(x_i)} \right]_{f(x)=f_{m-1}(x)}, \quad (3.10)$$

with i as the index of the i -th example.

3.2.4 Support Vector Machine (SVM)

SVMs utilize a series of linear functions creating a hyper space to learn the classification task [287]. In this process SVM models use an optimization technique to statistically derive the hypothesis from the learning dataset. SVMs aim to look for hyperplanes dividing the hyperspace of the dataset which enable classifying the images of the dataset. This goal is only achievable if one has access to optimizing algorithms capable of handling large amounts of data [328]. SVMs are greatly suitable for binary classification problems e.g. healthy/diseased tissue, deformed/unreformed protein network structure and high/low fracture possibility in bones. If we assume a set of samples l where each observation is encoded as a (\mathbf{x}, \mathbf{y}) -pair with $\mathbf{x} \in R^N$ being input image and $\mathbf{y} \in [[0, 1], [1, 0]]$ being binary classes. The SVM looks for the best separating hyperplane which can be defined

by means of a normal vector \mathbf{w} . One could construct a pair of planes parallel to the separating hyperplane as:

$$\text{for } \mathbf{y} = [1, 0], \quad \mathbf{w} \cdot \mathbf{x} \geq b + 1, \quad (3.11)$$

$$\text{for } \mathbf{y} = [0, 1], \quad \mathbf{w} \cdot \mathbf{x} \leq 1 - b, \quad (3.12)$$

where b denotes the offset of the parallel planes from the original. The goal of the SVM model is to find the \mathbf{w} , which often requires nonlinear computationally expensive solutions [329]. However, with the help of linear kernels dimension of the input data is increased while the overall size of it is decreased. Moreover, the dimension-wise error, ξ , and the cost function, C of the optimization process:

$$\frac{1}{2} \|\mathbf{w}\|^2 + C \cdot (\xi), \quad (3.13)$$

are subjected to the following constrain:

$$\mathbf{y}(\mathbf{w} \cdot \mathbf{x} - b) + \xi \geq 1. \quad (3.14)$$

SVM will carry out this optimization problem through iterations and hence find the separating hyper plane. Typically, numerical methods such as Adam optimization are employed [179]. Recently, SVMs are utilized in many ML-based protein network classification models [163, 203]. However, the feature extraction capability and therefore analysis of what is learned by SVMs are limited. Therefore, in this thesis, CNNs are utilized which are more advanced classification models with the possibility of investigating the learning process of the model.

3.2.5 Convolutional Neural Networks

Currently, the most used ML models for image classification, specifically for biomedical image classification, are CNNs [211]. CNNs consist of convolutional layers that utilize kernels to decrease the size of the data while accenting and extracting structural features correlating to the desired class. CNNs have been in use since the early 80s [107]. The success of CNNs in image classification was shown by Lecun et al in 1989 in recognizing hand-written text [199]. In 1995, for the first time, Lo et al. utilized a CNN for biomedical image analysis [215]. However, up until 2012 when Krizhevsky et al. took part with their work ImageNet in the competition for classifying a huge dataset of images [187], the research community did not pay much attention to CNNs. Their CNN, AlexNet, won the competition way ahead of the other contributors by utilizing many convolutional layers. From this point on, researchers realized that networks with more layers could unleash a great potential in many fields of data analysis. This was the rise of deep neural networks (DNNs).

This success was also noticed by medical image processing community. Hence, deep learning has become a prominent contributor to the filed of biomedical image analysis. Shen et al. wrote a detail overview of deep learning applications for biomedical image analysis [302].

Similar to SVMs, deep learning, as a supervised ML algorithm, can be presented as

$$f(\mathbf{x}, \Theta) = \mathbf{y}, \quad (3.15)$$

where each image \mathbf{x} is paired with a class vector \mathbf{y} by search for the model parameters Θ . This search is carried out by minimizing a loss function $L(\mathbf{y}, \hat{\mathbf{y}})$, which measures the difference between the real label, \mathbf{y} , and the predicted label, $\hat{\mathbf{y}}$. When the loss is below a desired threshold, the CNN has reached the goal model $f(\mathbf{x}, \Theta)$.

This search and optimization is carried out by means of training a neural network which consist of activations, a , and model parameters $\Theta = (\mathbf{W}, B)$, with \mathbf{W} denoting a set of weights and B the bias terms. a is a linear operation on image \mathbf{x} and the model parameters followed by a nonlinear transformation σ . This can be shown as:

$$a = \sigma(\mathbf{W}^T \mathbf{x} + b). \quad (3.16)$$

The nonlinear transformation, σ , is usually performed by Sigmoid or hyperbolic tangent functions [211]. Stacking up multiple layers of transformations creates a deep neural network shown as:

$$f(\mathbf{x}, \Theta) = \sigma(\mathbf{W}_n^T \sigma(\mathbf{W}_{n-1}^T \dots \sigma(\mathbf{W}_1^T \mathbf{x} + b) + b) + b). \quad (3.17)$$

The terminology 'hidden layers' is usually used for the layers placed after the input layer of the neural network that map the input onto output. A deep neural network is simply a CNN with multiple hidden layers [211] (Fig 3.2).

After the last layer, the activations are used to perform a mapping of a probability distribution onto the classes. This could be done, for example, using a softmax function as:

$$\text{Softmax}(\mathbf{y}|\mathbf{x}; \Theta) = \frac{e^{\mathbf{W}_i^T \mathbf{x} + b_i}}{\sum_{n=1}^N e^{\mathbf{W}_n^T \mathbf{x} + b_n}}, \quad (3.18)$$

with \mathbf{W}_i as the weight vector mapping to class i (Fig 3.3).

To find the best fitting Θ which includes all the trained weights and bias variables (W_i and b_i , respectively) for the dataset D one selects a subset of D (a batch) and update Θ according to the gradients produced by passing the batch through the network. This process could be performed through calculating maximum likelihood with the gradient descent method. Maximizing likelihood could be considered as minimizing the negative possibility, which can be further expressed in a logarithmic form as:

$$\text{argmin}_{\Theta} - \sum_{n=1}^N \log[P(y_n|\mathbf{x}_n; \Theta)], \quad (3.19)$$

which is called cross-entropy loss function [304].

Training a DNN

Each training step of a DNN consists of a feed-forwards step and a backward computation step. In the feed-forward step, the image is put through the network. After applying the weights and summing up with bias parameters in each layer, the output will be sent to the next layer of the network. After the last layer, a probability distribution for the image is

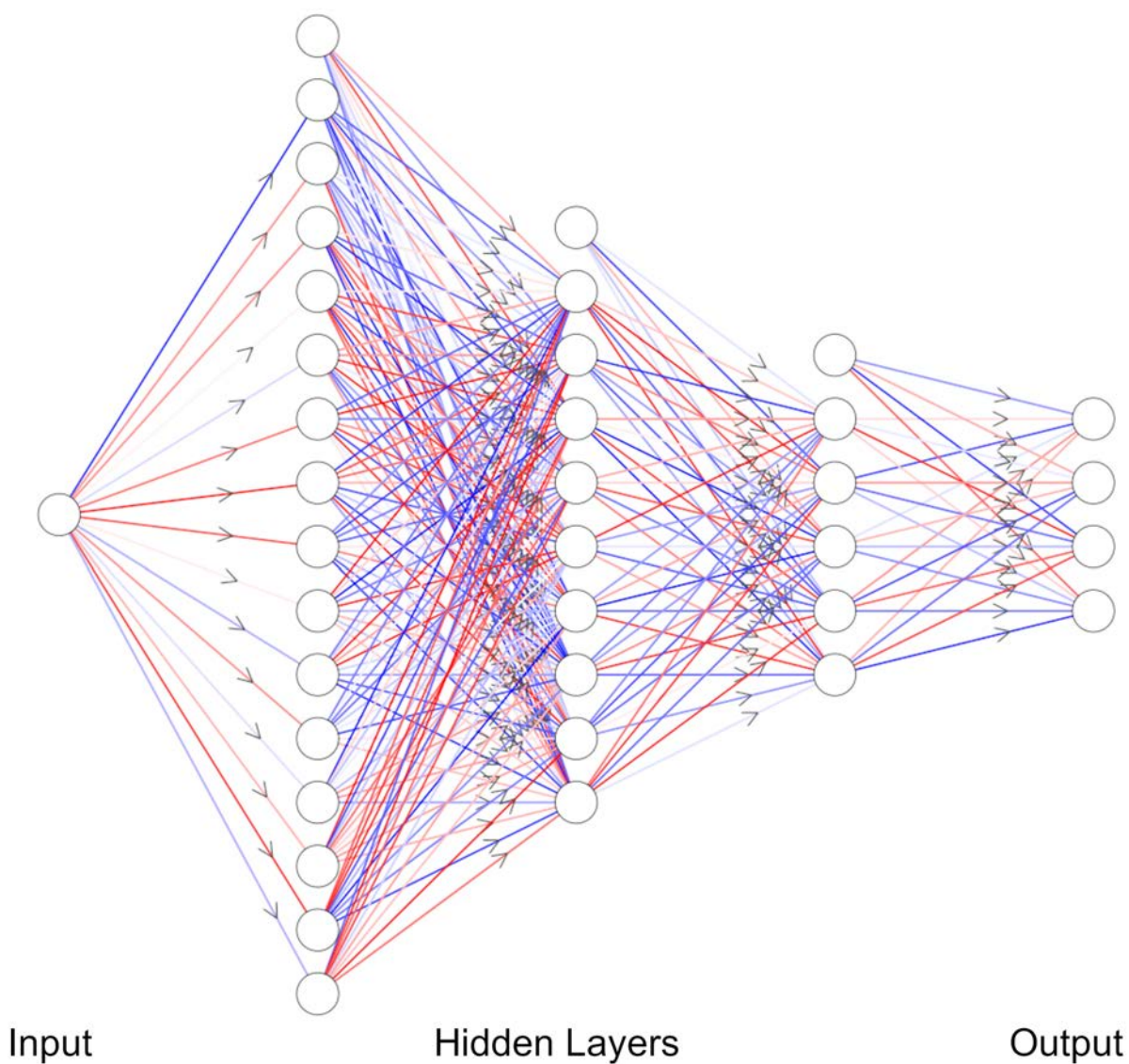


Figure 3.2: Visualization of a convolutional neural network. The input layer is convoluted, while passing through the network creating a hyperspace of neurons. The training process aims at optimizing the weights (arrows) to minimize the loss of the network. Arrows are color coded from blue to red as low to high weight values, respectively.

calculated. Afterwards, the probability distribution is transformed to a label (\mathbf{y}) and the loss value (J) is calculated by comparing it to the real label ($\hat{\mathbf{y}}$) as shown in Algorithm 1.

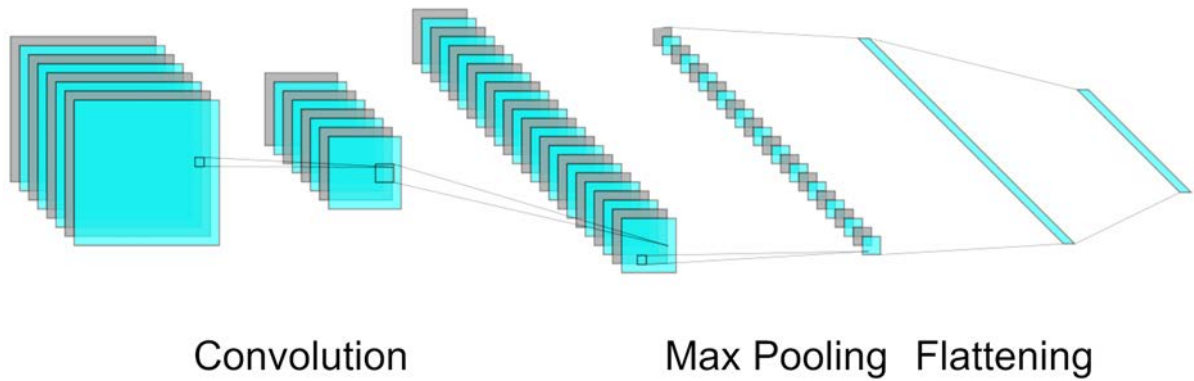


Figure 3.3: Visualization of a operations in a DNN. Convolution, max pooling and flattening are the three most typical operations taking place in a network that affect the dimensions of the dataset.

Algorithm 1 Feed forward step

Data: image

initialization $\mathbf{h}^{(0)} = \mathbf{x}$

for $k = 1, 2, \dots, l$ do

$\mathbf{a}^{(k)} = \mathbf{b}^{(k)} + \mathbf{W}^{(k)}\mathbf{h}^{(k-1)}$

$\mathbf{h}^{(k)} = f(\mathbf{a}^{(k)})$

end for

$\hat{\mathbf{y}} = \mathbf{h}^{(l)}$

$J = L(\hat{\mathbf{y}}, \mathbf{y})$

The activation in each layer is convoluted with multiple kernels in parallel as follows:

$$(a * K)(i, j) = \sum_m \sum_n a(m, n)K(i - m, j - n), \quad (3.20)$$

with \mathbf{K} denoting a $2D$ kernel moving across the input and convolving parts of image (windows). These convolution processes through the layers result in extracting features corresponding to the mapping. Since the input of each layer is the output of previous one, the deeper the layers, the more complex features will be built upon and extracted. In essence, training a DNN is the act of finding the kernels that extract the relevant features from the image for the task of mapping.

The backward computation step determines the gradient (\mathbf{g}) of the error in each layer of the network, in a backward manner. To do so, using the chain rule, the gradients are propagated with respect to the next hidden layer. The weights and biased will be tweaked in the direction of the gradients for the next training iteration (cf. Algorithm 2). In case of a successful training process, iterations over these 2 steps, results in finding a local minimum for the loss value; hence performing the correct prediction.

Algorithm 2 Backward computation step

Data: imageinitialization $\mathbf{g} \leftarrow \nabla_{\hat{\mathbf{y}}} J = \nabla_{\hat{\mathbf{y}}} L(\hat{\mathbf{y}}, \mathbf{y})$ for $k = l, l - 1, \dots, 1$ do $\mathbf{g} \leftarrow \nabla_{\mathbf{a}^k} J = \mathbf{g} \odot f'(\mathbf{a}^k)$

Compute gradients on weights and biases

 $\nabla_{\mathbf{b}^k} J = \mathbf{g}$ $\nabla_{\mathbf{W}^k} J = \mathbf{g} \mathbf{h}^{(k-1)\text{T}}$

propagate the gradients w.r.t. the next lower hidden layer

 $\mathbf{g} \leftarrow \nabla_{\mathbf{h}^{(k-1)}} J = \mathbf{W}^{(k)\text{T}} \mathbf{g}$ end for

Training process is excessively resource demanding. Only since less than 15 years, with the availability of powerful graphics processing units (GPUs) and more recently tensor processing units (TPUs), training a DNN is practical. Currently, supervised end-to-end training of DNNs are very popular not only because of availability of powerful computation facilities, but also because of development of highly specialized coding environments such as Tensorflow [1] which are very efficient for training DNNs.

4 Analyzing Structure-function Relationship at the Nano Scale: Protein Networks

At the nano scale of protein networks, this work focuses at developing a series of methods for an automatic and fast assessment of cytoskeletal protein networks (PN) based on 3D microscopy images. The approach can be broken down into: 1) designing an image processing algorithm that quantitatively describes the structure of a PN allowing not only distinction between different PNs but also between different states of the same PN, 2) creating an in-silico experimental setup permitting a quantitative representation of the mechanical responses of the PN and 3) using feature-based ML algorithms (e.g. random forest) to correlate the extracted structural features to the mechanical behavior of the PN. Creating such ML models allows an end-to-end application of PN state assessment from microscopy images as well as determination of the structural features developed in the network to create such mechanical characteristics.

The developed methodologies presented in this chapter, their validation and applications are previously published in [13], [10], [11], [255], [12] and [9].

4.1 FtsZ Protein Network Structure and Functionality

FtsZ protein family, as the evolutionary progenitor of actin and tubulin [278], has complex biopolymer networks which clearly resemble a cytoskeletal protein network in the chloroplasts of the moss *Physcomitrella patens*. As shown in chapter 2, the concept of the cytoskeleton as the driving factor in determination of cell shape is well established. In the case of eukaryotic organelles, however, there are still many unanswered questions in terms of skeletal functionality of the present proteins. It has been shown that these organelles undergo relatively large deformations and shape transformations while keep their structural integrity (similar to cells). Reski et al. [278] proposed that the FtsZ protein network is essential for the structural integrity of these plant organelles. Therefore, he coined for the term "plastoskeleton". He chose this term to portray the similar structural functionality of FtsZ protein network in chloroplast to the cytoskeleton in cell [229, 255, 279].

Plants came to existence in an endosymbiotic process in which a eukaryotic cell took a living cyanobacterium in itself and used it as a chloroplast [119]. This process was truly extraordinary since afterwards the two organisms started to coexist with each other creating one living. This involved not only gene transfer but also required restructuring of cell compartments and hence the redefinition of protein functionalities of protein [191]. In the meantime, it is accepted that FtsZ is a prokaryotic homolog of the eukaryotic tubulin [89] and during plastid division comes into play with ARC6, a descendant of a

cyanobacterial cell division protein, which orchestrate the eukaryotic cell division [236].

Most bacteria have only one isoform of the FtsZ protein. However, plants possess up to five isoforms of FtsZ protein in two families FtsZ1 and FtsZ2 [229]. All the FtsZ families can be traced back to the same cyanobacterial protein. Moreover, the presence of multiple families of FtsZ points toward distinguishing functionalities. One can name three distinguishing factors for FtsZ1 and FtsZ2: 1) FtsZ1 has the serine residue similar to tubulin and FtsZ2 has a threonine residue similar to bacterial FtsZ [83]. 2) In contrast to FtsZ1, FtsZ2 has a conserved C-terminal domain which organizes the interactions between different proteins involved in cell division [82]. 3) The biochemical characteristics of FtsZ1 and FtsZ2 are different.

Chlorophyll-containing chloroplast is the most investigated plastid which carries out the task of photosynthesis in plants (Fig 4.1). It is common to see more than 100 chloroplasts in a plant cell [16], specifically during leaf cell growth. This maximizes the capacity to produce energy from CO_2 . Chloroplast also takes part in other vital functions such as amino acid and fatty acid synthesis. This makes plastids essential organelles of cells. In chloroplast, the molecular process of division has been thoroughly studied. This process is carried out by utilizing three contractile elements. At first, a ring of FtsZ protein (Z ring) is assembled around the chloroplast. Afterwards, a further ring formed by ARC5/DRP5B is created. At last, a plastid dividing ring (PD) is formed on cytosolic surface [333]. In the process of division, the mentioned rings contract on the membrane in a way that the two sides start to separate from each other. This continues till one chloroplast becomes two. The exact division mechanism is not totally known.

Studies have suggested that pairs of FtsZ proteins might come together to carry out the plastid division [333]. This is based on the fact that an overexpression of FtsZ families result in chloroplast number decreasing as well as an increase in chloroplast size [252]. Furthermore, studies about the FtsZ in chloroplast of the *Physcomitrella patens* i.e. Martin et al. [230] and Gremillon et al. [121] have shown the contribution of FtsZ to the structural integrity of the chloroplast [277]. The FtsZ isoforms have network structures similar to cytoskeletal networks with relatively lower complexity of the structure. It has been suggested that FtsZ protein might be a molecular connection between cell and organelle division in moss [176]. Fluorescence energy transfer (FRET) has enabled researchers to show the hierarchical order of interaction between different FtsZ isoforms [121]. However, up to this day it is unclear how the structure of the FtsZ participates in the mechanical task of forming the plastid shape. Moreover, the questions about the evolutionary design of these protein structure (similar to cytoskeletal proteins, Fig 4.2) to carry loads remains unanswered.

The similarity of FtsZ to cytoskeletal proteins in their material characteristic, network structure and functionality on one side, and the lower complexity of the FtsZ protein network makes it the perfect candidate for this work. Therefore, for the nanoscale part of this research, the focus is on analyzing the structure of FtsZ protein and understanding the structure-function relationship by developing and applying ML-based models. The designed methodologies are thoroughly validated and are ready to be used on more complicated networks.

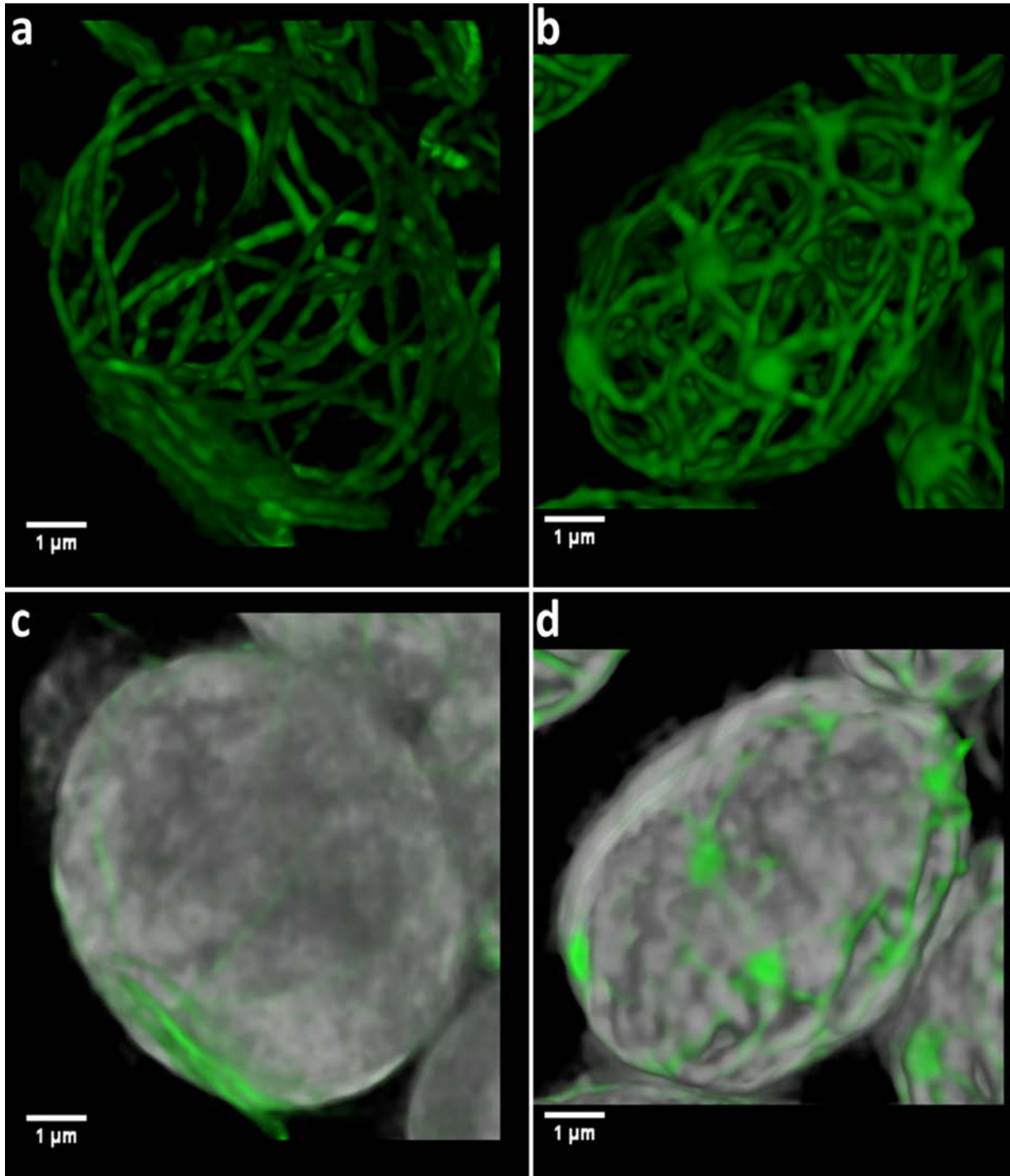


Figure 4.1: Network architectures of *FtsZ1-2* (a) and *FtsZ2-1* (b). *FtsZ1-2* and *FtsZ2-1* networks within host chloroplasts (c and d, respectively). Image is courtesy of Bugra Özdemir and Ralf Reski.

4.1.1 State of the Art in Analyzing the Structure of Protein Networks

Examining protein-networks in their natural environment is crucial for understanding their roles in cellular processes. Previous studies, which investigated protein networks,

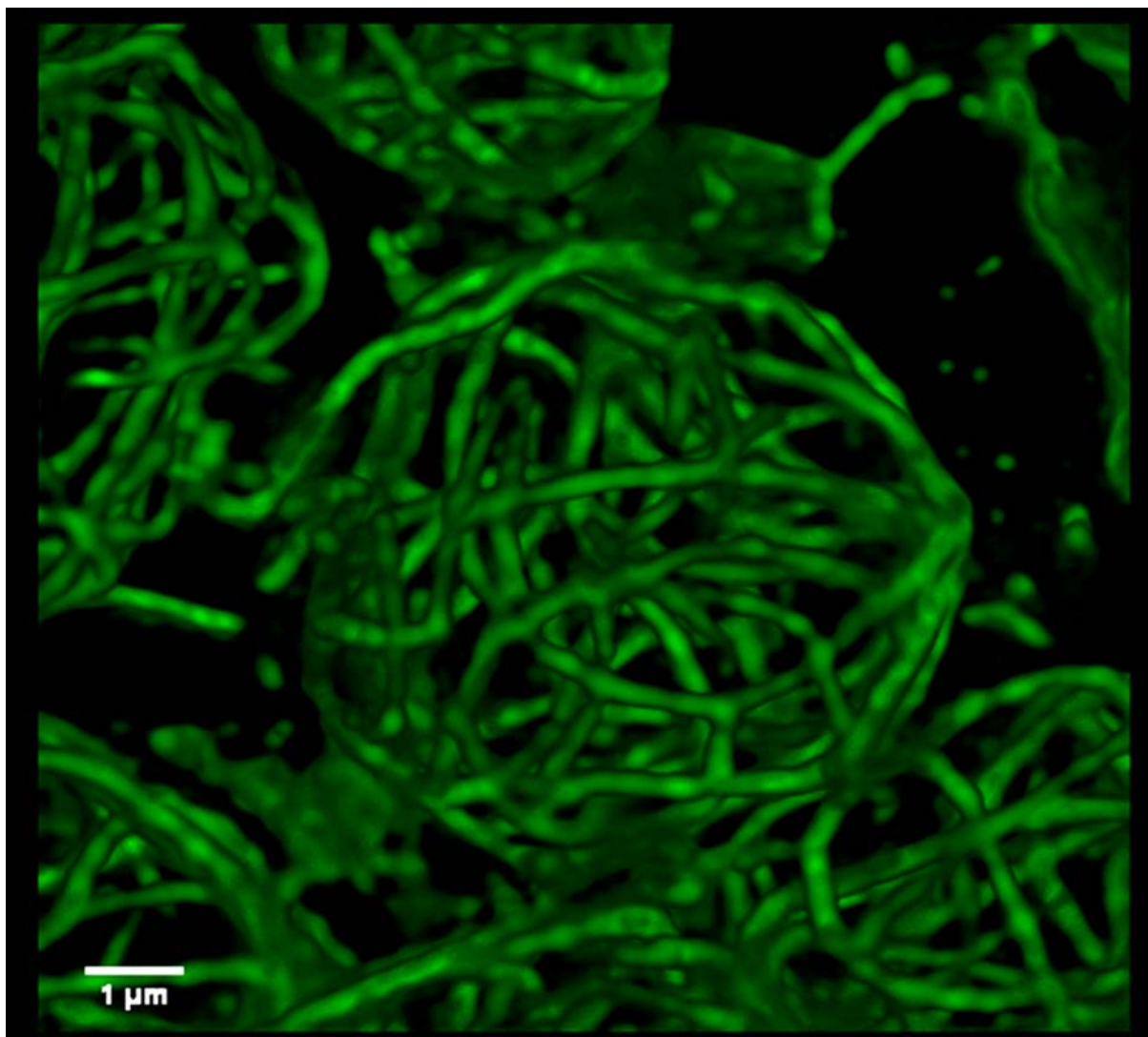


Figure 4.2: *Plastoskeleton of a plastid shown by a 3D reconstructions of confocal image datasets of plastoskeletal networks formed by FtsZ1-2 isoform. Image is courtesy of Bugra Özdemir and Ralf Reski.*

mainly focused on biochemical aspects. Imaging of fluorescent-labeled proteins in living cells is a powerful technique for studying protein network overall shape but also its structural details in a spatial and functional perspective [133, 151, 354]. Recent advances within the imaging field, e.g., noninvasive multicolor or 3D imaging at the nanometer scale [151, 354], enables the imaging of cytoskeletal structures in detail. Three-dimensional imaging of actin has been performed using both stochastic optical reconstruction microscopy (STORM) [368] and photoactivated localization microscopy (PALM) [318]. STORM and PALM further enabled visualization FtsZ, the bacterial homolog of eukaryotic tubulin [18, 144]. Other methods such as stimulated emission depletion microscopy (STED) are able to resolve neurofilaments [342], keratin filaments [348], and primary cilia [375]. Many studies have captured Z-stacks of images using confocal microscopy, while relatively few studies have analyzed the cytoskeleton in 3D. Structured-illumination microscopy (SIM) has been used to resolve actin filament arrays and microtubules in 3D [300, 347]. Addition-

ally, the three-dimensional organization of FtsZ in dividing bacteria could be visualized [18, 144, 316]. The fast advancing imaging technologies allow recently completely new 3D and time-resolved visualizations of physiological processes [54, 60, 140, 212, 271] and are therefore advancing our understanding of protein network morphology and physiology. However, extraction of information about morphology and behavior of these networks is to date largely limited to qualitative observations.

The lack of analytical tools for quantifying the structures remains a bottleneck, as manual analysis of large data sets requires a great amount of time and are prone to bias and error. Previous studies on the automated analysis of protein network data focused mainly on segmentation and extraction of the biopolymer network structures [263, 311, 352, 366, 369], tracing the shape of individual filaments in 2D [5] or only on curvature and orientation in 3D [370]. A recent study looking at more details of the network is limited to 2D [381]. However, a computerized analysis of the structure of protein networks in 3D would enable the tracking of dynamical processes or the identification of pathological changes in an automated manner. Additionally, linking the overall shape of a cell (or plastid) to the organization of its internal supporting network structure would give further insights into cell mechanics.

4.2 A Method to Describe and Learn the Structure of Protein Networks

To enable an enhanced investigation of morphological aspects of protein networks, a novel automated image processing method is proposed. This allows a detailed quantitative spatial network analysis. This method processes high-resolution 3D image data sets of protein networks to investigate the network structure from two different yet strongly connected perspectives. The geometrical characteristics of the network as a continuous body are separated from the properties of the subunits of the structure and their connections. First, the gross morphology of the network is considered. The introduced descriptors provide a quantitative answer to the question "how does the network look like?". The second one studies the protein network on a smaller scale with the aim of quantification of the organizational characteristics of the network components and their relative positioning, connections and distributions. Therefore, a spatial graph representing the network as a set of nodes, segments and connections, is extracted from the 3D geometry. This part of the quantification investigates the design of the network and aims to answer the question "how is the structure built?". For both perspectives, a number of robust and quantitative descriptors are introduced to enable a reproducible, quantitative characterization of the organization of protein networks.

The method is introduced and tested by applying it to confocal microscopy images of fluorescent-labeled FtsZ proteins of *Physcomitrella patens* [240] (Fig. 4.3), a homolog of the eukaryotic cytoskeleton protein tubulin. Based on these data, an image-based characterization of a protein network structure on a sub-cellular level using measures extracted from the gross morphology as well as the arrangement of the network components is developed.

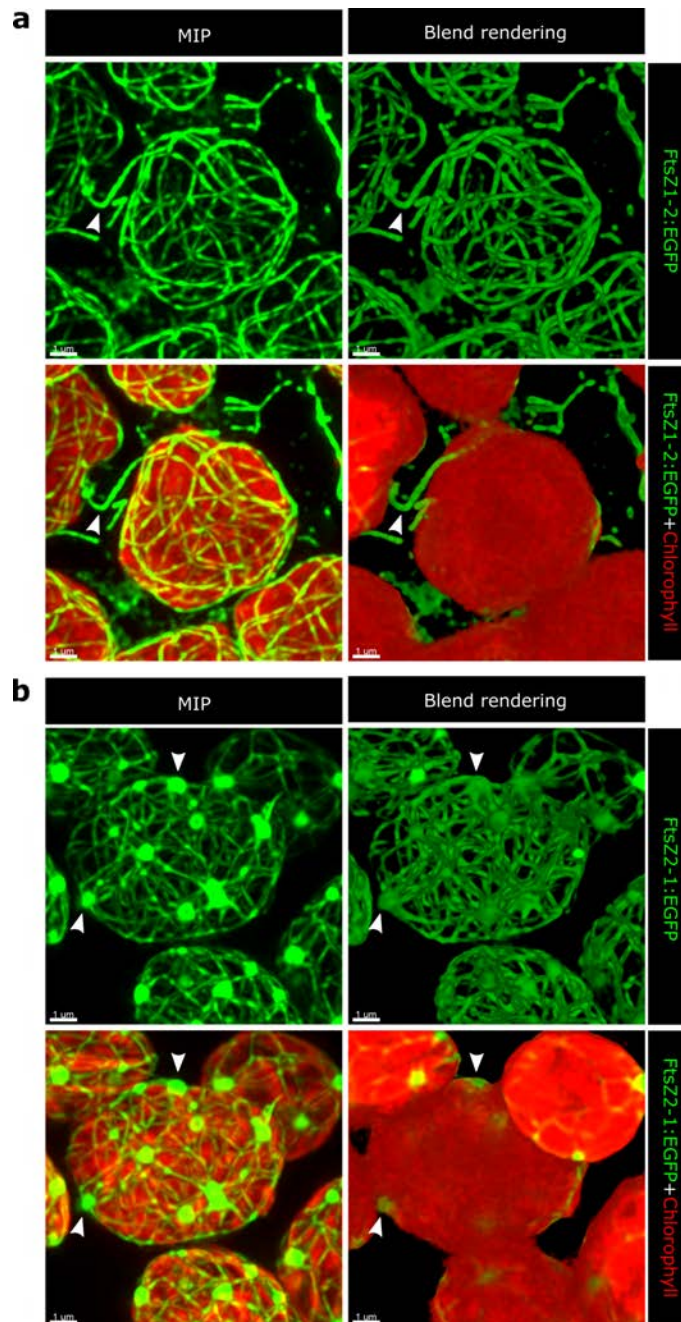


Figure 4.3: Examples of networks and the corresponding chloroplasts hosting them. a) *FtsZ1-2* networks show uniform size for segments and nodes. A common feature of *FtsZ1-2* networks is the presence of extraplastidic filaments which sometimes connect multiple chloroplasts of a cell (arrowheads). b) *FtsZ2-1* networks show detectable heterogeneity in node size with the meganodes being noticeably larger. The meganodes are usually located at the chloroplast surface (arrowheads). Unlike *FtsZ1-2*, in the networks of *FtsZ2-1*, no inter-plastidic connections are observed and occurrences of the extraplastidic filaments in general are very scarce. Image is courtesy of Bugra Özdemir and Ralf Reski.

4.2.1 Protein Labeling and Confocal Laser Scanning Microscopy

FtsZ protein networks of *Physcomitrella patens* have relatively simple but dynamic structures [11]. This makes FtsZ the ideal first application to demonstrate and test the developed method. Furthermore, the similarity to eukaryotic cytoskeleton proteins, like microtubuli, shows that these methods and ideas can also be easily applied to more complex network structures. This is due to the fact that cytoskeletal PNs are, besides a similar molecular structure, also assembled of the same basic structural units (points, nodes, elements, and segments).

Total RNA was isolated from wild type *Physcomitrella patens* ("Gransden 2004" ecotype) protonema using TRIzol Reagent (Thermo Fisher Scientific, USA) and used for cDNA synthesis using Superscript III reverse transcriptase (Life Technologies, Carlsbad, CA, USA). The coding sequence of PpFtsZ1-2 was PCR-amplified from this cDNA and cloned into the reporter plasmid pAct5::Linker:EGFP-MAV4 (modified from Kircher et al. [180]) to generate the fusion construct pAct5::PpFtsZ1-2:Linker:EGFP-MAV4. Then, 50 μg of this plasmid was used for the transfection process. The moss material was grown in a bioreactor [141, 143] and transfected according to the protocol described by Hohe et al. [142]. The transfected protoplasts were incubated for 24 h in the dark, subsequently being returned to normal conditions ($25 \pm 1^\circ\text{C}$; light-dark regime of 16 : 8 h light flux of $55 \mu\text{mol s}^{-1} \text{m}^{-2}$ from fluorescent tubes, Philips TL - 19 - 65W/25).

3D microscopy was performed directly on live cells between the 4th and 7th days after the transfection, using a Leica TCS 8T-WS microscope. Images were generated using HCX PL APO 100x/1.40 oil objective with a zoom factor of 10.6. For the excitation, a white laser adjusted to 488 nm was applied. The detection range was set to 503 – 552 nm for the EGFP channel and 664 – 725 nm for the chlorophyll channel. The pinhole was adjusted to 106.1 μm . Resulting images have a voxel size of 21 nm in $x - y$ dimensions and 240 nm in z dimension. The image data sets were subsequently deconvolved using Huygens Professional software (Scientific Volume Imaging B.V) based on the theoretical point spread function and the Classical Maximum Likelihood Estimation (CMLE) algorithm. Confocal imaging was performed by Bugra Özdemir. Examples are shown in Fig. 4.3.

4.3 Designing a Protein Network Structure Descriptor Method

To extract quantitative measures of the network structure from 3D microscopic images, an image processing framework containing several steps is designed. First, raw images (Fig. 4.4b) are segmented using a semi-automatic iterative approach (Fig. 4.4c); second, a 3D geometric volume model is created and its overall shape is analyzed (Fig. 4.4d). Third, it is converted into a spatial graph, which allows to extract the network topology (nodes, connections, segments; Fig. 4.5). From these two representatives of the network, descriptors of the overall shape of the network and descriptors of the detailed morphology of the network and the sub-structure are determined.

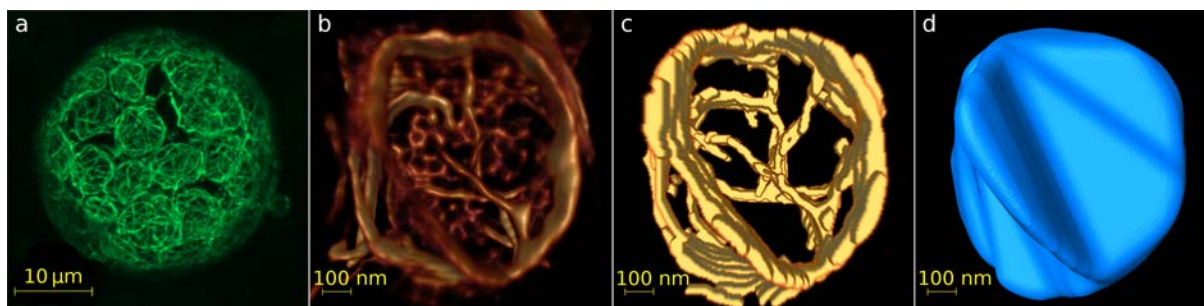


Figure 4.4: (a) Confocal microscopy images of several fluorescent-labeled *FtsZ* proteins inside chloroplasts of one *Physcomitrella patens* cell (voxel size: 101 nm in $x - y$ dimensions and 300 nm in z dimension). (b) Raw 3D image of one protein network of *FtsZ* (voxel size: 21 nm in $x - y$ dimensions and 240 nm in z dimension). (c) Segmented network. (d) Wrapped hull determined from segmented image. Images in (c) and (d) have the same voxel size as (b).

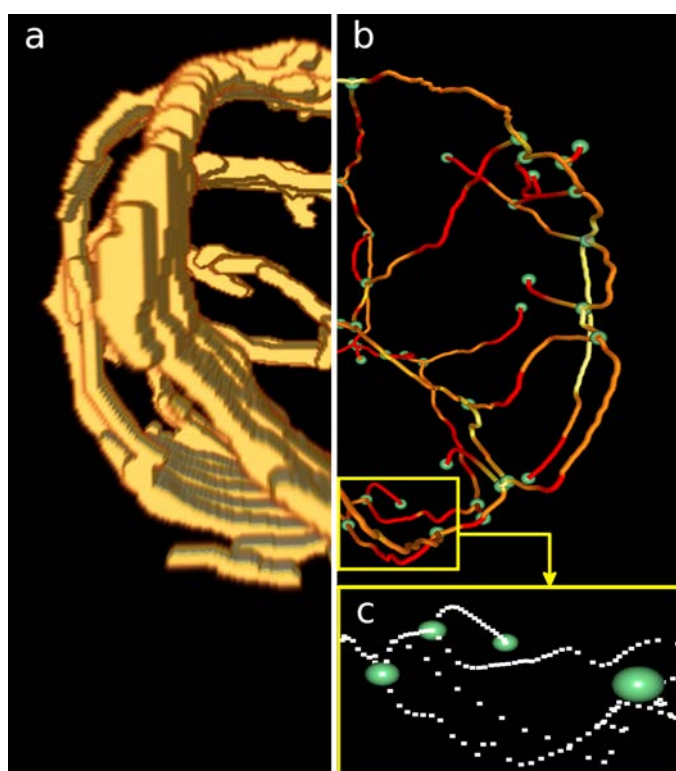


Figure 4.5: Transformation of the Segmented Image into a Spatial Graph. (a) Segmented image of a protein network of *FtsZ*. (b) The spatial graph extracted of the segmented image. Nodes are shown in light green and segments are shown in a yellow \rightarrow red color code with red representing thicker segments. (c) Zoomed in part of the network showing individual points in white.

Segmentation to Extract Network

The image is segmented using an adaptive local threshold algorithm based on median value in each 3D window (window size = $10 * 10 * 10$ voxels and constant value = 10). Next, the remaining filament discontinuities inside the network are manually corrected.

Segmentation was performed in FEI Amira 6.2.0 (Thermo Fisher Scientific, USA).

Extraction of Network Gross Morphology

The gross morphology of the network is studied as a whole. Therefore, a solid outer surface is defined for the segmented image to find the volume enclosing the network. First, for each slice of the 3D image stack the convex hull, represented by the smallest convex set containing all the voxels, is determined. The combination of all convex hulls of all slices forms a wrapped hull around the whole network (FEI Amira 6.2.0 (Thermo Fisher Scientific, USA)). Second, instead of the detailed network, the solid outer surface of the network represented by its wrapped hull is analyzed. A shape matrix describing the shape and the orientation of the wrapped hull of the network structure is calculated, adapted from the shape analysis for whole cells and pulmonary systems presented by Mc Creadie et al. [232] and Chandran et al. [57], respectively. Therefore, each voxel is represented as $\mathbf{X}(i) = \{x, y, z\}$, with x, y and z being the geometrical coordinates of voxel i . Furthermore, for each voxel, the displacement vector from the center of mass is defined as $\mathbf{M}(i) = \mathbf{X}(i) - \mathbf{C}$, with \mathbf{C} as the center of the mass. The shape matrix (S) representing the solid outer surface is built as:

$$\mathbf{S} = \frac{1}{n} \sum_{i=1}^n \begin{bmatrix} M_x(i)M_x(i) & M_x(i)M_y(i) & M_x(i)M_z(i) \\ M_y(i)M_x(i) & M_y(i)M_y(i) & M_y(i)M_z(i) \\ M_z(i)M_x(i) & M_z(i)M_y(i) & M_z(i)M_z(i) \end{bmatrix}, \quad (4.1)$$

with n as the number of voxels in the segmented image. This 3×3 matrix is created for the covariance of the coordinates of all voxels of the wrapped hull. This part was done in Matlab 2017a (MathWorks, USA).

Calculation of Network Shape Descriptors

All the following steps are performed using an inhouse Matlab code (Matlab 2017a, MathWorks, USA). Shape descriptors are defined and calculated based on the segmented image, its wrapped hull and its shape matrix to characterize the spatial extensions of the network as a whole:

1. The network volume is defined as

$$V_{PN} = n_{PN} * \delta_x * \delta_y * \delta_z \quad (4.2)$$

and calculated from the number of the foreground voxels (n_{PN}) of the segmented image. δ_x , δ_y and δ_z are the extensions of the voxels in x -, y - and z -directions, respectively.

2. The enclosed volume of the network is computed as

$$V_{EN} = n_{EN} * \delta_x * \delta_y * \delta_z \quad (4.3)$$

and defined as the space occupied by the network and the empty space inside the network. It is determined by counting the number of voxels (n_{EN}) inside the wrapped hull.

3. The network volume density, ρ_{PN} , describes how densely the volume inside the network (wrapped hull) is occupied by material. It is determined as the ratio of the enclosed volume and the network volume

$$\rho_{PN} = \frac{V_{PN}}{V_{EN}}. \quad (4.4)$$

4. The greatest and smallest diameters of the network, d_{PN}^{max} and d_{PN}^{min} , respectively, are calculated by scaling the respective eigenvalues of the shape matrix, as introduced for whole cell analysis [232]:

$$\begin{aligned} d_{PN}^{max} &= 2\sqrt{5}\lambda_{s,3}, \\ d_{PN}^{min} &= 2\sqrt{5}\lambda_{s,1}, \end{aligned} \quad (4.5)$$

where, $\lambda_{s,3} > \lambda_{s,2} > \lambda_{s,1}$ are the eigenvalues of the diagonalized resulted symmetric shape matrix, which define the ellipsoid axes of the wrapped hull.

Spatial anisotropies in the network shape are quantified by analyzing the ratios between the diameters/eigenvalues and the parameters stretch and oblateness of the network are introduced. These descriptors have been previously presented to analyze the shape of bone cells [226].

5. The stretch of the network, St_{PN} , describes the elongation of the protein network and is calculated as the difference between the largest ($\lambda_{s,3}$) and smallest eigenvalue ($\lambda_{s,1}$) of the shape matrix, normalized by the largest one:

$$St_{PN} = \frac{\lambda_{s,3} - \lambda_{s,1}}{\lambda_{s,3}}. \quad (4.6)$$

$St_{PN} \in [0, 1]$, where 0 corresponds to a perfect sphere and 1 refers to an infinitely stretched object (cylinder).

6. The oblateness of the network, Ob_{PN} , is defined as

$$Ob_{PN} = 2 \cdot \frac{\lambda_{s,2} - \lambda_{s,1}}{\lambda_{s,3} - \lambda_{s,1}} - 1. \quad (4.7)$$

$Ob_{PN} \in [-1, 1]$ classifies rod-like and plate-like structures. If the second eigenvalue, λ_2 , is closer to the greatest eigenvalue, λ_3 , then the object is considered to be elongated. An oblateness value equal to -1 indicates a perfect rod and a value of 1 a perfect plate.

Extraction of a Spatial Graph

To extract information about the network micro-structure, a transformation to a numerical representative, defined by points, nodes and segments, representing the different elements of the complex network, is performed. This transformation process is built upon the concept of tensegrity structures and spatial trusses introduced by Ingber et al. for the analysis of cytoskeleton and endothelial mechanotransmission [154, 155], adapted from

an implementation for extracting network geometry of collagen gels by Stein et al. [314]. First the edge voxels are determined using the gradient ∇f of the image f :

$$\nabla f = \frac{\partial f}{\partial x} \mathbf{e}_x + \frac{\partial f}{\partial y} \mathbf{e}_y + \frac{\partial f}{\partial z} \mathbf{e}_z, \quad (4.8)$$

where \mathbf{e}_x , \mathbf{e}_y and \mathbf{e}_z are unit vectors forming an orthogonal basis. Second, the centerlines of the filamentous structures are identified (Fig. 4.5b) based on calculating a distance map of all voxels from the nearest edge voxel. Afterwards, points are placed at the centerline of each structure entity [10]. A point is placed at any part of the structure at which a change in either the thickness or the direction of the filament occurs (Fig. 4.5c). Hence, the distances between the points are based on the resolution of the original image and complexity of the structure. Last, all consecutive points are connected by elements. As a result, the following components are determined to numerically represent the network (Fig. 4.5b-c):

- Points: The basic entity of the extracted spatial graph. Points are connected through elements.
- Elements: Connection between two points.
- Nodes: Points that are connected to more than two other points.
- Segments: A sequence of elements starting from one node and ending at another node.
- Connection: Intersection of segments.

For further analysis, the following information is extracted at each point: an identification (ID) number, coordination, thickness of the filament at that point and the IDs of the neighboring points to which this point is connected to. The network extraction steps were performed in FEI Amira (Thermo Fisher Scientific, USA).

Calculation of Network Element Descriptors

The segmented image and the information from the spatial graph are further analyzed together to quantify details of the network structure details (inhouse Matlab code (Matlab 2017a, MathWorks, USA):

- Node descriptors (Fig. 4.6):
 1. Number of nodes in the network, N_n .
 2. Node thickness th_{n_i} is determined by the diameter of the filament at the location of the node, n_i .
 3. Node density, ρ_n , is defined by

$$\rho_n = \frac{N_n}{V_{EN}}, \quad (4.9)$$

and determined by the number of nodes normalized to the volume enclosed by the network ($1/\mu\text{m}^3$). It has to be taken in mind, that this is not the same as the network volume density.

4. Node-to-node distance, $d_{n_i n_j}$,

$$d_{n_i n_j} = \|n_i - n_j\|_2 = \sqrt{(x_i - x_j)^2 + (y_i - y_j)^2 + (z_i - z_j)^2}, \quad (4.10)$$

is calculated as the Euclidean distance between two neighboring nodes, n_i and n_j , with coordinates x_i, y_i and z_i , and x_j, y_j and z_j , respectively.

5. The node-to-surface distance, $d_{n_i s}$, represents the closest distance of the node n_i to the surface of the network. This element descriptor represents the local distribution of the nodes within the network.
6. Compactness of the network, C_{PN} , is defined by

$$C_{PN} = \frac{d_{nc} - d_{ns}}{d_{nc}}, \quad \text{with} \quad d_{nc} = \frac{1}{n} \sum_{i=1}^n d_{n_i c}, \quad \text{and} \quad d_{ns} = \frac{1}{n} \sum_{i=1}^n d_{n_i s}, \quad (4.11)$$

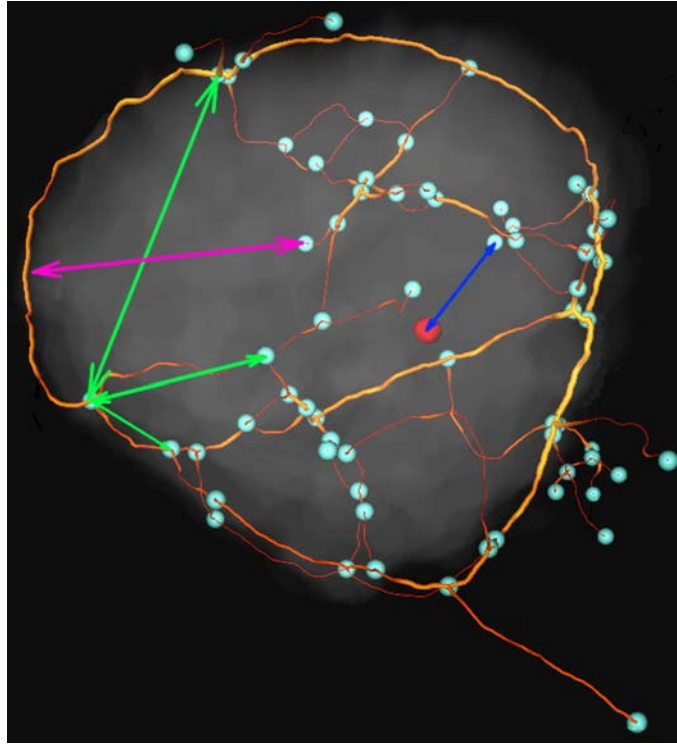


Figure 4.6: Node descriptors. A spatial graph of a protein network of *FtsZ* represented by nodes (light green) and segments (which are shown in a yellow \rightarrow red color code with red representing thicker segments.). The red dot indicates the position of the center of the gravity of the network. The green arrows show the distances between two connected nodes ($d_{n_i n_j}$). The blue arrow indicates the distance of a node to the center of gravity $d_{n_i c}$. The purple line represent the distance of a node to the surface of the network $d_{n_i s}$.

where, the node-to-center distance, $d_{n_i c}$, is the distance of each node to the center of gravity of all nodes. It is calculated according to node-to-surface

distance (Eq (4.10)) by replacing the second node with the center of gravity. The compactness of the network is defined as the difference between the mean distance to the center of gravity and the mean distance to the network surface of all nodes, normalized by the mean distance to the center of gravity; $C_{PN} \in [0, 1]$. For $C_{PN} = 1$, all the nodes are placed at the surface of the network. In contrary, C_{PN} converges toward 0 if all nodes are placed near the center of gravity.

7. Node-to-surface to node-to-center distance ratio, $d_{n_i s}/d_{n_i c}$, provides information on whether the node is located closer to the surface of the network or to the center of gravity.
- Segment descriptors (Fig. 4.7a):
 1. The total number of segments is denoted by N_s .
 2. Segment length L_s is defined as

$$L_s = \sum_{i=1}^{n_p-1} l_i, \quad (4.12)$$

where l_i is the Euclidean distance between two consecutively placed points on the segment, S, and n_p is the number of the points forming segment S.

3. Segment curvature κ_s is determined as the menger curvature, i.e.,

$$\kappa_s = \frac{2|\mathbf{v}_{pn1} \times \mathbf{v}_{pn2}|}{|\mathbf{v}_{pn1}||\mathbf{v}_{pn2}||\mathbf{v}_{nn}|}, \quad (4.13)$$

where, n_1 and n_2 are the nodes at the start and end of the segment and p is the point on the segment which has the greatest distance to the straight line from n_1 to n_2 . These three points (n_1 , n_2 and p) form a triangle (shown in blue in figure 4.7a). Segment curvature is calculated as radius of the circle passing through these three points by calculating \mathbf{v}_{pn1} , \mathbf{v}_{pn2} and \mathbf{v}_{nn} as vectors from p to n_1 , from p to n_2 and from n_1 to n_2 respectively.

4. Mean segment thickness th_s is given by

$$th_s = \frac{1}{n_{ps}} \sum_{i=1}^{n_{ps}} th_i, \quad (4.14)$$

where n_{ps} is the number of points on the segment and th_i is the thickness of the filament at point i on the segment.

5. Segment inhomogeneity I_s characterizes how much the segment geometry changes along its length. This can be extracted from the number of points, as these represent the locations where the segment changes in terms of thickness or direction:

$$I_s = n_{ps}, \quad (4.15)$$

where n_{ps} is the number of points on a segment and I_s serves as a quantifier of eccentricity of the points on the segment. A higher number of points on a segment means that the segment exhibits more deviations in thickness and direction.

6. Mean point-to-point distance $d_{p_i p_j}$ denotes the mean of all distances between two consecutive points on a segment.

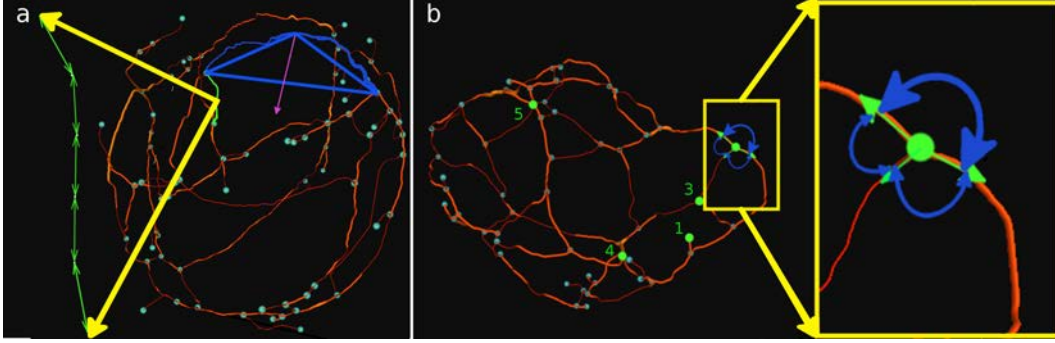


Figure 4.7: Segment and connection descriptors. (a) Local thickness of the segments th_s are shown in a yellow \rightarrow red color code with red representing thicker segments. and the diameter of the representing line element. The zoomed part of the segment marked by green color shows how the length of the segment is calculated by the summation of the distances between the points on that segment. Curvature of a segment is shown by the purple arrow. The triangle formed by starting and ending nodes and the point on the segment with greatest distance from the straight line crossing the two nodes is shown by blue. (b) Types of connections and evaluation of angles in a sample protein network. Examples of nodes with one, three, four and five connections are marked with their numbers, respectively. The blue arrows show the angles between the 3 vectors of a node with 3 connections.

- Connection descriptors (Fig. 4.7b):
 1. The mean number of connections per node, n_{c_i} , is the number of segments starting/ending at a specific node. Nodes which connect to only one other node are not included in this measure.
 2. Open nodes, n_{oe} , denotes the percentage of all nodes in the network that are only connected to one other node, i.e., nodes that are end nodes.
 3. The mean angles between the segments at a connection, $\bar{\theta}_{c_i}$ is defined as

$$\bar{\theta}_{c_i} = \frac{1}{n} \sum_{j=1}^n \theta_j, \quad (4.16)$$

with,

$$\theta_j = \arccos \frac{\mathbf{v}_k \cdot \mathbf{v}_l}{|\mathbf{v}_k| |\mathbf{v}_l|}, \quad k, l \in \{1, \dots, n\}, \quad (4.17)$$

where $\bar{\theta}_{c_i}$ is the average of angles (θ_j) between segments meeting in one connection. Angle θ_j is evaluated by calculating the angle between the vectors \mathbf{v}_k and \mathbf{v}_l , which start from node n_i located at the center of the connection and go to the first point on each of the meeting segments. Hence, for a node with three connections, three different angles for each pair of outgoing segments (three pairs) are calculated as θ_j , therefore, $\bar{\theta}_{c_i}$ is the mean value of these 3 calculated angles (Fig. 4.7b, indicated in blue).

Descriptors are calculated using an inhouse Matlab code (Matlab 2017a, MathWorks, USA).

4.3.1 Validation of Feature Extraction Algorithm for PNs

I validate the developed image processing workflow by comparing data determined manually and the computed values using the analytical tools on a dataset of $n = 9$ images. Therefore, manual segmentation and node extraction is performed (Fig. 4.8a) for all data sets. Moreover, validation of the end-to-end classification is covered with proving the independence of the results on the dataset separation.

Validation of Segmentation

Although several segmentation strategies exist [311, 369], to date no gold standard for this specific segmentation problem has been developed. However, the focus of this study lies on the quantification of structural characteristics of protein networks and not on advancing the existing segmentation techniques. Here, a relatively simple segmentation approach based on an adaptive threshold is chosen. However, further calculated parameters depend on the segmentation outcome. Therefore, A validation of this part is performed. To do so, the images have been manually segmented (MS) and the segmentation results are compared to the results of the segmentation using the local adaptive threshold (AS) technique. Segmentation results were compared using a Bland Altman diagram [34], where mean values of the two techniques are plotted on the x -axis and the difference between them is plotted on the y -axis.

Manual segmentation resulted in a trend of $5 \pm 5\%$ (1100 voxels) on average greater segmented image ($p=0.06$). For 8 of the 9 images the differences in voxel number lie in an acceptable range of ± 1.96 SD (Fig. 4.8b). Therefore, this error for the purpose of the current study is acceptable.

Validation of Node Identification and Placement

Furthermore, the node identification/placement is a crucial step, as the quantification of the element descriptors depends on it. Therefore, the nodes in all nine networks have been manually extracted (MNE) and are taken as the reference (ground truth) for the node placement step (ANE) of the proposed method (Fig. 4.8a). All further descriptors are directly derived from these two intermediate steps and are therefore not validated here.

First, the number of extracted nodes in each network is determined. Second, the vertex error is calculated,

$$E_V = \frac{1}{2|N_m|} \sum_{\mathbf{p}_m \in N_m} \min_{\mathbf{p}_a \in N_a} \|\mathbf{p}_m - \mathbf{p}_a\| + \frac{1}{2|N_a|} \sum_{\mathbf{p}_a \in N_a} \min_{\mathbf{p}_m \in N_m} \|\mathbf{p}_a - \mathbf{p}_m\|, \quad (4.18)$$

and the Hausdorff distance,

$$H_D = \max\left\{ \max_{\mathbf{p}_m \in N_m} \min_{\mathbf{p}_a \in N_a} \|\mathbf{p}_a - \mathbf{p}_m\|, \max_{\mathbf{p}_a \in N_a} \min_{\mathbf{p}_m \in N_m} \|\mathbf{p}_m - \mathbf{p}_a\| \right\}, \quad (4.19)$$

[241] between the nodes in the manually and automatically extracted networks. N_m and N_a denote manually and automatically extracted networks, \mathbf{p}_m and \mathbf{p}_a are the nodes in

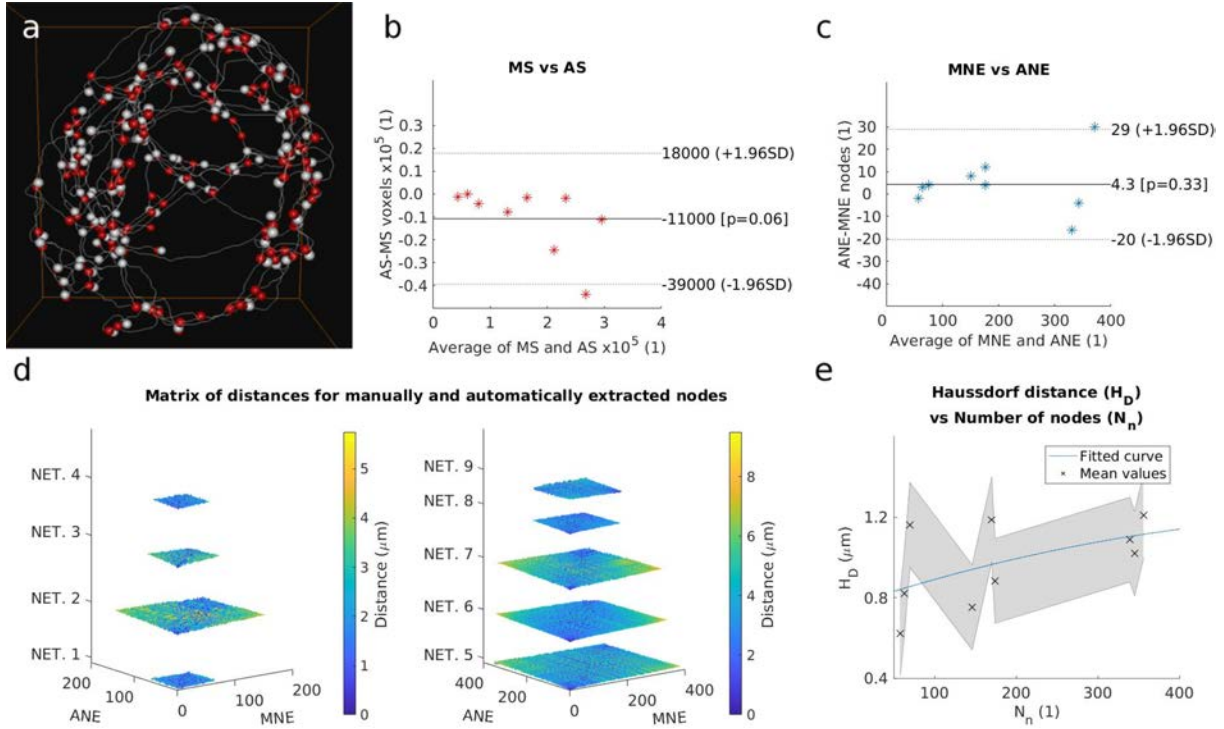


Figure 4.8: Validation. (a) Automatically (white) and manually extracted nodes (red) of the same sample network. (b) Bland Altman diagram for the volume of manual segmentation (MS) and local adaptive threshold segmentation (AS) of 9 data sets. (c) Bland Altman diagram for number of extracted nodes in manually (MNE) and automatically extracted networks (ANE). (d) Calculated matrices for distances between manually (MNE) and automatically extracted nodes (ANE). For each image the distances between the nodes from the two techniques are represented as a 2D matrix color-coded with values for distances between the two methods. (e) Scatter plot of number of nodes in the network vs. the Hausdorff distance between the networks in the manually and automatically extracted networks. The standard deviation of calculated Hausdorff distances for 9 networks is shown as shaded error bars and a polynomial curve (blue curve) for the data from 9 image data sets ($f(x) = -0.001x^2 + 1.33x + 768$ and $R^2 = 0.29$) is fitted to the scatter plot

the manually and automatically extracted networks, respectively. Third, the distances between the nodes in the manually and the automatically extracted networks have been calculated and a color-code is assigned. The value of the cell (m, n) represents the distance between the n^{th} -manually extracted and m^{th} -automatically extracted node. Last, the relation between the Hausdorff distance and number of the nodes in the network, which is directly related to the size and complexity of the network, has been analyzed.

No significant differences between the node numbers determined manually and with the automated method were determined, only a trend of 4.2 more nodes using the proposed automated method ($p=0.33$) was found. For 8 out of 9 networks the differences are in the acceptable range of ± 1.96 SD (Fig. 4.8c). The vertex error is $0.19 \pm 0.4 \mu\text{m}$ and the Hausdorff distance is $0.94 \pm 0.20 \mu\text{m}$, respectively. Considering the voxel sizes, these values lie in the range of the errors calculated by Xu et al. [370] and Xu et al. [369]: [1.08, 7.15]

and $[1, 10]$ pixels. In all networks, except network 2 (8 out of 9), for each node in the manually extracted network, there exists a node in the automatically extracted network within a distance of $2\mu m$ (dark blue color; Fig. 4.8d). This confirms the acceptable error for the method's ability to place nodes. When the number of nodes increases, the Hausdorff distance tends to merge towards a value less than $1.3\mu m$, where the second derivative of the second-order polynomial curve ($f(x) = -0.001x^2 + 1.33x + 768$ and $R^2 = 0.29$) fitted to the scattered diagram is -0.002 (Fig. 4.8e). It is assumed to have a similar Hausdorff distance for higher node numbers, which would allow applying this method to more complex protein networks, such as cytoskeletal protein networks. Considering the image resolution and overall size of the networks, the Hausdorff and vertex error values can be considered small enough to allow a quantitative analysis of the images. However, when interpreting the results they have to be taken into account.

4.3.2 Structural Feature Extraction for the FtsZ1-2 Isoform

As first application, the developed tool is tested on dataset of $n = 9$ 3D confocal microscopy images of FtsZ1-2 protein networks of chloroplasts of *Physcomitrella patens*. To identify relationships between calculated descriptors, regression analysis were performed and Pearson correlation coefficients reported. Unless otherwise indicated, all results are presented as mean \pm standard deviation (SD). All statistical tests were performed in Matlab (Matlab, 2017a, MathWorks, USA).

What is the shape of the network?

Primary gross morphology features of the network as a whole were evaluated (Fig. 4.9). A wrapped hull of a network and its three diameters are shown for a sample network in Fig. 4.9a-d. The enclosed volume of the network V_{EN} showed a great variation ($84.9 \pm 56.9 \mu m^3$), whereas the network volume V_{PN} ($17.2 \pm 9.74 \mu m^3$) and network volume density ρ_{PN} (0.23 ± 0.06) displayed smaller variations. The greatest and smallest diameters of the network, d_{PN}^{max} and d_{PN}^{min} , are $9.45 \pm 4.32 \mu m$ and $4.75 \pm 2.47 \mu m$. Furthermore, the stretch of the network St_{PN} showed a smaller variation (0.51 ± 0.11) than the oblateness of the network Ob_{PN} (-0.20 ± 0.38 ; Fig. 4.9 e-h).

Nodes - basis of the network

Individual nodes are identified and analyzed. For the investigated networks a wide range of number of nodes was found (199 ± 130 ; Fig. 4.10a-d), whereas the size of individual nodes (node thickness $50 \pm 10 nm$) and normalized parameters like the compactness and node density were more homogeneous (0.75 ± 0.10 and $2.52 \pm 0.63 node/\mu m^3$, respectively). Additionally, the relative positions of the nodes in the network give further insight into the construction of the network. Connected nodes have been identified and the average node-to-node distance ($0.57 \pm 0.05 \mu m$) was determined. Analyzing the distribution of distances showed, that 90% of all nodes are closer than $0.93 \mu m$ to their closest neighbor. In contrast, nodes have only an average distance of $0.50 \pm 0.20 \mu m$ to the surface of the network, with 90% of them being closer than $1.16 \mu m$ to the surface (Fig. 4.10e,f). Moreover, the node-to-center distance showed a considerable variation between the networks (Fig. 4.10g) whereas

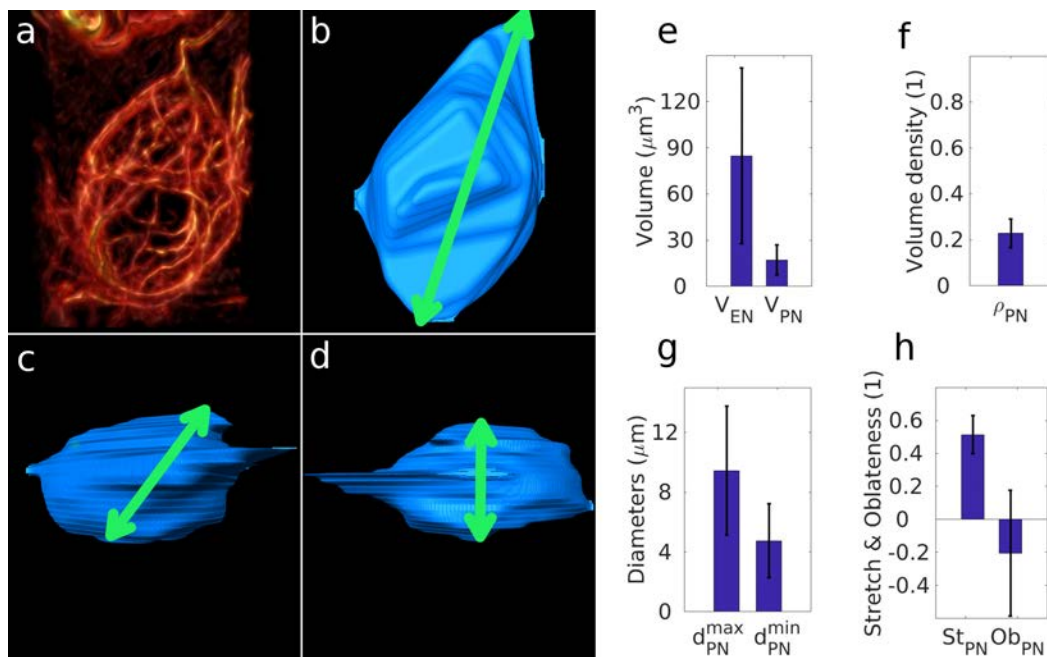


Figure 4.9: Network shape descriptors. (a) Raw image of a representative sample network of *FtsZ*. (b-d) Wrapped hull of the same protein network shown from three perspectives with the three diameters of the network shown as green arrows. The diameters were extracted from the ellipsoid, defined by the shape matrix of the outer surface.. (e) Enclosed volume of the network and network volume. (f) Network volume density. (g) The greatest and smallest diameters of the networks. (h) Stretch and oblateness of the networks. $n=9$, data shown as mean \pm standard deviation.

the node-to-surface to node-to-center distance ratio (Fig. 4.10h) showed less variation in different networks ($2.20 \pm 0.74 \mu\text{m}$ and 0.28 ± 0.09 , respectively).

Segments - filamentous nature of the network

The analyzed networks had 258 ± 168 segments with a mean thickness of $25 \pm 5 \text{ nm}$ and a mean length of $0.78 \pm 0.07 \mu\text{m}$. To obtain further details, distributions of curvatures, lengths and inhomogeneities of segments were analyzed (Fig. 4.11a). The most observed curvature was $4.35 \mu\text{m}^{-1}$ (Fig. 4.11b), the distribution of lengths peaked at $0.33 \mu\text{m}$ (Fig. 4.11c), and the segment inhomogeneity, which quantifies the local changes of properties of a segment, peaked at 9.30 (Fig. 4.11d).

Connections - How is the network built?

In the next step, the structural characteristics of connections between segments are investigated. A closer look at the nodes and the connections where filaments meet, is demonstrated in Fig. 4.11e for a sample network. The most observed number of connections at a node was 3 and the second most observed was 4. Moreover, in average 3.11 ± 0.04 connections exist per node and $8.76 \pm 2.33\%$ of all nodes were open nodes. The distribution of angles differed depending on the amount of connections at a node. At nodes with 3 connections, a high probability of finding an angle around 90° exists

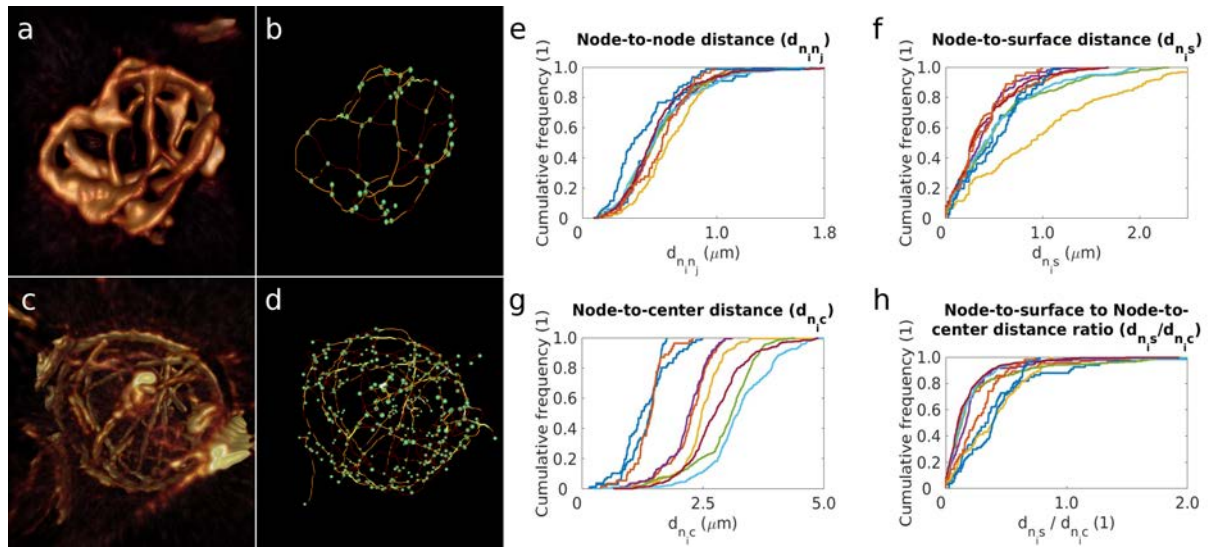


Figure 4.10: Evaluated element descriptors for nodes. (a) Example of a FtsZ protein network with relatively low node number and (b) the corresponding spatial graph with emphasized nodes in green. (c) Example of a FtsZ protein network with relatively high node number and (d) the corresponding spatial graph with emphasized nodes in green. In the spatial graph the segments are shown in a yellow \rightarrow red color code with red representing thicker segments. (e) Normalized cumulative frequency of the node-to-surface distances of the networks. Each line represents one image. (f) Normalized cumulative frequency of the node-to-node distances in networks. Each line represents one image. (g) Normalized cumulative frequency of the node-to-center distances in networks. Each line represents one image. (h) Normalized cumulative frequency of the node-to-surface to node-to-center distances ratio in networks. Each line represents one image.

(Fig. 4.11f), whereas at nodes with 4 connections no preferred angle could be identified (Fig. 4.11c).

From small to big networks

Combining information of shape and elements provides insight into relative changes in the size of the networks. Investigating the relationship between enclosed volume of the networks and calculated shape descriptors such as stretch and oblateness (Fig. 4.11g) show low correlations ($R^2 = 0.18$ and $R^2 = 0.00$, respectively). In contrast, a higher correlation exists between the number of the nodes in the network and the distance of the nodes from the center (Fig. 4.11h), showing that a higher number of nodes results in nodes being located further away from the center of mass ($R^2 = 0.81$). The size of the network also correlates strongly with the number of nodes in the network ($R^2 = 0.89$; Fig. 4.11i). If the network volume is twice as big (e.g. $100 \rightarrow 200 \mu\text{m}^3$), the number of nodes is also approximately doubled; but with increasing network size the node placement is not homogeneously propagated, as the average distance of the nodes from the center increased at the same time by a factor of 1.5. Furthermore, the combination of node-to-surface and node-to-center distance measurements (Fig. 4.10e and Fig. 4.10g) suggests that the average value of compactness for the data is closer to 1 than to 0. This is

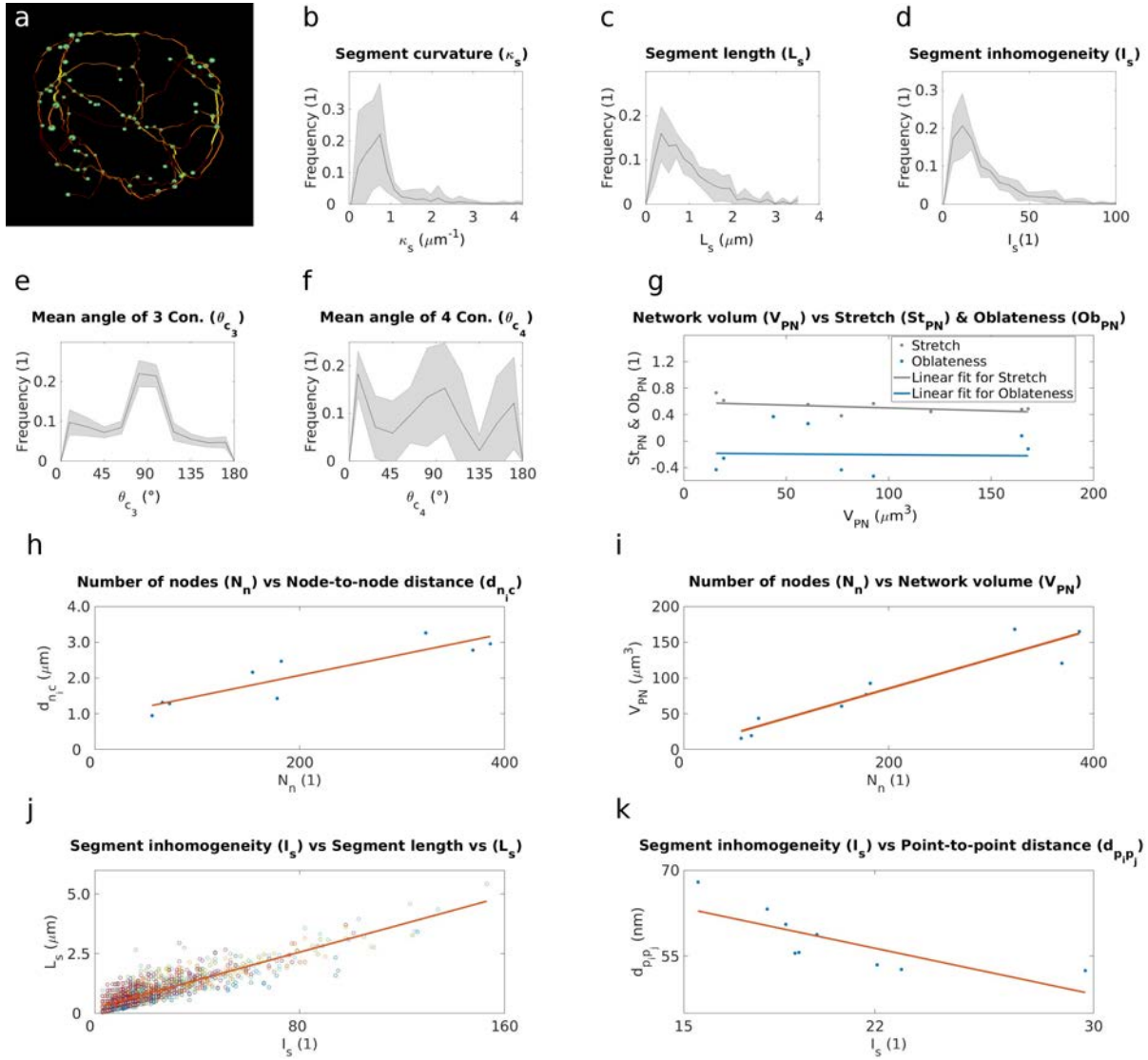


Figure 4.11: Element descriptors of connections and segments and derived analysis of calculated descriptors. (a) Sample network with segments shown in a yellow \rightarrow red color code with red representing thicker segments. (b) Normalized distribution of segment curvature. (c) Normalized distribution of segment length. (d) Normalized distribution of segment inhomogeneity. (e) Normalized distribution of angles at nodes with three connections. (f) Normalized distribution of angles at nodes with four connections. $n=9$; data shown as mean \pm standard deviation. (g) Network volume vs. stretch (gray) and oblateness (blue) ($R^2 = 0.18$, $R^2 = 0.00$). (h) Number of nodes vs. average node-to-center distance ($R^2 = 0.81$). (i) Number of nodes vs. volume ($R^2 = 0.89$). (j) Segment inhomogeneity vs. segment length ($R^2 = 0.76$). Data from all segments of nine networks are presented here. Each circle represents a segment, each color represents a data set. (k) Segment inhomogeneity vs. mean distance between points on segments ($R^2 = 0.59$). $n=9$.

confirmed by calculating the average compactness (Compactness=0.73). Besides these global relationships between the size of networks and shape and element descriptors,

segment growth can be analyzed on a local scale. On one hand, with longer segments the segment inhomogeneity increases (Fig. 4.11j). On the other hand, the increase in segment inhomogeneity results in smaller distances between the points within segments (Fig. 4.11k).

The results presented so far show that the designed structural features are capable of quantitatively describing protein network structure. Therefore, in the next step, the capability of the designed structural features to distinguish two FtsZ isoforms is put to test.

4.3.3 Distinguishing FtsZ isoforms: a Statistical Approach

In this part of the chapter, the second application of the developed quantitative imaging method for structural characterisation and comparison of FtsZ1-2 and FtsZ2-1 network structure is presented. Here, 40 confocal microscopy images ($n = 20$ 3D images per isoform) were analysed with this method to identify and quantify structural differences in the phenotypes of the two isoforms. For all outcome measures, differences between isoforms were assessed by unpaired Student's t-test. All values are presented as mean \pm standard deviation. Statistical significance was set at $p = 0.05$. Distributions are calculated as mean \pm standard deviation of normalised probability or normalised cumulative probability of descriptors from the network of each image.

Network Gross Morphology

To carry out a quantitative comparison of structural features of FtsZ1-2 and FtsZ2-1 networks, the method showcased in section 4.3 is utilized [10, 11, 13].

Network shapes show a great range of variations. However, quantitative comparison of the networks structures belonging to the two isoforms reveals that three out of seven structural features i.e., enclosed volume of the network, network density and smallest diameter of the network exhibit distinctive (statistically significantly different) features, while the four other shape descriptors are generic. The volume enclosed by FtsZ1-2 networks ($69.5 \pm 48.9 \mu\text{m}^3$) is significantly greater than that enclosed by FtsZ2-1 ($39.9 \pm 15.4 \mu\text{m}^3$) networks ($p = 0.01$; Fig. 4.12e). However, FtsZ1-2 and FtsZ2-1 networks have similar network volumes ($17.7 \pm 10.2 \mu\text{m}^3$ and $14.0 \pm 4.4 \mu\text{m}^3$, respectively, Fig. 4.12f). This reveals that the space not occupied by material within the FtsZ1-2 networks is greater than in FtsZ2-1. Quantitatively, this can be seen in the significantly lower network volume density for FtsZ1-2 (0.30 ± 0.10) compared to that for FtsZ2-1 (0.36 ± 0.07 ; $p = 0.02$ Fig. 4.12g). Besides volume and density, the overall shapes of the networks show differences between the two isoforms, as the smallest diameter is in FtsZ1-2 significantly greater than in FtsZ2-1 ($3.34 \pm 2.36 \mu\text{m}$ vs. $1.80 \pm 0.79 \mu\text{m}$; $p = 0.01$; Fig. 4.12h). In contrast, the greatest diameter of the networks (FtsZ1-2: $11.8 \pm 5.96 \mu\text{m}$; FtsZ2-1: $8.86 \pm 4.76 \mu\text{m}$), the stretch of the networks (FtsZ1-2: 0.69 ± 0.20 and FtsZ2-1: 0.77 ± 0.11) and the oblateness of the networks (FtsZ1-2: -0.17 ± 0.35 and FtsZ2-1: 0.02 ± 0.37) are not significantly different for the two isoforms (Fig. 4.12h-j). However, the difference in the sign of oblateness value for FtsZ1-2 and FtsZ2-1 points towards a trend of a more flat and plate-like shape of FtsZ1-2 networks.

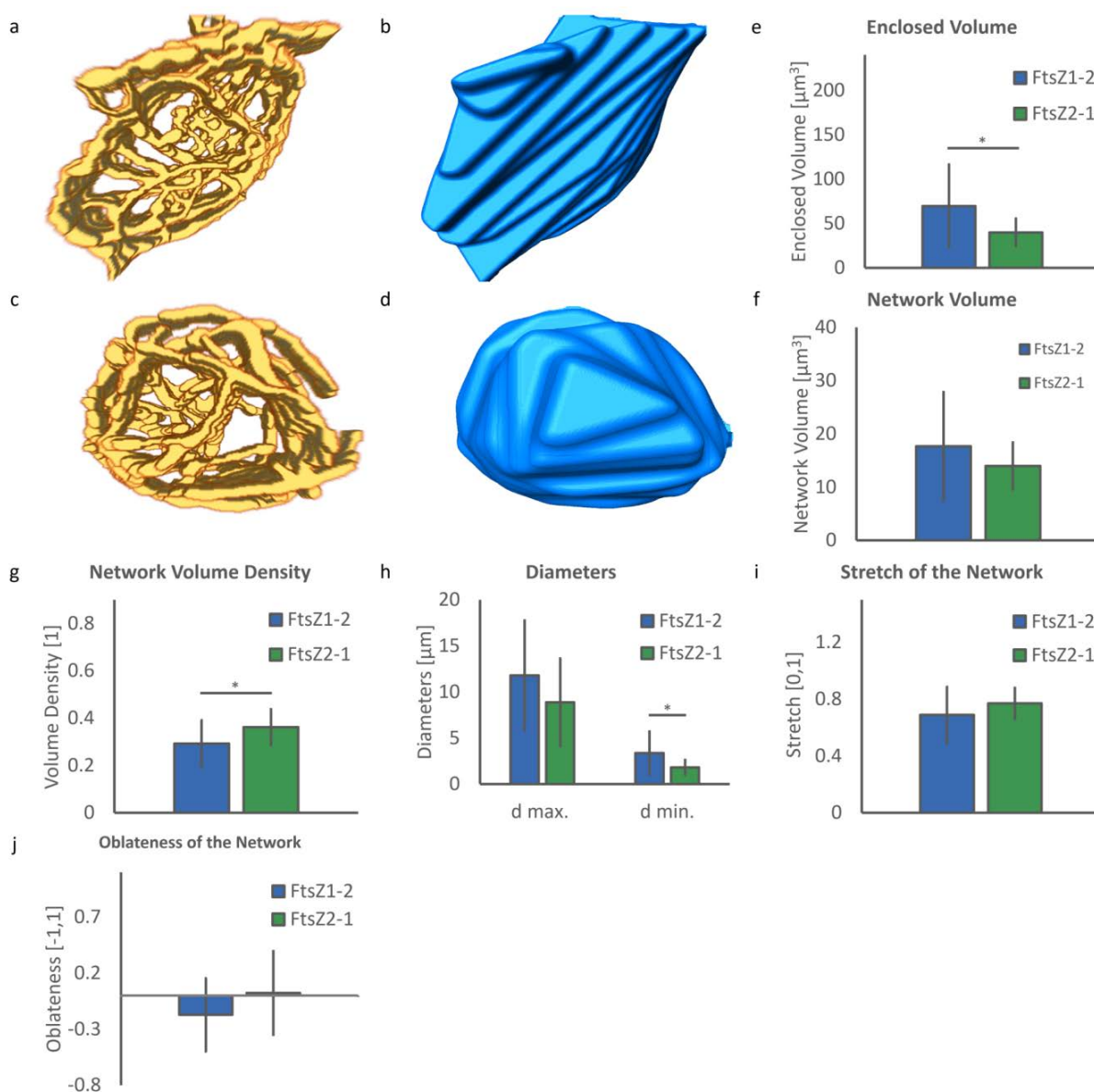


Figure 4.12: Analysis of gross morphological shape of *FtsZ1-2* and *FtsZ2-1* networks. a) Representative sample of a segmented network of *FtsZ1-2*. b) The outer surface (wrapped hull) of the segmented network in (a). c) A representative sample of a segmented network of *FtsZ2-1*. d) The outer surface created based on the wrapped hull of the segmented network in (c). e-j) Quantitative analysis of network shape with. $n=20$ images per isoform. *FtsZ1-2* is shown in blue and *FtsZ2-1* is shown in green colour. Data is shown as mean \pm standard deviation. * indicates significant difference between isoforms. e) Enclosed volume of the network. f) Network volume. g) Network volume density. h) Greatest and smallest diameters of the network. i) Stretch of the network. j) Oblateness of the network.

Network nodes

To analyse morphological details of the structural components of the protein network, the segmented images were transformed into a spatial graph consisting of points, nodes, segments and connections (Fig. 4.13a, b). Points were placed at filaments where a local change in segment characteristic such as orientation or thickness occurs. Elements are the structural unit connection points. Nodes are defined as points that are connected to more than two other points. Nodes are meeting points of the filaments in the network. Segments are the filaments connecting one node to another. For a quantitative characterization of these elements, structural features were computed. FtsZ1-2 networks consist of significantly more nodes than FtsZ2-1 networks (197 ± 142 vs. 126 ± 32 ; $p = 0.04$, Fig. 4.13c). The number of nodes shows a great distribution within the class of FtsZ1-2 networks. Despite the difference in the number of nodes in the networks, compactness and node densities, which are directly related to the number of the nodes, are not statistically different for the two isoforms (FtsZ1-2: 0.71 ± 0.09 and 3.15 ± 1.20 , respectively and FtsZ2-1: 0.72 ± 0.07 and 3.43 ± 1.00 , respectively, Fig. 4.13d, e). This is due to the similarities in network volume being the dominant parameter in the evaluation of these two shape descriptors. The mean size of nodes and node thickness are similar for the FtsZ1-2 and FtsZ2-1 isoforms (mean value per network: FtsZ1-2: $24.6 \pm 10.7nm$ and FtsZ2-1: $22.9 \pm 7.19nm$, respectively; Figure 4.13f). However, the analysis of the normalized distributions of all node thicknesses in the networks reveals noteworthy results (Fig. 4.13g). For nodes with thickness up to 100 nm the distributions for the two isoforms are almost identical. However, in FtsZ2-1 a small portion of nodes (approximately 1%) have thickness values between 100 – 140nm whereas in FtsZ1-2 networks no nodes of these sizes exist. This small fraction of nodes in FtsZ2-1 comprises the meganodes. The analysis of relative distances revealed that in both types of networks individual nodes are located closely to the surface and other nodes, but further away from the center of the network. In FtsZ1-2 networks there is a trend of this distance to the center and being even greater than in FtsZ2-1 ($p = 0.06$). 78% of all nodes of the FtsZ2-1 networks lie in a distance of less than $2.5 \mu m$ from the center of gravity of the network, whereas in FtsZ1-2 networks only 59% are within the same distance (Fig. 4.13i). On the other hand, more nodes in FtsZ2-1 networks are located closely to the network surface (90% vs. 80% within $1 \mu m$; Fig. 4.13k). Besides this difference, local node distributions in the networks are similar (Fig. 4.13j,l). Mean node-to-center distances (FtsZ1-2: $2.07 \pm 0.60 \mu m$ and FtsZ2-1: $1.76 \pm 0.360 \mu m$), node-to-node distances (FtsZ1-2: $0.58 \pm 0.080 \mu m$ and FtsZ2-1: $0.59 \pm 0.080 \mu m$), node-to-surface distances (FtsZ1-2: $0.57 \pm 0.160 \mu m$ and FtsZ2-1: $0.48 \pm 0.230 \mu m$) and node-to-surface to node-to-center distance ratio (FtsZ1-2: 0.29 ± 0.09 and FtsZ2-1: $0.27 \pm 0.070 \mu m$) (Fig. 4.13h) are not statistically different between the two isoforms.

Network segments

The number of the segments in FtsZ1-2 (237 ± 206) shows a great variation and is slightly, but not significantly greater than in FtsZ2-1 (183 ± 49 ; $p = 0.07$; Fig. 4.14a). In contrast, segment length (mean length: FtsZ1-2: $0.81 \pm 0.11 \mu m$; FtsZ2-1: $0.84 \pm 0.12 \mu m$, Fig. 4.14b) and its normalized distribution (Fig. 4.14c) are remarkably similar in both networks. The segments in FtsZ1-2 networks are significantly less curved than in FtsZ2-1

($0.50 \pm 0.20 \mu m^{-1}$ and $0.65 \pm 0.14 \mu m^{-1}$ respectively, Fig. 4.14d) resulting in another distinctive element descriptor ($p = 0.01$). Besides the higher mean, the distributions of curvatures are similar for the two isoforms. Analogously, the segments in FtsZ2-1 networks are on average thicker than the ones in FtsZ1-2 networks ($34.4 \pm 6.82 nm$ and $28.9 \pm 6.41 nm$, respectively, Fig. 4.14f; $p = 0.02$). Although the normalized distributions of segment thickness (Fig. 4.14g) for both isoforms below a thickness of $80 nm$ are very similar, almost 5% of the segments in FtsZ2-1 networks have a thickness between 80 and $120 nm$ while almost no segments in FtsZ1-2 network are so thick. These thick segments in FtsZ2-1 are the ones meeting at the meganodes. The mean and normalized distributions of segment inhomogeneity (Fig. 4.14h and i) are almost identical in both isoforms, (FtsZ1-2: 18.5 ± 4.56 and FtsZ2-1: 18.8 ± 3.97). The same pattern is observed for point-to-point distances (FtsZ1-2: $62.7 \pm 13.3 nm$ and FtsZ2-1: $58.7 \pm 11.4 nm$, Fig. 4.14j) and its normalized distribution (Fig. 4.14k).

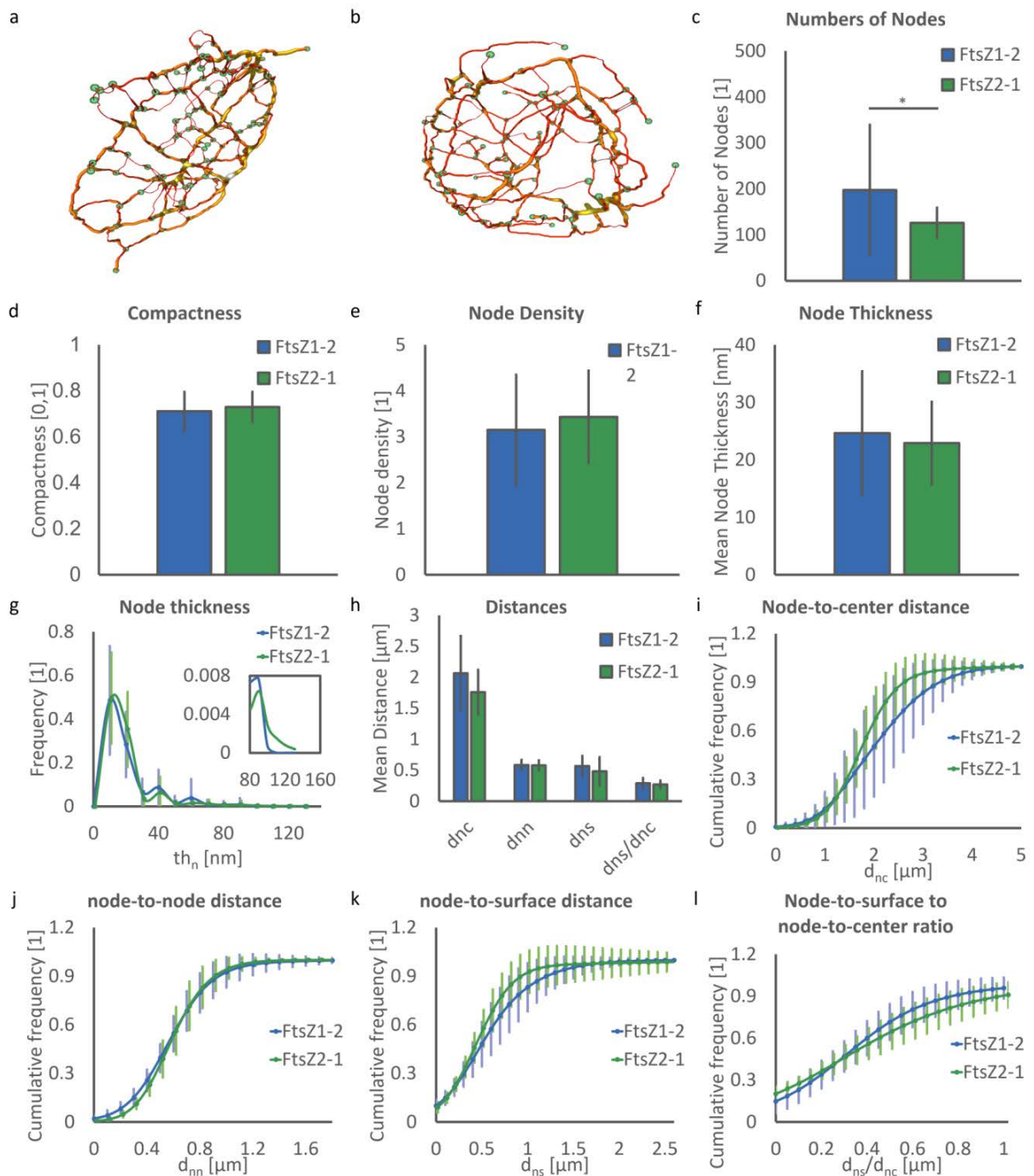


Figure 4.13: Spatial graphs and evaluated nodal parameters. *a)* A sample spatial graph of a FtsZ1-2 network. *b)* A sample spatial graph of a FtsZ2-1 network. Nodes in both networks of (a) and (b) are shown in green spheres. The segments are colour coded based on their thickness with red (thinner segments) yellow (thicker segments). *c)* Number of nodes. *d)* Compactness of the network. *e)* Node density. *f)* Mean values of node thickness per network. *g)* Normalized distribution of node thickness. Enlarged part in right top corners highlights the sizes of meganodes. *h)* Mean values of node-to-center distance per network, node-to-node distance, node-to-surface distance and node-to-surface to node-to-center distance ratio. *i)* Normalized cumulative distribution of node-to-center distance. *j)* Normalized cumulative distribution of node-to-node distance. *k)* Normalized cumulative distribution of node-to-surface distance. *l)* Normalized cumulative distribution of node-to-surface to node-to-center distance ratio.

Network connections

The number of connections in the two isoforms are very similar (FtsZ1-2: 3.14 ± 0.06 and FtsZ2-1: 3.12 ± 0.05 , Fig. 4.15a). This similarity is due to the fact that both networks contain nodes with mostly three connections. On the contrary, the percentage of open nodes is significantly higher in FtsZ1-2 networks (FtsZ1-2: $6.14 \pm 3.10\%$ and FtsZ2-1: $3.50 \pm 2.06\%$, $p < 0.01$; Fig. 4.15b). Considering an open node as a filament that leaves the network, i.e. connects to other networks, then the increase in open-nodes demonstrates the tendency of the filaments to leave the chloroplast. The low p-value in this analysis is also consistent with the fact that extraplasmidic filaments are much more frequently observed in FtsZ1-2 networks than in FtsZ2-1 networks. Assessment of the mean values and distribution of angles between segments in the most observed connections (three and four connections, Fig. 4.15c-g, respectively) reveals similar connectivity inside FtsZ1-2 and FtsZ2-1 networks. Both networks have angles around 80° in nodes with three and four connections (FtsZ1-2: 78.9 ± 4.78 and 77.2 ± 17.4 and FtsZ2-1: 80.1 ± 4.60 and 78.7 ± 13.9 , respectively). It is worth noting that in both network types, the standard deviation of angles in nodes with four connections is higher than in nodes with three connections (Fig. 4.15g).

The results presented here show that the set of designed structural features allow extracting distinguishing structural characteristics of FtsZ1-2 and FtsZ2-1 isoforms by showing 7 out of 25 statistically significant features. Therefore, in the next step, the capability of the designed machine learning algorithm to automatically classify isoforms is put to test. Furthermore, the feature importance is compared to the previously identified distinguishing features.

4.3.4 Protein Network Classification: a Machine Learning Approach

To perform an end-to-end classification of the FtsZ isoforms, a random forest model is designed and trained. This allows further to find the distinguishing characteristics of two FtsZ isoforms. To do so, the ML model is trained on the 25 calculated structural features of the protein networks ($n = 37$) for 1) performing an end-to-end classification of the networks and 2) determining the importance of the structural features in this classification task.

I employed a Random Forest Model to perform the classification task based on the extracted features, which is the state of the art method for classification based on a set of unstructured features [42, 256]. The random forest model (RF) is designed to carry out the task of mapping the structural feature set (\mathbf{F}) to a class of FtsZ1-2 or FtsZ2-1:

$$RF(\mathbf{F}) = \text{isoform}, \quad (4.20)$$

with \mathbf{F} defined as:

$$\mathbf{F} = [V_{EN}, V_{PN}, \rho_{PN}, d_{PN}^{max}, d_{PN}^{min}, St_{PN}, Ob_{PN}, N_n, th_n, \rho_n, d_{nn}, d_{ns}, d_{nc}, d_{ns}/d_{nc}, C_{PN}, N_{op}, N_s, L_s, \kappa_s, th_s, I_s, d_{pp}, n_c, n_{oe}, \theta_3, \theta_4]. \quad (4.21)$$

The dataset containing the 26 structural features was eight times randomly divided into training ($n=30$) and testing ($n=7$) sets. As shown in 3.2.3, employing a random forest

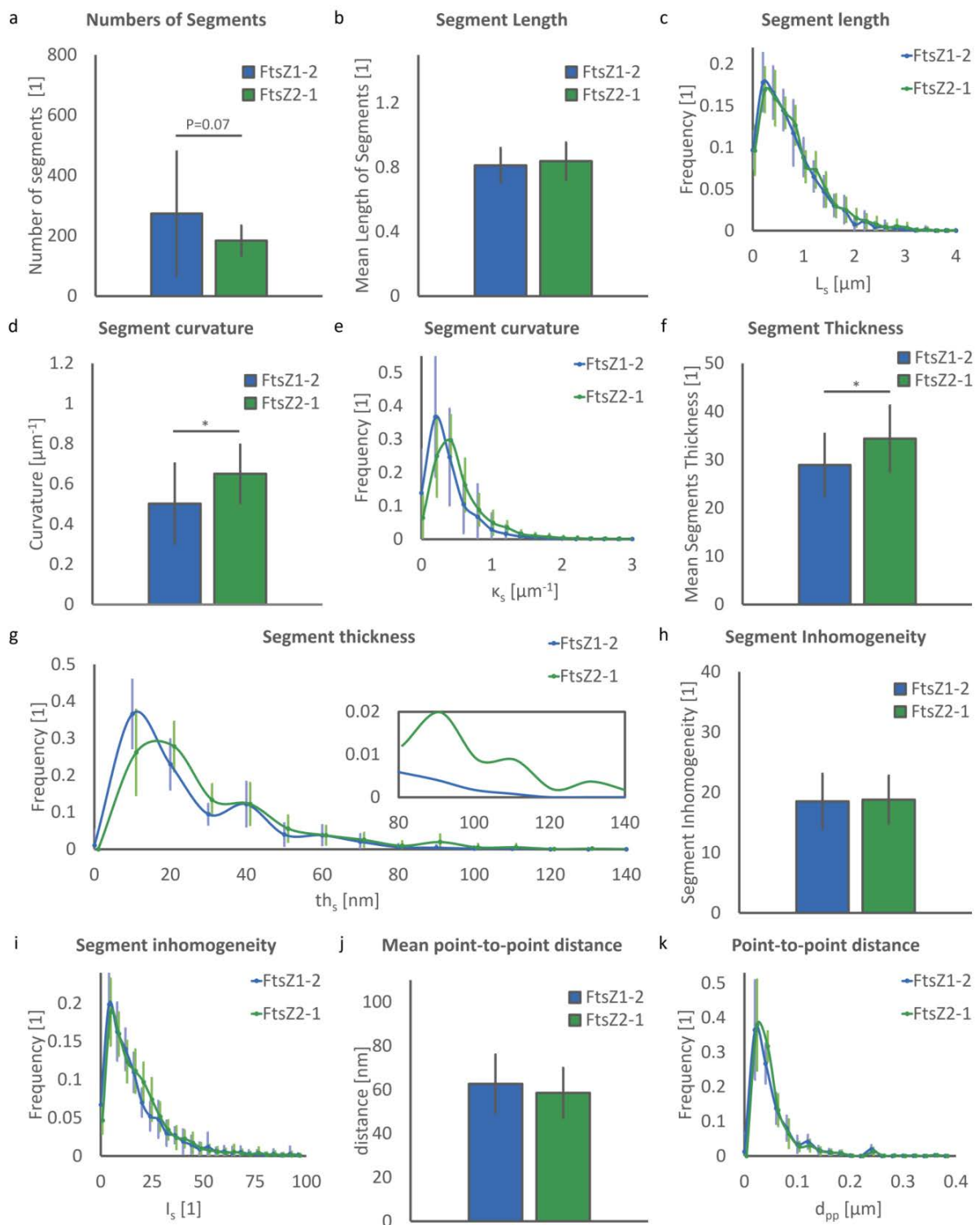


Figure 4.14: Evaluation of element morphology. a) Number of the segments. b) Mean values of segment length. c) Normalized distribution of segment length. d) Mean values of segment curvature per network. e) Normalized distribution of segment curvature in FtsZ1-2 and FtsZ2-1 isoforms. f) Mean values of segment thickness. g) Normalized distribution of segment thickness. Enlarged part in right top shows segments above 80nm thickness. h) Segment inhomogeneity. i) Normalized distribution of segment inhomogeneity. j) Mean values of point-to-point distance per network.

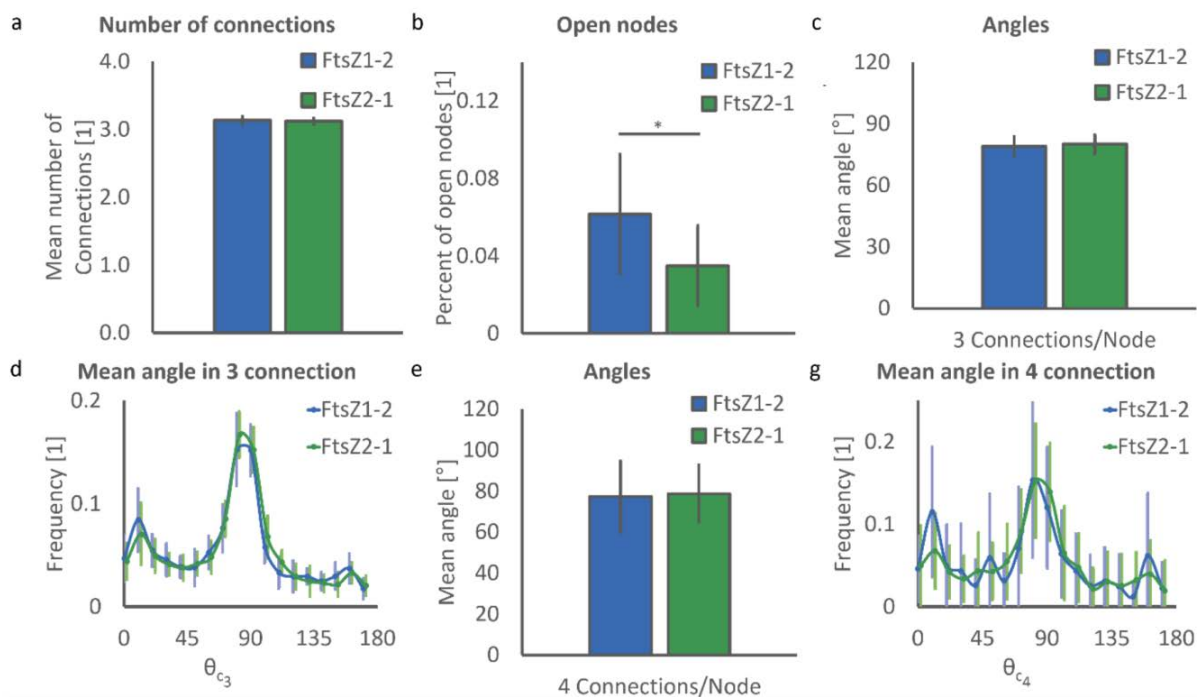


Figure 4.15: Evaluation of element morphology. a: Number of the segments. b: Mean values of segment length. c: Normalized distribution of segment length. d: Mean values of segment curvature per network. e: Normalized distribution of segment curvature in FtsZ1-2 and FtsZ2-1 isoforms. f: Mean values of segment thickness. g: Normalized distribution of segment thickness. Enlarged part in right top shows segments above 80 nm thickness. h: Segment inhomogeneity. i: Normalized distribution of segment inhomogeneity. j: Mean values of point-to-point distance per network. Normalized distribution of point-to-point distance.

model guaranties the absence of overfitting [98]. Therefore, no validation set is needed. Each testing sets consisted of at least three samples of each isoform. For each data division, a random forest classification model was built upon the extracted structural features with the isoform (FtsZ 1-2 vs. FtsZ 2-1) as output class. This allows refuting dependency of the classification results on train/test dataset division. The Gini index was used as attribute selection measure [43, 256]:

$$G_{C_i} = \sum_{j \neq i} \sum (f(C_i, T)/|T|)(f(C_j, T)/|T|), \quad (4.22)$$

with T denoting the whole feature set, $(f(C_i, T)/|T|)$ determining the probability of selected case belonging to the class C_i (FtsZ1-2 or FtsZ2-1). All random forest algorithms were implemented using the machine learning library Scikit-learn in Python [262].

The importance of each structural feature on the model predictions for an individual instance for both the classification model and surrogate mechanical model are analyzed by noising up each feature and comparing the plurality of out-of-bag vote and the reality to measure a wrong prediction rate [42]. In the surrogate models, the extracted structural characteristics with high importance for the model are considered responsible for inducing the observed mechanical behaviour.

The 8 trained models reached 6 out of 7 correct predictions (Fig. 4.16a; Table 4.1). A correctly classified FtsZ2-1 isoform and a correctly classified FtsZ1-2 isoform, as well as the wrongly classified isoform (FtsZ1-2) are depicted in Fig. 4.16b-d, respectively. In the classification task, an average $F1$ score of 0.83 ± 0.11 and an area under the ROC curve of 0.86 ± 0.08 (Fig. 4.16e) was reached. The classification task took in average 5.1 *sec*.

Analyzing the importance of each of the structural features in the classification models reveals which features contribute most and which least to the isoform structural classification. The five most important structural features are the percentage of open ends ($19 \pm 5\%$, $p < 0.01$), segment curvature ($12 \pm 9\%$, $p = 0.05$), network volume density ($8 \pm 4\%$, $p = 0.03$), compactness ($6 \pm 3\%$, $p = 0.24$), and the mean segment thickness ($5 \pm 7\%$, $p = 0.01$). These have in total 50% of the overall importance in the classification models (Fig. 4.16f). Interestingly, the number of open ends and the smallest diameter of the network were significantly different between the two isoforms, but of less importance for classification.

Table 4.1: Performance metrics of the trained classification model.

Metric	Accuracy	F1-score	area under ROC
Value	6/7	0.83 ± 0.11	0.86 ± 0.08

4.3.5 Discussion

So far in this chapter, a newly developed quantitative imaging and machine learning method specifically designed to extract structural features of protein network structures from 3D microscopy images and to automatically classify them is presented. The details of the method as well as the thorough validation process to test its robustness is presented.

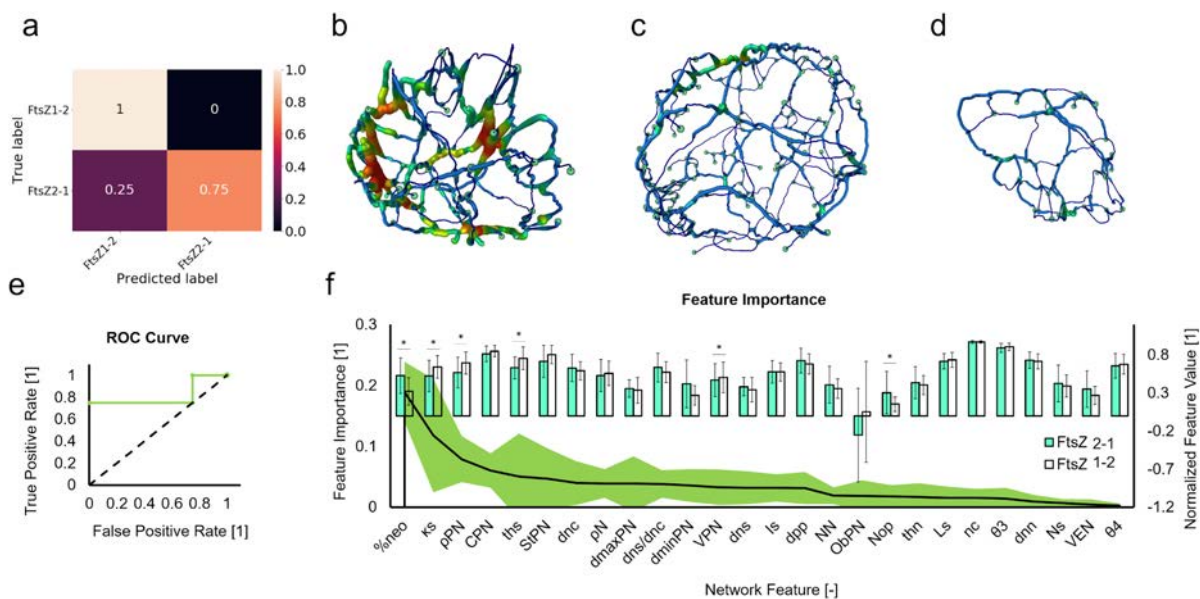


Figure 4.16: End-to-end classification of isoforms. a) Confusion matrix of prediction performance with 3 out of 3 correct predictions for FtsZ1-2 and 3 out of 4 correct predictions for FtsZ2-1. b) A sample spatial graph of correctly classified FtsZ2-1. c) A sample spatial graph of correctly classified FtsZ1-2. d) A sample spatial graph of wrongly classified FtsZ1-2. e) ROC curve of model prediction. f) Mean classification importance for the structural features as well as normalized feature values (normalized to maximum of each feature). Data shown as mean \pm standard deviation. * indicates a significant difference between isoform (un-paired students' t-test).

The method were then used as a first application to analyze the assembly of FtsZ protein network and relating its structure to its functionality. Moreover, as a second application, the method was used to investigate distinguishing structural features of two FtsZ isoforms naming FtsZ1-2 and FtsZ2-1. These two isoforms are believed to be the major forces in organizing the morphology of the chloroplast [228]. However, due to different evolutionary paths in their design, they participate in different manners in the mechanical functionality of the plastoskeleton.

Describing FtsZ Structure

To date, analysis of protein network structures as basis for cytoskeletal behaviour assessment is mainly qualitative. However, with current advanced microscopy and labeling techniques, localized cytoskeletal behavior can be imaged with great detail, allowing for a quantitative network analysis. Here, the possibilities to quantitatively describe the structure of protein networks are analyzed and a tool set, which contributes to such a quantitative network analysis is provided. To show the capabilities of this tool set, it was validated using 3D sets of confocal microscopy images of FtsZ.

The observed variations in calculated shape descriptors (Fig. 4.9 e-g) of FtsZ show that although there exist great variations between the sizes of the analyzed networks, the network volume density shows lower deviation from the mean value. This conveys that in

networks from small to big, the network volume density does not change remarkably. In cases of ellipsoidal-like network shapes, like for FtsZ [122], morphological characteristics such as diameters of the network and relationships between these calculated descriptors can be analyzed (Fig. 4.9g). Therefore, stretch and oblateness of the network are identified (Fig. 4.9h). The stretch values indicate a deviation of the shape of the networks from a sphere to a more stretched geometry while the oblateness measurements convey the tendency toward more rod-shaped networks. However, the greater variation in oblateness shows that stretch is, for the analyzed data sets, a better measure of the shape for the network.

Analysis of the element components of protein network allows detailed quantification of the subunits of the network. This analysis enables to quantitatively describe the characteristics of structural units of the network: nodes, connections and segments. Node-to-surface distances are relatively similar for all analyzed FtsZ networks, the distance of the nodes from the center of mass shows a great variation between networks. Quantifying relative positions of the nodes is in future applications useful in terms of studying dynamic settings of networks and to identify changes that occur in the network as a result of external stimuli on the structure of the network or internally motivated changes.

The shape measures allow to relate changes of the protein network size and shape to alterations of the plastid, or cells in the case of other protein networks, morphology, which will allow in future applications to relate protein network alterations to cellular processes. For example, during cell division the cell, and accordingly the cytoskeleton, elongates from its initial form to a more stretched shape [334]. Furthermore, in cancerous cells, cytoskeleton protein transformations lead to changes in mechanical properties of the cancer cells in contraction, stretchability and deformability [190]. For example, epithelial-to-mesenchymal transition in colorectal cancer cells results in transformation of the cytoskeleton into a spindle-like shape losing their polarity [372]. Moreover, propagation of tau filaments from cell to cell in Tauopathic diseases have been shown to result in protein network changes [72, 204]. All these process could be investigated quantitatively with the herein introduced shape descriptors in future studies.

Analysis of segments have been previously shown by Smith et al. [311] and Alioscha et al. [5] to link actin filaments fragments in segmented images and by Stein et al. [314] for extracting network geometry of collagen gels. Moreover, Xu et al. [370] analyzed different filamentous protein networks. To obtain a complete protein network analysis method, these entities are included in the shape and element analysis and adapted the calculation of these to the structural quantification method. Analyzing the segments of the network does not only shed light on the local attributes of the filaments, but also allows to draw further conclusions on the mechanical properties of the networks, as e.g. the curvature of the segments allows to quantify mechanical forces on the filament [272] or effects of shear stress [5]. Segment length can be used to track changes that will transform the architecture of the network in a more fundamental way. The angles between the segments meeting in one connection give insight into the shape of individual sub-compartments of the network. Also, it might be applicable to track the effects of external stimuli on the network such as shear forces, which elongate the filaments and change the angles between them in the network [5]. In the here analyzed networks a great variation of angles between connections was observed, which might be caused by such external stimuli. Therefore, tracking structural descriptors might enhance the understanding of the dynamic setup

of network structures, by allowing to monitor and quantify changes occurring in various processes that alter the shape of the network.

Linking shape and element descriptors gives insights into how the shape of protein networks changes during different processes without being transformed into a more stretched or plate-like shape. More nodes resulted in nodes being located further away from the center of mass. This shows that FtsZ networks might grow in size by adding nodes in radial direction from the center of gravity close to the surface, consequently resulting in networks with higher volume. Moreover, the relation between the size of the network and number of nodes in the network conveys the possibility of a preferred approach of the network to grow. The network seems to grow in volume by adding more nodes to the existing network instead of preserving the nodes and adding more connections to the existing nodes. Finally, it was found, that there exists a direct correlation between the length of the segments and the inhomogeneity of the segments.

The presented method has several limitations. It is the study of protein networks in living cells. Therefore, assembly and disassembly is a dynamic process that generates inhomogeneities. Furthermore, the spatial resolution, especially in z-resolution, does not allow to resolve all small structures in the images and therefore, impacts the results as well. However, the fast advancing field of microscopy technology will allow to overcome this limitation in future applications. A main limitation of the method is the segmentation, as it is in most imaging studies. Global threshold algorithms such as the Otsu-Algorithm [254] are commonly used to extract the geometry of filaments [381]. However, the presence of imaging-specific artifacts, like filament discontinuities, high signal-to-noise ratio resulting from presence of overexposed pixels and dynamics of the network, decrease the efficiency of global algorithms. As long as this is not overcome, an adaptive thresholding algorithm, which accounts for intensity variations, suffices. However, variations in the input image quality effects the segmentation outcomes, therefore a manual correction is applied, which introduces user bias. An enhanced segmentation in future studies could include linkage of filament fragments, as previously presented for microtubule network architecture phenotypes in fibroblasts [381]. Therefore, care must be taken in the analysis to avoid systematic errors. One also should keep in mind that the approach used here might not be directly applicable to other network shapes, as an ellipsoidal shape was assumed, approximated by 2 vectors and 3 scalar quantities. For other (more complex) shapes, different shape models have to be used.

The regulations of individual proteins and their functions have been investigated in detail in the past [79]. Here, a method to quantify the structure of protein networks was presented. Proteins forming networks in biological environments are many copies of a few key pieces, which can be assembled into a wide range of structures depending on how the pieces are assembled. The method presented here provides a quantitative tool to investigate this meso-scale of the assembly. This analysis can potentially be used to study temporal evolution of the network by batch processing consecutive frames of a time lapsed life image sequence. Analyzing the structure of the network in each frame and tracking changes of structural features might allow relating internal and external stimuli to the modifications of the structure by utilizing a network-based simulation model and might contribute to determining functionality of the network. Here, the FtsZ protein network structure was analyzed and aspects of this internal organization was revealed. In the future, the developed method can be applied to compare networks for identify-

ing relationships of structural and functional differences. Furthermore, more complex networks, such as cytoskeletons [362, 380] can be analyzed. This is possible since these are built of the same basic structural units. This analysis would facilitate understanding the links between the interactions of the individual units of the network and the large-scale cellular behaviors depending on them [100]. Linking network structure and functionality by tracking dynamic structural changes over time and comparing different states or types of networks, may allow to more precisely identify (mal)functions or design protein-engineered biomaterials for applications in regenerative medicine.

Quantitative Structural Comparison of FtsZ1-2 and FtsZ2-1

Among the five different single-gene knockout lines in moss, the FtsZ1-2 and the FtsZ2-1 are particularly interesting. Although these two genes show similar levels of expression in chloronema cells, the chloroplast morphology in the same tissue is drastically different between the respective knockout lines. This implies that the morphological differences between the chloroplasts of the two mutant lines are likely to be due to the differences in sequence, structure and function of the two isoforms. These differences between FtsZ1-2 and FtsZ2-1 could influence the 3D network architectures formed by these isoforms. Therefore, a comprehensive analysis of the network morphology and connectivity for each FtsZ isoform and identification of the distinctive network features between the different isoforms could provide hints at the specific functions of these proteins. In particular, the mechanobiological study of the relationships between the FtsZ networks and the chloroplast shape and integrity would benefit from such a comparative morphological characterisation.

A visual inspection of the 3D-reconstructed images of FtsZ1-2 and FtsZ2-1 networks reveals only few distinctive features between the two isoforms. These include the extra-plastidic filaments of FtsZ1-2 networks and the meganodes of FtsZ2-1 networks. Both of these observations, which are based on visual inspection, are confirmed by the quantitative analysis which reveals that i) the proportion of the open nodes in FtsZ1-2 networks is significantly higher than that in FtsZ2-1 networks and that ii) the meganodes occur only in the FtsZ2-1 networks where they constitute about 1% of all nodes. Therefore, the developed method of quantitative analysis proves to be useful in testing the validity of visually detected structural phenomena, and also quantifies the extent, to which these phenomena are represented in the respective network classes. Besides testing the validity of already detected distinctions, the quantitative analysis also identifies further distinctive features, which avoid detection via visual inspection of images. These include shape descriptors such as enclosed volume, network volume density and small diameter of the network as well as elemental descriptors such as total number of nodes, segment curvature and segment thickness. In addition to these structural features that are significantly different between the two isoforms, the quantitative analysis also provides information about the general behaviour and trends that the two network classes. For instance, nodes of the networks are not evenly distributed within the enclosed network volume. Rather, they are located relatively closely to the surface of the networks and far away from the network center. This proximity to the surface could be due to a possible function that the nodes may have at the chloroplast surface. This result is also consistent with the findings of the visual analysis that meganodes of FtsZ2-1 are located at the chloroplast surface and often associated with surface indentations. I also show that certain isoform-specific network

features occur at the sites of specific types of structural deformations at the chloroplast surface. These altered chloroplast morphologies detected in the transfected cells deviate from the typical lens shape of the chloroplasts normally observed in the non-transfected cells, and could thus be attributed to the elevated levels of FtsZ. Thus, the manner of these shape variations can provide clues concerning the tensile or compressive forces that the FtsZ filaments could bear and exert on the chloroplast surface. Further, the patterns of the morphological deformations of chloroplasts varies with the specific isoform, indicating that the FtsZ isoforms act differently in their ability to modify the chloroplast structure. These findings are consistent with the findings of the knockout experiments in which inactivation of FtsZ1-2 and FtsZ2-1 resulted in distinctively different degrees of chloroplast deformation.

In order to gain further insights into the influence of the FtsZ protein family on chloroplast morphogenesis, the early-to-late progression of network formation and relevant changes in chloroplast morphology can be monitored via time-lapse fluorescent imaging. The presented image analysis method can be adapted for the characterisation of the temporal changes in the network organisation and turnover of FtsZ filaments. To learn about the mechanical properties of FtsZ networks, laser ablation microscopy could be implemented.

Automatic Classification of Isoforms based on Structural Features

The ML-based classification model trained on the extracted structural features achieved high accuracy (6 out of 7 correct prediction, F1 score of 0.83). Moreover, by 8 random test/train dataset divisions the dependency of classification results on dataset division was eradicated. Analyzing the feature importance in the classification task reveals the most distinguishing structural features: the number of the open end filaments, the curvature of the filaments, the volumetric density of the protein networks, compactness of the network and the filament thickness. These features also showing significantly different values for the FtsZ isoforms (besides compactness) [255] and confirms that the model automatically extracts the distinguishing features. The classification model achieved on par accuracy with deep learning based protein networks classification methods [186, 260], while adding the ability of extracting specific structural features enabling the classification model to perform predictions.

4.4 Simulating the Mechanical Behaviour of Protein Networks

From the micro-scale of cytoskeleton to the macro-scale of connective tissues, bio-polymer networks are pervasive in biology as key promoters of strength, support and integrity. And even beyond these pure mechanical functions, cellular mechanics has been proven to be crucial for a wide range of biological functions and dysfunctions, as cells sense external physical signals and translate them into a cellular response. In cytoskeletal protein networks, a strong relationship exists between structure and the functionality of the network, such as the role of microtubule during mitosis [165], cell movement with the help of actin assembly/disassembly [257] and utilizing intermediate filament network for stabilizing mechanical stresses [101]. Therefore, investigating the structure of the protein networks

helps to better understand their functionality/dysfunctionality. In the recent decades, the application of physics to biological systems has made substantial steps in elucidating mechanical phenomena as a key to other biological function of individual cells and tissues. It has been shown that mechanical processes convey biochemical signals, and are therefore crucial for cell functions including proliferation, polarity, migration and differentiation. Connections between the mechanical properties of cells and the initiation as well as progress of pathologies such as cancer [124, 324] highlights the link between molecular changes within the cytoskeleton and structural and functional changes of the entire cell. For instance, Suresh showed that the elasticity of red blood cells infected by malaria exhibit higher stiffness than healthy cells [323]. Further, cancer cells are typically found to be softer than normal cells, however, due to mechanosensitivity their stiffness changes by altering cytoskeletal structures when they come in contact with different environments. This allows them to adhere to a certain substrate that affects their rheological properties. For example, a decrease in the level of actin in the cytoskeleton of cancerous cells was shown to be associated with changes in mechanical properties of the cell [175]. Therefore, in-depth knowledge of cellular and sub-cellular mechanics might allow recognizing and classifying cells at different physiological and patho-physiological stages. However, this would require combining structural as well as mechanical analysis at the sub-cellular scale.

Mechanical stability and shaping on the molecular scale, is today not completely understood. It is further not clear, if mechanical processes, besides conveying biochemical signals, also convey purely mechanical signals to invoke structural change. The concept of the cytoskeleton as a shape-determining scaffold for the cell is well established, however, the tight coupling of actin, microtubule and neurofilament networks impedes a separate analysis. To date, computer models of cytoskeletal biopolymer networks are based on tensegrity models simplifying geometry [156] or unconcerned with the realistic geometry of such structures such as the ones using viscoelastic modeling of cytoskeleton [235]. However, in depth analysis of structure-function relationship requires a model investigating geometrical as well as mechanical characteristics. FtsZ protein family in the chloroplasts of the moss *Physcomitrella patens*, generate complex polymer networks, showing striking similarity to the cytoskeleton. In bacteria, FtsZ is a part of the bacterial cytoskeleton providing a scaffold for cell division [2, 251, 331]. Moreover, as chloroplasts in loss-of-function mutants show distinct shape defects, these FtsZ networks might provide scaffolds that ensure the stability and structural integrity of the chloroplasts [250]. Additionally, gene knock-out experiments has shown that the FtsZ network is capable of undergoing large deformations upholding its structural integrity [228]. This adaptive stability is presumably linked to the developed structural characteristics of FtsZ networks; making the cytoskeletal FtsZ network an ideal first application for introducing and testing an approach that links structural features of a cytoskeletal network to mechanical function.

In this section, the mechanical behaviour of the FtsZ protein networks is investigated through a series of FE simulations designed to describe the mechanical responses of the networks in a generic way. Again, FtsZ protein are utilized as a play-ground for testing and validating the proposed methodologies due to the relative simplicity of their structures and the fundamental similarities to cytoskeletal protein networks in functionality (plastosome vs cytoskeleton) and molecular structure.

4.4.1 Mechanical Nano FE Modeling

RNA Isolation, molecular cloning, isolation and transfection and CLSM imaging were carried out according the procedures described in 4.2. This resulted in a dataset of $n = 37$ (21 FtsZ2-1 and 16 FtsZ1-2 isoforms).

To investigate the mechanical response of the protein networks to external load a generic in-silico experiment reflecting a compression against a slide, as commonly applied in whole cell tests was designed [248]. To capture the overall mechanical behaviour of each network in a comparative manner, compression tests along the three principal axis of each system were modeled employing a geometry preserving nano-FE approach. It is important to note that, the goal of this setup is to depict the mechanical behaviour of the protein network morphology rather than replicating the real physical condition and dynamics of the biopolymers in their biological roles. Such tasks would need to consider the highly complicated interactions of the network with its surrounding. Something that is not completely understood to date.

3D Protein Network Model Generation

Protein network surface meshes were defined from the segmented images using a triangular approximation algorithm coupled with a best isotropic vertex placement algorithm [383] to achieve high triangulation quality. The surface area of the resulting surface mesh was calculated and further remeshed using $n_t = \rho_t A_t$, with n_t as the number of triangles in the remeshed surface, $\rho_t = 900 [triangle/\mu m^2]$ as the constant density of surface mesh and A_t as the surface area. Furthermore, the remeshed surface was smoothed by shifting the vertices towards the average position of its neighbours. The enclosed surfaces were filled with volumetric tetrahedral elements, resulting in an adaptive multi-resolution grid using FEI Amira 6.3.0 (Thermo Fisher Scientific, USA).

The principal directions of the network were determined by calculating the convex hull of network and its shape matrix. The eigenvectors ($EV1$, $EV2$ and $EV3$) of this shape matrix represent the principal directions of the network, $V_i \forall i \in \{1, 2, 3\}$. Based on the calculated eigenvectors, an orthogonal unit vector coordinate system was created and the tetrahedral grid was transformed to it. Furthermore, the difference between the primary directions and x, y and z unit vectors is calculated by means of $\cos \theta = (\mathbf{EVi} \cdot \mathbf{e}_i) / |\mathbf{EVi}| |\mathbf{e}_i|$, where θ denotes the angle between the primary direction and the corresponding unit vector. Afterwards, for each eigenvector, the pair of mesh/grid points in the direction of the eigenvector exhibiting the largest distance was determined. This resulted in three node couples, N_{i1} and $N_{i2} \forall i \in \{1, 2, 3\}$.

The geometry of the protein network was imported to the finite element (FE) simulation software Abaqus 6.14 (Dassault Systèmes, France). For each protein network three compression simulations (one per principal direction) were created by placing two rigid plates at each pair of nodes (direction 1 : N_{11} and N_{12} , direction 2: N_{21} and N_{22} and direction 3: N_{31} and N_{32}) perpendicular to the eigenvector direction. The protein network and the rigid plates were set to have rough contact, when any two points coming in contact will stick together with a relative penetration tolerance of 0.001.

Boundary Conditions

The generic boundary conditions for each simulation setup (one simulation for each primary direction: $EV1$, $EV2$ and $EV3$, respectively) consist of: 1) fixing the rigid plate attached to N_{i1} for all six degrees of freedom (3 displacement and 3 rotations) and 2) applying a displacement (U_i equal to a fraction, α , of the initial distance of the two plates (d_i) that corresponding to the primary compression direction (towards N_{i1}) of the rigid plate and N_{i2} : $U_i = \alpha d_i$). The other five degrees of freedom (2 displacement and 3 rotations) are fixed (Fig. 4.17). To investigate mechanical response of the network in case of small deformations, we chose $\alpha = 0.02$. Compression tests along all three primary directions were performed and compared to identify spatial dependencies. Furthermore, for analyzing changes in the structural behaviour with increasing deformation grade, we increased the displacement of the plate gradually by steps of $\delta\alpha = 0.02$ in 10 steps. Due to the computational complexity, in this part, the focus is only on one direction, which was selected based on comparing the simulation results of three directions under small deformations. The results are gathered at each step. As the rigid plate moves, due to compression of the network, more points of the network (nodes) come into contact with the moving plate and start moving with it. As the network is compressed between the rigid plates alongside its primary directions, without applying force/displacement on a selective set of nodes a deterministic mechanical behaviour of the network is simulated.

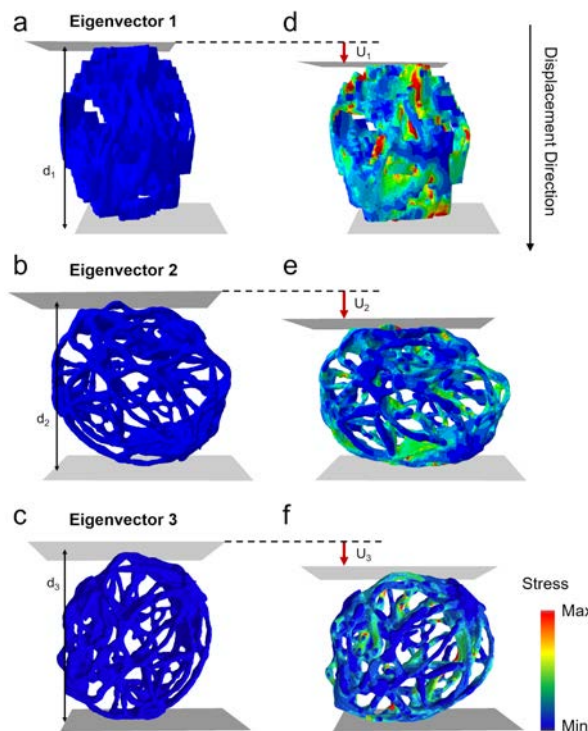


Figure 4.17: Simulation setups. a-c) Initial conditions for pressing a sample protein network in primary directions $EV1$, $EV2$, and $EV3$, respectively. d-f) Stress distribution after applying the U_i displacement to the top plate in $EV1$, $EV2$, and $EV3$ directions, consecutively. Scaling factor: 5.

Constitutive Law and Material Parameters

To perform the mechanical simulations, apart from the geometry and the boundary conditions, one requires a constitutive law and a set of material parameters. These represent the general mechanical behaviour of the material at hand in any given situation by relating the stresses of the system to strain values at each material point. To my knowledge, to date no constitutive law has been developed for describing mechanical behaviour of the FtsZ network. Although FtsZ is a tubulin-like cytoskeletal GTPase, it has been reported to be flexible and a similar force transmission to actin has been suggested [51]. FtsZ appears to polymerize with multifilament bundles [90, 294], their rigidities are assumed to be comparable to or larger than those of actin [8], which is a two-filament bundle [146]. Although more complicated constitutive laws for the mechanical behaviour of single actin filaments has been proposed [35, 147, 341], linear elasticity is the prevailing choice for cytoskeletal networks in whole-cell models [21, 73, 172, 377]. Since the focus is on the effects of structural features of the network on its mechanical behaviour, an isotropic, homogeneous and linearly elastic mechanical response similar to actin is modeled:

$$\boldsymbol{\sigma} = \lambda \operatorname{tr}(\boldsymbol{\epsilon}) \mathbf{I} + 2\mu\boldsymbol{\epsilon}, \quad (4.23)$$

where $\boldsymbol{\sigma}$ and $\boldsymbol{\epsilon}$ are the stress and strain tensors and λ and μ are Lamé and shear constants representing the material parameters. λ and μ are functions of elasticity module E and Poisson's ration ν as follow:

$$\lambda = \frac{E\nu}{(1+\nu)(1-2\nu)}; \quad \mu = \frac{E}{2(1+\nu)}. \quad (4.24)$$

With the constitutive law at hand, the next step is to determine the constant parameters present in the constitutive law i.e. material parameters (Eq. 4.24). The material property commonly used to described the mechanical behaviour of filamentous biopolymers is flexural rigidity, κ [96, 97, 112], which is the force couple required for one unit of curvature [194]. κ is defined as $\kappa = EI$, where I is the second moment of inertia. In the context of mechanics of filamentous protein filaments, the flexural rigidity is calculated as $\kappa = k_B T l_p$, with $k_B = 1.38 \cdot 10^{-23}$ J/K being the Boltzmann constant, T is the temperature and l_p as the corresponding thermal persistence length. Multiple experimentally determined values for the persistence length of FtsZ filaments using atomic force microscopy have been reported [148, 149, 218, 242]. Recently, persistence length and flexural rigidity of FtsZ filaments reported by Turner et al. as $\kappa = 4.7 \pm 1.0 \times 10^{-27}$ Nm² and $l_p = 1.15 \pm 0.25 \mu\text{m}$ [340] is commonly employed [88]. As it was previously reported, the average thickness of the filamentous elements of the FtsZ network is 117 ± 28 nm [255]. Considering a circular cross section [90] results in $I = 1.81 \times 10^{-29}$ m⁴. Therefore, the elasticity modulus used here is determined as $E = 2.6 \times 10^2$ Pa and the Poisson's ratio $\nu = 0.5$ [88, 184, 275].

Calculated Mechanical Parameters

I performed 111 3D nano FE simulations (3 simulations per image/network) on a CPU cluster with 32 cores, a simulation took in average 19 ± 7 hours (20% compression). To quantitatively assess the mechanical behaviour of the protein networks, we determine

mean stress and strain of the networks, σ_{mean} and ϵ_{mean} , as the average of Von Mises stresses and principal strains calculated by the L1 norm of their vectors.

Cytoskeletal structures are reported to fail by buckling or rupture [189]. Therefore, we further analyzed the structural stability of the network by calculating a buckling failure factor based on critical stresses σ_{crit} and a rupture failure factor based on critical strains ϵ_{crit} . Buckling of a single filament is assumed to occur if stresses local above the critical stress occur. A filament is assumed to rupture, if strains above a critical strain value occur locally. In terms of classical engineering mechanisms, these thresholds represents a yield point at which the structures incur a permanent deformation [109]. Since a local failure might not lead to a collapse of the whole network structure, we define failure factors based on the assumption that if a certain portion m of all elements ($m \cdot n_{all}^{elem}$) exhibit stresses or strains above the critical stress or strain value, the whole structure will fail by buckling or rupture of an individual or several segments, as introduced for other biological materials [248, 266]. Furthermore, nonlocal elasticity [62, 303] has been used to model buckling of single filaments of cytoskeleton biopolymers. As to date, these threshold values have not been experimentally investigated for protein networks. Therefore, we report only the portion of elements above the critical stress or strain as a failure factor, where higher values represent higher failure probability. I define buckling failure factor as $FB = n_{\sigma_{crit}}^{elem} / n_{all}^{elem}$, and rupture failure factor as $FR = n_{\epsilon_{crit}}^{elem} / n_{all}^{elem}$. n_{all}^{elem} is the total number of elements, $n_{\sigma_{crit}}^{elem}$ and $n_{\epsilon_{crit}}^{elem}$ are the number of elements with stress and strain above the failure criteria for buckling and rupture, respectively. To my knowledge, σ_{crit} and ϵ_{crit} of FtsZ are yet to be studied. Despite fundamental structural differences, F-actin and FtsZ show a similar mechanical behaviour (F-actin rigidity: $\kappa = 7.5 \cdot 10^{-26}$ [112, 159]). Therefore, the values reported for F-actin ($\sigma_{crit} = 3.2 Pa$ and $\epsilon_{crit} = 0.2$ we used [159, 275]).

Statistical Analysis

For further distinguishing the mechanical of behaviour of FtsZ1-2 and FtsZ2-1 isoforms, statistical analysis between σ_{mean} , ϵ_{mean} , FB and FR was performed using repeated measures ANOVA and paired or unpaired student's t-tests, as appropriate, followed by Bonferroni corrections for multiple comparisons. All values are presented as mean \pm standard deviation and statistical significance was set at $p < 0.05$.

4.4.2 Continuum Mechanical Analysis of FtsZ1-2 and FtsZ2-1 isoforms

A total of 3D images of $N = 16$ FtsZ1-2 and $n = 21$ FtsZ2-1 isoforms (see examples in Figure 4.18a, e) were processed and resulted in visually distinct different spatial graphs (Fig. 4.18b, f), convex hulls (Fig. 4.18c, g) and FE meshes for each protein network (Fig. 4.18d, h). The average distributions of stress and strain (percentile of maximum stress and strain values in each network), in case of small deformations (2% compression), show similar overall mechanical responses to compression in the different primary directions within one isoform ($p \geq 0.03$ (student's test, Bonferroni correction for three comparisons; Fig. 4.19a-d). Therefore, we consider mean stresses σ_{mean} and strains ϵ_{mean} as representatives for the mechanical responses of the network. Following, mean values are analyzed for comparing load directions, magnitudes and effects of isoform on mechanical response.

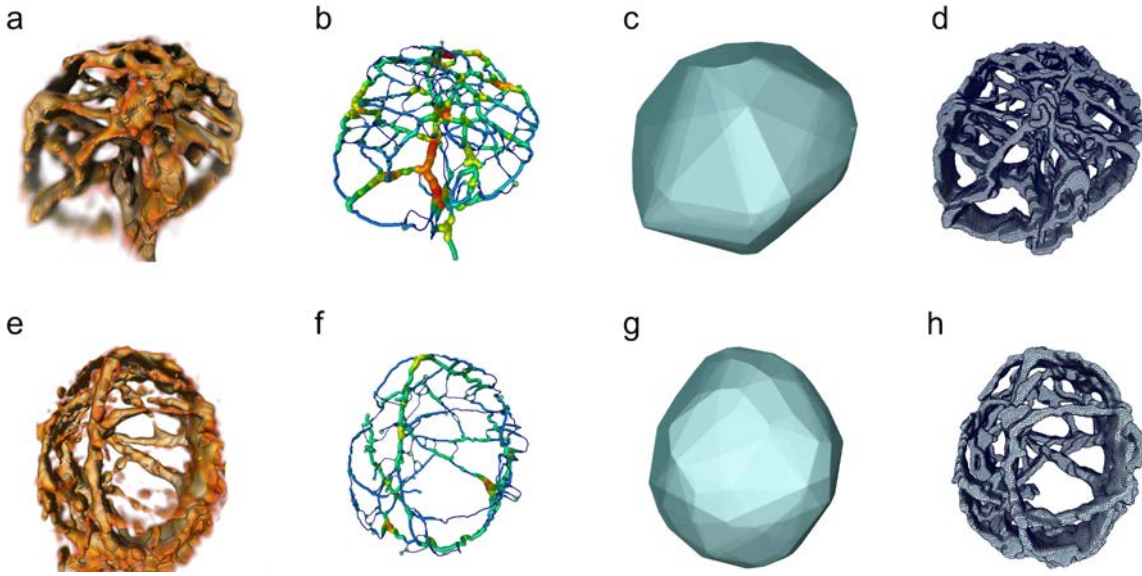


Figure 4.18: Image pre-processing of *FtsZ1-2* (a-d) and *FtsZ2-1* (e-h) isoforms. a) Sample 3D CLSM image of *FtsZ1-2* isoform, b) resulting spatial graph, c) resulting convex hull and d) resulting volume mesh. e) Sample 3D CLSM image of *FtsZ2-1* isoform, f) resulting spatial graph, g) resulting convex hull and h) resulting volume mesh.

All (mean) mechanical parameters were affected by load direction as well as isoform (ANOVA, $p < 0.01$). Detailed analysis of load directions revealed, that mean stresses were in *FtsZ1-2* significantly lower when loading in EV2 direction compared to the other two directions ($p = 0.01$, Fig. 4.19e). For *FtsZ2-1* buckling failure was significantly lower for loading direction EV1 compared to EV3 ($p < 0.01$, Fig. 4.19h). Comparing isoforms revealed, that in EV2 direction all mechanical parameters (σ_{mean} , ϵ_{mean} , FR , FB) were in *FtsZ2-1* significantly higher than in *FtsZ1-2* ($p \leq 0.04$; Fig. 4.19e-h). Additionally, *FtsZ2-1* responded to compression in EV3 direction with a significant higher strain than *FtsZ1-2* ($p = 0.049$; Fig. 4.19f).

4.4.3 From Small to Large Deformations

Because of the overall similarity in mechanical response at 2% displacement between the directions and since the variations of the two significant different parameters in the three principal directions (*FtsZ1-2*: $\sigma_{mean} = 55\%$ and *FtsZ2-1*: $FB = 35\%$) can be explained by differences in stretch (*FtsZ1-2* $St = 0.76 \pm 0.11$, *FtsZ1-2* $St = 0.67 \pm 0.20$, $p = 0.05$) calculated according to [13], it was decided to evaluate the mechanical response in large deformation setup only for one principal direction. EV3 was selected due to the overall highest (combining *FtsZ2-1* and *FtsZ1-2*) mean values 2% displacement in all four parameters ($\sigma_{mean} = 1.7 \pm 1.3 Pa$; $\epsilon_{mean} = 0.7 \pm 0.6 e-3$; $FR = 1.6 \pm 3 e-3$; $FB = 4.2 \pm 1.9 e-1$).

In comparing the mechanical behaviour of isoforms, analyzing the (quasi-static) compression process (2% \rightarrow 20%) revealed similarity in mechanical responses with increasing deformation (Fig. 4.20). For all four calculated parameters at all displacement steps, no

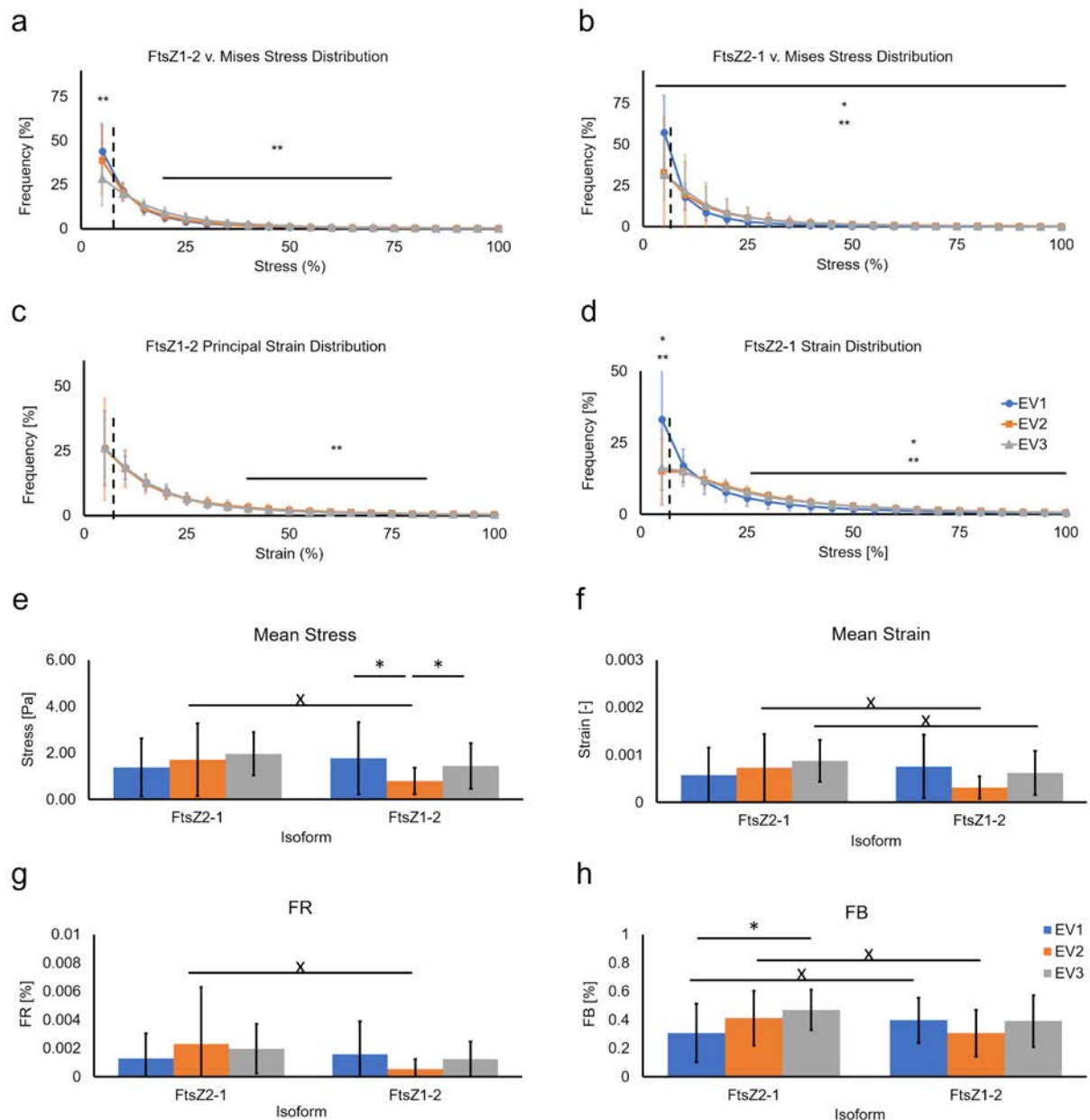


Figure 4.19: Mechanical responses to small deformations (2% compression). *a, b*) Stress distributions in *FtsZ1-2* and *FtsZ2-1* networks, respectively, in response to compression in EV1 (blue), EV2 (orange) and EV3 (gray) directions. *c, d*) Strain distributions in *FtsZ1-2* and *FtsZ2-1* networks, respectively. Dashed line indicates mean values. *e-h*) Calculated mechanical parameters from small deformation simulations of *FtsZ1-2* and *FtsZ2-1* isoforms in EV1 (blue), EV2 (orange) and EV3 (gray) directions. *e*) σ_{mean} . *f*) ϵ_{mean} . *g*) FR *h*). FB. Data is shown as mean \pm standard deviation. * denotes a significant difference between load directions (student's *t*-test, Bonferroni correction), X denotes a significant difference between isoforms. Data is shown as mean \pm standard deviation.

significant differences between the isoforms were observed (Fig. 4.20c-f).

For mean stress, mean strain and rupture failure factor (Fig. 4.20c-e), a gradual non-linear increase in both network types was detected with increasing displacements; in contrast, FB converges for both isoforms toward a constant failure factor of 1% from 10% displacement (Fig. 4.20f). Lastly, the stress-strain relationship stays linear for both isoforms during the simulation steps which point towards an overall linear behaviour of the network as a whole, as was expected by utilizing a linear material law (Fig. 4.20g).

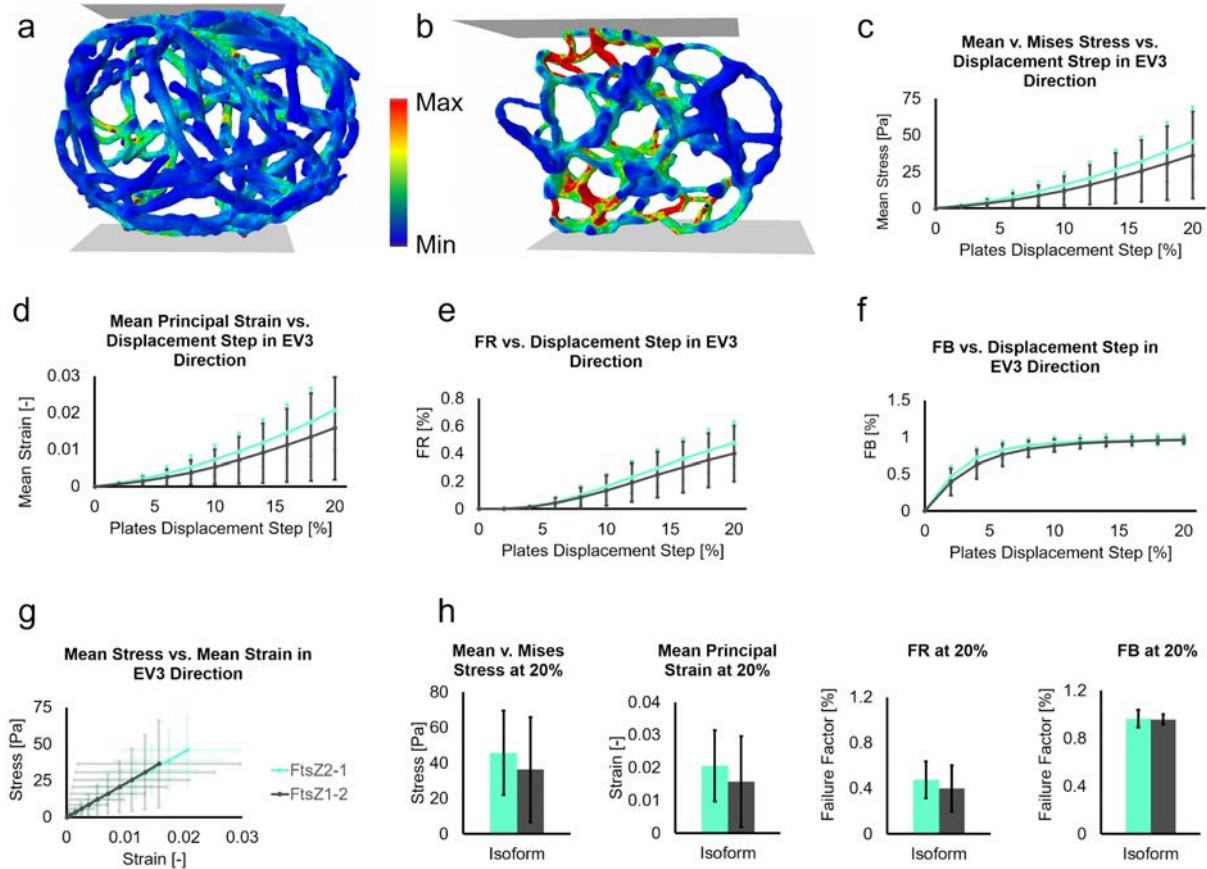


Figure 4.20: Changes in mechanical response with increasing compression. *a, b)* Stress distributions at 20% displacement in sample networks of *FtsZ1-2* and *FtsZ2-1*, respectively. *c)* Mean stresses in *EV3* direction $\sigma_{mean_{EV3}}$. *d)* Mean strains in *EV3* direction $\epsilon_{mean_{EV3}}$. *e)* Rupture failure factor in *EV3* direction $FR_{mean_{EV3}}$. *f)* Buckling failure factor in *EV3* direction $FB_{mean_{EV3}}$. *g)* Mean stress vs mean strain in *EV3* direction. *h)* Calculated mechanical parameters ($\sigma_{mean_{EV3}}$, $\epsilon_{mean_{EV3}}$, $FR_{mean_{EV3}}$ and $FB_{mean_{EV3}}$ respectively) at the 20% displacement step. Results are presented as mean \pm standard deviations. * denotes a significant difference based on student's *t*-test ($p < 0.05$) between *FtsZ1-2* (gray) and *FtsZ2-1* (green). Displacement step size 2%, minimum displacement 2%, maximum displacement 20%.

Comparing the mechanical responses at 20% displacement, shows no significant difference between the two *FtsZ* isoforms (Fig. 4.20h). At 20% displacement, buckling failure factor (*FtsZ1-2*: 1.0% and *FtsZ2-1*: $1.0 \pm 0.1\%$) is significantly higher than the rupture failure factor (*FtsZ1-2*: $0.4 \pm 0.2\%$ and *FtsZ2-1*: $0.5 \pm 0.2\%$, $p \leq 0.01$). However the

first derivative of the failure factors with respect to the displacement (FR : FtsZ1-2: 0.02, FtsZ2-1: 0.03 and FB : FtsZ1: 0, FtsZ2-1: 0) shows that with increasing displacement, FR would become the dominating failure factor.

4.4.4 Discussion

The simulations clearly show that the mechanical protein networks respond to external loads, depending on their orientation and the load direction. Moreover, the response is different between FtsZ1-2 and FtsZ2-1 isoforms. This is to author's best knowledge the first detailed in silico investigation applied on detailed spatial cellular mechanics of cytoskeletal protein structures. This allows the virtual assessment of sample-specific responses to applied loads. Assessing the isoform-specific mechanical responses supports the assumption that the two main isoforms have different structural roles [228]. Further, this is in accordance with the differences in functionality and morphology of the two isoforms observed in yeast cells [331, 332]. Dependency on load direction might be related to the previously reported plate like shapes of these isoforms (negative oblateness as reported in Özdemir et al. [255]). Previous studies employing simplified geometries, such as tensegrity models [156], allowed to theoretically study cellular mechanism such as cell reorientation [367]. More detailed FE models have been developed to investigate mechanical role of cytoskeletal components [21] and cell mechanosensitivity [377]. However, the generic simplified geometries considered for cells, e.g ellipsoids [114, 268], even with embedded cytoskeleton filament directions, potentially prevents comprehending the influence of structural features in the mechanical behaviour of cytoskeletal protein networks. The developed approach of performing μ FE simulations for close-to-realistic geometry of the network allows investigating the subcellular components separately by decoupling them from the surrounding to the ongoing research. To date, contribution of cytoskeletal structures to whole cellular mechanics is only indirectly inferred by utilizing AFM [206]. However, since the mechanical behavior of a cellular structure is determined by many components, such as of the structure of the cortical, intra-cellular (non-cortical) cytoskeletal, and nuclear networks, as well as their distribution in space, decoupling the individual components or investigating remains challenging [21, 68, 343]. It has been suggested that measurements using AFM sharp tips tend to emphasize biomechanical properties of the cell cortex, whereas measurements using AFM round-tips tend to emphasize the mechanical behaviour of the intra-cellular network [343]. Combining such measurements differentiating cellular component effects with a structural detailed models, as shown here, would possibly further advance the

The vanishing differences in mechanical behaviour of the two isoforms (Fig 4.20c-f) points towards a similar (or combined) contribution of the isoforms to the plastid mechanics in response to large chloroplast deformation. Moreover, FtsZ isoforms show a nonlinear increase in stress and strain with increase in network deformation. This has previously been shown for microtubule [208, 378] and actin filaments [110]. Hence, one can expect a similar load bearing functionality of the FtsZ (as plastoskeleton). Furthermore, up to a compression rate of 20%, buckling remains the prevailing failure factor. However, the convergence of FB to 1% after 10% displacement, shows the tendency of the network to minimizing the probability of buckling. This indicates an adaptive stability of FtsZ networks, as previously suggested [10, 228]. In contrast, although, the rupture failure

increases up to 20% compression rate, it remains significant lower than the bulking failure factor which makes it a less defining parameter for network failure. This might be due to FtsZ filaments experiencing high strain values leading to rupture after buckling at the location of buckling similar to fragmentation of buckled actin filaments [86].

The designed FE simulation setup has limitations. First, the imaging resolution might affect the simulation results as well as the mapping of surrogate models. However, we have previously shown that my quantitative imaging method is capable of resolving the micro-structure of FtsZ networks [255]. Second, the commonly used linear elastic material model in FE simulations of cytoskeletons [21, 73, 172, 377] might not completely depict the behaviour of the network. However, by utilizing a linear elastic model, besides being comparable to previous studies, we focused on the influences of structural features on the observed mechanical characteristics e.g. adaptive stability. Future studies may focus on combining the approach of precisely modeling the micro structure with experimental techniques, such as atomic force microscopy, to further investigate material properties of FtsZ. Third, the loading conditions of the simulations do not exactly duplicate reality where a combination of active dynamic forces [340] as well as osmotic pressure [116] drive the morphological changes of the network. Moreover, the FtsZ isoform is surrounded by other proteins as well as other materials such as inter-organelle fluids. The designed simulation setup provides a generic platform to investigate the structure-function relationship in FtsZ protein network rather than a one-to-one simulation of dynamics of plastids. Finally, the failure criteria used in this study are experimentally derived from actin filaments [275, 351], since no failure criteria has been experimentally derived for FtsZ to date. However, due to the assumed similarity in structural functionality between the FtsZ network and actin networks and the similarity of rigidity in FtsZ and actin filaments, actin failure criteria might represent FtsZ behaviour to a certain extent.

4.5 Combining Machine Learning and Simulations to Investigate Protein Network Functionality

State of the art imaging techniques permit resolving micro-structural details of protein networks. Computational analysis of acquired images facilitates quantifying components and assembly of these networks [13], and may allow tracking structural changes of the network assembly triggered by internal or external stimuli, connecting the structure to functionality or distinguishing between network types [255]. Machine learning (ML) algorithms have proven to be remarkably capable for automating such complex image analysis [167] and have been shown to be able to correlate image content to biological structural functionality [14, 17, 231]. Recently the concept of ML-based surrogate models have shown great success in accelerating the performance of numerical simulations of complex mechanical environments [106] as well as predicting material properties [93]. A ML-based approach could link structural features to mechanical characteristics allowing answering abstract questions such as "How are FtsZ biopolymers capable of exhibiting adaptive stability?" or "Interplay of which structural changes in the cytoskeleton of a cancerous cell leads to changes in stiffness?"

Here, an automated ML approach applied to 3D life confocal microscopy images as a tool to link structural features defining cytoskeletal network type to its mechanical

behaviour enabling an online evaluation of structure-function relations at the sub-cellular scale is presented. This is carried out by combining a mechanical characterization of protein networks through 3D nano finite element modeling and an automatic mapping of structural features to the mechanical responses of networks (Fig. 4.21). The introduced method creates a surrogate model to predict the sub-cellular mechanical responses of the network. Analyzing the prediction process of the surrogate model based on the structural feature allows us to deduct the presumed structure-function relationship.

The method is tested and applied to elucidate isoform-specific structure-function relationships of FtsZ networks. Future applications to more complex networks may allow to investigate sub-cellular mechanotransduction as well as cytoskeletal restructuring induced stiffness changes.

4.5.1 Machine Learning Surrogate Mechanical Model

To investigate the mechanical functionality of the protein networks based on their structure, we utilize a ML approach. This allows to extract structural features correlated to the mechanical behaviour of the networks. Analyzing the extracted features, enables us to identify design approaches developed by nature for carrying out mechanical functionality. To do so, we trained a set of ML models on the 26 calculated structural features of the protein networks for mapping the structure of the network to its mechanical behaviour employing a regression model. This further allows to identify the structural features contributing most to the surrogate mechanical predictions.

To investigate the structural approach employed by nature in the networks for developing the mechanical functionality i.e. adaptive stability, a set of surrogate models as a tool to map the structural features of the protein networks to their mechanical behaviour is designed. First, four multi output regression random forest models were trained [42] by forming trees mapping the 26 structural feature on the calculated mechanical parameters (σ_{mean} , ϵ_{mean} , FB and FR) for all three primary directions ($EV1$, $EV2$ and $EV3$) in a combined manner. Second, based on the simulation results of the large deformation in the $EV3$ direction, a set of single output regression random forest models we trained for each of the calculated mechanical parameters (σ_{mean} , ϵ_{mean} , FB and FR ; four models per mechanical parameter). For each ML model, a random dataset division with 32 and 5 networks for each training and test including at least 2 networks from each isoforms was carried out. All random forest algorithms were implemented using the machine learning library Scikit-learn in Python [262].

The performance of each surrogate model is assessed by calculating R^2 values between predictions and simulation results. Furthermore, a linear fit for scattered data of simulation vs. prediction was calculated from all four surrogate models per mechanical parameter; where, R_E^2 of the linear fit and the difference of its first derivative to one ($E_a = |1 - a_{SM}|$) are determined.

The importance of each structural feature on the model predictions for an individual instance for the surrogate mechanical model are analyzed by noising up each feature and comparing the plurality of out-of-bag vote and the reality to measure a wrong prediction rate [42]. In the surrogate models, we consider the extracted structural characteristics with high importance for the model responsible for inducing the observed mechanical behaviour.

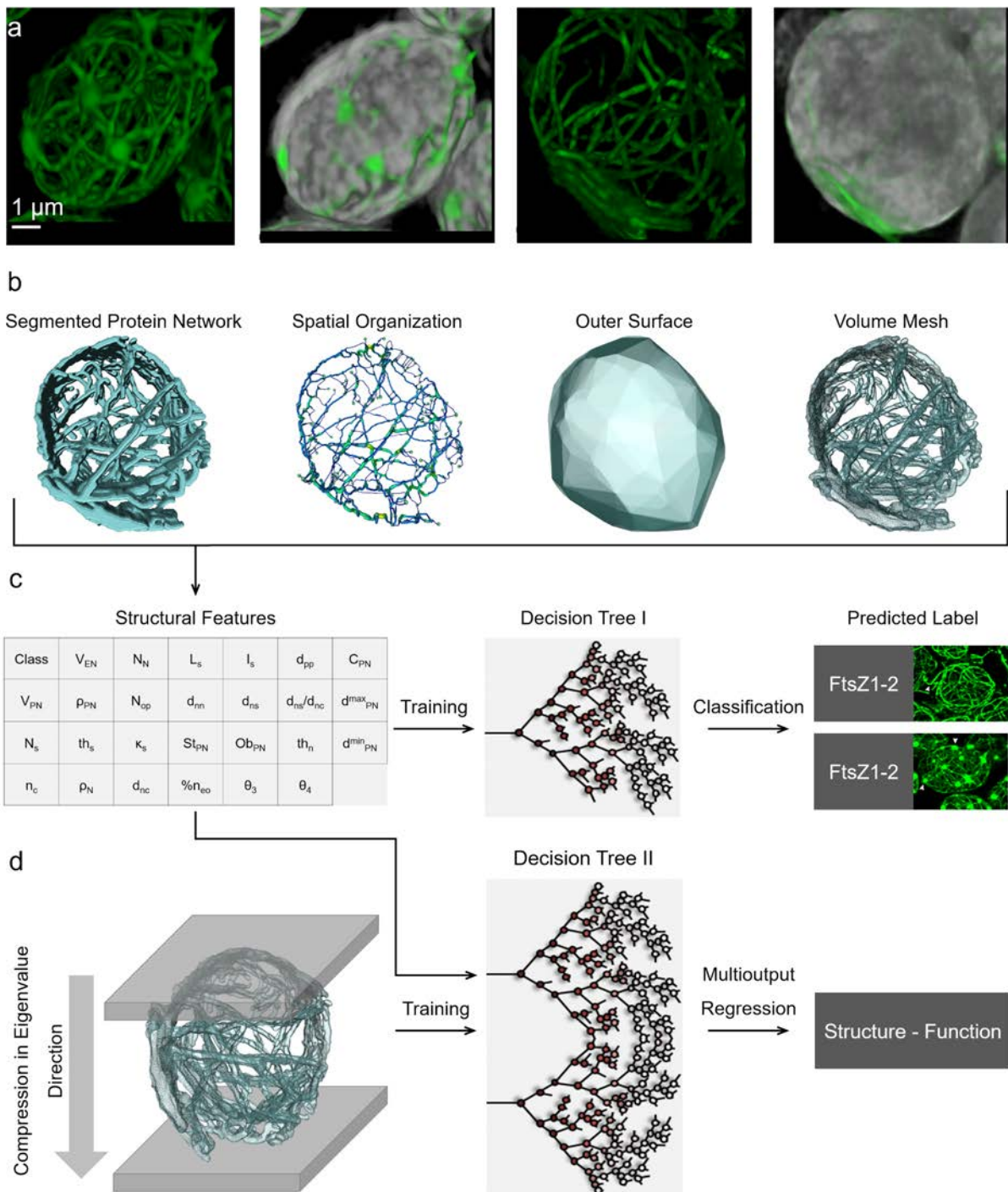


Figure 4.21: End-to-end prediction of FtsZ mechanical behaviour from CLSM images. *a)* Sample 3D CLSM images of FtsZ isoforms. *b)* Sample 3D segmented image and its spatial graph, mesh and convex hull. *c)* 25 shape and element descriptors are extracted and used as input features for training a random forest model to classify FtsZ1-2 and FtsZ2-1 isoforms. *d)* A second random forest model (multi-output regression) is trained on the structural features to predict the results of the mechanical simulation of compressing the network in its principal directions (3 Eigenvalues).

4.5.2 Mechanical Behaviour Prediction

The trained surrogate model can predict the mechanical response in small (2%) and large (20%) deformations purely based on structural features with a high correlation between simulated and predicted mechanical parameters. In case of small deformation, the predictive models show high performance for predicting σ_{mean} ($R^2 = 0.90$, $E_a = 0.03$ and $R_E^2 = 0.83$; Fig. 4.22a) and the ϵ_{mean} ($R^2 = 0.81$, $E_a = 0.04$ and $R_E^2 = 0.45$; Fig. 4.22b). However, for FR ($R^2 = 0.69$, $E_a = 0.04$ and $R_E^2 = 0.69$; Fig. 4.22c) and FB ($R^2 = 0.72$, $E_a = 0.06$ and $R_E^2 = 0.60$; Fig. 4.22d) the prediction abilities of models are lower. In case of large deformations, however, all four mechanical parameters are predicted with high accuracy. The best performing of the 4 trained models shows great prediction metrics for σ_{mean} ($R^2 = 0.99$, $E_a = 0.03$ and $R_E^2 = 0.98$; Fig. 4.22e), ϵ_{mean} ($R^2 = 0.98$, $E_a = 0.01$ and $R_E^2 = 0.98$; Fig. 4.22f), FR ($R^2 = 0.97$, $E_a = 0.01$ and $R_E^2 = 0.95$; Fig. 4.22g) and FB ($R^2 = 0.99$, $E_a = 0$ and $R_E^2 = 0.98$; Fig. 4.22h).

The analyzed structural features have different importance in predicting the mechanical response in case of large deformations. This importance distribution is different for the different mechanical parameters. For the mean stresses, the most important features (50% of total importance) are segment inhomogeneity (I_S : $17 \pm 5\%$), network density (ρ_{PN} : $16 \pm 9\%$), segment thickness (th_S : $9 \pm 3\%$) and number of open nodes (N_{op} : $8 \pm 2\%$; Fig. 4.22i). In case of mean strains, segment inhomogeneity (I_S : $37 \pm 18\%$), number of open nodes (N_{op} : $12 \pm 17\%$), network density (ρ_{PN} : $8 \pm 12\%$) and oblateness of the network (Ob_{PN} : $6 \pm 10\%$) were the most important structural feature (Fig. 4.22j). The defining structural features for rupture failure factor are network density (ρ_{PN} : $18 \pm 8\%$), segment inhomogeneity (I_S : $13 \pm 9\%$), node density (ρ_N : $9 \pm 3\%$) and segment thickness (th_S : $8 \pm 12\%$; Fig. 4.22k). As far as the buckling failure factor is considered, node-node distance (d_{nn} : $34 \pm 20\%$), segment inhomogeneity (I_S : $22 \pm 12\%$), point-point distance (d_{pp} : $8 \pm 8\%$) and number of segments (N_S : $5 \pm 7\%$) are the most important features for the surrogate models (Fig. 4.22l).

4.5.3 Discussion

The random forest-based surrogate model is capable of predicting the mechanical behaviour of protein networks in response to external loading, as the model reaches during 2% as well as 20% compression a high performance: $0.69 \leq R^2 \leq 0.90$ and $0.97 \leq R^2 \leq 0.99$, respectively. However, the relatively higher accuracy for large deformations points toward higher correspondence of the extracted structural features to the mechanical behaviour of the network in response to large deformations. This specifically coheres to the hypothesis that these networks are able to undergo large deformations without losing their structural integrity, as previously postulated [228]; hence, possessing structural features conforming to response in case of large deformations. The high accuracy in mapping the structural features to the mechanical behaviour of the networks further demonstrates the potential load bearing functionality of FtsZ protein in chloroplasts. Furthermore, this shows that the capability of the network to keep its stability by undergoing deformations relies not only on material properties of the biopolymer but probably more prominently on the structural features of the network. This is in accordance with the effects of the network architecture on the overall mechanical behaviour reported in actin protein network [85]. In summary, to author's best knowledge, this is the first detailed investigation of these

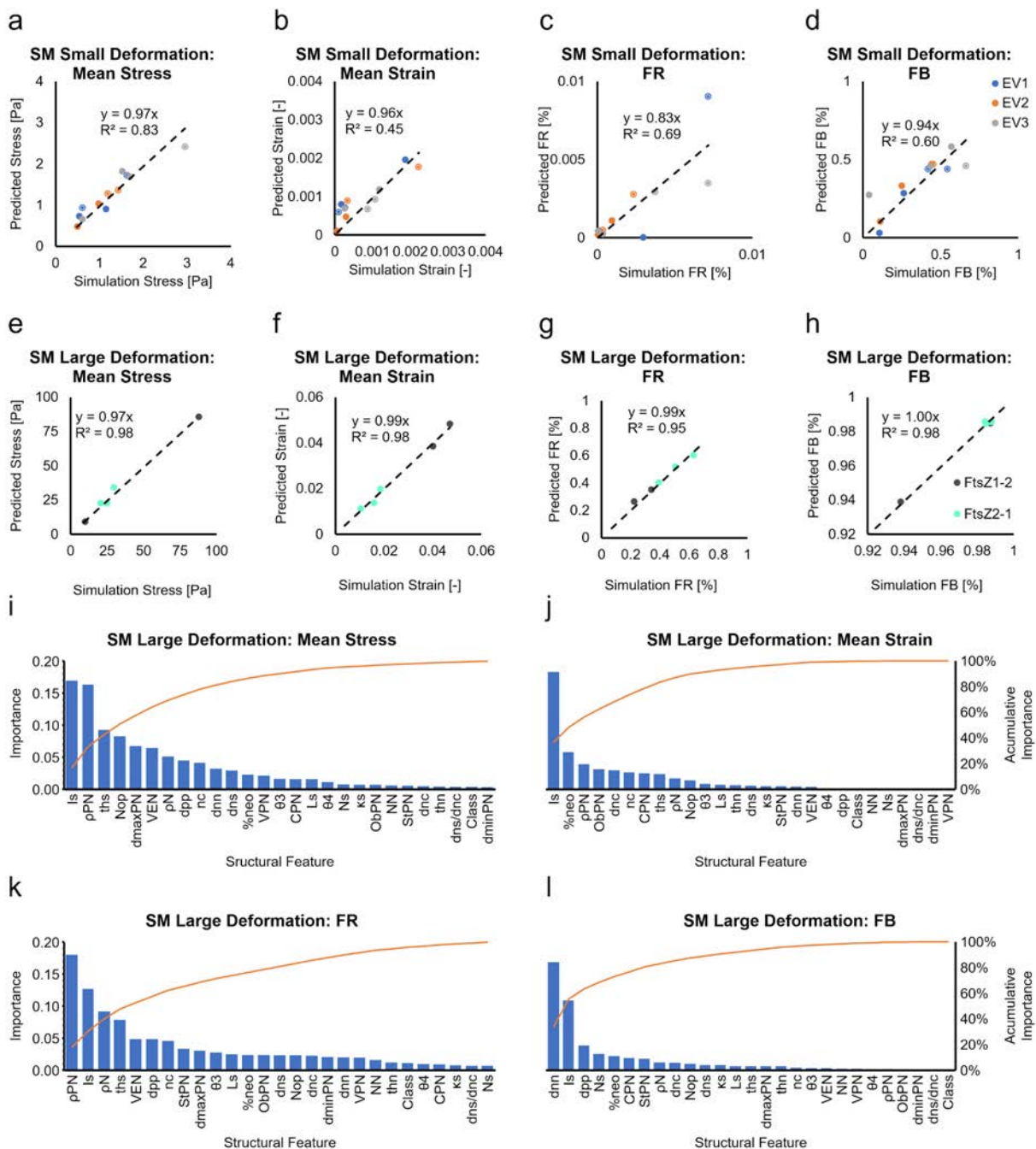


Figure 4.22: Surrogate mechanical model. a-d) Surrogate model prediction vs. simulation results for the test set networks for small deformation in each primary direction (EV1: blue, EV2: orange and EV3: gray. a) σ_{mean} . b) ϵ_{mean} . c) FR. d) FB. Networks of FtsZ1-2 in the test set are shown as solid circles and FtsZ2-1 as circles with an out ring. Black line represents a liner fit to the data points. e-h) Surrogate model prediction vs. simulation of best performing model results for the test set networks for large deformation in EV3 direction. e) σ_{mean} . f) ϵ_{mean} . g) FR. h) FB. Gray and green represent FtsZ1-2 and 2-1 respectively. Black line represents a liner fit to the data points. i-l) Mean importance of structural features for the set of surrogate model predicting each mechanical parameter, i) σ_{mean} . j) ϵ_{mean} . k) FR. l) FB. The orange line represents cumulative importance.

sample-specific structure-mechanical performance correlations. This empowers us with a image-based virtual mechanical testing method to investigate the manifestation of the mechanical characteristics in the structural features of the network.

By analyzing the importance of the features of the surrogate models in predicting stresses and strains of the network, it could be shown that the structural characteristics of the filaments (local changes of direction and thickness (I_S), average thickness (th_S) and open end filaments (N_{op})) as well as network overall morphology (network density (ρ_{PN}) and oblateness (Ob_{PN})) are the structural features mostly contributing to the large deformation mechanical response of the networks. This can be interpreted as the FtsZ network being capable of preventing the increase in failure possibility due to buckling of filaments by developing specific distances between their nodes (average d_{nn} in FtsZ1-2 and FtsZ2-1: $5.9\mu m$), local changes of direction and thickness of filaments ($I_S = 18.8$), the distance between the local changes of filaments ($d_{pp} = 60nn$) and number of filaments in the network ($N_S = 207$). This could potentially be used to design adaptively stable structures capable of undergoing large deformations or bio-engineering mechanically optimized responsive biomaterials [207, 213].

Here it was shown, that combining confocal imaging with μ FE analysis employing a machine learning framework allows for an image-based surrogate cellular mechanics prediction. Additionally, by providing an identification of structural features determining this mechanical response to a given stimuli, we could for the first time, directly investigate the structure-function relationship of individual protein networks in a sample-specific manner. The ML surrogate model trained on in-silico data generates accurate and fast predictions of sub-cellular mechanics ($R^2 > 69\%$ and $R^2 > 97\%$ for small and large deformation respectively). The method provides a framework for further investigations of structural functionality of protein networks in plants as well as in humans, as it would allow to monitor the structure-mechanical response of cytoskeletal structures during morphological changes over time, such as cell shaping by actin [136]. Further, cytoskeletal changes, which have been shown to occur in certain diseases, such as cancer [371] and Alzheimer's disease [23] could be more precisely quantified and may be a target for future drug development. Advanced structural characterization can help to improve monitoring and understanding the structural state of protein networks due to internal or external stimuli such as cellular processes and disease and may help to optimize treatments for cytoskeletal affecting disease such as cancer and Alzheimer's disease.

4.6 Summary

In this chapter, the manifestations of specific mechanical functionalities in distinct structural features of a biological subcellular network structure was investigated. The novel method combines machine learning, μ FE analysis and quantitative confocal microscopy imaging to analyze the mechanical behaviour of FtsZ protein networks and to identify the evolutionary developed structural features involved in the mechanical load bearing functionality of these networks, by combining a descriptive, a predictive and a prescriptive task. In the descriptive task, FtsZ isoforms are classified based on their structural features. Moreover, the predictive task of the surrogate models, maps the structural features to the mechanical behaviour derived from μ FE simulations and, further allows to perform the prescriptive tasks of identifying the features optimized by nature for obtain-

ing a certain mechanical response to external stimuli. The model further provides a fast and computationally inexpensive solution for the demanding detailed biomechanics μ FE simulations of a protein network via surrogate modeling.

5 Analyzing Structure-function Relationship at the Micro/Macro Scale: Bone

At the micro/macro scale, many research has been devoted to establishing the structure-function relationship. Specially, bone as a load bearing tissue, has been investigated extensively. The load bearing functionality provided by the bone's structure is effected by certain physiological and patho-physiological processes. Therefore, a set of perturbations are utilized in this thesis to study the structure-function relationship in bone. To do so, machine learning models enabling to link the structure of bone encoded in images to the effects these perturbations on the bone structure were developed. The chosen perturbations are: 1) maturation-related changes in bone structure, 2) mechanical loading aiming at reversing the aging-related changes and 3) alterations in bone structure due to diseases. In order to do this, as a part of a preclinical study that allows inducing controlled structural adaptations, a deep neural network (DNN) was designed to predict the "skeletal age" of a subject based on X-ray images. In addition, a tool was developed to analyze the learned structural features corresponding to the maturation stages. Furthermore, this DNN is applied on images of bone treated with in vivo loading to study the rejuvenation effects of this mechanical treatment. In a clinical study, the DNN was modified to investigate manifestation of bone-structure-altering Osteogenesis Imperfecta in patients. The goal was to automatically identify specific disease types. This overall approach allowed an unbiased automatic investigation bone structural changes induced by the aforementioned mechanical function-altering perturbations.

The structure-function relationship is more mechanically driven in comparison to protein networks. However, alongside mechanical functionality, many biological stimuli such as maturation, aging and diseases drive the architecture of the bone structure. Another fundamental difference between the bone and protein network structures is the availability of large amount of high-resolution imaging data in the field of bone-structure-analysis which is intuitively due to presence of less physical small-scale-imaging restrictions. Hence, deep learning models, which are specifically designed to analyze structured rich-content data such as high resolution 3D images has been employed. Therefore, the in [4.2](#) developed quantitative image preprocessing method is not needed for this purpose. Hence, for the remaining of this dissertation the focus moves from training on specifically extracted structural features to automatic extraction of structural features which correlate to the functionality of interest.

In this chapter, a series of ML-based methods developed to investigate structural changes in bone due to aging, in vivo loading treatment and osteogenesis imperfecta disease are presented. This is done by designing purpose-oriented deep neural networks for assessment of state of the bone. As a part of a preclinical study, we investigate the

morphometric and densitometric changes that bone experiences in the process of aging (see 5.2). This is done by creating a DNN that is capable of an end-to-end short-term bone age assessment. The robustness of the model is further validated in a three-fold manner. This novel age assessment DNN is utilized in 5.3 to investigate the potential rejuvenation effects due to in vivo loading. In 5.4, the DNN is extended to detect the state of the bone in different types of osteogenesis imperfecta disease. Moreover, by analyzing the learning process of the networks through saliency maps and designed attention values, localized manifestation of bone state into the bone structure is investigated.

The developed methodologies presented in this chapter, their validation and applications are previously published in [14, 15].

5.1 General Background on Bone

5.1.1 Bone Biology

Bone is considered a connective tissue whose main functionality is to provide support and protection. This means that bone not only provides the mechanical load bearing framework of the body, but it also, protects organs from external impacts and forces. Moreover, bone enables force generating and managing parts of the body, such as muscles and tendons, to transmit these forces into movement.

Bone Morphology

Humans usually have 213 bones [75]. They can be categorized into 3 groups: 1) long bones e.g. femur, 2) flat bones e.g. skull bone components and 3) irregular bones e.g. vertebrae. In this research, the developed models for analysing the structure and functionality of tibiae and fibulae in 5.2 and 5.3 and radius in 5.4 are presented. Therefore, for the rest of overview information, the focus will be on long bones.

Long bones, can be divided into three compartments: 1) epiphysis at both ends, 2) diaphysis in the form of a hollow tube in the middle and 3) the connection between these two which is called metaphysis [66]. Often, the growth plate separates metaphysis and epiphysis during growth. This results in longitudinal growth of the bone. The growth plate calcifies when puberty is finished [259]. This work focuses on metaphyseal bone.

From a morphological point of view, bone has two main compartments, i.e. the cortical and trabecular bone. The former covers almost 80% of the bone mass and the latter, the rest 20%. The diaphysis and the thin shell of the metaphysis, the cortical bone is very dense. It is constructed of many cylindrical modular elements with a canal in their center that contains the blood and lymph vessels as well as nerves and Volkmann's canals. The nutrients required in bone are transported in these canals [66] as well as in the interconnecting canaliculi. Trabecular bone exists in epiphyseal and metaphyseal in medullary cavities (Fig. 5.1). This bone compartment is a interconnected 3D network of trabeculae. Due to the greatly manifested structure-function relationship in bone, the structure and hence its porosity vary heavily depending on the bone location and age. Porosity, is mostly considered the distinguishing factor between trabecular and cortical bone. The bone porosity in cortical compartment ranges between 0.05 and 0.20; whereas, in trabecular bone porosity of 0.4 up to 0.95 has been measured. The higher part of

the spectrum exists in bones of elderly [237]. Further, the transitional part between the trabecular and the cortical bone is considered the third compartment of the bone, as the transition between the densities in the two main compartments takes place in a continuous manner [152].

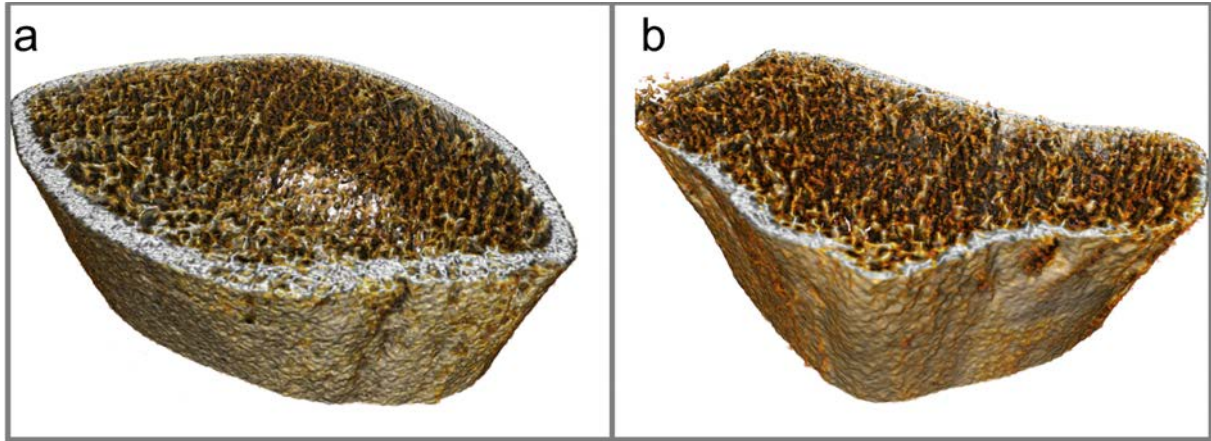


Figure 5.1: *Multi scale bone structure. a, b) Sample tibia and radius of an adult male human, respectively.*

At the microscopic level, the same modularity of the structure is observed in both cortical and trabecular bone. They both contain an organic and an inorganic phase. Collagen fibers create the bone matrix and organize the structure of the organic phase of the bone and provide its elasticity. These fibres, similar to other proteins, create a network structure. The inorganic phase is responsible for the high mechanical stiffness of the bone and consists of mainly calcium phosphate.

The micro-structure of bone is highly dynamic and adapts to internal and external stimuli. This dynamic behaviour is manifested into the processes of modeling and remodeling.

Modeling and Remodeling in Bone

Despite the appearance of bone as a static biological structure, there exist a great dynamism in the biological processes taking place at the microscopic level in bone. Two of the processes that simultaneously take place in bone are damage repair and adaptive restructuring as a response to mechanical load. This leads to an increase in efficiency with respect to load carrying and preventing structural failure. As a result of these two processes main structural characteristics of bone, bone mass and material properties, are constantly changing. This dynamic adaptation of structure takes place by a balance between bone formation and bone resorption which leads to adaption of the bone mechanical behaviour (stiffness and flexibility). This follows the evolutionary process of optimizing material use and reaching required performance. Therefore, bone modeling as a combination of bone formation and resorption, takes place in both bone compartments through life.

Osteoblasts, osteoclasts and osteocytes are the cells in bone contributing to bone modeling and remodeling [66]. Removing bone matrix is performed by osteoclast. Whereas, osteoblasts are responsible for formation of bone. The bone formation is performed when

a group of osteoblasts experience a differentiation, which leads to being surrounded by unmineralized osteoid [66]. Up to 95% of bone cells are osteocytes, which are placed in fluid-filled lacunae and create a highly interconnected network [27]. It is commonly accepted that osteocytes are mechanosensitive and capable of detecting strain and damage in bone. Therefore, the osteocyte network is believed to be orchestrating the modeling and remodeling process of osteoclasts and osteoblasts.

Bone (re)modeling takes place on the surface of the bone, specifically, on the surface of the cortical bone: on outer periosteal and inner endocortical and on trabecular. It is believed that up to 50% yearly bone turnover can be observed in cortical compartment in the first two years of a human's life. This rate drops to 2% to 5% in elderly. Trabecular bone exhibits up to ten times higher turnover rate than cortical bone [66, 258]. As the term turnover describes the bone volume replacement, it is dependent on the surface-to-volume ratio of bone. This ratio is reported to be up to five times higher in trabecular bone than in the cortical bone compartment [258]. This means that despite a lower (re)modeling rate, the trabecular compartment could have higher turnover.

Adaptive Structural Behaviour of Bone

Genetics is the main force behind the skeleton morphology. However, the macro/micro-architecture of bones is formed through the adaptation process to resist mechanical forces being applied on it. Carl Culman, a German engineer, was the first person to notice that the architecture of trabecular bone correlates to trajectories of the principal stresses in 1867. Afterwards, the renowned Julius Wolff created a mathematical model by analysing the drawings of Hermann von Meyer, a Swiss anatomist, asserting that the mechanical forces are the main players in determination of the trabecular structure. Hence, Wolff's law of bone transformation [364]. Wolff's main focus was on the design of the bone structure rather than the (re)modeling. By then, it was already established that bone adaptation is a product of self regulation taking place in bone. Roux, in 1881 [286], asserted that the adaptation of bone is towards functional optimization; hence, an evolutionary functional design.

Up to now, many thorough studies, specifically experimental studies, have investigated and supported this notion. For instance, it has been shown that in extreme scenarios such as astronauts being deprived of gravitational force or patients lying on bed for long periods of time, the bone morphology changes drastically [78, 197]. On the contrary, the bone mass in professional athletes such as soccer players and gymnasts have significantly higher than non-athletes [52, 94].

Most experimental studies investigating the effects of exercise on the structure of longitudinal bones have focused specifically on bone density. They succeeded in showing that an increase in physical activity in all three phases of skeletal life, naming young growing, adult and elderly, leads to positive effect on bone density [174, 353]. However, it is clear that the type of exercise has a clear effect on the outcome. For example, contrary to the public belief, strength training such as weight lifting has no positive effect on bone structure in both adults and elderly [134]. The stimulus has to be dynamic based, c.f. the many vibration studies [126]. However, up to this point, it has been nearly impossible to pick the local effective/relative mechanical stimuli on the bone in human exercise studies. This is due to the fact that the influence of different factors such as the duration or frequency of mechanical signals are difficult to distinguish. Moreover, it is very challenging

to measure the load that is applied on the bone during exercise directly.

If it is considered that the goal of exercise treatment is to reduce fracture risk, one has to investigate the mechanical signal that would maximize the adaptive bone structure changes. To do so, many animal models with controlled in vivo loading settings have been developed to investigate adaptive behaviour of cortical and trabecular bone. This includes loading rabbit femur [234] and rat tibia [4]. The recent research focus has been shifted to mouse models such as loading of mouse tibia [105, 123]. These studies in animals showed that dynamic mechanical signals and changes in strains applied to bone affect the bone structure [288]. Moreover, factors such as amplitude of loading cycles, strain frequency and duration of resting between loading affect the bone adaptive response [63, 247]. Furthermore, animal models have been used to study the effects of non-mechanical parameters e.g. age, sex, estrogen level and osteoporosis medication such as bisphosphonate on bone adaptation [202, 223, 319].

There are still many gaps in our knowledge about adaptive responses of the bone with aging and diseases. Although it is clear that exercise and the resulting mechanical signals can reduce aging-induced bone loss, the specific mechanical effect on the bone at the osteocyte level as well as the signaling leading to the cellular coordinated response of the bone is yet to be fully understood. Finding a treatment which is less reliable on medication and more on physical exercise is desirable. This request, however, a better understanding of the aging-, as well as, loading-induced structural changes in bone.

5.1.2 Aging and Bone Loss

A combination of bone mass, architecture and the mechanical characteristics of the bone material dictates the capability of the bone to resist fractures [102]. It is commonly believed that the bone mass increases for the first two decades of life and reaches its peak in the 20s. Afterwards, throughout life, the bone mass decreases constantly [22]. The resulting changes in the bone architecture lead to a decrease in bone strength with aging. As the bone strength decreases, the possibility of mechanical scenarios in which impacts more than the bone's critical failure values occurring increases. This often results in fractures in elderly.

Osteoporosis

Osteoporosis is a skeletal disease in which an increase in bone fragility and possibility of fracture as a result of deterioration of bone mass and strength takes place [67]. It is reported that 50% and 20% of the above 50-years-old Caucasian male and females, respectively, will experience a fracture in the rest of their lives [170]. This makes osteoporosis a very important public health issue. Osteoporotic fractures are mostly seen in vertebrae, proximal femur and distal forearm. However, this disease could be manifested as low bone density fractures in all bones. Moreover, patients who have had a fracture are more likely to experience more fractures in their lifetime.

Treating Bone Loss

Currently, medications utilize two different approaches to deal with osteoporotic bone loss: 1) by increasing bone formation by using anabolic agents and 2) by decreasing

bone resorption with the help of anti-resorptive agents. The later approach is mostly used in currently prescribed drugs such as estrogen and bisphosphonates [209, 210]. The increase in bone formation at the moment is only possible by the use of teriparatide which is the amino-terminal fragment of parathyroid hormone [243]. However, this requires daily injections, which makes it very difficult for the patients. Recently, more advanced osteo-anabolic drugs e.g. Sclerostin neutralizing antibodies, have been developed and are currently used in clinical trials [335].

It is yet a challenge to resolve the anabolism process in bone and its triggering parameters. If one would be able to determine the structural response to mechanical stimuli, it might be possible to prescribe exercise-based and drug-free treatments for osteoporosis and similar diseases. Such treatment should produce a signal which only targets the desired anabolic process without causing any harmful side effect. This results in a positive bone adaption in both mass and structure without the disadvantages of using drugs.

5.1.3 Models of Age-related Bone Loss and Osteoporosis

Due to the ethically-risen problems of performing experiences on humans, in many research field, animal models with replicated physiology and patho-physiology of human are used. In the field of bone research, mouse models are the go-to animals. In 2002 the DNA of mouse was sequenced [64], which makes mouse the second mammal after humans with completely sequenced DNA. This, also made it possible to create transgenic mice. Furthermore, due to similarities of genetics and patho-physiology between humans and rodents, it is possible to carry out translational research. Moreover, as a result of breeding between genetically related parents, the mice used in experiments are almost completely genetically identical. Therefore, the mice with identical genotype have organs have the same characteristics such as morphology and development process (phenotype). As a result, experimental studies with inbred mice exhibit greater reproducibility.

The use of inbred mice for bone research makes it possible to investigate the influence of specific genes in bone diseases. This is possible through overexpression or knock-out genes where a control group is compared to the group with the modified genes. Furthermore, By modifying genetics of the mice, one is able to remove the expressions of targeted proteins. This enables shutting down signalling pathways of to the cells. Afterwards, it is possible to compare the bone structure and mechanical responses in the wild-type mice with the transgenic mice. Combining this approach with replicating the mechanical stimuli occurring in humans can potentially lead to the presence of the pathology in the mouse model.

Due to the similarity of skeletons of humans and mice, hind limb bones of mice are usually used to investigate long bone pathologies [44]. Despite all the possibilities of translational studies from animals to humans, it is important to note that minuscule genetic differences between the species might cause great phenotype differences. For example, the murine skeleton steady grows due to lack of osteonal (re)modeling of cortical bone. Moreover, the inflammatory responses of humans and mice are also greatly different [299].

5.1.4 Osteogenesis Imperfecta

Osteogenesis imperfecta also known as "brittle" bone disease refers to a group of rare heritable bone dysplasia disorders. OI occurs in 1 in every 15000-20000 births [244]. In 85% of cases, OI is caused by mutations in genes encoding type I collagen (COL1A1 and COL1A2), leading to increased bone fragility attributed to reduced bone mass and quality. Historically COL1-related OI has been classified based on clinical severity using Silence type I (mild), type II (perinatally lethal), type III (severe) and type IV (moderate) [305]. The collagenous matrix and mineralized components create more than 90% of the bone tissue. The mineralization begins by osteoblasts producing alkaline phosphatase which brings about creation of mineral crystals at the locations of phosphate nucleation [195, 196]. The formation of these crystals around collagen is the process of bone matrix mineralization. All OI patients have an excessively highly mineralized bone matrix [244]. Fratzl-Zelman et al. have shown similarity in crystal sizes in OI type I patients and healthy control group [103]. However, the OI patients experience an approximately 12% increase of relative bone volume fraction. This is a result of higher amount of crystals in their bone matrix. Moreover, the gene mutations in OI patients result in thinner collagen fibers and further apart collagen molecules [246]. This results in more spaces available between collagens in the bone matrix; hence, more crystals in between the collagen fibers.

The basic multi-cellular unit (BMU) which consist of osteoblast, osteocytes and osteoclasts determines the bone turnover. Collagen type I is one of the proteins produced in osteoblasts, which is the most prominent component of the bone matrix. In patients with OI type III and IV, a mutation in collagen protein takes place which hinders the folding of the triple helix [274]. This might result in the substitution of Gly of sequence Gly-X-Y with another amino acid in COL1A1 or COL1A2 chain, which leads to a deviance of form in the triple helix [376]. The disturbance in folding process of changes of the conversion process of Lys carried out by post-translational modifying enzymes [244]. Patients with OI type I experience no mutation in collagen I and the folding process. However, more than half of their collagen is created in an environment with higher enzymes-to-collagen ratio.

5.2 A Deep Learning Approach for Bone Age Assessment from μ CT Images

Human and animal studies show that skeletal maturation and aging affect both, bone micro-architecture [282, 326, 361] and tissue material properties [183, 285]. Formation and resorption dynamics in trabecular [29] and cortical bone [30] are altered with aging in a site-specific manner [28, 31]. As a result, with increasing age a net bone loss occurs [3, 326], often resulting in osteoporosis and a subsequent increase in fragility fracture risk [171]. The rules governing age-related alterations in bone composition, organization, and elasticity across structural hierarchies are, however, to date not completely understood. Disease, like osteoporosis, or age change the dynamical processes of material decomposition in bones that lead to changes in the micro- and macro-structure, in bone strength and, subsequently to an increase in the likelihood of fracture [74].

Given the fact that osteoporosis causes worldwide more than 8.9 million fractures per year [139], it is essential to develop a precise and comprehensive analysis of phenotypic

changes and abnormalities at all relevant length scales. Assessing the onset of osteoporosis and disease progression is therefore challenging. Within clinical practice, dual energy X-ray absorptiometry (DXA) and biochemical markers remain the standard methods of monitoring osteoporotic patients receiving pharmacological treatments. The T-score is derived from measurements of the areal bone mineral density (aBMD), which is obtained by DXA [168]. DXA is a useful clinical tool, but has several limitations including restriction to a two-dimensional image, lack of distinction between trabecular and cortical bone, lack of information on bone microarchitecture, difficulties in edge detection and projection artefacts. Additionally, the predictive ability of this method is low [36, 281] with less than half of all nonvertebral fractures occurring in postmenopausal women having an osteoporotic T-score [298]. Biochemical markers are indirect indicators of the rates of formation and resorption of bone and give no insight into its quality or mechanical properties. Furthermore, like all biochemical markers they are subject to pre-analytical, analytical and post-analytical sources of variability and the results may be affected by a range of non-skeletal conditions. High-resolution peripheral quantitative computed tomography (HR-pQCT) is emerging as a powerful non-invasive bone imaging modality capable of assessing volumetric BMD, microarchitecture and strength, and distinguishing cancellous and cortical bone. Additionally, micro-finite element and homogenized finite element models based on HR-pQCT imaging are increasingly used to predict bone stiffness and strength [69, 384]. The Bone Microarchitecture International Consortium (BoMIC), which combined individual-level prospective data from eight cohorts (7254 individuals, mean age: 69 ± 9 years), recently reported that HR-pQCT parameters improved fracture prediction beyond femoral neck aBMD or fracture risk assessment tool (FRAX) scores alone [292].

To employ quantitative methods that determine the time-dependent changes in bone structure and, hence, the underlying dynamic process, without knowing its entire mechanical loading history. This knowledge, however, must be the basis for studies aiming to monitor bone health and bone fracture predictions. From a macrostructural point of view, bone consists of porous cortical and trabecular bone. The remaining space hosts different biological cells as well as blood vessels. In cortical bone, this porosity is organized in a tree-type branching structure of canals. In trabecular bone, these canals are penetrating each other, yielding a micro-structure made up of single plates and struts [127]. The vascular pore channels are connected via canaliculi to cave-like single pores called lacunae [296]. The entire extracellular space outside the pores appears as a nanocomposite of collagen-rich and collagen-free domains. The hierarchical and dynamic nature of bone make an assessment of the "state" of bone challenging. The rules governing age-related alterations in bone composition, organization, and elasticity across structural hierarchies are, however, to date not completely understood. Additionally, human and animal studies showed, that maturation and aging affect both, bone micro-architecture [282, 326, 361] and tissue material properties [183, 285], as formation and resorption dynamics in trabecular [29] and cortical bone [30] are altered with aging in a site-specific manner [28, 31]. As a result, with increasing age a net bone loss occurs [3, 326], often resulting in osteoporosis and subsequent increased fragility fracture risk [171]. While osteoporosis-related fractures occur primarily at corticocancellous sites (e.g. metaphysis or vertebrae), stress fractures often occur in cortical sites [48, 270]. Consequently, a precise and comprehensive analysis of phenotypic changes and abnormalities at all the relevant scales is crucial to

identify osteoporosis onset and progression. For osteoporosis, for example, there is no standard practice to monitor patients receiving treatment. Assessing onset and progression as well as assessing the effects of novel and existing treatments for age-related bone loss and osteoporosis is therefore challenging. Although there exist pre-clinical studies aiming to assess bone maturation and (re)modeling, they all focus on selectively extracted mechanical or morphological features such as mineralization [99, 219] or bone volume [129, 181, 239] and their alterations. Preclinical studies using micro-computed tomography (μ CT) aiming to assess bone maturation and (re)modeling have focused on selectively extracting mechanical or morphological features such as mineralization [99] or bone volume [129, 181, 239] and their alterations [28, 219]. Although these approaches decode certain aspects of structural changes in bone, they neglect the underlying interplay and concurrency of (re)modeling and (de)mineralization. The measures extracted from these properties are selective and therefore not sufficient to predict fracture in diseases such as osteoporosis. To provide more precise descriptions of the disease phenotype, the diverse manifestations must be captured allowing one to distinguish healthy bones from diseased ones and young bones from aged ones to define disease onset and progression into sub-classes. This would permit a much more precise understanding of bone quality, as well as a better prediction of fracture risk and treatment outcome.

A major challenge in disease diagnosis is interpreting information-rich (imaging) data. This challenge is at the same time a great opportunity, as there exists nowadays artificial intelligence-based methods that have the capabilities and power to analyze relationships within rich datasets, e.g., relationships of particular dynamic biological phenomena. Artificial intelligence, for example, has been used to diagnose Alzheimer disease based on Magnetic Resonance Imaging (MRI) [321] or to analyze skin lesion for diagnosing malignancy [92]. Similar to the previous two examples, one can also use artificial intelligence to analyze (re)modeling of bone using X-ray images (eg. μ CT, HR-pQCT). As scatter and attenuation information of μ CT images contain information about material composition, distribution and amount, they potentially contain all structural information that is needed to assess bone maturation [238]. Despite the fact that recent studies can extract from 2D and 3D X-ray image data more features describing bone quality through assessment of vBMD and microstructure [32, 39, 49, 224, 226, 289], information on bone (re)modelling rates are only obtained through invasive histomorphometry analysis of iliac crest bone biopsies. Fortunately, recent advances in artificial intelligence towards deep learning now enable further data analysis by utilizing high-throughput image data. Compared to traditional machine learning methods [211, 302], deep learning methods do not only exhibit an improved prediction accuracy, but also provide the ability to visualize learned features, to link discovered features with clinical relevance. The first applications for bone age assessment in pediatrics using deep neural networks (DNN) showed already some success in classifying/predicting bone age from 2D X-ray images [200, 313, 337]. Further, they provide confidence that DNN-based methods can also provide insights into the underlying processes of skeletal maturation and bone (re)modeling.

In this section, a deep learning approach applied to 2D projection X-ray images of bones as an end-to-end tool for site-specific, spatio-temporal assessment of bone tissue maturation and intervention effects is presented. By simultaneously evaluating several relevant hierarchies, the method allows us to reconstruct continuous biological processes such as aging or adaptation of bone. This method was developed and evaluated on pre-

clinical μ CT data of mouse bones and investigated bone adaptation in response to in vivo tibial compressive loading. First the method is evaluated to identify short-term, skeletal maturation-related changes in the proximal tibiae and fibulae based on μ CT images. To do so, short-term (15 days) dynamic skeletal maturation processes in adult female mice bones are analyzed.

5.2.1 In vivo Monitoring of Tissue Maturation and Adaptation

In total, 79 μ CT image sets of both proximal tibiae and fibulae were collected during two weeks of tissue maturation (right limb) and adaptation (left limb) during a bone adaptation study performed in 2013-2014 at Charité Universitätsmedizin Berlin (Fig. 5.2a). Both limbs, including the tibia and fibula, were scanned and combined within one imaging procedure (cf. Fig. 5.2b). In vivo μ CT was performed at an isotropic voxel size of $10.5 \mu\text{m}$ (vivaCT40, Scanco Medical, Switzerland; 55 kVp, 145 mA, 600 ms integration time, no frame averaging). The mice were scanned starting from the growth plate and was extended for 432 slices ($4536 \mu\text{m}$) in the distal direction. To prevent motion artifacts and obtain reproducible scan regions and bone orientations, mice were anesthetized and kept during the scans in a fixed position using a custom-made mouse bed. In time intervals of 5 days between imaging sessions, 4 sets of images were acquired. Two weeks of aging in mice are approximately equal to one year of aging in humans [80]. Datasets were previously morphometrically analyzed using formation and resorption dynamics analysis software [29, 30, 32]. Furthermore, previous analysis showed that repeated radiation (4 scans) did not effect bone microstructure [361]. The scanner was calibrated weekly against a hydroxyapatite (HA) mineral phantom; and monthly for determining in-plane spatial resolution. Animal experiments were carried out according to the policies and procedures approved by the local legal representative (LAGeSo Berlin, G0333/09).

Image Preprocessing Pipeline

Raw data were reconstructed using standard filtered backprojection implemented in the software of the scanner. Resulting images were cropped to contain the tibia and fibula in independent image sets (Fig. 5.2c). These images varied considerably in size, location and orientation of the bone. Therefore, a preprocessing pipeline that standardizes the images is essential for training a deep learning model. The first step of this pipeline normalizes the sizes of the input images, in which, the algorithm determines the maximum extension in lateral-medial and anterior-posterior direction as well as the most distal bone part inside the image. Second, preserving their aspect ratios, a padding of the images in lateral-medial and anterior-posterior direction is performed (Fig. 5.2d). Therefore, a stripe of additional voxels with the same gray values is placed at the border of the image on the padded plane perpendicular to the padding direction. Next, images are cropped to the minimum z -stack number (of all the images) from distal direction. The 3D images are projected in medial-lateral direction onto the anterior-posterior / distal-proximal plane ensuing a 2D image, which, due to the medial-lateral symmetry, nullifies the symmetry-related skeletal difference between the left and right tibia and fibula. After pre-processing, all 2D images are 733 (y) by 161 (z) pixels in size (Fig. 5.2e).

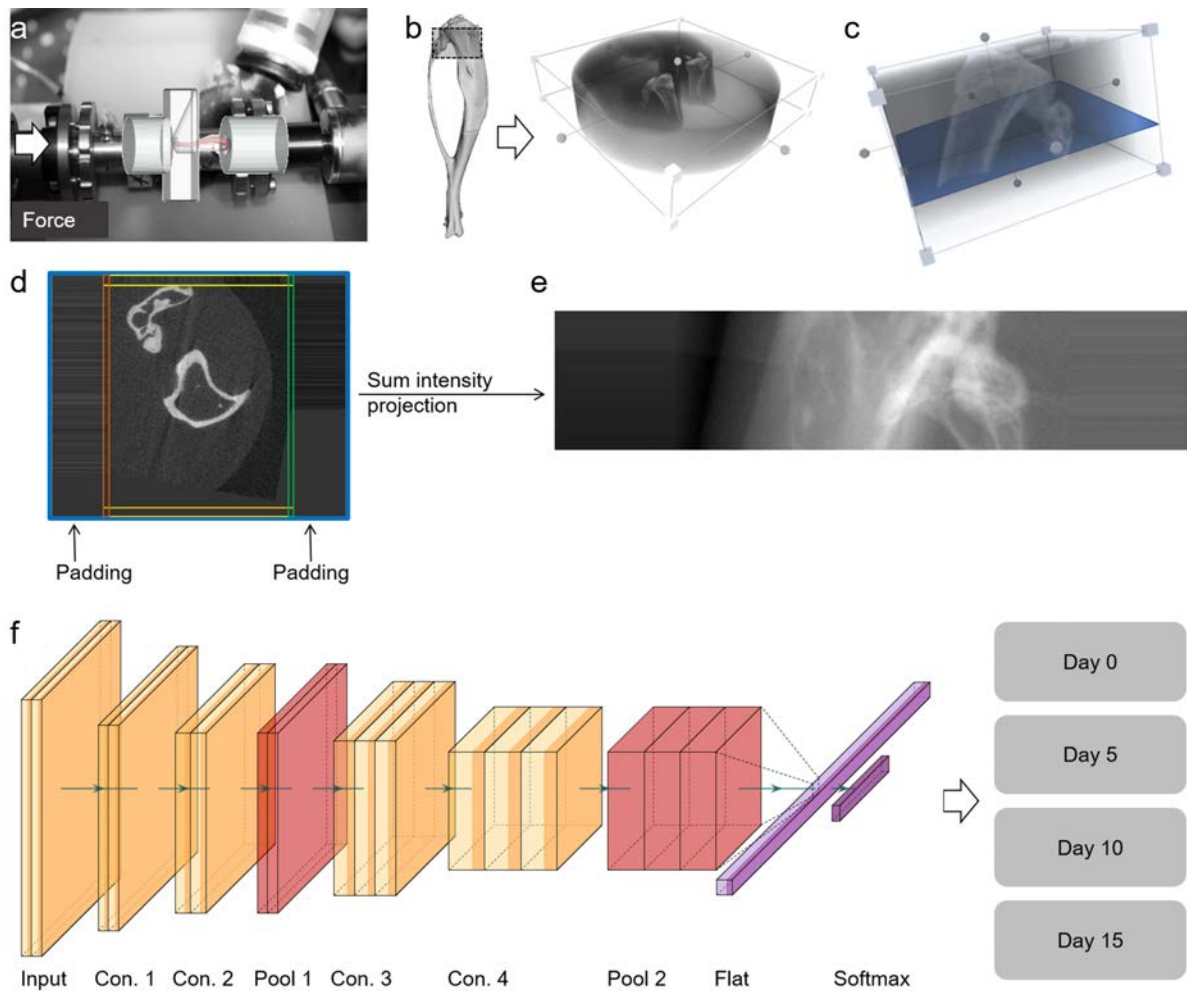


Figure 5.2: Overall work flow and network architecture. *a)* Experimental setup of applying load to the bone. *b)* Imaged ROI and 3D raw data containing both right (control) and left (loaded) tibiae and fibulae. *c)* Cropped 3D image containing only one tibia and fibula. Blue plane indicates an exemplary slice on which the padding step is applied. *d)* Each slice (inside the colored stripes) is padded with border stripes of pixels (colored stripes: padding) in each direction: yellow and orange \rightarrow posterior-anterior, red and green \rightarrow lateral-medial directions. *e)* Sum intensity projection of the 3D image in *C* after padding. *f)* BAAM network architecture including convolutional layers (Con.), pooling layers (Pool), flattened layer (Flat), softmax layer and the four output classes.

Assigning Datasets

Datasets were separated into three groups: 1) A training and validation set, 2) a test set to further eliminate the possibility of overfitting of the trained model, and 3) an application set. The training and validation sets consists of 71 images from 18 mice at all time points of the right control tibia. The test set contains 8 images of two randomly selected mice separated from the training and validation set (2 image per time point). The application set contains 78 images of the left loaded tibia and fibula.

Data Augmentation

DNNs require a large amount of training data for stable convergence and high classification accuracy. Therefore, data augmentation was performed. This was done by systematically increasing the size of the training set with geometric transformations. As suggested by [187, 307], images of the training and validation sets are augmented by applying rotations (-15° to $+15^\circ$; 1° steps) and translations (-22% to $+22\%$; 2% steps in both directions) to increase training accuracy and further prevent overfitting. Maximum augmentation values were chosen to cover potential occurring deviations between images due to the imaging setup. This resulted in a total of 23430 images. Last, images are randomly separated into training and validation sets containing 80% and 20% of the augmented images, respectively.

5.2.2 Deep Bone Age Assessment Model (BAAM)

A customized DNN consisting of 7 layers with four convolutional, two pooling and one fully connected layer (Fig. 5.2f) was designed. The output layer consists of four classes: day 0, day 5, day 10, day 15. Its performance compared to other possible architectures was evaluated (cf. 5.2.4).

By passing an image through the convolutional layers, feature-maps of the image are produced at which the position of the encrypted patterns in kernels are accentuated. This leads to extraction of hidden features of the structure. The deeper the image goes through the network, the more complicated patterns are recognized by the network to perform a classification. At each convolutional layer, the feature map extraction is performed by activating the neurons with the rectified linear function and adding a set of bias terms. These weights and bias values are optimized at each training iteration to provide a higher accuracy.

Feature-maps are down-sampled after the 2nd and 4th convolutional layer with a window size and stride equal to 2. The kernels in all convolutional layers are $3 * 3$ with a stride of 1. In the consecutive convolutional layers, 4, 8, 16 and 32 feature maps are computed, respectively. The activation of the last convolutional layer is flattened into a vector and passed it to an ending fully connected layer with 32 and 4 features from which the last one represents the 4 age classes. At last, a softmax function is applied on the flattened layer to calculate the probability distribution for each age class.

Training Algorithm

The model is trained with the Adam optimization algorithm [179]. The network is initialized with a truncated normal distribution function (standard deviation: 0.1). Training is

carried out for 7000 iterations with a batch size of 100 images. At every 500th step the model is applied on a batch of 200 images of the validation set. The initial learning rate is set to 0.1, then an exponential decay at every 25th step with a 0.96 rate is performed. Implementation, training, validation and testing of the network was performed using Google TensorFlow [1] on a computer with a single Nvidia Geforce GTX 1070 GPU.

Network Performance Evaluation and Validation

Architecture and hyper parameters of the BAAM network are chosen based on its ability of age prediction in for the validation and test sets. Based on a sensitivity analysis (5.2.4), the best performing DNN was chosen and its age prediction performance was validated by determining the accuracy of the network for three groups to i) verify the capability of BAAM to perform an end-to-end age prediction based on 3D μ CT image data, ii) eradicate the possibility of overfitting during prediction, iii) demonstrate the capability of transferring the age prediction capability from right to left tibia and fibula, and iv) demonstrate the robustness of the model to predict the age of mice that it has not been trained with. These are: 1) 100 randomly selected images of the validation set, 2) the 8 images of the test set, which contains only images of mice it has not seen before, 3) all (n=20) images of day 0 of the loaded left tibia and fibula of the application set. These samples represent physiologically loaded tibia and fibula, as at day 0 of the experiment the left limb has not been subjected to loading treatment yet. Confusion matrices (CM) are determined for all three evaluations, further sensitivity was calculated for all time points.

5.2.3 Analysis of Key Skeletal Maturation Regions and Features

The trained BAAM network (after the last training and validation step) applied to the only physiological loaded right tibia (each time point) is further evaluated to identify key regions and features describing the age of the bones. To determine the regions in the images that the network is focusing on for age prediction, saliency maps are calculated. Respectively, a backpropagation is calculated for computing the vanilla gradients [87, 308]. The loss gradient is additionally backpropagated to the input data layer. By taking the L1-norm of the loss gradient of the input layer, the resulting heat map intuitively represents the importance of each pixel for age prediction. These maps convey the locations in the image at which the network focuses to predict the age of the bone. At last, saliency maps are normalized to a [0 – 1] range to enable comparability between different images.

To determine the spatial localization of attention of the network in the process of age assessment, six subregions were defined within the proximal tibia and fibula. Therefore, first the tibia and fibula were manually segmented. Next, these two labels were further divided into 3 regions with the same heights (0.56 mm), o.e., proximal (T1, F1), middle (T2, F2), and distal (T3, F3), cf., Fig. 5.3. The summation of intensity values of the saliency map in each region normalized to the summation of intensity values of the saliency map in the bone region (tibia and fibula) are defined as a measure to indicate the importance of each region for the age estimation (Attention, [0 – 1]).

5.2.4 Results: Bone Age Assessment

Performance Evaluation and Bone Age Prediction

After 1000 training iterations, the accuracy of age prediction (training and validation sets) reached 92% and 93% with a loss of 0.21 and 0.20, respectively. After 7000 iterations, the accuracy and loss values for training and validation sets were 100%, 99%, 0.02 and 0.03, respectively (Fig. 5.4a, b). Therefore, the network was considered as trained after 7000 iterations.

For 100 randomly selected images of the validation set (21, 29, 26 and 24 images of days 0, 5, 10 and 15, respectively), the network correctly predicted all classes except for day 10, where 96% were assigned correctly to day 10 and 4% were assigned to day 15. The resulting confusion matrix for comparison of predicted and true age of the images is almost completely diagonal (Fig. 5.4c). In the test set, 7 out of 8 images were correctly predicted (Fig. 5.4d). Only one image of day 15 was wrongly classified as day 0. In the group of images of the left tibia acquired at day 0, 19 out of 20 images were predicted correctly, only one image was wrongly classified as day 5, resulting in 95% accuracy (Fig. 5.4e). With these accuracy values above 95% in all evaluations, the network is considered performing sufficient for age-prediction.

Sensitivity Analysis of Network Architecture and Hyper Parameters

Accuracy in age prediction for the validation and test sets of five similar, evaluated network architectures compared to BAAM have been determined to find the best performing network.

Various networks with different architectures and hyper parameters have been trained on the training set and applied to the validation and test sets. The best performing network based on the accuracy of age prediction on validation and test sets has been selected to analyze the application set. Although, there exist unlimited variations of these elements, only a subset could provide meaningful results for decoding the aging and rejuvenation processes. Therefore, different network architectures with various network depth, network layout (convolutional (C), pooling (P) and fully connected (F)) and the kernel size in each convolutional layer have been designed and tested. In this section, a comparison of network performances for five selected designed network in which the key parameters are tweaked to reach the highest prediction accuracy are presented. The five networks have following details:

1. Network 1:
 - Depth: 7.
 - Layout: C, C, P, C, C, P, F.
 - Kernel sizes: 8, 16, 16, 32, 64, 64, 64.
 - Number of iterations: 7000.
2. Network 2:
 - Depth: 7.
 - Layout: C, C, P, C, C, P, F.

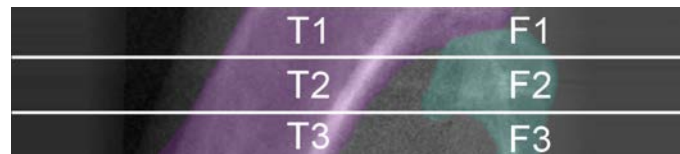


Figure 5.3: *Extracted labels for tibia (purple) and fibula (green) and the 6 regions with equal proximal-distal height on each label. T1-T3 and F1-F3 regions belong to tibia and fibula, accordingly.*

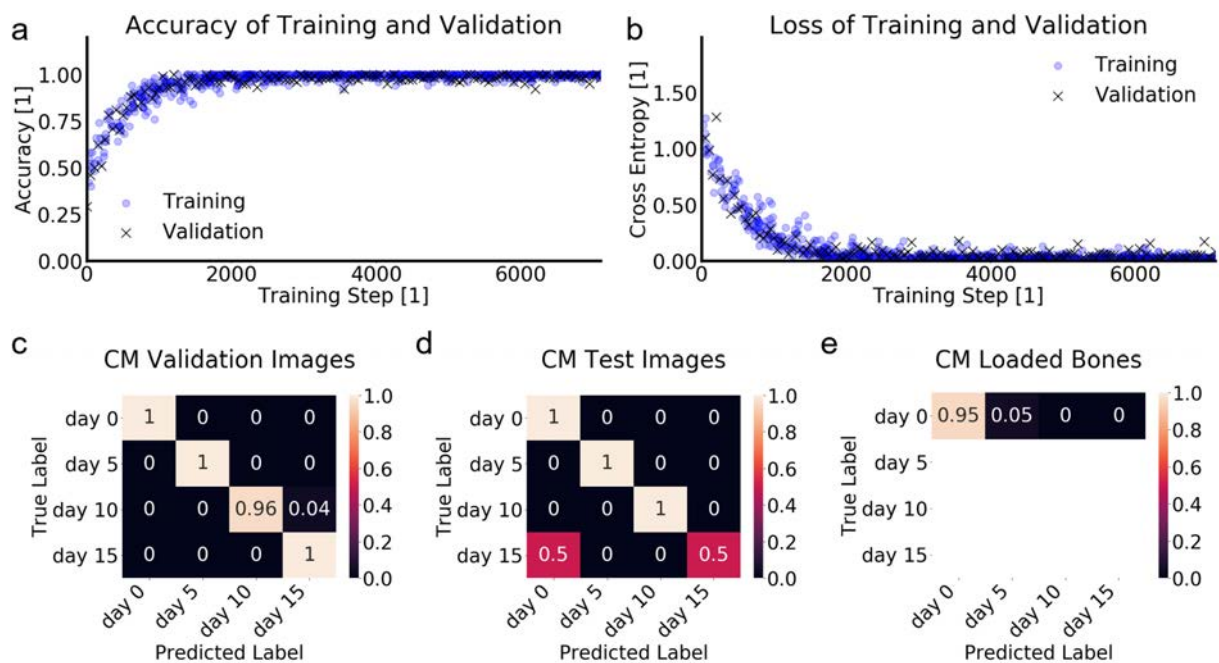


Figure 5.4: *Age prediction results and validation. a) Accuracy of age prediction on training set (blue \circ) and validation set (black \times) vs. training step. b) Calculated loss value of age prediction for training set (blue \circ) and validation set (black \times) vs. training step. Accuracy and loss of age prediction on the validation set is calculated at every 50th training step. c) Confusion matrix of applying BAAM on validation set. d) Confusion matrix of applying BAAM on test set. e) Confusion matrix of applying BAAM on images with age of day 0 of application set. c-e) Predicted age of samples are compared to their actual age. Values are normalized by the number of images per age class.*

- Kernel sizes: 16, 32, 32, 64, 128, 128, 128.
 - Number of iterations: 7000.
3. Network 3:
- Depth: 10.
 - Layout: C, C, P, C, C, P, C, C, P, F.
 - Kernel sizes: 4, 4, 4, 8, 8, 8, 16, 32, 32, 32.
 - Number of iterations: 7000.
4. Network 4:
- Depth: 8.
 - Layout: C, C, P, C, C, P, F, F.
 - Kernel sizes: 4, 8, 8, 16, 32, 32, 32, 32.
 - Number of iterations: 7000.
5. Network 5:
- Depth: 4.
 - Layout: C, C, P, F.
 - Kernel sizes: 4, 8, 8, 8.
 - Number of iterations: 7000.

Analyzing the accuracy and loss values of age prediction during training of different networks (Fig. 5.5) shows that despite a correlation between depth of the its accuracy, going infinitely deeper does not necessary lead to better results. Evidently, the network with lowest number of layers (network 5) has the weakest performance by reaching 86% accuracy with loss value of 0.27 (Fig. 5.5a, b; gray line). While, BAAM, network 1, network 2 and network 3 with depth of 7, 7, 7 and 10 respectively achieve similar good performances (accuracy: Fig. 5.5a, b; black, green, red and yellow lines respectively). Therefore, after a certain depth, no extra performance is gained. The reached accuracy and loss values for all the networks after 7000 training iterations is shown in Table 5.1.

Next, comparing the prediction results of different networks for the validation set was based on their confusion matrices. This further demonstrates that networks 1-4 (Fig. 5.6a-d) have similar good performance and network 5 (Fig. 5.6e) fails to predict day 5 images correctly. It can further be seen that BAAM (Fig. 5.6f) provides the most diagonal confusion matrix, hence it is the best performing network.

At last, the age prediction performance of the networks on the test set demonstrates the superiority of BAAM over other designed networks. While, networks 1-5 achieve 5, 5, 6, 5 and 5 correct predictions out of 8 images of test set respectively (Fig. 5.7a-e), BAAM reaches the highest number of correct age prediction with 7 out 8 (Fig. 5.7f).

The analysis of overall achievements of presented networks as examples of variance in characteristics of DNNs lead to designing the BAAM network. It over-performs the sample presented networks in age prediction for training, validation and test sets. Therefore, it is further utilized to decode the aging and rejuvenation processes.

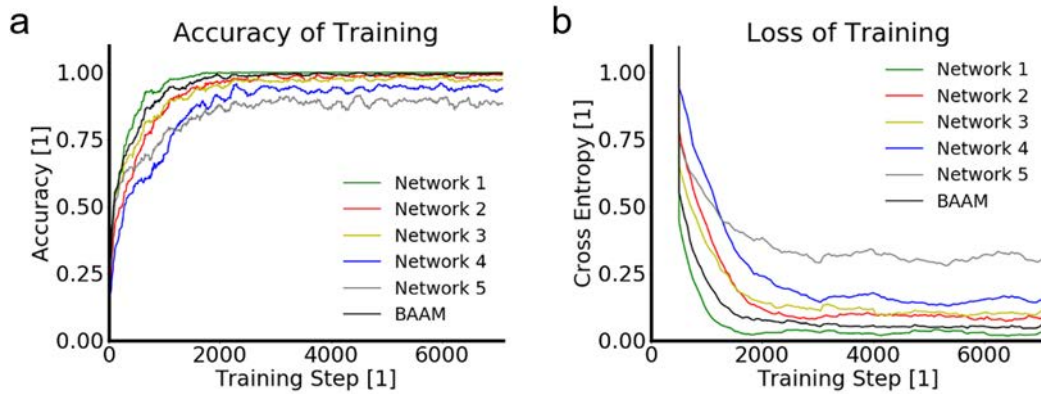


Figure 5.5: Network performances during training. a) Accuracy of age prediction for training set vs training iterations for 5 sample networks and BAAM. b) Smoothed loss value of age prediction for training set vs training iterations for 5 sample networks and BAAM.

Network	Depth	Validation Accuracy	Loss	Test Accuracy
1	7	0.99	0.00	5/8
2	7	0.98	0.02	5/8
3	10	0.98	0.11	6/8
4	8	0.92	0.18	5/8
5	4	0.86	0.27	5/8
BAAM	7	0.99	0.05	7/8

Table 5.1: Network performances. The accuracy and loss values of the networks with different architecture at the end of 7000 training iterations.

5.2.5 Results: Decoding Bone Tissue Maturation Process

Saliency maps were calculated for all correctly classified images. One further image was excluded due to a different orientation of the bone. The different regions received different amounts of attention from the network during the process of age estimation (ANOVA; $p < 0.01$; Fig. 5.8 a-f). Comparing the network attention devoted to different regions of the bone revealed, that at day 0 ($42\% \pm 22\%$) and day 5 ($33\% \pm 9\%$) T3 received significantly higher attention than all other regions ($p \leq 0.01$). At day 10, T2 and T3 ($p \leq 0.04$) and at day 15 T1, T2 and T3 ($p \leq 0.02$) received significantly higher attention than the other regions. In general, all tibial regions received at day 0 and day 15 higher attention than all fibular regions ($p \leq 0.03$). At day 5 and day 10, only T3 received a higher attention than all fibular regions ($p \leq 0.04$).

The attention of the network to the different regions changed with time (ANOVA; $p < 0.01$). In the tibia, the attention on T1 for age prediction is on day 0 ($24\% \pm 9\%$) significantly higher than on day 5 ($16\% \pm 10\%$; $p < 0.01$) and day 10 ($16\% \pm 12\%$, $p = 0.01$). At day 15, only a trend could be identified ($21\% \pm 9\%$; $p = 0.14$; Fig. 5A). T2 receives similar attention at all time points; $21\% \pm 14\%$, $23\% \pm 11\%$, $24\% \pm 18\%$,

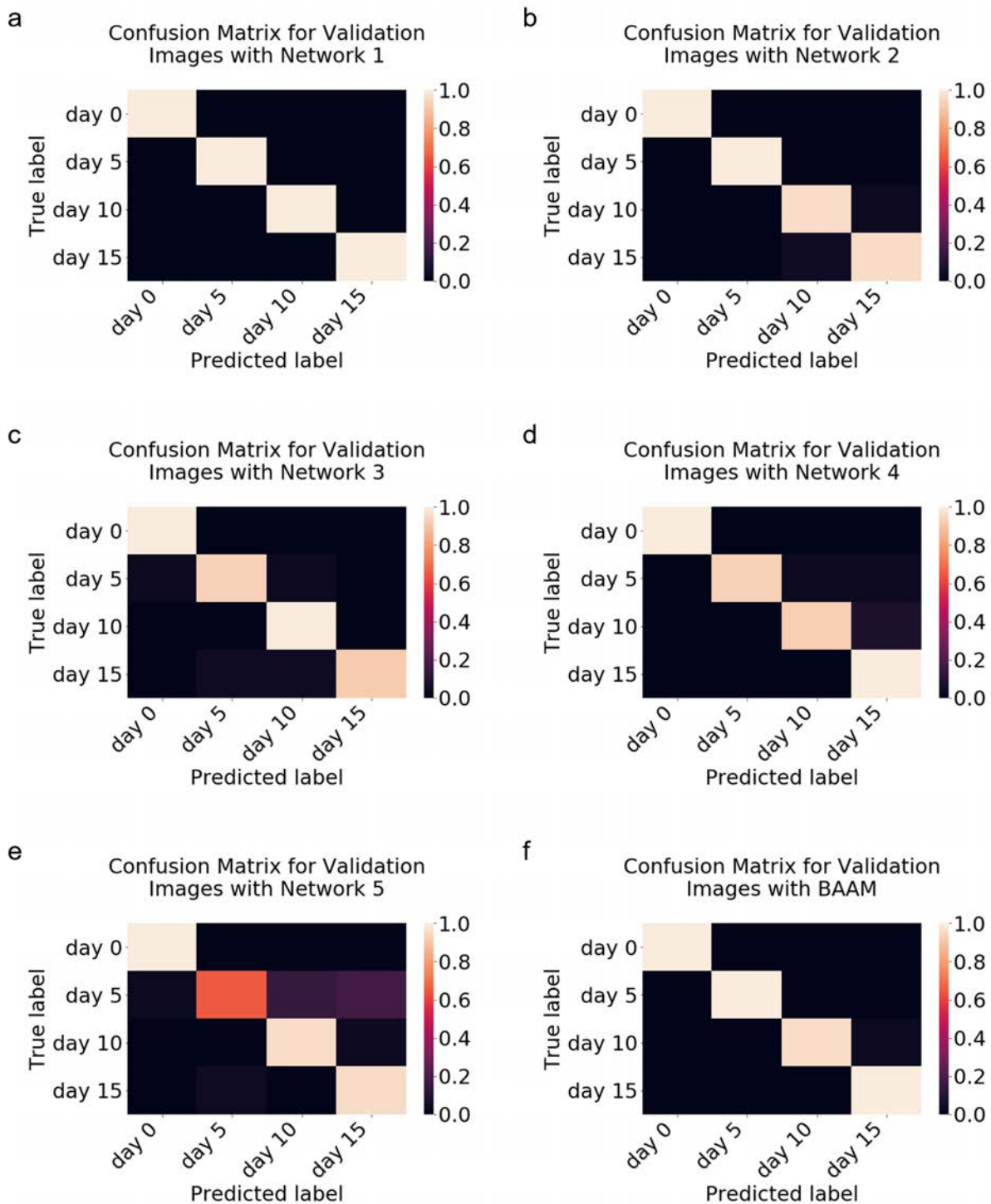


Figure 5.6: Results of age prediction for the validation set. a-e) Networks 1-5 accordingly. f) BAAM. In a-f Predicted age of samples are compared to their actual age. Values are normalized by the number of images per age class.

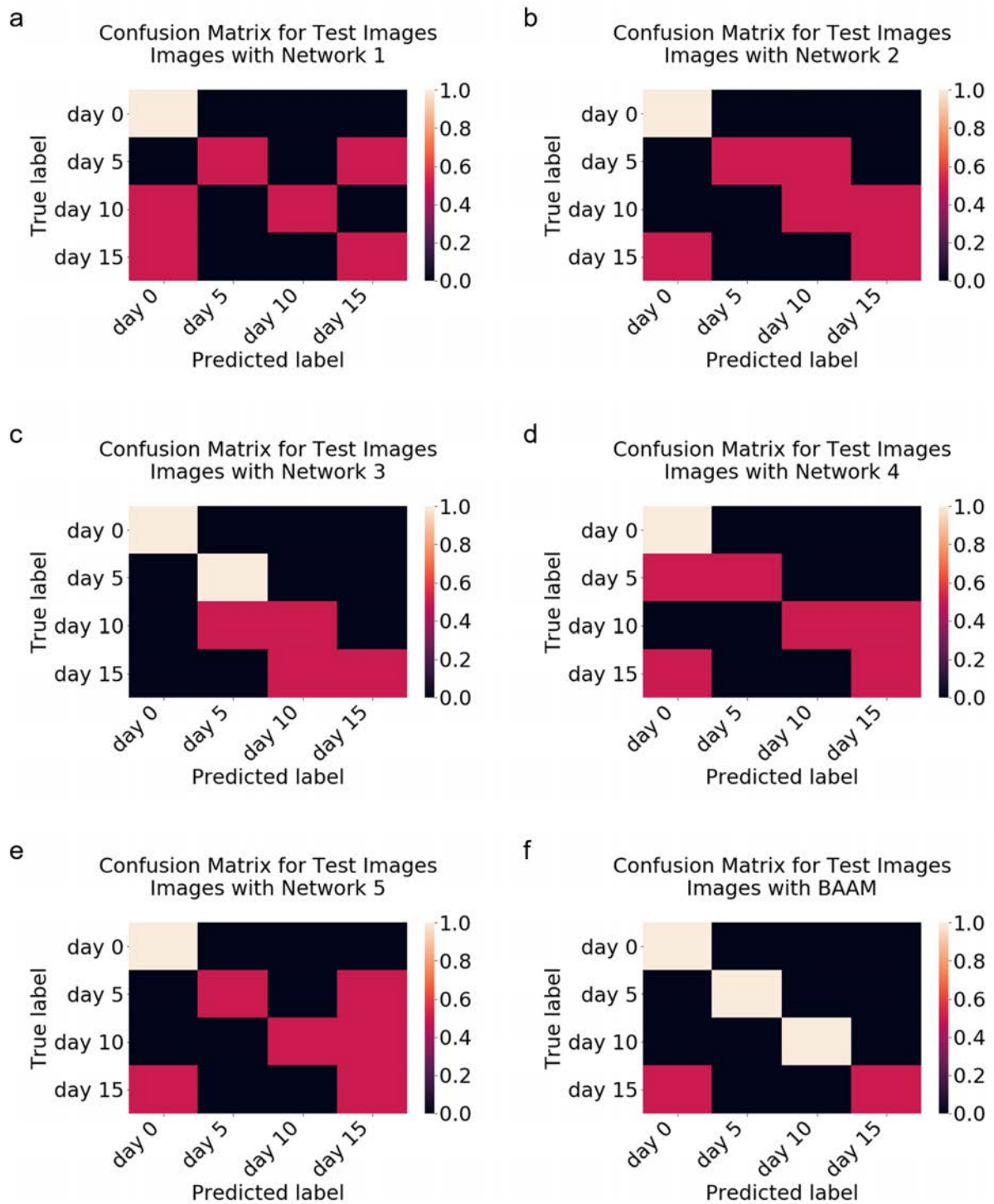


Figure 5.7: Results of age prediction for test set. a-e) Networks 1-5 accordingly. f) BAAM. In a-f Predicted age of samples are compared to their actual age. Values are normalized by the number of images per age class.

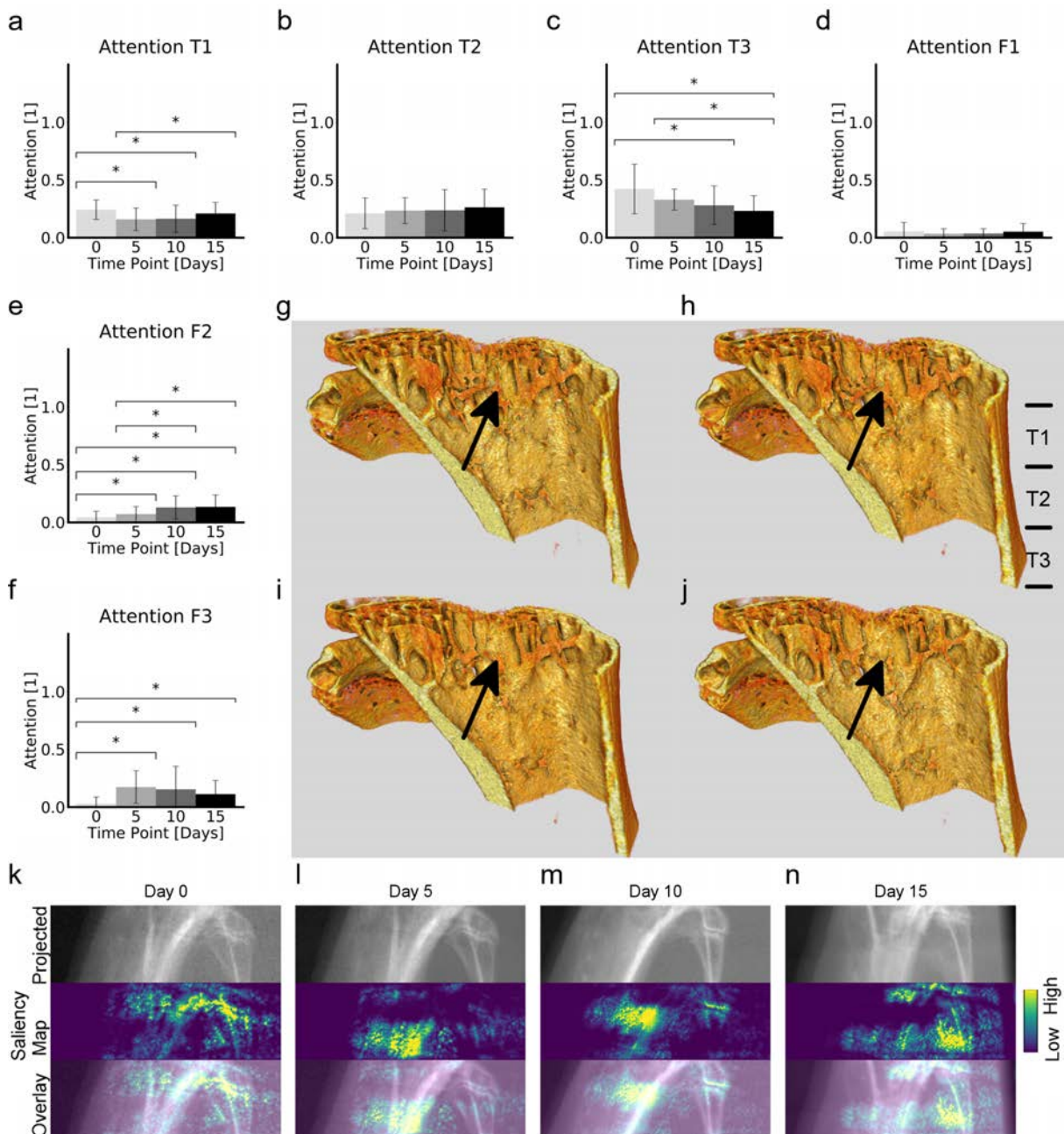


Figure 5.8: Maturation process. a-f) Temporal changes in attention devoted by network to the six regions for age classification in control group. a-c) Proximal tibia T1, T2, and T3, d-f) Proximal fibula F1, F2, F3. Data shown as mean \pm standard deviation. * indicates a significant difference. g-j) 3D visualization of the same tibia and fibula with a longitudinal cut exposing bone micro-architecture for day 0, day 5, day 10 and day 15. The arrow indicates one area in which microstructural remodeling occurred over the 15 days. k-n) Samples of projected images (gray scale image, top), saliency map (color coded from blue to yellow indicating low to high attention, middle) and the overlay of projected image and its saliency map (bottom). k) day 0, l) day 5, m) day 10, n) day 15.

and $26\% \pm 16\%$. In region T3, a continuous decrease in attention during maturation takes place ($42\% \pm 22\% \rightarrow 23\% \pm 13\%$), leading to a significant reduced attention from day 10 onward ($p \leq 0.01$). In the fibula, attention to the F1 regions remains small throughout the 15 days ($5\% \pm 8\%$, $3\% \pm 4\%$, $4\% \pm 4\%$, $5\% \pm 7\%$). The attention to F2 significantly increases with maturation ($4\% \pm 5\% \rightarrow 13\% \pm 11\%$, $p \leq 0.01$). It also significantly increases in each time step except the time step from day 10 to 15 (day 0 \rightarrow 5 \rightarrow 10 : $4\% \pm 5\% \rightarrow 7\% \pm 7\% \rightarrow 13\% \pm 10\%$, $p \leq 0.02$). In region F3, attention jumps from $3\% \pm 6\%$ at day 0 to $17\% \pm 14\%$ at day 5 ($p < 0.01$). Afterwards a slight drop from $15\% \pm 20\%$ (day 10) to $11\% \pm 12\%$ occurs at day 15 ($p = 0.08$). A cross-sectional cut through a 3D representation of one bone at each time-point shows similarities and changes of the structures (Fig. 5.8g-j). Representative saliency maps are shown in (Fig. 5.8 k-n). Qualitative analysis of the attention devoted to tibia and fibula reveals that the network focuses on clusters of pixels for its analysis.

5.2.6 Discussion

It is known that bone fracture resistance increases with skeletal maturation and aging, as well as in response to certain therapy. Whole bone fracture resistance is determined by bone quantity, which encompasses geometric, microarchitectural, and material properties (i.e., trabecular architecture, mineralization, crosslinking, microcracks). Little is known about the interplay between all of these properties/factors contributing to compromised or recovered bone quality. Most previous studies have focused on individual features, while lacking global optimization, as individual contributions of static (e.g. trabecular bone volume or bone mineral density distribution) or dynamic (e.g. bone formation rate) feature as well as the global interplay of localized dynamic processes of modeling, remodeling, mineralization and demineralization to overall changes of the bone are not known to date.

Here, a deep learning approach to tackle this challenge by creating a model that utilizes the complete content of X-ray attenuation images is proposed. A μ CT image-based method enabling an end-to-end age prediction with high accuracy is developed. This method allows identifying bone sub-regions relevant for this classification. The developed method is utilized to study skeletal tissue maturation and the localized rejuvenation effects of in vivo dynamic controlled loading on mouse bone tissue age.

The results show that complex processes, such as bone tissue maturation and adaptation, can be reconstructed by in vivo image-based deep learning and quantitative analysis of learned features. Even subtle changes, as occurring during one remodeling cycle of mice bones [32], could be identified, as the model predicts four time points between 26 and 28 week old mice based on in vivo μ CT images with an accuracy of more than 95%. This classification is presumably linked to bone mass, shape, micro-architecture and material properties alteration through different length scales, as all these processes change in a site-specific manner during growth, maturation and aging. These changes take place by modeling, remodeling, mineralization and demineralization processes [29, 47, 219, 222, 258, 312] and are directly or indirectly encoded in the image created by interaction of photons with matter, as the resulting attenuation is, besides bone mass in the photon beam, dependent on the local atomic number, and therefore calcium content.

Additionally, a link between the age prediction dynamics to age-related trabecular bone

loss occurring between the age of 26 and 28 weeks [361] is shown. This is in accordance with other studies reporting a loss in trabecular bone volume in C57Bl/6 mice from 26 weeks onward [115]. Therefore, these mice are expected to be in a phase of starting trabecular bone loss. However, in the proximal fibula, an increase of cortical bone volume in the same mice between 19 to 22 weeks [239] is observed. Unfortunately, this and other studies investigated the fibula bone volume changes only in young mice during skeletal maturation [181, 239]. In adult humans, higher age-related deterioration of the tibia than the fibula has been reported [233]. Here, no significant changes in the fibula bone volume was detected, therefore also no correlations between age prediction and fibula bone volume existed. However, it has to be taken into consideration, that the volume of interest was centered on the proximal tibia.

Here, it is further shown, that localization of aging-related information in the bone identified by the model can be extracted in a quantitative manner. This localization of age-information effects, here quantified by attention distribution of the network extracted using a saliency map as post-processing, differed between regions and was affected by time. The age information seems to be more manifested in the tibia than in the fibula, as at all time points more than 68% of the attention of the network is focused on the tibia. In line with this, the highest structural changes could be identified in the trabecular region of the tibia, with a 14% loss of bone volume. This trabecular loss has been previously quantified in more detail [29]. In general, the most distal part of the proximal tibia (T3) received the greatest attention, but over time there was decreasing in attention. This is in line with previous described structural changes in the tibia, where a strong loss of trabeculae during adulthood [99, 361] and a nearly complete disappearance of trabeculae after 78 weeks [29] is reported. The second highest attention was received by the region located closest to the growth plate (T1), where longitudinal growth, and therefore modeling and primary (fast) mineralization occur. This growth persists with aging, although it slows down after puberty [129]. Therefore, it can be assumed, that the network focuses on the regions with the most changes in bone volume and density occurring over the monitored 15 days. In the fibula the attention was the lowest in F1. However, it must be considered, that the most proximal part of the fibula is located below the tibia (see Fig. 5.8g-j). Attention to F2 and F3 varied with time, which might be linked to fibular (re)modeling. In general, attention was located in clusters (see Fig. 5.8k-n) not individual trabeculae, which let us conclude that mineralization (change in grey values) and (re)modeling together affect the age estimation.

Having a robust bone age assessment deep neural network at hand allows investigating effects of internal or external stimuli on the aging process. 5.3, focuses on, how the trained BAAM could be utilized to study the process in which in vivo loading affects the aging process and therefore, the macro/micro-structure of the bone towards a younger appearance.

5.3 Analyzing Effects of in vivo Loading Treatment on Skeletal Age

In this section, BAAM's ability for identification of treatment results and relating these to load-induced surface (re)modeling ("rejuvenation")-effects is investigated (Fig. 5.9).

Furthermore, by analyzing the learning process of the DNN through saliency maps, the spatial localization of the network attention is quantified, permitting determination of where in the bone the "skeletal age" information is manifested.

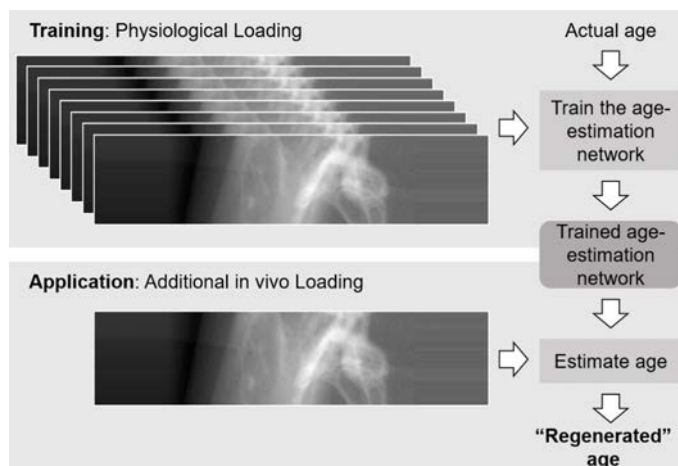


Figure 5.9: First, the network is trained on physiologically loaded bones to predict age (top). Second, the trained network is applied on images of bones treated with additional loading to investigate the rejuvenation effects of treatment (bottom).

5.3.1 *In vivo* Mechanical Loading

The 20 mice (female C57Bl/6J, 26 weeks old at beginning of experiments, Jackson Laboratories, Sulzfeld, Germany) underwent two weeks of *in vivo* cyclic compressive loading of the left tibia [29, 361]. Loading was applied 5 days/week (M-F) for 2 weeks while mice were anesthetized (216 cycles applied daily at 4Hz, delivering -11N loads, $1200\ \mu\text{e}$ on the medial surface of the tibial mid-shaft, determined by prior *in vivo* strain gauging experiments; Fig. 5.2a). The right tibia served as physiologically loaded internal control. The first loading session occurred on the first day of *in vivo* imaging.

5.3.2 Decoding Effects of *in vivo* Loading using BAAM

The bone age prediction model is therefore further applied to the application set (defined in 5.2.1, containing images of the *in vivo* loaded tibiae and fibulae; Fig. 5.9). The predicted age of each bone at each time point is compared to the actual bone age to investigate rejuvenating effects of load-induced bone (re)modeling on skeletal age. Rejuvenation is defined as the delta age predicted at day 0 and day x divided by the delta time between day 0 and day x. Key regions and features describing the estimated rejuvenated age of the bones are determined (saliency maps).

5.3.3 *In Vivo* Loading and 3D Bone Volume Changes

A separate set of 104 3D images were Gaussian filtered and binarized using a global threshold of 273/1000 (456 mg HA/cc), which was determined based on the grey value histogram of the whole ROI. This dataset was acquired by pooling images from two

separate studies carried out by Birkhold et al. [32] and Willie et al. [361]. Fibula and tibia were manually separated, automated segmentation was performed to separate trabecular and cortical bone regions of tibiae, as described earlier [32]. Total tibia bone volume (tibia BV, μm^3), tibia trabecular bone volume (tibia tb.BV, μm^3), tibia cortical bone volume (tibia ct.BV, μm^3), and fibula bone volume (fibula BV, μm^3) are determined. Correlations between bone volumes and real/predicted age are determined.

Statistical Analysis

The effect of loading (left loaded tibia, right control tibia), region (tibia: T1, T2, T3; fibula: F1, F2, F3) and time point (day 0, 5, 10, 15) as well as interactions between terms was assessed using repeated measures ANOVAs. Differences between actual bone age and predicted bone age as well as between loaded and control bones were assessed by paired Student's t-tests. Values are presented as mean \pm standard deviation and statistical significance was set at $p < 0.05$.

5.3.4 Results: Rejuvenation Effects of in vivo Loading

To study potential rejuvenation effects of mechanical loading on bones, 78 images (2 images were removed from the dataset due to low quality) of bones subjected to in vivo loading are analyzed (application set). At day 0, 95% of bones were classified with their actual age. For the loaded bones at day 5, 10, and 15, the predicted age differed noticeably from the actual age (Fig. 5.10a). After 5 days of loading, 47% of the images were classified as being 5 days older, 26% as being 5 days younger, and only 16% were identified with their actual age. After 10 days of loading, 55% of the bones were classified as younger than their actual age (30% as day 0 and 25% as day 5). A total of 35% were identified with their actual age and 10% were classified as to be older. After 15 days of loading, 74% of the bones were classified as younger than their actual age. For 5%, BAMM predicted that the images belong to mice that were 15 days younger, 11% appeared to be 10 days younger and 58% were classified as 5 days younger than their actual age. Only 26% of the bones were classified by its actual age, i.e., day 15.

Investigating the rejuvenation effects during the course of loading (Fig. 5.10b, green line) reveals that with increasing duration of loading (day 5 \rightarrow day 10 \rightarrow day 15) higher percentage of images are classified younger than their actual age (25% \rightarrow 55% \rightarrow 74%). On the other hand, 5%, 58%, and 10% of samples at day 0, 5 and 10, respectively were classified older than their actual age. The amount of samples categorized with their actual age increases from day 5 to day 10 but decreases as loading treatment continues (16%, 35% and 26% for day 5, 10, and 15, respectively). Resulting mean assigned age was 7.63 ± 5.62 at day 5, 6.58 ± 5.01 at day 10 and 10.26 ± 3.90 at day 15. This results in rejuvenation effects of -2.37 ± 5.62 at day 5, 3.68 ± 4.96 at day 10 ($p < 0.01$) and 5.00 ± 3.73 at day 15 ($p < 0.01$; Fig. 5.10c).

Loading affected the attention of the DNN network (ANOVA; $p < 0.01$). Additionally, the distribution of attention between regions was affected by loading (ANOVA; $p < 0.01$). Comparison of attention in different regions between loaded and control limb reveals that – with the exception of F1 ($p = 0.02$) – there is no significant difference in attention in different regions between the left and right limbs at day 0 (Fig. 5.10d). After 5 days of loading, there is no significant difference in attention in T1-T3 and F1-F3 (Fig. 5.10e).

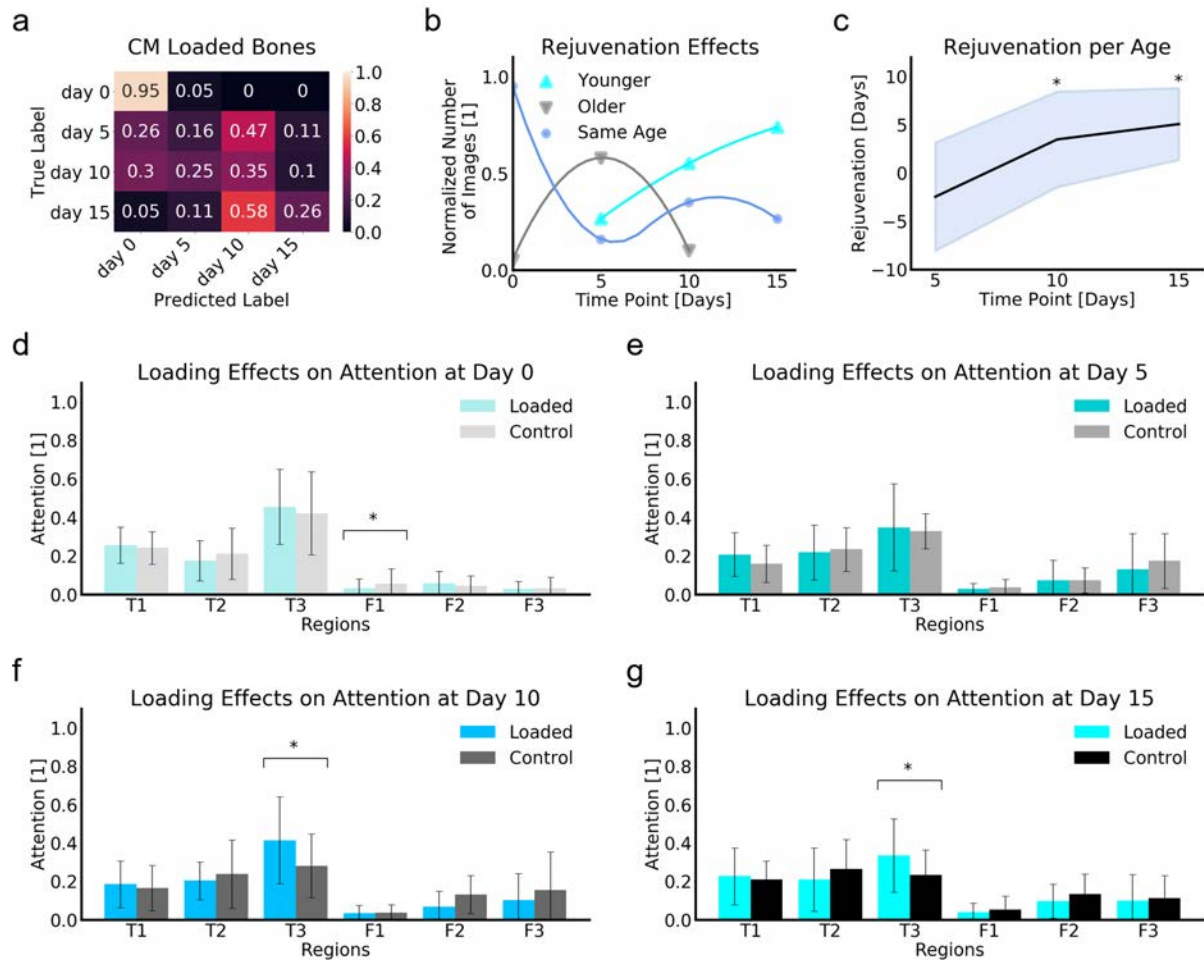


Figure 5.10: *Rejuvenation process.* a) Confusion matrix of applying the BAAM network on application set consisting of images of bones treated with extra loading. Predicted age of samples are compared to their actual age. Values are normalized by the number of images per age class. b) Rejuvenation effect of extra loading treatment vs loading duration. Normalized number of rejuvenated images vs loading period: green. Normalized number of images classified with their actual age vs loading period: gray. Normalized number of images classified older than their actual age vs loading period: blue. The lines are 3rd degree polynomial fits to the scattered data. c) Mean rejuvenation per age group with standard deviation as highlighted area. d-g) Attention in proximal tibia (T1-T3) and fibula (F1-F3) in control and loaded bones. d) Day 0. e) Day 5. f) Day 10. g) Day 15. Values are shown as mean ± standard deviation. * indicates a significant differences between loaded and control bones (student's *t*-test, $p < 0.05$).

After 10 and 15 days of loading; however, the attention in the T3 regions is significantly higher on the loaded side than on the control limbs ($28\% \pm 17\%$ vs. $41\% \pm 23\%$, $p = 0.01$ and $23\% \pm 13\%$ vs. $33\% \pm 19\%$, $p = 0.04$ at days 10 and 15, accordingly, (Fig. 5.10f-g). This difference might be related to presence of paw preference (called handedness) in mice [26].

5.3.5 Results: Localized Rejuvenating Manifestation of in vivo Loading

To analyze the importance of each region within the process of rejuvenation, images of the day 15 loaded bones were categorized based on their predicted time points: "day 0", "day 5", "day 10" and "day 15". Afterwards, saliency maps of each of these groups were compared to their counterparts from the control group. Moreover, the distribution of attention was compared between each pair of rejuvenated bones and control bones for each time-point (Fig. 5.11a, b). After 15 days of loading, regions T1, T2, and T3 received $23\% \pm 14\%$, $21\% \pm 16\%$, and $33\% \pm 19\%$ of the attention, respectively. F1, F2, and F3 received $4\% \pm 5\%$, $10\% \pm 9\%$, and $10\% \pm 13\%$ of the attention, respectively. In all tibial regions, no significant difference between bones predicted younger and control bones of these specific ages were found for any of the four time points. The single bone (imaged at day 15) predicted as day 0 received 30% attention at T1 (control: $24\% \pm 9\%$), 17% at T2 (control: $21\% \pm 14\%$) and 33% at T3 (control: $42\% \pm 22\%$). The bones predicted as "day 5" received $14\% \pm 3\%$ at T1 (control: $16\% \pm 1\%$; $p = 0.24$), $32\% \pm 19\%$ at T2 (control: $23\% \pm 12\%$; $p = 0.32$), and $52\% \pm 15\%$ at T3 (control: $33\% \pm 10\%$; $p = 0.16$). The bones predicted as "day 10" received $23\% \pm 18\%$ at T1 (control: $16\% \pm 12\%$; $p = 0.13$), $23\% \pm 19\%$ at T2 (control: $24\% \pm 18\%$; $p = 0.45$), and $34\% \pm 22\%$ at T3 (control: $28\% \pm 17\%$; $p = 0.23$). The bones predicted as "day 15" received $23\% \pm 10\%$ at T1 (control: $21\% \pm 10\%$; $p = 0.38$) and $25\% \pm 10\%$ at T3 (control: $25\% \pm 16\%$; $p = 0.22$). Only for the 5 bones, which were predicted as a loaded bone "day 15", i.e., no effect of the loading was observed, a significant difference with respect to the control bones being imaged at day 15 could be identified at the T2 region ($13\% \pm 8\%$, vs. control: $25\% \pm 16\%$; $p = 0.01$).

The single bone predicted as "day 0" received 6% attention at F1 (control: $6\% \pm 9\%$), 12% at F2 (control: $4\% \pm 5\%$) and 1% at F3 (control: $3\% \pm 6\%$). The bones predicted as "day 5" received significant less attention at all fibular regions: F1 $1\% \pm 1\%$ (control: $3\% \pm 4\%$; $p < 0.01$), F2 $0\% \pm 0\%$ (control: $7\% \pm 7\%$; $p < 0.01$), and F3 $1\% \pm 0\%$ (control: $17\% \pm 15\%$; $p < 0.01$). The bones predicted as "day 10" received at F1 and F3 comparable attention as the control ones of day 10 ($3\% \pm 3\%$ control: $3\% \pm 4\%$; $p = 0.22$; $12\% \pm 15\%$; control: $15\% \pm 20\%$; $p = 0.32$). F2 received less attention than the control bones of this age ($5\% \pm 5\%$; control: $13\% \pm 10\%$; $p < 0.01$). The bones predicted as "day 15" received at F1 and F3 attention that is comparable to the control ones of day 15 ($7\% \pm 7\%$ control: $5\% \pm 7\%$; $p = 0.24$; $10\% \pm 10\%$; control: $11\% \pm 12\%$; 0.42) and F2 received more attention than the control bones of this age ($22\% \pm 3\%$; control: $13\% \pm 10\%$; $p < 0.01$; Fig. 5.11b). Saliency maps for selected images from each of the four time points are given in Fig. 5.11c-f.

In summary, distribution of attention was in 89% of the after 15 days analyzed loaded left tibia comparable to the right control of the time point (day 5, 10 or 15) they were

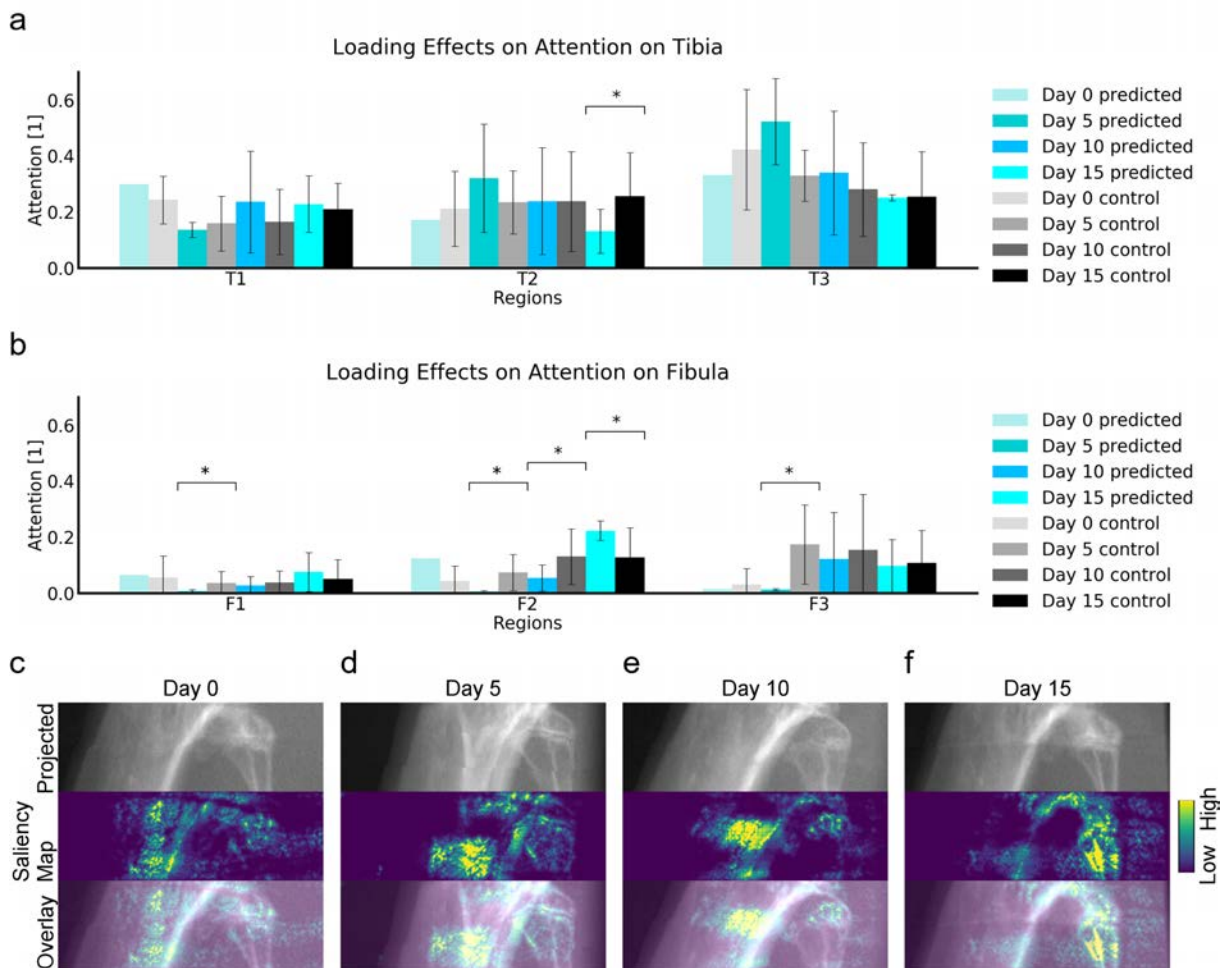


Figure 5.11: Rejuvenation process. a, b) Attention at bones subjected to 15 days of loading and classified as day 0, 5, 10, or 15 compared to attention of these groups in the control limbs. a) Attention to T1-T3 regions. b) Attention to F1-F3 regions. Data shown as mean \pm standard deviation. * indicates a significant difference (student's *t*-test, $p < 0.05$). c-f) Samples of projected images (gray scale image, top), saliency map (color coded from blue to yellow indicating low to high attention, middle) and the overlap of projected image and its saliency map (bottom) from loaded group. c) day 0. d) day 5. e) day 10. f) day 15.

predicted to resemble. In the fibula, 56% of comparison cases showed no significant difference (9 comparison cases per tibia/fibula = 3 regions \times 3 time points). This further confirms that the load-induced bone (re)modeling in these mice generates similarities between older loaded bones and younger control bones, therefore a rejuvenation effect of loading can be concluded.

5.3.6 Results: Rejuvenation and Bone Volumetric Changes

The tibia and fibula total bone volume and cortical bone volume did not change significantly within the 15 days (Table 5.2). Tibial trabecular bone volume decreases significantly from day 0 (0.30 ± 0.07) to day 15 (0.24 ± 0.05 ; $p < 0.01$). Loading significantly affected total tibia bone volume (all time points; $p \leq 0.01$), cortical tibia bone volume (all time points; $p \leq 0.02$) and trabecular tibia bone volume (day 0 and 15; $p \leq 0.01$, Table 5.3). A significant, but weak correlation was found between Tibia BV in loaded limbs and real age, Tibia ct.BV and real age, and Tibia ct.BV and estimated age (Table 5.4). Additionally, trabecular bone volume (Tibia tb.BV) in control limb correlated significantly, but weak with real age. Trabecular bone volume (Tibia tb.BV) in loaded limb correlated weak, but significantly with estimated age (Table 5.4).

Morphometry Control Bones				
	day 0	day 5	day 10	day 15
Fibula BV [mm^3]	0.78 ± 0.16	0.79 ± 0.17	0.82 ± 0.19	0.78 ± 0.15
Tibia BV [mm^3]	2.53 ± 0.13	2.53 ± 0.16	2.54 ± 0.14	2.50 ± 0.12
Tibia tb.BV [mm^3]	0.30 ± 0.07	0.28 ± 0.07	0.25 ± 0.06	0.24 ± 0.05
Tibia ct.BV [mm^3]	2.23 ± 0.13	2.25 ± 0.13	2.28 ± 0.13	2.26 ± 0.10

Table 5.2: Morphometry parameters of tibia and fibula determined based on *in vivo* μ CT images at day 0, 5, 10, 15 of right control fibula and tibia subjected only to physiological loading. Data shown as mean \pm standard deviation.

Morphometry Loaded Bones				
	day 0	day 5	day 10	day 15
Fibula BV [mm^3]	0.83 ± 0.15	0.82 ± 0.15	0.82 ± 0.17	0.81 ± 0.12
Tibia BV [mm^3]	$2.69 \pm 0.18^*$	$2.74 \pm 0.17^*$	$2.84 \pm 0.14^*$	$2.86 \pm 0.14^*$
Tibia tb.BV [mm^3]	0.33 ± 0.06	0.31 ± 0.06	$0.31 \pm 0.06^*$	$0.33 \pm 0.06^*$
Tibia ct.BV [mm^3]	$2.36 \pm 0.19^*$	$2.43 \pm 0.19^*$	$2.52 \pm 0.14^*$	$2.53 \pm 0.15^*$

Table 5.3: Morphometry parameters of tibia and fibula determined based on *in vivo* μ CT images at day 0, 5, 10, 15 of left fibula and tibia subjected to additional axial compression loading. Data shown as mean \pm standard deviation. * indicates a significant difference between loaded and control bones (student's *t*-test, $p < 0.05$).

Correlations Bone Volume vs. Time						
	Loaded				Control	
	Real age		Predicted age		Real age	
	R^2	F	R^2	F	R^2	F
Fibula BV [mm^3]	0.01	0.59	0.02	0.29	0.00	0.96
Tibia BV [mm^3]	0.15	0.01*	0.05	0.11	0.00	0.65
Tibia tb.BV [mm^3]	0.00	0.98	0.10	0.03*	0.12	0.02*
Tibia ct.BV [mm^3]	0.14	0.01*	0.11	0.02*	0.01	0.43

Table 5.4: Regression analysis: Correlations between morphology (bone volume) and time points (real age and predicted age). Weak correlation are shown in bold, * indicates significance of correlations ($p < 0.05$).

5.3.7 Discussion

Bones receiving additional loading were estimated to be younger. Already after day 5 of loading, predicted age starts to diverge from actual age, which might suggest a restructuring in response due to the new local loading conditions. From day 10 onward, the bones appear to be significantly younger (4 and 5 days younger after 10 and 15 days of loading, respectively). This might reflect an increase in bone strength after restructuring. However, this needs to be investigated in detail by analyzing orientation of individual trabeculae or in-silico modeling of bone strength. Previous studies showed in adult C57BL/6 mice adaptive adjustments in the shape of formation and resorption sites at trabecular [29, 193] and cortical sites [28], mineralization dynamics [219] as well as material properties on a macro- and micro-scale [25] in response to loading. These adaptations have been shown to differ between different bone sites, such as endocortical and periosteal surface [31] or at metaphyseal versus diaphyseal sites [25, 28], leading to bone shape adaptation, as e.g. second moment of inertia at proximal metaphysis changes with loading in 22 week old mice [53]. All this information is potentially analyzed in a combined manner by the deep neural network. Here, a link to bone volume changes was established and a significant correlation between predicted age and cortical as well as trabecular bone volume was found. Future studies will investigate further correlations, e.g., by quantifying structural changes in sites identified as age-determining.

To investigate, if the observed restructuring leads to a younger appearance of the bones, the distribution of attention on loaded bones after 15 days, classified younger, was compared to the control bones of the classified ages. The similarities of distribution of attention, together with the comparability of correlations in 1) predicted age and trabecular bone volume in loaded bones and 2) real age and trabecular bone volume in control limbs, let us speculate, that loading induces tibial restructuring towards a younger appearing bone. This rejuvenation is strongly manifested in the dynamic trabecular structure. This is also the only bone compartment, where an age-related short-term loss of bone volume in the control limb and a constant bone volume with time in the loaded limb is detected. This finding is further supported by previous studies investigating trabecular bone gain in response to loading [222, 320, 361] by comparing loaded proximal tibia of adult mice with internal nonloaded control limbs.

In the cortical compartment of the loaded tibia, a bone volume gain was found, which made this bone compartment most similar to the control bones of day 0. This finding is supported by Sugiyama et al., who found similar load-induced cortical volume gain in the proximal tibia of adult mice [320]. A previous study, showed that adaptive bone formation in the lateral metaphyseal region is greater than in the medial region while medial adaptive resorption is greater than in the lateral region. A slight positive anterior and posterior remodeling balance was reported. Further, adaptation occurs by increasing periosteal formation [28]. This suggest a structural adaptation of cortical bone for the sake of increasing its moment of inertia as a response to the bending force. In the fibula, regardless of the observed rejuvenation, in 4 out of 9 comparisons, significant differences in attention distribution between loaded bones classified younger and the control bones of the classified age was observed. Therefore, since the fibula is generally assumed to be mechano-sensitive [239], load-induced changes seem to trigger a fibula restructuring that does not lead to a younger appearance of the bone. However, it must be considered, that the imaging region was optimized for tibial analysis. Future studies might include a greater fibula region into the analysis as fibula adaptation is in general not well studied.

To conclude, loading seems to change the appearance of bones towards a younger age. In this study, this effect is greater in the tibiae than in the fibulae and mainly manifested in the trabecular region, which is the compartment most affected by bone loss in early osteoporosis [249]. Since fragility fractures in relatively young individuals are mainly vertebral compression fractures, therefore "trabecular fractures" [325], an adaptation towards a younger trabecular bone might be in combination with an macroscopic adapted cortical shell contributing to reducing fracture risk in early osteoporosis.

Current methods assessing bone maturation and aging mainly focus on specific dynamic features [32, 39, 49, 224, 226, 289]. Recently developed machine learning methods, however, consume the complete image content while performing a classification task. Recently, first applications to preclinical and clinical image data of bone showed, that a machine learning classification into healthy and disease state is achievable [301, 309]. Going from there, in the next step, a framework allowing for a tracking of dynamic bone changes in physiological aging/maturation conditions was developed. Additionally, by training with physiologically loaded bones and applying the network on in vivo loaded bones, it is demonstrated that loading causes bone (re)modeling and the dynamics of this bone (re)modeling, without the need for transfer learning is analyzed [120, 345]. Compared to the DNN developed for skeletal bone age assessment in pediatrics [200, 313, 337], here, a further step towards a prognostic tool is taken. Saliency maps were previously suggested to qualitatively visualize the importance of different bones in maturation of pediatric hands [201]. Here, a quantitative analysis of the distribution of learned features by employing saliency maps [308] is shown. This allows to identify the localization of age-relevant information in bone. Future investigations may analyze the dynamics of aging and treatment-induced regeneration in a site-specific manner.

The methodology presented in sections 5.2 and 5.3 has also limitations. First, the chosen samples may not represent a larger population. However, the method is validated in a three-fold manner and received an accuracy of above 95%. Additionally, structural parameters derived from μ CT and histomorphometric indices of bone formation, which was measured previously in these mice, are similar to those reported in similarly aged female *C57Bl/6* mice [145, 222]. Adhering to the principles of the three Rs, specific-

ally reduction of animal number, motivated us to re-examine these datasets, rather than perform new studies on additional mice. Second, skeletal aging in mice differs to that in humans [164] and thus, translation of these results to human bone behavior requires further investigation. Since age-related bone loss in humans resembles to a certain extent findings in mice [3, 326], it can be speculated that a future application to human bone might resolve similar patterns.

Given the proven performance on reconstructing bone tissue maturation and adaptation processes, it is expected that this study will be able to pave the way for future studies to investigate a wide variety of biological processes involving continuous morphological changes. This may include developmental and aging stages, the progression of diseases [264, 373] or the response to treatments, and dynamic processes that have often been reduced to binary classification problems. Automated computational analysis, as shown here, could reveal morphological changes at much earlier stages than recognized previously. Therefore, the effects of loading duration on overall bone adaptation might be another future application, as recently shorter loading durations have been suggested [322, 374]. Furthermore, as features can be used to classify biological structures based on morphology [12], a combination of the proposed deep learning and saliency maps approach can lead to more detailed insights into the contribution of individual localized biological processes on the overall adaptation "state" of the bone. Moreover, translational research using transfer learning techniques will allow transferring the here developed network to human application based on 2D or 3D data, providing the potential of real-time assessment of bone quality in a clinical setting. Here, a method for estimating bone age as a surrogate for bone quality in mice imaged with μ CT is described. The method can be rapidly translated to clinical applications by examining clinical μ CT (eg. HR-pQCT at a voxel size of 61 microns), which is increasingly used in clinical trials to investigate vBMD and microstructural changes in response to pharmacological treatments [59, 339].

In sections 5.2 and 5.3, a novel method which combined an experimental study with longitudinal imaging and a deep learning framework is presented. This allowed for a bone (tissue) age prediction and an identification of bone sites that primarily contribute to age classification. Thus, it was possible to directly track short-time aging in bone in a temporal manner. By quantitatively analyzing saliency maps of learned features, it could be shown that the metaphyseal parts closest and most distant to the growth plate are highly contributing to the temporal age information encoded in bone images during tissue maturation. It could be further shown that loading triggers dynamic processes leading to a younger appearance of the bone. More specifically these rejuvenating effects could be temporally quantified, as the bone receiving 15 days of loading treatment was classified 5 days younger than the contra-lateral internal control. It was further demonstrated that the here used loading regime induces structural correspondence between younger and older tibiae, while in fibulae, despite causing (re)modeling, no rejuvenation effect could be detected. One possible biological interpretation of these findings is that loading recovers the age-related bone loss in the tibia - therefore it rejuvenates, whereas the fibula, which is at the age investigated in the present study does not incur bone loss, and therefore is adapting to the loading in a non-physiological manner (in terms of rejuvenation-related strengthening through bone (re)modeling). These findings and the introduced method provide an ideal framework to further improve our understanding of skeletal aging in mice as well as in humans. It further demonstrates that machine-learning based charac-

terization can help to better monitor and understand dynamic changes in bones due to aging and disease and may help to optimize treatments for bone disease such as age-related bone loss and osteoporosis.

5.4 A Deep Learning Approach for Analyzing Osteogenesis Imperfecta (OI)

In this section, the idea of developing a deep learning-based model that performs an end-to-end bone quality assessment from rich-content image data is continued. As described in 5.1.4, OI is a bone disease that affects the bone micro/macro-architecture and causes higher fracture risk. The current approach for assessing bone quality, in bone altering diseases such as OI, is through determination of predefined skeletal features which may be incapable of describing the complex nature of the bone altering stimuli. For example, large heterogeneity in radial and tibial vBMD and microarchitecture measured with HR-pQCT appears to exist between adult subjects within each OI type (I, III, or IV) [128, 182]. This heterogeneity may be related to previous treatment regimes experienced by the patient, but regardless of the cause, it complicates the relationship between disease phenotype and bone fragility.

Although dual-energy X-ray absorptiometry (DXA) remains the clinical standard to assess bone quality, specifically areal bone mineral density (BMD) in the spine and hip of OI subjects, it has several disadvantages. HR-pQCT has emerged as a promising higher resolution alternative imaging modality that unlike DXA is not dependent on bone size and can distinguish between the trabecular and cortical bone compartments. HR-pQCT allows the acquisition of 3D scans of human peripheral bones (eg. radius and tibia), to assess volumetric BMD and micro-architecture. Thus, HR-pQCT imaging has the potential to improve our ability to assess bone quality, since it allows for the evaluation of skeletal features beyond BMD.

In clinical studies, OI type is determined based on phenotype analysis. However, up to now, no comprehensive analysis of OI manifestation in the bone's micro/macro architecture has been carried out. Recently, Roven et al. have performed a comparison between bone quality describing parameters (cf. chapter 2) e.g. cortical bone area, trabecular bone area, Ct.Th, CT.Pm, BV/TV, in OI patients, early-onset osteoporosis and a control group. They have shown that in some of these calculated parameters e.g. TB.N and BV/TV, there exists a significant difference between OI patients and the control groups [284]. However, as discussed in sections 5.2 and 5.3, these parameters are not completely capable of describing bone quality. Therefore, there is still much unknown about the manifestation of OI disease in bone structure. Moreover, although it is known that different types of OI have distinguishing effects on bone structure, characteristics of these effects are yet to be studied. Despite the differences in OI severity, there is considerable overlap in traditional HR-pQCT parameters between OI types. Additionally, the large heterogeneity in radial vBMD and microarchitecture measured with HR-pQCT may lead to failure in OI type identification [128, 182]. This calls for a better assessment of bone quality as "the totality of features and characteristics that influence a bone's ability to resist fracture" allowing to investigate the causes of increased skeletal fragility [38].

As explained in 5.2, ML provides the capability to analyze the manifestation of a certain

perturbation on bone captured in high resolution image data. Similar to aging and in vivo loading, manifestation of OI disease in bone can be analyzed using rich-content images and ML. As HR-pQCT images contain information about material composition, distribution and amount, they potentially contain all structural information that is needed to assess OI [244]. Despite the fact that recent studies can extract more morphometric features from HR-pQCT image data describing bone quality through assessment of vBMD and microstructure [284], information on bone quality in OI patients are only obtained through invasive histomorphometry analysis of iliac crest bone biopsies [276]. As it is shown in the course of this chapter, deep learning enables the analysis of high-throughput image data acquired in a non-invasive manner. Based on the considerable success of BAAM in the first application of resolving the complex bone aging process in a preclinical study, deep learning was chosen as the platform to create a comprehensive human bone quality resolving method. Furthermore, BAAM supplied the confidence that the DNN-based methods can provide insights into the underlying processes of bone perturbations through investigating the learning process of the models. However, extraction of tangible comprehensive structural features learned by the DNNs has proven to be challenging. Therefore, a ML model where a secondary morphometric parameter classifier provides further information into the structural features learned by the DNN is designed. Therefore, the combination of a DNN and an ensemble method-based classifier (random forest) was utilized to investigate manifestation of OI in bone using HR-pQCT images.

Here, the developed ML approach to investigate the multi-scale structural features of bone corresponding to OI disease types is presented. The bone quality assessment model (BQAM) deep neural network trained on HR-pQCT images capable of automatically detecting OI type is presented. Furthermore, by investigating the learning process of BQAM, the localization of the bone structural features corresponding to OI types as well as the effects of OI type on bone micro architecture is extracted. Additionally, by training a random forest classifier on a selected set of extracted morphometric parameters from HR-pQCT images of OI patients, the distinguishing morphometric features for detecting OI types is investigated. This novel approach of utilizing an unstructured data classifier model (random forest) to gain more knowledge about what is learned by the DNN, allows a detailed investigation of manifestation of OI in bone.

5.4.1 HR-pQCT Image Acquisition

HR-pQCT can typically acquire scans of distal radius and tibia in vivo [349]. During image acquisition, the limb of the patient is fixed in a shell to avoid motion artifacts [265]. At first, a 2D X-ray scan depicting a scout view of the bone is obtained. Afterwards, at 4% of the distal length, the reference point for scanning is placed (Fig 5.12a, b). Next, as described in 3.1.2, a 3D reconstructed volume of radius using filtered backprojection is acquired. After reconstruction, the acquired 3D image covering 10.1 mm of bone distal length (Fig 5.12c, d) has a volume of $168 \times 1536 \times 1536$ voxels with a homogeneous size of $60.7 \mu\text{m}$. Next, 168 2D slices (1 voxel thickness) in the distal direction, perpendicular to the plane created from dorsal-palmar and rustral-caudial directions, are extracted from the 3D image. Consequently, each slice is a 2D image of 1536×1536 pixels. The imaging protocol has the following setting: X-ray tube current and potential are 95 mA and 60 kVp, respectively. The image acquisition takes approximately 3 minutes. The single-scan

effective radiation dose is less than $5 \mu Sv$ [188]. Comparing this to other image acquisition techniques e.g chest X-ray (radiation dose: $20 \mu Sv$), HR-pQCT is clearly less harmful with respect to the exposed radiation dose.

After image acquisition, the scanner software is used to extract the cortical and trabecular bone compartments [192, 346]. From the extracted compartments and by using a series of image processing algorithms, the following set of parameters are determined: bone volume, bone volume density, structure model index, trabecular thickness, trabecular separation, trabecular number and connectivity density, and cortical thickness. Moreover, for all the scans, the segmented trabecular compartment and the cortical masks of the bones were directly calculated by the scanner software.

HR-pQCT images of radii of adult OI patients, were acquired under the supervision of Prof. Bettina Willie at Shriners Hospital for Children - Canada, Department of Pediatric Surgery, McGill University in a study funded by Mereo BioPharma Group PLC.

Image Preprocessing

All the 3D images (size: $168 \times 1536 \times 1536$) were cropped to contain only the radius bone. The differences in bone size in patients resulted in heterogeneity in image sizes. Only scans with motion artifact level ≤ 3 were used [261]. Due to differences in age and severity of manifestation of OI in bone structure, great variations were observed in the distal length of the bones. Therefore, to analyze the bone structure at roughly the same location in different patients, the middle slice (reference line) ± 5 slices above and beyond the middle slice were chosen from each patient. This resulted for each patient in 11 2D slices covering $667 \mu m$ of the bone distal length. Therefore, the structural changes occurring in bone in the distal direction is also captured in the dataset.

Due to high heterogeneity in OI bone structure, the cropped slices had different sizes. To homogenize the size of the 2D slices, first, the maximum size of a slice (number of pixels) in dorsal-palmar and rustral-caudial directions of all the cropped slices were determined. Afterwards, all images were padded with stripes of "0" values such that all images had the same size. The resulting 2D slice had a size of 597×476 pixels (Fig. 5.13).

Data Assignment

Two different datasets including images of radius were used in this study. First dataset (dset1), which was utilized in the deep learning-based analysis, consists of HR-pQCT scans from 40 adult patients (male and female, ages between 25 and 75) of OI type I ($n = 26$), III ($n = 3$) and IV ($n = 11$) acquired using the Xtreme CT II. The second dataset (dset2), consists morphometric parameters of 96 adult patients (male and female, age between 25 and 75 years) of OI type I ($n = 56$), III ($n = 14$) and IV ($n = 24$) from first and second scanner generations (XCT I and XCT II). The second dataset (dset2) was used to train the random forest model. Images of dset1 were included in dset2. Patients from dset1 and dset2 were randomly divided into a training set (dset1: 80% of patients = 32 patients, divided into 352 2D slices; dset2: 83% of patients = 80 patients) and a test set (dset1: 20% of patients = 8 patients, 88 2D slices; dset2: 17% of patients = 16 patients).

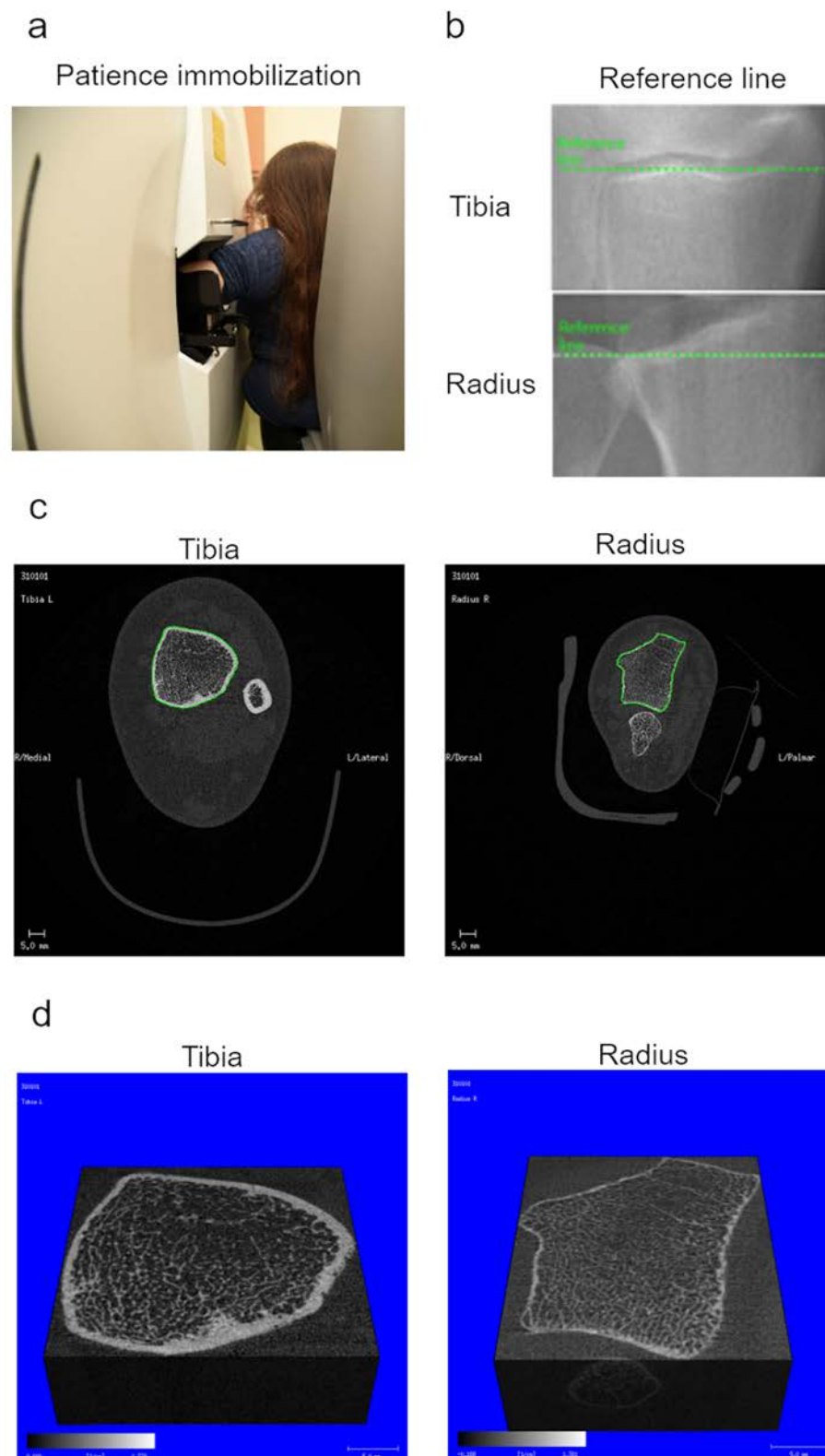


Figure 5.12: HR-pQCT image acquisition. a) Patient immobilization and placement in the scanner. b) Determining the reference line for the tibia (top) and radius (bottom) to begin the scanning process. c) A sample slice of the 3D scan of tibia (left) and radius (right) including bone, tissue and fixing equipment. d) A 3D cropped sample of tibia (left) and radius (right) including only the bone (aim image).

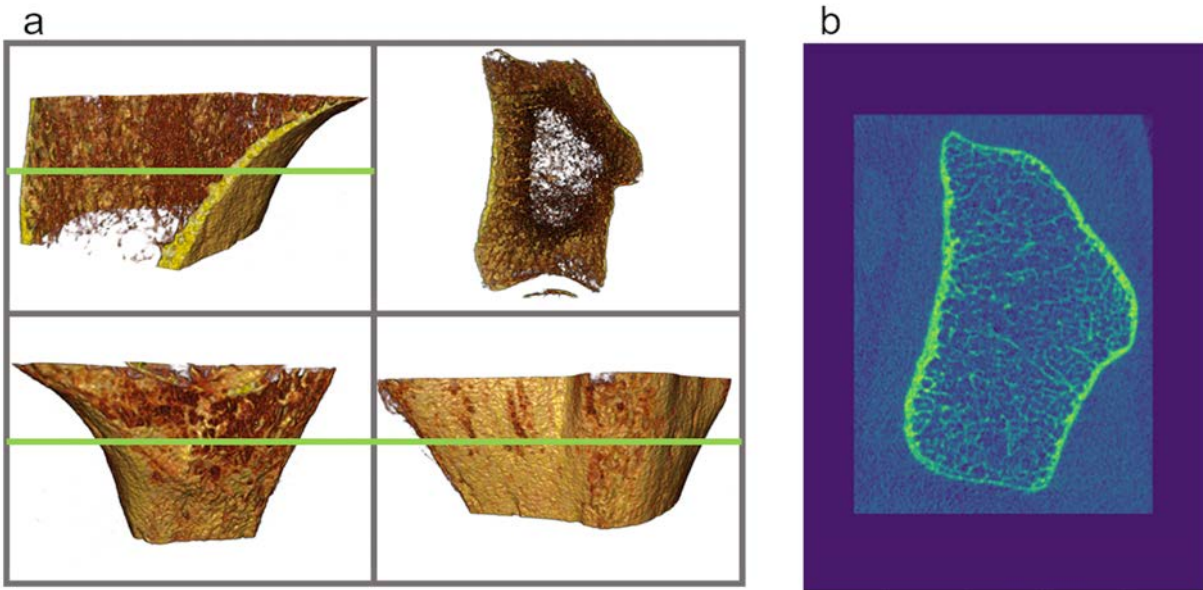


Figure 5.13: *Image preprocessing. a) 4 views of a sample OI type I 3D scan. The green line shows the reference line where the middle scan is placed at. b) The sample middle slice padded to reach the maximum size observed in the dataset.*

Data Augmentation

DNNs require large datasets for training to achieve stable convergence and high classification accuracy. Therefore, a data augmentation step was performed, in which the size of the training set is synthetically increased by performing geometric transformations. As suggested by Krizhevsky et al. [187] and Simard et al. [307], images of the training set are augmented by applying rotations (-30° to $+30^\circ$; 10° steps using nearest neighbour interpolation), translations (-10% to $+10\%$; 5% steps in both directions) and horizontal flipping. Maximum augmentation values were chosen to cover potential occurring deviations between images such as asymmetry of the left and right hand or location of the bone in the images due to the imaging setup. Augmentation techniques such as applying noise/filter and elastic deformations were avoided since that could potentially affect OI related bone features. This results in a total of 24640 images in dset1 training set. No augmentation was performed on dset2 since the random forest algorithm is not prone to overfitting.

5.4.2 Deep Bone Quality Assessment Model (BQAM)

To create an end-to-end bone quality assessment model (BQAM) for classifying OI types, a DNN was designed and trained on 2D slices from the rich-content 3D HR-pQCT images. To do so, the BAAM network (cf. 5.2) was modified to analyze HR-pQCT images of adult OI patients. Moving from a DNN that was designed to analyze genetically inbred mice bones to a DNN that investigates human bone data introduced multi-facade challenges. On one hand, the network should become more complex in terms of bigger convolutional layers as well as its depth to account for variations between the images of genetically diverse human bones. On the other hand, special care should be devoted to prevention

of overfitting potentially occurring by utilizing a complex DNN. A customized DNN consisting of 15 layers with eight convolutional, three pooling, two fully connected layers and two dropout layers was designed (Fig. 5.14). The output layer consists of three classes: OI type I, III and IV.

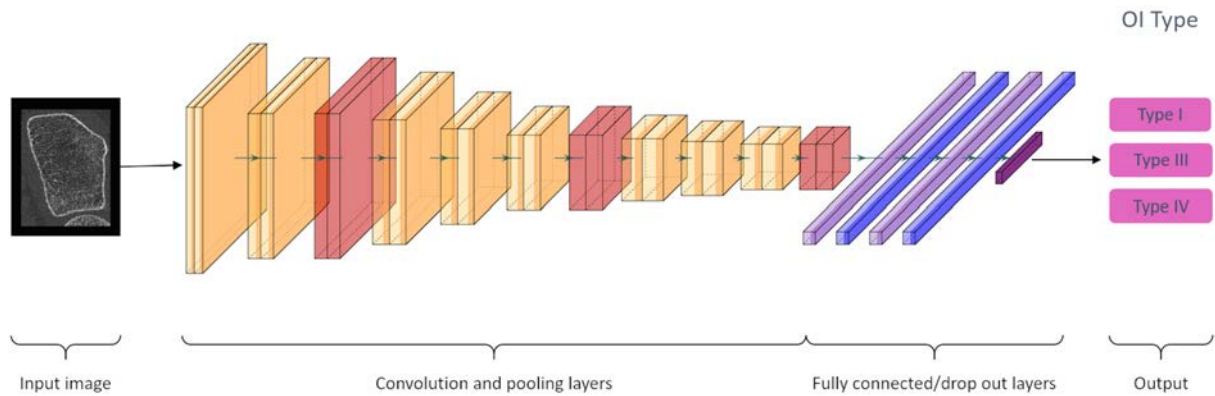


Figure 5.14: BQAM network for classifying OI type.

BQAM Network Architecture

BQAM processes input images through convolutional layers where sets of kernels are applied/trained by moving across the 2D slice. By passing an image through the convolutional layers, feature-maps of the image are determined at which the position of the encrypted patterns related to each OI type are accentuated. This leads to extraction of hidden features of the bone structure corresponding to OI types. The deeper the image goes through the network, the more complicated bone structural patterns are recognized by the network. At each convolutional layer, the feature map extraction was performed by activating the neurons with the rectified linear function and adding a set of bias terms. These weights and bias values are optimized at each training iteration to provide a higher accuracy in OI type assessment. The fully connected layers are where the neurons of each layer are linked to all neurons in the prior layer allowing to relate the features through the scales of bone structure to perform the bone quality assessment task. At each dropout layer, with a possibility of 50%, half of the neurons of the network are neglected to make a decision. Dropout layers are helpful to decrease the possibility of overfitting. Hence, the network will be able to detect OI in bones with large variations due to differences in age and gender of the patients. As mentioned before, for a more thorough introduction to deep learning, the reader is referred to Goodfellow et al. [117] and LeCun et al. [198]. Feature-maps are down-sampled after the 2nd, 5th and 8th convolutional layers with a window size and stride equal to 2. The kernels in all convolutional layers are 3 * 3 with a stride of 1. In the consecutive convolutional layers, 4, 8, 8, 16, 16, 32, 32 and 64 feature maps are computed, respectively. The activation of the last convolutional layer was flattened into a vector and passed to the fully connected layers with 128, 128 and 3 features from which the last one represents the 3 OI classes. At last, a softmax function is applied on the last flattened dropout layer to calculate the probability distribution for each OI class. By training BQAM on selected 2D slices, a fraction of the 3D information from HR-pQCT images might be neglected. However, a similar 3D deep neural network

trained on the 3D HR-pQCT image would require exceedingly higher GPU memory and computation power making the training process currently almost impossible for desktop computers. Future studies might investigate possible 3D extensions of the network.

Training Algorithm

BQAM is trained with the Adam optimization algorithm [179]. The network is initialized with a truncated normal distribution function (standard deviation: 0.1). Training is carried out for 2000 iterations with a batch size of 50 images from training set. At every 50th step, the model is applied on a batch of all images of the test set to check for overfitting. The initial learning rate is set to 0.1, then an exponential decay at every 25th step with a 0.96 rate is performed. Implementation, training, validation and testing of the network was performed using Google TensorFlow 1.7 [1] on a GPU cluster with two Nvidia Pascal P100 GPUs.

Analysis of Key Regions and Features for OI Manifestation

The trained BQAM network (after last training and validation step) is applied to the all 440 slices of 40 patients and further evaluated to identify key regions and features describing manifestation of OI within the radius bone. To determine the regions in the images that the network focuses on to predict OI type, saliency maps are calculated by determination of vanilla back propagated gradients [87, 308] for images passing through the network. The loss gradient is additionally backpropagated to the input data layer. By taking the L1-norm of the loss gradient of the input layer, a heat map demonstrating the localization of pixel importance is calculated. Moreover, to further resolve the specific structural features of the bone that the network focuses on, the vanilla backpropogated maps are put through a smoothing process [310]. To do so, each image is randomly noised multiple times and the average saliency map of the noised up images as the smoothed gradient (smoothed saliency map) is calculated. In these maps, pixel intensity denotes the importance of this specific pixel for the given task (OI prediction). To define a localized quantitative importance factor for the OI detection process process, first, masks for the trabecular, cortical and the tissue present in each slice are extracted (Fig 5.15). The attention is defined as $\sum_{i=1}^n p_i^r / \sum_{i=1}^m p_i^{all}$, where (p_i^r, n) and (p_i^{all}, m) are the pixel values of the normalized saliency map and the number of pixels in each subregion and the whole radius bone respectively ($Attention \in [0 - 1]$). Therefore, attention value represents the normalized importance of the defined subregions in trabecular compartment, cortical compartment and the tissue (lack of bone) for the OI classification task.

OI Effects on Bone Micro-architecture

To further investigate the localized manifestation of different OI types in bone micro-architecture, the correspondence of the saliency maps with thickness of the bone structure is investigated. To do so, first, a distance map for three different labels of the bone naming cortical and trabecular bone as well as the tissue labels are determined. A distance map intuitively shows the thickness of the structure at any point of it. Each pixel value of the distance map is the number of pixels to the closest zero pixel (background). The distance maps are calculated using a L2 norm by a moving 5×5 window going across the image.

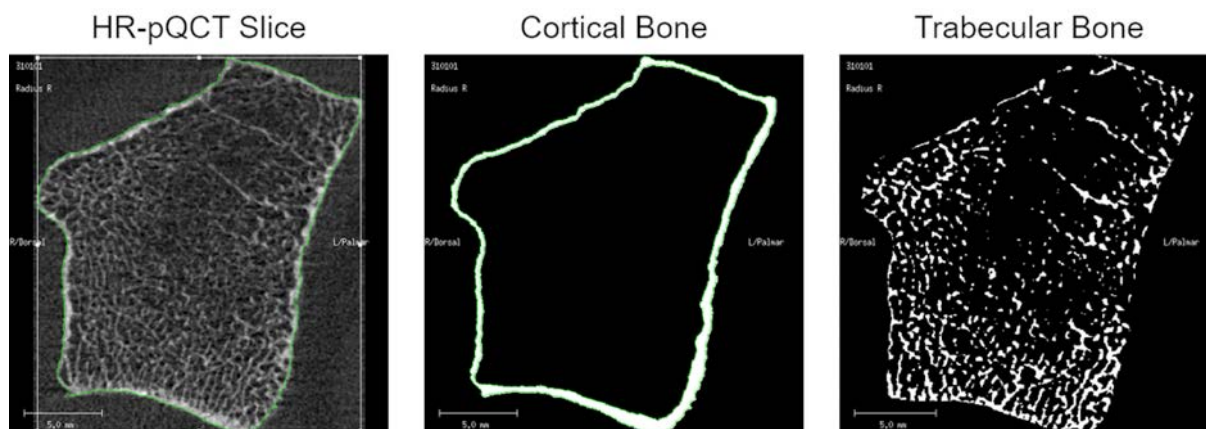


Figure 5.15: *Hr-pQCT slice and the two extracted masks for cortical and trabecular bone compartments.*

Afterwards, the normalized saliency map is multiplied by the distance map pixel-wise. Next, the summation of the pixel values in the resulted image is considered the "thickness attention", Th_{att} for each of the compartments in the bone. The higher the Th_{att} , the higher value for importance of localized thickness in distinguishing between OI types in that bone compartment.

The Th_{att} for the three bone compartments of all the images of 40 patients are calculated.

5.4.3 A Random Forest Model for Morphometric Parameters Analysis

In order to extract the structural parameters of importance corresponding to the localized structural features learned by BQAM, a random forest model is trained on selected morphological features. The morphological features were selected based on the bone parameters commonly used to investigate OI [244, 245, 284]. The features are calculated from HR-pQCT scans and are shown in Table 5.5.

The random forest model is trained to perform the classification task based on the calculated features. The designed model is built as described in 4.3.4 with the three possible output classes: OI type I, III and IV.

5.4.4 Results: BQAM Analysis of OI

BQAM Performance in OI Classification

A qualitative analysis of scans of different OI types shows that despite differences in bone macro/micro-architecture, it is challenging to distinguish them with the naked eye (Fig 5.16).

BQAM performs this end-to-end classification to almost perfect results. First, the performance of the BQAM network is evaluated. The trained network reaches 99% accuracy (loss: 0.03) in predicting OI type in the training and validation datasets (Fig. 5.17a, b). The confusion matrix of BQAM OI prediction performance (Fig. 5.17c, d) shows that

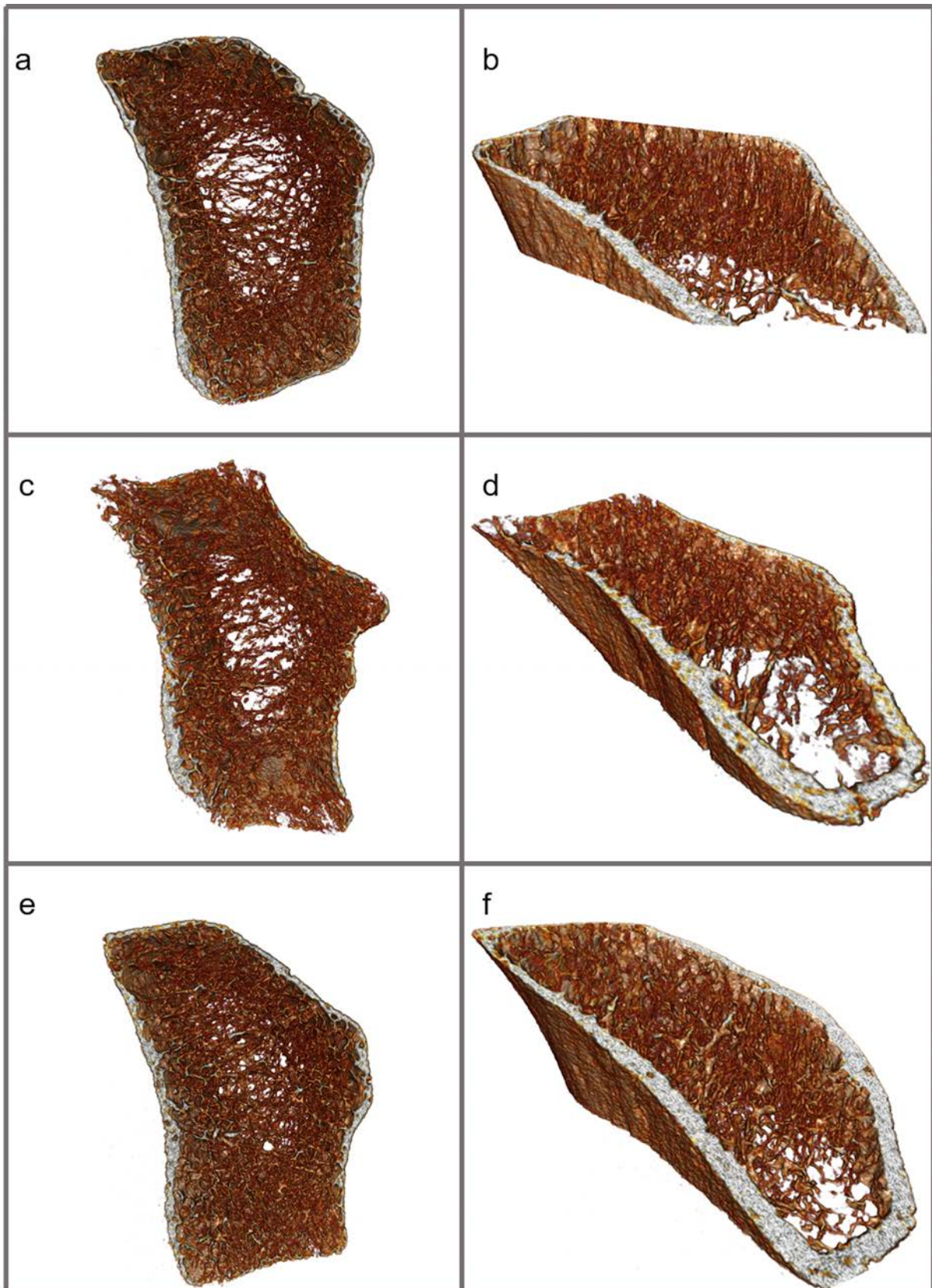


Figure 5.16: Sample scans of radius in three OI types. a, c, e) dorsal-palmar/rustral-caudial view of a sample radius of OI type I, III and IV respectively. b, d, f) A cross sectional cut of a sample radius of OI type I, III and IV consecutively.

Variable	Dimension	Description
Tb.vBMD	$mgHA/ccm$	Trabecular volumetric bone mineral density
Tt.vBMD	$mgHA/ccm$	Total volumetric bone mineral density
BV/TV	mm^3/mm^3	Bone volume fraction
Met/Inn	-	Peripheral to medullary trabecular bone density ratios
TTb.Th	mm	Trabecular thickness
Tb.Sp	mm	Trabecular separation
Tb.N	$1/mm$	Trabecular number
Tb.1/N.SD	mm	Inhomogeneity of trabecular network
Tt.Ar	mm^2	Total area
Tb.Ar	mm^2	Trabecular area
Ct.vBMD	$mgHA/ccm$	Cortical volumetric bone mineral density
Ct.Th	mm	Cortical thickness
Ct.Ar	mm^2	Cortical area

Table 5.5: Features determined by HR-pQCT analysis describing bone quality.

apart from a small error in predicting OI type IV (4 out of 55 wrongly predicted) all the other images were predicted correctly. With these accuracy values, the network is considered to be performing sufficient for OI detection.

Decoding Localized Manifestation of OI

Analyzing the OI-detection results in detail shows structural similarities and subtle difference in micro-architecture of bones in different OI types. Qualitative analysis revealed subtle structural differences in both tubercular and cortical compartments (Fig. 5.18a-c). Overlaying classified images with their specific saliency maps shows a significantly changing distribution of attention in different OI types.

A quantitative analysis revealed, that the different regions of the bones received different amounts of attention, therefore contributing differently to the OI detection (ANOVA: $p < 0.01$; Fig. 5.18d). Localized Attention values for all OI types together shows that OI manifestation is at its highest in soft tissue compartments (0.44 ± 0.12). Afterwards, the trabecular (0.30 ± 0.10) and at last the cortical (0.25 ± 0.10) compartments are in the focus of BQAM. In images of OI type I, III and IV, differences in attention order for the three compartments were observed (type I: Ct: $0.21 \pm 0.08 \rightarrow$ Tb: $0.31 \pm 0.09 \rightarrow$ Tiss: 0.48 ± 0.11 , type III: Tiss: $0.31 \pm 0.06 \rightarrow$ Tb: $0.32 \pm 0.10 \rightarrow$ Ct: 0.37 ± 0.08 and type IV: Ct: $0.31 \pm 0.07 \rightarrow$ Tb: $0.29 \pm 0.08 \rightarrow$ Tiss: 0.40 ± 0.11 ; Fig. 5.18e).

OI Effects on Bone Micro-architecture

The visual analysis of the Th_{att} maps and the distance maps shed light on the manifestation of OI in the micro-architecture of the bone (Fig 5.19a-c). Th_{att} amongst the compartments had the lowest value (Overall Th_{att} : Ct: $9 \pm 4.5 e3$, Tb: $16.2 \pm 7.6 e3$ and

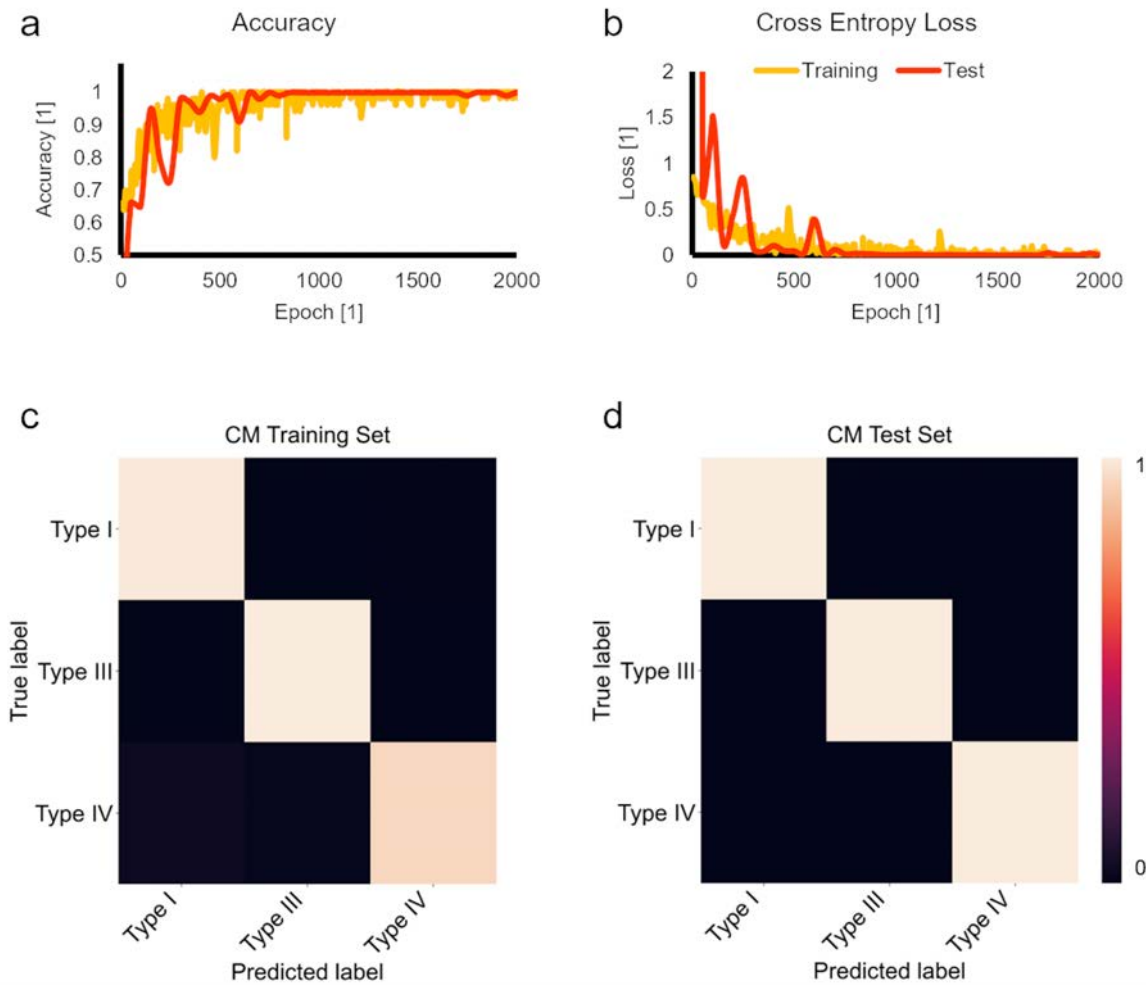


Figure 5.17: OI classification performance. a, b) Accuracy and loss values of OI type prediction on training set (orange line) and test set (red line) vs. training step. Accuracy and loss of OI type prediction on the test set is calculated at every 50th training step. c) Confusion matrix of BQAM determined for 200 images of training set. d) Confusion matrix of BQAM determined for all images (88 slices) of test set. Predicted OI type of patients are compared to their actual OI type. Values are normalized by the number of images per OI class.

Tiss: $25.4 \pm 12.7 \text{ e}3$, $p \leq 0.01$; Fig 5.19d). Moreover, the distribution of Th_{att} is different in the three OI types (type I: Ct: $9.4 \pm 4.7 \text{ e}3$, Tb: $14.9 \pm 7.1 \text{ e}3$ and Tiss: $27.6 \pm 11.6 \text{ e}3$, type III: Ct: $6.8 \pm 2.5 \text{ e}3$, Tb: $18.3 \pm 6.2 \text{ e}3$ and Tiss: $11.7 \pm 4.3 \text{ e}3$ and type IV: Ct: $8.6 \pm 4.2 \text{ e}3$, Tb: $18.7 \pm 8.3 \text{ e}3$ and Tiss: $23.9 \pm 14.3 \text{ e}3$, $p \leq 0.01$; Fig 5.19e). However, the order of Th_{att} values in different compartments are identical in OI type I and IV (Tiss>Tb>Ct).

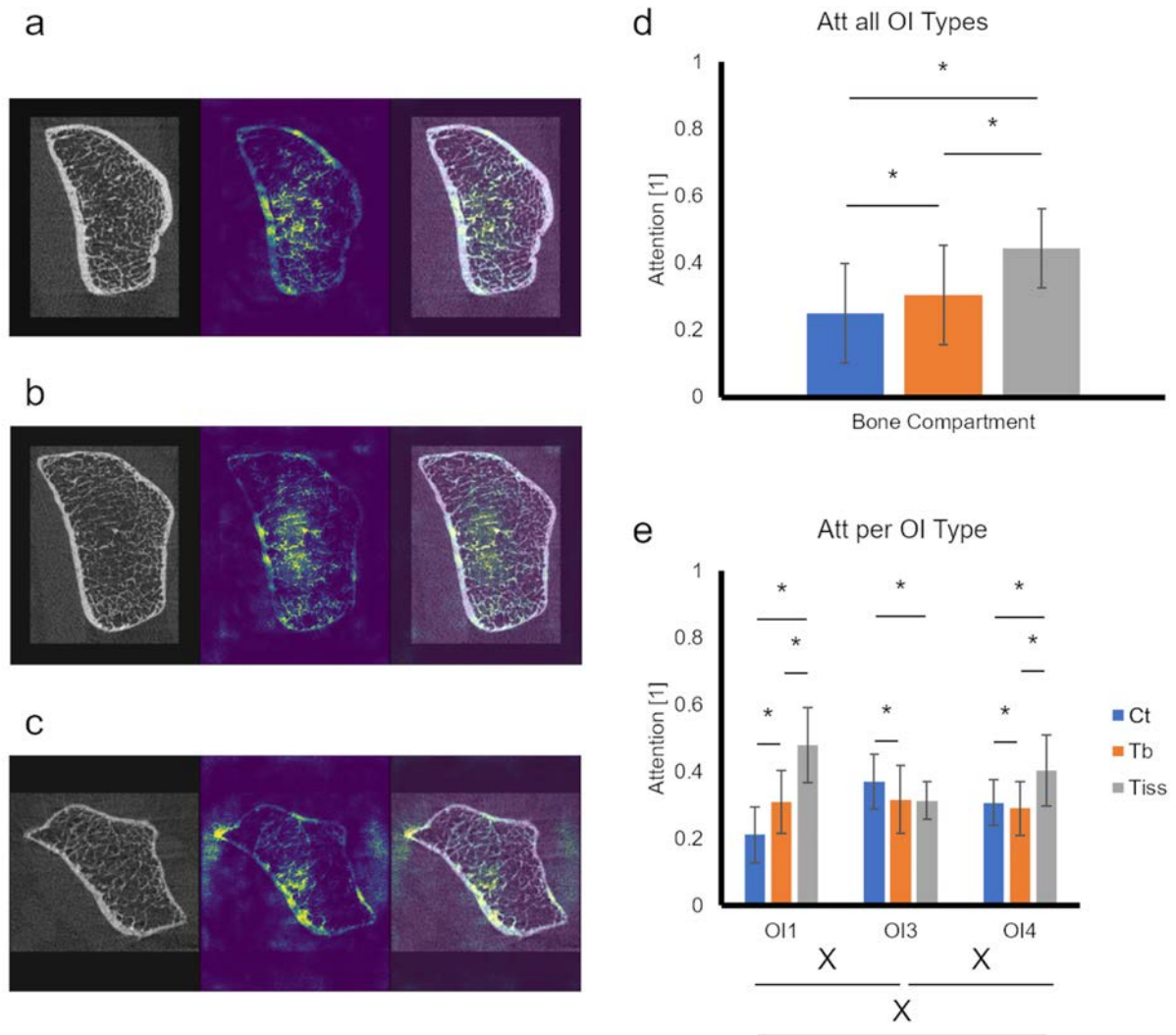


Figure 5.18: Localized Manifestation of OI. a-c) Sample slices from the HR-pQCT scan (gray scale, left), the saliency map of the scan (middle) and the overlap of saliency map and the scan (right) for OI type I, III and IV respectively. Saliency map are color as blue (low) to yellow (high) attention values. d) Attention devoted by network to the three regions for OI detection in all subjects for cortical bone compartment (Ct), trabecular bone compartment (Tb) and the soft tissue in trabecular bone compartment (Tiss). Localized Attention values for all OI types together. e) Attention values in different OI types. Data shown as mean \pm standard deviation. * indicates a significant difference in attention of different bone regions ($p < 0.05$). \times shows a significant difference between OI types ($p < 0.05$).

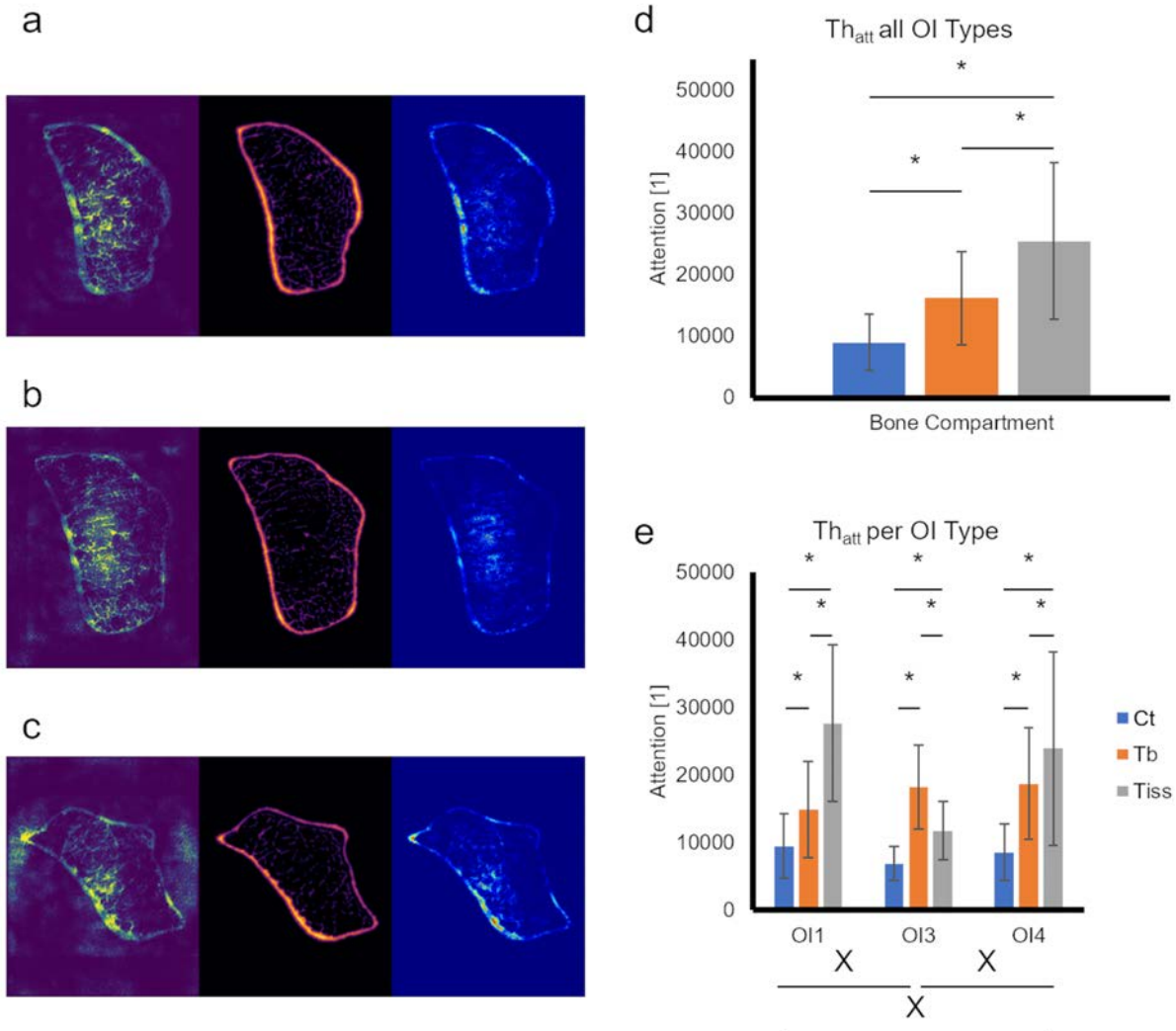


Figure 5.19: OI manifestation in bone micro-architecture. a-c) Sample saliency maps of the of a slice (left), the distance map of the bone (middle) and the multiplication of saliency and distance maps (right) for OI type I, III and IV respectively. Saliency map are color as blue (low) to yellow (high) attention values. Distance maps are color coded from black (low) to red (high) thickness values. d) Th_{att} determined for the three regions for OI detection in all subjects for cortical bone compartment (Ct), trabecular bone compartment (Tb) and the tissue in trabecular bone compartment (Tiss). e) Th_{att} determined in different OI types. Data shown as mean \pm standard deviation. * indicates a significant difference in Th_{att} of different bone regions ($p < 0.05$). \times shows a significant difference between OI types ($p < 0.05$).

5.4.5 Results: OI-corresponding Structural Features

Random Forest Model Performance

Based on the 13 selected morphological features, the random forest trained model predicted 15 out of 16 correctly. The lowest precision of OI types was seen in OI type IV (75%) and the lowest F1 score was seen in OI type III (0.8). The complete metrics of the random forest model OI classification can be seen in Table 5.6.

OI type	Precision	F1-score	Support
IV	0.75	0.86	4
III	1	0.80	3
I	1	1	9

Table 5.6: Random forest model metrics in OI determination.

Analyzing the importance of each of the bone parameters in the classification models reveals the features contributing most and least to the OI detection model. The four most important structural features are the trabecular number (TB.N: 14%), cortical thickness (Ct.Th: 12%), inhomogeneity of trabecular network (Tb.1/N.SD: 10%) and trabecular separation (Tb.Sp: 10%). These have in total 45% of the overall importance in the classification models (Fig. 5.20).

5.4.6 Discussion

Here, a ML-based approach to investigate OI is presented. OI, affects the structure of bones by influencing bone turn over as well as material characteristics of the bone [227]. OI is commonly detected in phenotype analysis [344]. Genotyping has led to detection of up to 18 different types of OI in patients. Similar to other bone structure affecting diseases, e.g., osteoporosis, the onset of OI has been investigated by analyzing morphometric measures and progression such as volumetric bone mineral density (vBMD), trabecular thickness (Tb.Th), cortical thickness (Ct.Th) etc. [284]. However, no study could be found that focused on differences between the impacts of OI types on bone micro/macro structure. Moreover, as we have shown before, the usual analysis of bone structure changing based on morphometric parameters is not sufficient to describe the multi-scale aftermath of bone structure altering diseases [14]. Therefore, in regard to OI disease, two main questions remain unanswered: 1) How does different OI types affect the bone micro/macro structure? and 2) Which bone quality parameters represent the manifestation of OI in bone? To answer these question, two ML-based models based on HR-pQCT scans are developed: 1) A DNN that, for the first time, performs an end-to-end classification of OI types from scans of the radius. 2) A random forest model that predicts OI type based on morphometric features. The designed DNN and random forest models reached 99% and 94% accuracy on the test data, respectively. Although, the deep learning approach achieves higher accuracy, it requires much more computation power. Moreover, by utilizing the designed random forest model and determination of the important morphometric parameters for the OI classification task, the learned features of BQAM are brought into light.

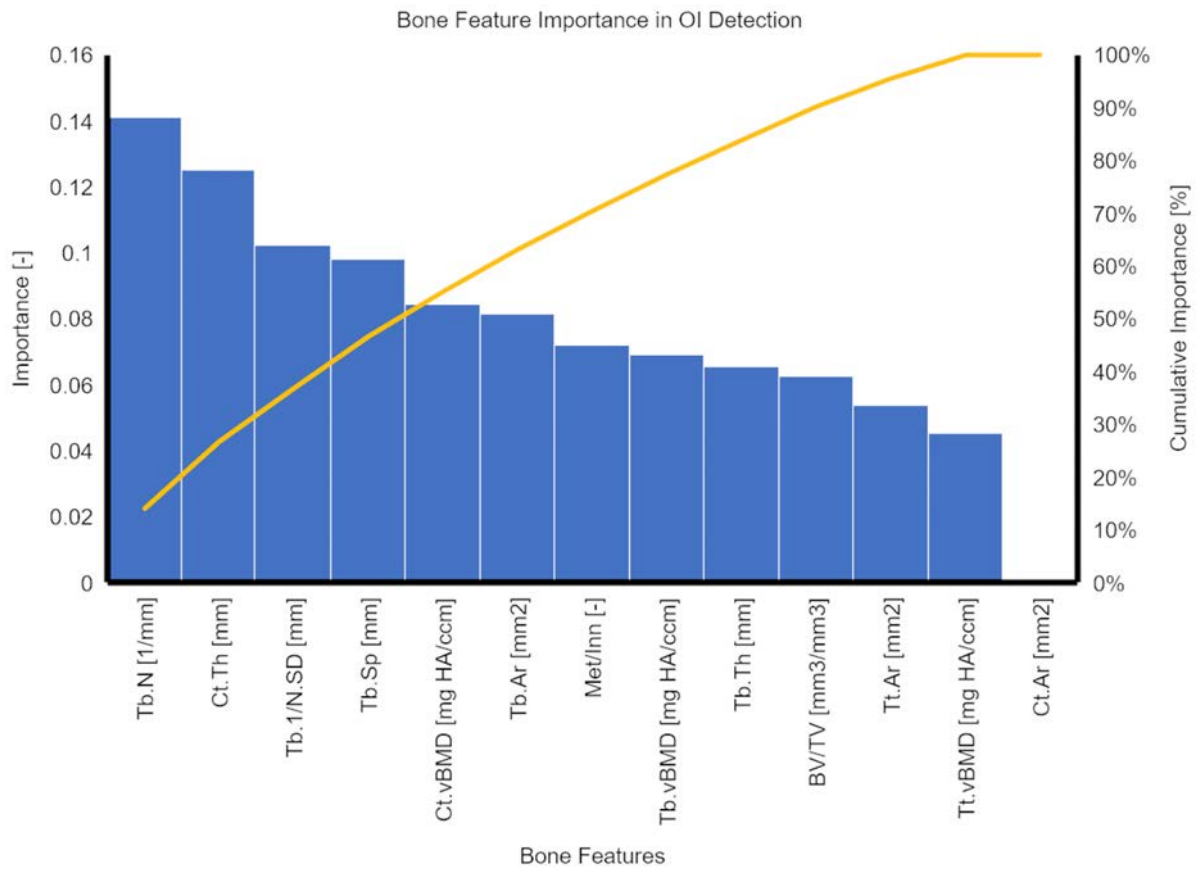


Figure 5.20: Mean classification importance for the bone features in OI detection.

The developed end-to-end OI detection DNN reached 99% accuracy on the test dataset. This is the first time that a completely automatic OI detection model with the presented accuracy was created. Moreover, the variation of age and gender in our training and test dataset confirms that our model is primarily detecting OI-related bone features, rather than aging or gender dependent features.

The attention values devoted to the overall dataset containing all three OI types clearly shows that manifestation of OI is at highest in the soft tissue in between the trabeculae ($p \leq 0.01$). Trabecular bone has the second highest importance ($p \leq 0.01$) and at last the cortical bone compartment is important for OI detection ($p \leq 0.01$). The attention values here could be considered as the inverse measurement for similarities between OI types. Therefore, the cortical compartment of bone showed the least differences between different OI types while the trabecular bone is more distinct. This is further confirmed by the random forest model for OI classification since three out of the four most important bone features for the classification model belong to the trabecular bone compartment (TB.N (14%), Tb.1/N.SD (10%) and Tb.Sp (10%)).

The detailed analysis of attention values per OI type shed light on the interplay of features from different bone compartments in OI classification. In OI type I, the attention ranking is: cortical bone \rightarrow trabecular bone \rightarrow soft tissue ($p \leq 0.01$ for all three comparisons). However this order in OI type III reads as: soft tissue and trabecular bone \rightarrow cortical bone ($p \leq 0.01$) and for type IV as: trabecular bone \rightarrow cortical bone \rightarrow soft

tissue. This shows that the order of importance is different in OI types. In OI type I, the soft tissue is the most distinguishing character ($p \leq 0.01$); whereas, in type III, the features of the cortical bone was the distinctive characteristic ($p \leq 0.01$). In OI type IV, similar to type I, the soft tissue in trabecular compartment is the most important feature ($p \leq 0.01$); however, the cortical compartment was in the second place with respect to its importance ($p \leq 0.01$) and the difference between the soft tissue and cortical importance is less than what is seen in OI type I ($p \leq 0.01$). One potential interpretation of the local comparison of the attention values between OI types is that the manifestation of OI disease in type I is mostly prominent in lack of trabecular bone structure; whereas, in type III, the disease is more conspicuously present in the cortical structure of the bone. In OI type IV however, although the disease affects the soft tissue in trabecular compartment the most, it resides in the cortical bone more than the trabecular bone.

The micro-architectural manifestation of OI were investigated by linking the correspondence of the saliency maps to the thickness of bone structure across the bone compartments. The manifestation of OI is certainly more complicated than just the network focusing on thicker parts of the bone (Fig 5.19). The low Th_{att} value for the cortical compartment in all three OI types points towards similarities in cortical thickness across different types. In contrast the high Th_{att} in type I and IV shows the space between trabeculae is very important for detecting the OI types. Additionally, OI type III is mostly distinguished by focusing on the space between trabeculae and the thickness of trabecular bone. This showed that within the trabecular bone compartment (consisting of the trabeculae and soft tissue), despite high importance of the trabecular thickness, no obvious lack of micro-architecture is present because of OI disease.

The developed model here has some limitations. The designed models are trained and validated on images of the radius. Therefore, it is yet to be confirmed that the results shown here are valid for other bones such as the tibia with a more prominent load bearing functionality. Moreover, the number of images/patients in the datasets potentially affects the DNN models. Although, a thorough validation step is performed; images from more patients could potentially increase the robustness of our model. Additionally, by training on 2D slices, the information stored in the distal direction might be neglected. For the case of radius, this might not seriously affect our model because of lack of load bearing functionality in its distal direction. However, when transferring the results to other bones, one should consider applying 3D CNNs. Although, that would considerably increase the computational costs. At last, our study did not have a control group to analyze the onset of OI disease. Therefore, the results presented here are focused on manifestation of different OI types in bone rather than an absolute phenotype analysis.

The developed OI classification model can be directly improved by introducing a control healthy group to the training set. That can potentially lead to understand the effects of OI on the bone from a pure bone structural point of view. Moreover, future studies can further train our model on other bone structure-affecting diseases such as osteoporosis to obtain a more general bone quality assessment model. Additionally, further development of the designed DNN from 2D to 3D could be beneficial in using the wholesome of 3D HR-pQCT scans without any loss of information. However, further homogenizing preprocessing steps would be required to eradicate the variation in distal direction, which might affect the integrity of the bone macro/micro-architecture.

5.5 Summary

Here, a ML-based methodology developed to investigate structural changes in bone due to perturbations naming maturation, loading treatment and OI disease is presented. To do so, ML models for assessing the state of the bone are designed. In 5.2, in a preclinical study, the morphometric and densitometric changes that bone undergoes during aging are investigated. This is done by creating a DNN that is capable of an end-to-end short-term bone age assessment. The accuracy of aging assessment DNN was 96%. The robustness of the model is further validated in a three-fold manner. This novel age assessment DNN is utilized in 5.3 to investigate the potential rejuvenation effects of in vivo loading on bones showing that 15 days loading results in 5 days rejuvenated bone appearance in average. In 5.4, the DNN is further developed to detect the state of the bone in different types of osteogenesis imperfecta disease with 99% accuracy. Moreover, by analyzing the learning process of the networks through saliency maps and designed attention values, localized manifestation of bone state into the bone structure is investigated showing that the trabecular bone is more distinguishable between different OI types than the cortical compartment.

6 Conclusion

In this work, a data-driven approach to study the relationship between structure and function in biological networks using machine learning and continuum mechanics was designed, applied and validated. Here, the potentials of analyzing functionality and dysfunctionality of biological networks through studying their structure is shown and investigated. In the last chapter of this thesis, a summary of what was presented in previous chapters is provided and the potentials of further developments is discussed.

6.1 Summary and Main Contribution

This thesis focused on developing data-driven methods for analysis of structure-function relationship in biological networks. For this purpose, models in two different scales are designed allowing: analyzing protein networks and their mechanical functionality on the nano scale and analyzing bone structure and its load bearing functionality under the structural modifying elements such as aging, treatment and diseases.

Protein networks have been thoroughly studied from biochemical point of view. Recent studies have focused on the structural effects of stimuli such as diseases on the cytoskeletal protein networks. However, there existed a lack of a quantitative framework to describe the geometrical state of the networks. Therefore, for the first time, a quantitative imaging method that extracts a set of morphological and structural features from 3D microscopy image data was developed to quantitatively describe the state of protein network structure. The developed method allows an automatic transformation of a 3D light microscopy image of a protein network into a mathematical representative enabling a quantitative analysis of the effects of external stimuli on the structure of the network.

As a first application, this method is utilized to investigate the assembly of FtsZ protein networks *Physcomitrella paten* chloroplast. FtsZ shares structural and biochemical characteristics with cytoskeletal protein networks and its relative simplicity enabled a thoroughly performed validation of the robustness of the method. Furthermore, with the help of the developed model, the similarities as well as distinguishing characteristics of two FtsZ isoforms i.e. FtsZ1-2 and FtsZ2-1 are investigated. This allowed investigating the two FtsZ isoforms with different evolutionary backgrounds, which for the first time, shed light on the way each of the isoforms contribute to the integrity of the chloroplast. Moreover, by training a designed ML model on the outcome of the image processing framework, a tool capable of performing a protein classification with high accuracy (6 out of 7 correct predictions) is created by training on a considerably small dataset (37 images). Considering the amount of required data for the existing DNN- and SVM-based models for reaching high accuracy in protein network classification and the noticeable costs of data creation by means of confocal microscopy, the developed ML classification method advanced the field of protein classification by providing a computationally and experimentally beneficial tool. Moreover, the modest computational costs of the method

and its ease of use enables researchers to perform a protein classification task directly in the lab without access to a high-performance computing facilities. The drawback of the developed methodology is its reliance on the image resolution. This limits applying the model to images with lower resolution than CLSM resolution. However, the method could potentially be utilized on higher resolution images such as STED providing more accurate results.

In the next step, a μ FE continuum-mechanical simulation setup was developed aiming to investigate the mechanical characteristics of a protein network. To the author's best knowledge, this is the first time that a continuum-mechanical model of protein networks with realistic geometries were created which is capable of simulating a real experimental setup (compressing the chloroplast). This simulation setup allowed to investigate two debated concepts regarding the FtsZ of chloroplasts. First, the load bearing functionality of FtsZ was investigated. From the results of this investigation the idea of plastoskeleton of plastids became more evident. Second, the previously observed adaptive stability of the FtsZ protein network was depicted in a quantitative manner showing that the FtsZ protein network evolved to withstand bucking failure. Additionally, generating multiple μ FE models from each network allowed to perform a series of in silico experiments enabling to create a dataset consisting of simulation results. This is specifically valuable when performing in vitro experiments on protein networks are considerably costly.

At last, by having the two datasets of structural features (results of the image processing method) and mechanical characteristics (results of the μ FE simulations) of protein networks at hand, a ML model was created to map the structure to its mechanical functionality. The designed random forest regression models reached high accuracy in predicting the mechanical responds of the protein network ($R^2 \geq 0.97$). This provided an online mechanical behaviour prediction tool, and more importantly, the ability to extract specific structural features correlating to the investigated mechanical characteristics. This approach shed light on how the specific evolutionary design of FtsZ filaments (their curvature and connections) led to the aforementioned adaptive stability of the network. Therefore, the designed ML-based analysis of protein network structure from 3D microscopy images shed light on the mechanical functionality of the FtsZ protein network through the data-driven analysis of its structure.

In comparison to the nano structures of proteins, the bone tissue has been more thoroughly analyzed due to a longer history of imaging. This analysis has been mostly performed using a set of predefined bone structure parameters (cf. 3.1.2). Investigating functionality/dysfunctionality e.g. aging and fracture risk of bone tissue through studying these parameters has shown meaningful success. However, in this approach, the multi-scale nature of bone tissue and the interplay of different structural features in the structure-function relationship are neglected. Moreover, structural alteration due to aging, treatment or diseases such as OI might not be manifested in these predefined parameters, hence the possibility of bias in this approach. These shortcomings are potentially overcome in the data-driven ML-based approach of studying structure-function relationship presented in this thesis. This is due to the fact that the designed DNNs consume all the encoded information in images containing the multi scale structure of the bone tissue without neglecting any relevant information. Moreover, the presence of multiple consecutive convolutional layers allows correlating pixel-level to region-level features, hence the multi-scale essence of the bone structure is analyzed. Furthermore, automatic-

ally extracting structural features corresponding to the investigated bone altering stimuli provides an unbiased analysis of structural characteristics of bone being affected by the aforementioned perturbations.

The developed DNN (BAAM) is presented as an end-to-end tool for short-term aging prediction task using μ CT images. BAAM reached 95% accuracy in predicting skeletal aging in tibia and fibula of mice in a preclinical study. The thoroughly performed validation of BAAM showed its capability in learning the aging-induced structural alterations in bone. Furthermore, by investigating what was learned by BAAM by means of saliency maps and attention values, for the first time, the localized manifestation of aging information in bone was decoded .

As the second bone tissue altering perturbation, in-vivo loading as a bone treatment process was investigated. By applying the age predicting trained BAAM on images of in-vivo loaded tibiae and fibulae, it was shown that 15 days of loading results in an average 5 days rejuvenation effect in adult female mice. To the author's knowledge, this is the first time that such clear rejuvenation effect of cyclic loading treatment in bone tissue has been depicted. Moreover, specific localized alterations of the bone leading to this rejuvenated appearance was extracted. The designed ML-based analysis showed that the loading induced (re)modeling close to the growth plates of tibiae resulting in similarities between the old in vivo loaded bones and the younger control group.

With the success of BAAM in resolving the aging process in the preclinical study in mind, a more complex DNN was designed to perform an automatic bone quality assessment (BQAM). BQAM was used in a clinical study to perform a classification of OI disease type from HR-pQCT images reaching 99% accuracy. The heterogeneity of bone tissue observed in the learning dataset of BQAM (due to sex: male/female and age: 25-75) and the high prediction accuracy confirmed that BQAM learned the manifestation of OI disease on bones. Unlike the common DXA-based analysis of bone quality and fracture risk in OI patients, the developed ML-based model showed great success in correlating bone structural features to the OI disease. Furthermore, it was shown that the effects of OI in trabecular bone compartment is the main distinguishing factor for OI types. This approach has led to designing a series of newly defined more complex bone structure parameters (in comparison to BMD and other classical bone parameters) such as Att and Th_{att} enabling to link structure to functionality/dysfunctionality in bone.

The designed ML models and the resulting data-driven based analysis are the main contributions of this thesis. On the nano scale, this allowed an unprecedented look into mechanics of protein networks and specifically how FtsZ protein network is evolutionary designed to function as an adaptively stable plastoskeleton. On the micro/macro scale, advancing from an analysis of predefined bone parameters to a ML-based investigation allowed an automatic extraction of bone structural features correlating to the bone quality and the detailed effects of aging, cyclic loading and OI disease on this quality.

6.2 Future Basic Research and Clinical Perspectives

The designed protein network analysis models could be applied on images of cytoskeletal protein networks. With the increase in resolution in 3D microscopy, the developed method can produce more realistic representatives. Moreover, with the increase in availability of time-resolved 4D microscopy images, the developed method can be further used in a

dynamic setup. This would allow a direct monitoring/validation of predicted mechanical behaviour of protein networks.

The presented applications of the developed method concerned investigating the assembly of FtsZ isoforms, distinguishing between structure and functionality of different isoforms and investigating the structure-function relationship. This could be potentially modified to assess different states of the same network. Specifically, the method could be utilized to investigate the alteration of F-actin and microtubule cytoskeletal protein networks in cancer cells. Cytoskeleton in multiple stages of transformation of a cluster of normal cells to atypical hyperplasia and finally to a cluster of cancer (carcinoma) cells can be studied and quantitatively described by means of the developed method. This analysis can potentially lead to a prognostic tool potentially capable of detecting the cancer cells in the stage of atypical hyperplasia and before the cells becoming invasive leading to metastasis. To do so, light microscopy images of a cytoskeletal protein network, such as vimentin (from intermediate filaments family), which is known for undergoing structural and mechanical changes during the microevolution of cells from healthy to either a benign or a malignant tumor, needs to be carried out. Five cell cultures, containing GFP tagged vimentin protein, naming: 1) healthy, 2) mid-cancerous microevolution to a benign tumor, 3) benign tumor, 4) mid-cancerous microevolution to a malignant tumor and 5) malignant tumor, should be created and imaged. Afterwards, by putting these five datasets through the developed image processing and μ FE simulation analysis methods, a dataset of structural features corresponding to each of these five states will need to be produced. This allows training the designed ML models to perform a classification task (prognosis) as well as investigating the structure-function relationship in vimentin protein network of cells undergoing cancer microevolution. Moreover, the quantitative analysis of this transformation enables extraction of the altering structural features during the microevolution of a cancer cell. This could potentially lead to exploring reversing mechanisms which specifically treat the extracted altered features of the protein network as well as smart medicine designed to target only the detected cancerous cells.

With the deep learning-based BAAM model capable of analyzing aging and loading-induced changes within the preclinical study at hand; the next step could be to train the BAAM on high-resolution images of human bones. This clinical study could become more robust by modifying the model from a classification deep neural network to a regression model. To do so, the modified regression DNN could be trained on CT images of radius or tibia of adult healthy subjects. The collected dataset should contain enough images representing the heterogeneity of bone in adults occurring in the process of aging (e.g. 20 subject for each nominative bone age, male and female). Moreover, for older ages, in which higher heterogeneity in bone structure between subject is present due to aging-related bone loss, higher number of subjects need to be included. Training the modified BAAM on this dataset creates a comprehensive bone age assessment model. Other modifications such as moving towards 3D convolutional neural network could be beneficial given the fact that computation power is increasing every day. Moreover, BAAM could be trained on GPU clusters for faster prototyping and higher robustness. We utilized BAAM to study bone aging after maturation. Bone maturation in children and its manifestation in macro/micro-structure is a field that BAAM could be potentially utilized.

The BQAM network has shown that deep learning can be used to investigate a genetic disease affecting bone, which was previously detected only through phenotype analysis.

This network can potentially be trained on datasets including control groups to assess treatment effects by measuring the similarities to a healthy bone after receiving treatment. Such an approach has been shown in this thesis to measure the effects of loading treatment in bone aging. One could utilize BQAM and the mentioned approach to investigate effects of any treatment on diseased bone structure. Moreover, BQAM could be modified to a hourglass-shaped network which maps an image directly to another image. By doing this, one could potentially predict the structure of the bone after receiving treatment, given the proper training data.

BQAM could be trained on CT or X-ray images depicting healthy bones and diseased bones before and during a pharmaceutical treatment process. Studying osteoporosis with this approach could enable investigating treatment effects on the bone tissue. To do so, a binary classification BQAM could be trained on healthy/diseased bone images to perform a disease detection task. Afterwards, similar to the approach presented in [5.3](#), the trained BQAM could be applied to images created during the treatment process with different medication dosage and treatment duration. Analysing the probability distribution changes in images put through the BQAM network before and after the treatment allows investigating the effects of the treatment. This means, if treatment has led to structural changes in bone which are detected as an increased probability in healthy subject class, the bone is transforming towards a healthier bone; hence the effects of treatment is quantitatively described.

At last, the success of BQAM in detecting OI in bone points toward its potentials in detecting other bone structure altering diseases such as osteoporosis. Studies have used HR-pQCT images to study osteoporosis and fracture possibility. To this day, DXA is the most common index to investigate fracture risk in osteoporotic patients. However, DXA fails to predict fracture risk in many patients. The BQAM developed network could potentially be used to automatically produce a series of newer indexes for fracture risk with higher prediction success rates. Moreover, BQAM could be further trained (transfer learning) on publicly available bone image datasets e.g LERA, MRNet and MURA to learn other dysfunctionality corresponding structural features of bone. This can potentially lead to acquiring a comprehensive bone quality assessment model.

Bibliography

- [1] Abadi, M.; Barham, P.; Chen, J.; Chen, Z.; Davis, A.; Dean, J.; Devin, M.; Ghemawat, S.; Irving, G.; Isard, M.; Kudlur, M.; Levenberg, J.; Monga, R.; Moore, S.; Murray, D. G.; Steiner, B.; Tucker, P.; Vasudevan, V.; Warden, P.; Wicke, M.; Yu, Y.; Zheng, X. & Brain, G.: Tensorflow: a system for large-scale machine learning. In *OSDI*, 2016, vol. 16, pp. 265–283.
- [2] Adams, D. W. & Errington, J.: Bacterial cell division: assembly, maintenance and disassembly of the z ring. *Nature Reviews Microbiology* **7** (2009), 642.
- [3] Ahlborg, H. G.; Johnell, O.; Turner, C. H.; Rannevik, G. & Karlsson, M. K.: Bone loss and bone size after menopause. *N. Engl. J. Med.* **349** (2003), 327–334.
- [4] Akhter, M. P.; Raab, D.; Turner, C.; Kimmel, D. & Recker, R. R.: Characterization of in vivo strain in the rat tibia during external application of a four-point bending load. *Journal of biomechanics* **25** (1992), 1241–1246.
- [5] Alioscha-Perez, M.; Benadiba, C.; Goossens, K.; Kasas, S.; Dietler, G.; Willaert, R. & Sahli, H.: A robust actin filaments image analysis framework. *PLoS Comput Biol* **12** (2016), e1005063.
- [6] Allain, P. & Kervrann, C.: Physical modeling of microtubules network. In *Journal of Physics: Conference Series*, IOP Publishing 2014, vol. 542, p. 012005.
- [7] Allen, J. M. et al.: *The molecular control of cellular activity*. New York, Toronto and London: McGraw-Hill Book Co., Inc. 1962.
- [8] Andrews, S. S. & Arkin, A. P.: A mechanical explanation for cytoskeletal rings and helices in bacteria. *Biophysical journal* **93** (2007), 1872–1884.
- [9] Asgharzadeh, P.; Birkhold, A. I.; Trivedi, Z.; Özdemir, B.; Reski, R. & Röhrle, O.: A μ fe simulation-based surrogate machine learning model to predict mechanical functionality of protein networks from live confocal imaging. *bioRxiv* (2020).
- [10] Asgharzadeh, P.; Özdemir, B.; Müller, S. J.; Reski, R. & Röhrle, O.: Analysis of confocal microscopy image data of physcomitrella chloroplasts to reveal adaptation principles leading to structural stability at the nanoscale. *PAMM* **16** (2016), 69–70.
- [11] Asgharzadeh, P.; Özdemir, B.; Müller, S. J.; Röhrle, O. & Reski, R.: Analysis of physcomitrella chloroplasts to reveal adaptation principles leading to structural stability at the nano-scale. In *Biomimetic Research for Architecture and Building Construction*. Springer 2016, pp. 261–275.

- [12] Asgharzadeh, P.; Özdemir, B.; Reski, R.; Birkhold, A. I. & Röhrle, O.: Feature-based classification of protein networks using confocal microscopy imaging and machine learning. *PAMM* **18** (2018), 1–2.
- [13] Asgharzadeh, P.; Özdemir, B.; Reski, R.; Röhrle, O. & Birkhold, A. I.: Computational 3d imaging to quantify structural components and assembly of protein networks. *Acta Biomaterialia* **69** (2018), 206–217.
- [14] Asgharzadeh, P.; Röhrle, O.; Willie, B. M. & Birkhold, A. I.: Decoding the rejuvenating effects of mechanical loading on skeletal maturation using in vivo imaging and deep learning. *arXiv preprint arXiv:1905.08099* (2019).
- [15] Asgharzadeh, P.; Röhrle, O.; Willie, B. M. & Birkhold, A. I.: Decoding rejuvenating effects of mechanical loading on skeletal aging using in vivo μ ct imaging and deep learning. *Acta Biomaterialia* (2020).
- [16] Baker, N.: The development of photosynthetic capacity in leaves. *The growth and functioning of leaves*. Cambridge University Press, Cambridge (1983), 271–307.
- [17] Baldi, P. & Pollastri, G.: A machine learning strategy for protein analysis. *IEEE Intelligent Systems* **17** (2002), 28–35.
- [18] Bálint, Š.; Verdeny Vilanova, I.; Sandoval Álvarez, Á. & Lakadamyali, M.: Correlative live-cell and superresolution microscopy reveals cargo transport dynamics at microtubule intersections. *Proc. Natl. Acad. Sci. U.S.A.* **110** (2013), 3375–80, ISSN 1091-6490.
- [19] Barasoain, I.; Díaz, J. F. & Andreu, J. M.: Fluorescent taxoid probes for microtubule research. In *Methods in cell biology*. Elsevier 2010, vol. 95, pp. 353–372.
- [20] Barlow, H. B.: Unsupervised learning. *Neural computation* **1** (1989), 295–311.
- [21] Barreto, S.; Clausen, C. H.; Perrault, C. M.; Fletcher, D. A. & Lacroix, D.: A multi-structural single cell model of force-induced interactions of cytoskeletal components. *Biomaterials* **34** (2013), 6119–6126.
- [22] Baxter-Jones, A. D.; Faulkner, R. A.; Forwood, M. R.; Mirwald, R. L. & Bailey, D. A.: Bone mineral accrual from 8 to 30 years of age: an estimation of peak bone mass. *Journal of Bone and Mineral Research* **26** (2011), 1729–1739.
- [23] Benda, A.; Aitken, H.; Davies, D. S.; Whan, R. & Goldsbury, C.: Sted imaging of tau filaments in alzheimer’s disease cortical grey matter. *J. Struct. Biol.* **195** (2016), 345–352.
- [24] Benediktsson, J. A.; Palmason, J. A. & Sveinsson, J. R.: Classification of hyperspectral data from urban areas based on extended morphological profiles. *IEEE Transactions on Geoscience and Remote Sensing* **43** (2005), 480–491.
- [25] Bergström, I.; Kerns, J. G.; Törnqvist, A.; Perdikouri, C.; Mathavan, N.; Koskela, A.; Henriksson, H.; Tuukkanen, J.; Andersson, G. & Isaksson, H.: Compressive loading of the murine tibia reveals site-specific micro-scale differences in adaptation and maturation rates of bone. *Osteoporos. Int.* **28** (2017), 1121–1131.

- [26] Biddle, F. G.; Coffaro, C. M.; Ziehr, J. E. & Eales, B. A.: Genetic variation in paw preference (handedness) in the mouse. *Genome* **36** (1993), 935–943.
- [27] Bilezikian, J. P.: *Primer on the metabolic bone diseases and disorders of mineral metabolism*. John Wiley & Sons 2018.
- [28] Birkhold, A. I.; Razi, H.; Duda, G. N.; Checa, S. & Willie, B. M.: Tomography-based quantification of regional differences in cortical bone surface remodeling and mechano-response. *Calcif. Tissue Int.* **100** (2017), 255–270.
- [29] Birkhold, A. I.; Razi, H.; Duda, G. N.; Weinkamer, R.; Checa, S. & Willie, B. M.: The influence of age on adaptive bone formation and bone resorption. *Biomaterials* **35** (2014), 9290–9301.
- [30] Birkhold, A. I.; Razi, H.; Duda, G. N.; Weinkamer, R.; Checa, S. & Willie, B. M.: Mineralizing surface is the main target of mechanical stimulation independent of age: 3d dynamic in vivo morphometry. *Bone* **66** (2014), 15–25.
- [31] Birkhold, A. I.; Razi, H.; Duda, G. N.; Weinkamer, R.; Checa, S. & Willie, B. M.: The periosteal bone surface is less mechano-responsive than the endocortical. *Sci. Rep.* **6** (2016), 23480.
- [32] Birkhold, A. I.; Razi, H.; Weinkamer, R.; Duda, G. N.; Checa, S. & Willie, B. M.: Monitoring in vivo (re) modeling: a computational approach using 4d microct data to quantify bone surface movements. *Bone* **75** (2015), 210–221.
- [33] Bishop, C. M.: *Pattern recognition and machine learning*. Springer Science+ Business Media 2006.
- [34] Bland, J. M. & Altman, D.: Statistical methods for assessing agreement between two methods of clinical measurement. *The lancet* **327** (1986), 307–310.
- [35] Blundell, J. & Terentjev, E.: Stretching semiflexible filaments and their networks. *Macromolecules* **42** (2009), 5388–5394.
- [36] Bolotin, H.: Dxa in vivo bmd methodology: an erroneous and misleading research and clinical gauge of bone mineral status, bone fragility, and bone remodelling. *Bone* **41** (2007), 138–154.
- [37] Bosveld, F.; Bonnet, I.; Guirao, B.; Tlili, S.; Wang, Z.; Petitalot, A.; Marchand, R.; Bardet, P.-L.; Marcq, P.; Graner, F. et al.: Mechanical control of morphogenesis by fat/dachsous/four-jointed planar cell polarity pathway. *Science* **336** (2012), 724–727.
- [38] Bouxsein, M. L.: Bone quality: where do we go from here? *Osteoporosis international* **14** (2003), 118–127.
- [39] Bouxsein, M. L.; Boyd, S. K.; Christiansen, B. A.; Guldborg, R. E.; Jepsen, K. J. & Müller, R.: Guidelines for assessment of bone microstructure in rodents using micro-computed tomography. *J. Bone Miner. Res.* **25** (2010), 1468–1486.

- [40] Brangwynne, C. P.; MacKintosh, F. C.; Kumar, S.; Geisse, N. A.; Talbot, J.; Mahadevan, L.; Parker, K. K.; Ingber, D. E. & Weitz, D. A.: Microtubules can bear enhanced compressive loads in living cells because of lateral reinforcement. *J Cell Biol* **173** (2006), 733–741.
- [41] Bray, D.: Intracellular signalling as a parallel distributed process. *Journal of theoretical biology* **143** (1990), 215–231.
- [42] Breiman, L.: Random forests. *Machine learning* **45** (2001), 5–32.
- [43] Breiman, L.; Friedman, J.; Olshen, R. & Stone, C.: Classification and regression trees. wadsworth int. *Group* **37** (1984), 237–251.
- [44] Brodt, M. D. & Silva, M. J.: Aged mice have enhanced endocortical response and normal periosteal response compared with young-adult mice following 1 week of axial tibial compression. *Journal of Bone and Mineral Research* **25** (2010), 2006–2015.
- [45] Brown, R. & Lemmon, B.: Pollen development in orchids 1. cytoskeleton and the control of division plane in irregular patterns of cytokinesis. *Protoplasma* **163** (1991), 9–18.
- [46] Brownstein, J. S.; Freifeld, C. C. & Madoff, L. C.: Digital disease detection—harnessing the web for public health surveillance. *New England Journal of Medicine* **360** (2009), 2153–2157.
- [47] Buezli, P. R.; Lerebours, C.; Roschger, A.; Roschger, P. & Weinkamer, R.: Late stages of mineralization and their signature on the bone mineral density distribution. *Connect. Tissue Res.* **59** (2018), 74–80.
- [48] Buettmann, E. G. & Silva, M. J.: Development of an in vivo bone fatigue damage model using axial compression of the rabbit forelimb. *J. Biomech.* **49** (2016), 3564–3569.
- [49] Burghardt, A. J.; Buie, H. R.; Laib, A.; Majumdar, S. & Boyd, S. K.: Reproducibility of direct quantitative measures of cortical bone microarchitecture of the distal radius and tibia by hr-pqct. *Bone* **47** (2010), 519–528.
- [50] Buxton, G. A.; Siedlak, S. L.; Perry, G. & Smith, M. A.: Mathematical modeling of microtubule dynamics: insights into physiology and disease. *Progress in neurobiology* **92** (2010), 478–483.
- [51] Cabré, E. J.; Sánchez-Gorostiaga, A.; Carrara, P.; Roperio, N.; Casanova, M.; Palacios, P.; Stano, P.; Jiménez, M.; Rivas, G. & Vicente, M.: Bacterial division proteins ftsz and zipa induce vesicle shrinkage and cell membrane invagination. *Journal of Biological Chemistry* (2013), jbc–M113.
- [52] Calbet, J.; Dorado, C.; Diaz-Herrera, P. & Rodriguez-Rodriguez, L.: High femoral bone mineral content and density in male football (soccer) players. *Medicine and science in sports and exercise* **33** (2001), 1682–1687.

- [53] Carriero, A.; Pereira, A.; Wilson, A.; Castagno, S.; Javaheri, B.; Pitsillides, A.; Marenzana, M. & Shefelbine, S.: Spatial relationship between bone formation and mechanical stimulus within cortical bone: Combining 3d fluorochrome mapping and poroelastic finite element modelling. *Bone Rep.* **8** (2018), 72–80.
- [54] Case, L. B.; Baird, M. A.; Shtengel, G.; Campbell, S. L.; Hess, H. F.; Davidson, M. W. & Waterman, C. M.: Molecular mechanism of vinculin activation and nano-scale spatial organization in focal adhesions. *Nat. Cell Biol.* **17** (2015), 880–892.
- [55] Cetera, M.; Ramirez-San Juan, G. R.; Oakes, P. W.; Lewellyn, L.; Fairchild, M. J.; Tanentzapf, G.; Gardel, M. L. & Horne-Badovinac, S.: Epithelial rotation promotes the global alignment of contractile actin bundles during drosophila egg chamber elongation. *Nature communications* **5** (2014), 5511.
- [56] Chan, T. F. & Vese, L. A.: Active contours without edges. *IEEE Transactions on image processing* **10** (2001), 266–277.
- [57] Chandran, K. B.; Udaykumar, H. & Reinhardt, J. M.: *Image-based computational modeling of the human circulatory and pulmonary systems*, vol. 239. Springer 2011.
- [58] Chen, D.-Y.; Lipari, K. R.; Dehghan, Y.; Streichan, S. J. & Bilder, D.: Symmetry breaking in an edgeless epithelium by fat2-regulated microtubule polarity. *Cell reports* **15** (2016), 1125–1133.
- [59] Cheung, A. M.; Majumdar, S.; Brixen, K.; Chapurlat, R.; Fuerst, T.; Engelke, K.; Dardzinski, B.; Cabal, A.; Verbruggen, N.; Ather, S. et al.: Effects of odanacatib on the radius and tibia of postmenopausal women: improvements in bone geometry, microarchitecture, and estimated bone strength. *J. Bone Miner. Res.* **29** (2014), 1786–1794.
- [60] Chierico, L.; Joseph, A. S.; Lewis, A. L. & Battaglia, G.: Live cell imaging of membrane/cytoskeleton interactions and membrane topology. *Sci. Rep.* **4** (2014), 6056, ISSN 2045-2322.
- [61] Civalek, Ö. & Demir, Ç.: Bending analysis of microtubules using nonlocal euler–bernoulli beam theory. *Applied Mathematical Modelling* **35** (2011), 2053–2067.
- [62] Civalek, Ö. & Demir, C.: A simple mathematical model of microtubules surrounded by an elastic matrix by nonlocal finite element method. *Applied Mathematics and Computation* **289** (2016), 335–352.
- [63] Clinton, T. & Lanyon, L.: Regulation of bone formation by applied dynamic loads. *J Bone Joint Surg Am* **66** (1984), 397–402.
- [64] Consortium, M. G. S. et al.: Initial sequencing and comparative analysis of the mouse genome. *Nature* **420** (2002), 520.
- [65] Cormack, A. M.: Representation of a function by its line integrals, with some radiological applications. *Journal of applied physics* **34** (1963), 2722–2727.
- [66] Cowin, S. C.: *Bone mechanics handbook*. CRC press 2001.

- [67] Cummings, S. R. & Melton, L. J.: Epidemiology and outcomes of osteoporotic fractures. *The Lancet* **359** (2002), 1761–1767.
- [68] Curry, N.; Ghézali, G.; Kaminski Schierle, G. S.; Rouach, N. & Kaminski, C. F.: Correlative sted and atomic force microscopy on live astrocytes reveals plasticity of cytoskeletal structure and membrane physical properties during polarized migration. *Frontiers in cellular neuroscience* **11** (2017), 104.
- [69] Dall’Ara, E.; Pahr, D.; Varga, P.; Kainberger, F. & Zysset, P.: Qct-based finite element models predict human vertebral strength in vitro significantly better than simulated dexa. *Osteoporos. Int.* **23** (2012), 563–572.
- [70] Darwin, C.: *On the origin of species, 1859*. Routledge 2004.
- [71] De Choudhury, M. & Kiciman, E.: Integrating artificial and human intelligence in complex, sensitive problem domains: Experiences from mental health. *AI Magazine* **39** (2018), 69–80.
- [72] Decker, J. M.; Krüger, L.; Sydow, A.; Zhao, S.; Frotscher, M.; Mandelkow, E. & Mandelkow, E.-M.: Pro-aggregant tau impairs mossy fiber plasticity due to structural changes and ca++ dysregulation. *Acta Neuropathol. (Berl.) communications* **3** (2015), 23.
- [73] Deguchi, S.; Ohashi, T. & Sato, M.: Tensile properties of single stress fibers isolated from cultured vascular smooth muscle cells. *Journal of biomechanics* **39** (2006), 2603–2610.
- [74] Demontiero, O.; Vidal, C. & Duque, G.: Aging and bone loss: new insights for the clinician. *Ther. Adv. Musculoskelet. Dis.* **4** (2012), 61–76.
- [75] Dempster, D. W.; Lian, J. & Goldring, S.: Anatomy and functions of the adult skeleton. *Primer on the metabolic bone diseases and disorders of mineral metabolism* **7** (2006).
- [76] Dickinson, D. J.; Ward, J. D.; Reiner, D. J. & Goldstein, B.: Engineering the caenorhabditis elegans genome using cas9-triggered homologous recombination. *Nature methods* **10** (2013), 1028.
- [77] Dietterich, T. G.: Ensemble methods in machine learning. In *International workshop on multiple classifier systems*, Springer 2000, pp. 1–15.
- [78] Donaldson, C. L.; Hulley, S. B.; Vogel, J. M.; Hattner, R. S.; Bayers, J. H. & McMillan, D. E.: Effect of prolonged bed rest on bone mineral. *Metabolism* **19** (1970), 1071–1084.
- [79] Dos Remedios, C.; Chhabra, D.; Kekic, M.; Dedova, I.; Tsubakihara, M.; Berry, D. & Nosworthy, N.: Actin binding proteins: regulation of cytoskeletal microfilaments. *Physiol. Rev.* **83** (2003), 433–473.
- [80] Dutta, S. & Sengupta, P.: Men and mice: relating their ages. *Life Sci.* **152** (2016), 244–248.

- [81] D'Este, E.; Kamin, D.; Göttfert, F.; El-Hady, A. & Hell, S. W.: Sted nanoscopy reveals the ubiquity of subcortical cytoskeleton periodicity in living neurons. *Cell reports* **10** (2015), 1246–1251.
- [82] El-Kafafi, E.-S.; Mukherjee, S.; El-Shami, M.; Putaux, J.-L.; Block, M. A.; Pignot-Paintrand, I.; Lerbs-Mache, S. & Falconet, D.: The plastid division proteins, *fts1* and *fts2*, differ in their biochemical properties and sub-plastidial localization. *Biochemical Journal* **387** (2005), 669–676.
- [83] El-Shami, M.; El-Kafafi, S.; Falconet, D. & Lerbs-Mache, S.: Cell cycle-dependent modulation of *fts* expression in synchronized tobacco *by2* cells. *Molecular genetics and genomics* **267** (2002), 254–261.
- [84] Elson, E. L.: Cellular mechanics as an indicator of cytoskeletal structure and function. *Annual review of biophysics and biophysical chemistry* **17** (1988), 397–430.
- [85] Enrique, M. & Gardel, M. L.: Actin mechanics and fragmentation. *Journal of Biological Chemistry* **290** (2015), 17137–17144.
- [86] Enrique, M.; Martiel, J.-L. & Blanchoin, L.: Mechanical heterogeneity favors fragmentation of strained actin filaments. *Biophysical journal* **108** (2015), 2270–2281.
- [87] Erhan, D.; Bengio, Y.; Courville, A. & Vincent, P.: Visualizing higher-layer features of a deep network. *University of Montreal* **1341** (2009), 1.
- [88] Erickson, H. P. & Osawa, M.: Ftsz constriction force–curved protofilaments bending membranes. In *Prokaryotic Cytoskeletons*. Springer 2017, pp. 139–160.
- [89] Erickson, H. P.; Taylor, D. W.; Taylor, K. A. & Bramhill, D.: Bacterial cell division protein FtsZ assembles into protofilament sheets and minirings, structural homologs of tubulin polymers. *Proc. Natl. Acad. Sci. U.S.A.* **93** (1996), 519–23, ISSN 0027-8424.
- [90] Erickson, H. P.; Taylor, D. W.; Taylor, K. A. & Bramhill, D.: Bacterial cell division protein *fts* assembles into protofilament sheets and minirings, structural homologs of tubulin polymers. *Proceedings of the National Academy of Sciences* **93** (1996), 519–523.
- [91] Eringen, A. C.: Theory of nonlocal electromagnetic elastic solids. *Journal of Mathematical Physics* **14** (1973), 733–740.
- [92] Esteva, A.; Kuprel, B.; Novoa, R. A.; Ko, J.; Swetter, S. M.; Blau, H. M. & Thrun, S.: Dermatologist-level classification of skin cancer with deep neural networks. *Nature* **542** (2017), 115.
- [93] Evans, J. D. & Coudert, F.-X.: Predicting the mechanical properties of zeolite frameworks by machine learning. *Chemistry of Materials* **29** (2017), 7833–7839.
- [94] Fehling, P.; Alekel, L.; Clasey, J.; Rector, A. & Stillman, R.: A comparison of bone mineral densities among female athletes in impact loading and active loading sports. *Bone* **17** (1995), 205–210.

- [95] Feldkamp, L. A.; Goldstein, S. A.; Parfitt, M. A.; Jesion, G. & Kleerekoper, M.: The direct examination of three-dimensional bone architecture in vitro by computed tomography. *Journal of bone and mineral research* **4** (1989), 3–11.
- [96] Felgner, H.; Frank, R.; Biernat, J.; Mandelkow, E.-M.; Mandelkow, E.; Ludin, B.; Matus, A. & Schliwa, M.: Domains of neuronal microtubule-associated proteins and flexural rigidity of microtubules. *The Journal of cell biology* **138** (1997), 1067–1075.
- [97] Felgner, H.; Frank, R. & Schliwa, M.: Flexural rigidity of microtubules measured with the use of optical tweezers. *Journal of cell science* **109** (1996), 509–516.
- [98] Feller, W.: *An introduction to probability theory and its applications*, vol. 2. John Wiley & Sons 2008.
- [99] Ferguson, V. L.; Ayers, R. A.; Bateman, T. A. & Simske, S. J.: Bone development and age-related bone loss in male c57bl/6j mice. *Bone* **33** (2003), 387–398.
- [100] Fletcher, D. A. & Mullins, R. D.: Cell mechanics and the cytoskeleton. *Nature* **463** (2010), 485–492.
- [101] Flitney, E. W.; Kuczmarski, E. R.; Adam, S. A. & Goldman, R. D.: Insights into the mechanical properties of epithelial cells: the effects of shear stress on the assembly and remodeling of keratin intermediate filaments. *The FASEB Journal* **23** (2009), 2110–2119.
- [102] Forwood, M.: Mechanical effects on the skeleton: are there clinical implications? *Osteoporosis international* **12** (2001), 77–83.
- [103] Fratzl-Zelman, N.; Schmidt, I.; Roschger, P.; Glorieux, F. H.; Klaushofer, K.; Fratzl, P.; Rauch, F. & Wagermaier, W.: Mineral particle size in children with osteogenesis imperfecta type i is not increased independently of specific collagen mutations. *Bone* **60** (2014), 122–128.
- [104] Freund, Y.: Boosting a weak learning algorithm by majority. *Information and computation* **121** (1995), 256–285.
- [105] Fritton, J.; Myers, E.; Wright, T. & Van der Meulen, M.: Loading induces site-specific increases in mineral content assessed by microcomputed tomography of the mouse tibia. *Bone* **36** (2005), 1030–1038.
- [106] Fritzen, F.; Fernández, M. & Larsson, F.: On-the-fly adaptivity for nonlinear two-scale simulations using artificial neural networks and reduced order modeling. *Frontiers in Materials* **6** (2019), 75.
- [107] Fukushima, K.: Neocognitron: A self-organizing neural network model for a mechanism of pattern recognition unaffected by shift in position. *Biological cybernetics* **36** (1980), 193–202.
- [108] Fuller, H.; Fuller, R. & Pereira, R. M. R.: High resolution peripheral quantitative computed tomography for the assessment of morphological and mechanical bone parameters. *Revista Brasileira de Reumatologia (English Edition)* **55** (2015), 352–362.

- [109] Fung, Y. C.: *Biomechanics: Mechanical Properties of Living Tissues*. Springer-Verlag, New York 1993, 2nd ed. edn.
- [110] Gardel, M. L.; Kasza, K. E.; Brangwynne, C. P.; Liu, J. & Weitz, D. A.: Mechanical response of cytoskeletal networks. *Methods in cell biology* **89** (2008), 487–519.
- [111] Giger, M. L.: Machine learning in medical imaging. *Journal of the American College of Radiology* **15** (2018), 512–520.
- [112] Gittes, F.; Mickey, B.; Nettleton, J. & Howard, J.: Flexural rigidity of microtubules and actin filaments measured from thermal fluctuations in shape. *The Journal of cell biology* **120** (1993), 923–934.
- [113] Gladilin, E.; Gonzalez, P. & Eils, R.: Dissecting the contribution of actin and vimentin intermediate filaments to mechanical phenotype of suspended cells using high-throughput deformability measurements and computational modeling. *Journal of biomechanics* **47** (2014), 2598–2605.
- [114] Gladilin, E.; Gonzalez, P. & Eils, R.: Dissecting the contribution of actin and vimentin intermediate filaments to mechanical phenotype of suspended cells using high-throughput deformability measurements and computational modeling. *Journal of biomechanics* **47** (2014), 2598–2605.
- [115] Glatt, V.; Canalis, E.; Stadmeier, L. & Bouxsein, M. L.: Age-related changes in trabecular architecture differ in female and male c57bl/6j mice. *J. Bone Miner. Res.* **22** (2007), 1197–1207.
- [116] Glynn, J. M.; Miyagishima, S.-y.; Yoder, D. W.; Osteryoung, K. W. & Vitha, S.: Chloroplast division. *Traffic* **8** (2007), 451–461.
- [117] Goodfellow, I.; Bengio, Y. & Courville, A.: *Deep learning*. MIT press 2016.
- [118] Gov, N. S.: Active elastic network: cytoskeleton of the red blood cell. *Physical Review E* **75** (2007), 011921.
- [119] Gray, M. W.: The endosymbiont hypothesis revisited. In *International review of cytology*. Elsevier 1992, vol. 141, pp. 233–357.
- [120] Greenspan, H.; Van Ginneken, B. & Summers, R. M.: Guest editorial deep learning in medical imaging: Overview and future promise of an exciting new technique. *IEEE Trans. Med. Imaging* **35** (2016), 1153–1159.
- [121] Gremillon, L.; Kiessling, J.; Hause, B.; Decker, E. L.; Reski, R. & Sarnighausen, E.: Filamentous temperature-sensitive z (ftsZ) isoforms specifically interact in the chloroplasts and in the cytosol of physcomitrella patens. *New Phytologist* **176** (2007), 299–310.
- [122] Gremillon, L.; Kiessling, J.; Hause, B.; Decker, E. L.; Reski, R. & Sarnighausen, E.: Filamentous temperature-sensitive Z (FtsZ) isoforms specifically interact in the chloroplasts and in the cytosol of Physcomitrella patens. *New Phytol.* **176** (2007), 299–310, ISSN 0028646X.

- [123] Gross, T. S.; Srinivasan, S.; Liu, C. C.; Clemens, T. L. & Bain, S. D.: Noninvasive loading of the murine tibia: an in vivo model for the study of mechanotransduction. *Journal of Bone and Mineral Research* **17** (2002), 493–501.
- [124] Guck, J.; Schinkinger, S.; Lincoln, B.; Wottawah, F.; Ebert, S.; Romeyke, M.; Lenz, D.; Erickson, H. M.; Ananthakrishnan, R.; Mitchell, D. et al.: Optical deformability as an inherent cell marker for testing malignant transformation and metastatic competence. *Biophysical journal* **88** (2005), 3689–3698.
- [125] Guo, G.-D.; Jain, A. K.; Ma, W.-Y. & Zhang, H.-J.: Learning similarity measure for natural image retrieval with relevance feedback. *IEEE Transactions on Neural Networks* **13** (2002), 811–820.
- [126] Gusi, N.; Raimundo, A. & Leal, A.: Low-frequency vibratory exercise reduces the risk of bone fracture more than walking: a randomized controlled trial. *BMC musculoskeletal disorders* **7** (2006), 92.
- [127] Hahn, M.; Vogel, M.; Pompesius-Kempa, M. & Delling, G.: Trabecular bone pattern factor—a new parameter for simple quantification of bone microarchitecture. *Bone* **13** (1992), 327–330.
- [128] Hald, J. D.; Folkestad, L.; Harsløf, T.; Lund, A.; Duno, M.; Jensen, J.; Neghabat, S.; Brixen, K. & Langdahl, B.: Skeletal phenotypes in adult patients with osteogenesis imperfecta—correlations with colla1/colla2 genotype and collagen structure. *Osteoporosis International* **27** (2016), 3331–3341.
- [129] Halloran, B. P.; Ferguson, V. L.; Simske, S. J.; Burghardt, A.; Venton, L. L. & Majumdar, S.: Changes in bone structure and mass with advancing age in the male c57bl/6j mouse. *J. Bone Miner. Res.* **17** (2002), 1044–1050.
- [130] Hartwell, L. H.; Hopfield, J. J.; Leibler, S. & Murray, A. W.: From molecular to modular cell biology. *Nature* **402** (1999), C47.
- [131] Hawkins, T.; Mirigian, M.; Yasar, M. S. & Ross, J. L.: Mechanics of microtubules. *Journal of biomechanics* **43** (2010), 23–30.
- [132] Heidlauf, T. & Röhrle, O.: A multiscale chemo-electro-mechanical skeletal muscle model to analyze muscle contraction and force generation for different muscle fiber arrangements. *Frontiers in physiology* **5** (2014), 498.
- [133] Hein, B.; Willig, K. I. & Hell, S. W.: Stimulated emission depletion (sted) nanoscopy of a fluorescent protein-labeled organelle inside a living cell. *Proceedings of the National Academy of Sciences* **105** (2008), 14271–14276.
- [134] Heinonen, A.; Kannus, P.; Sievänen, H.; Oja, P.; Pasanen, M.; Rinne, M.; Uusi-Rasi, K. & Vuori, I.: Randomised controlled trial of effect of high-impact exercise on selected risk factors for osteoporotic fractures. *The Lancet* **348** (1996), 1343–1347.
- [135] Henderson, E.; Haydon, P. & Sakaguchi, D.: Actin filament dynamics in living glial cells imaged by atomic force microscopy. *Science* **257** (1992), 1944–1946.

- [136] Heng, Y.-W. & Koh, C.-G.: Actin cytoskeleton dynamics and the cell division cycle. *The international journal of biochemistry & cell biology* **42** (2010), 1622–1633.
- [137] Hepler, P. K. & Gunning, B. E.: Confocal fluorescence microscopy of plant cells. *Protoplasma* **201** (1998), 121–157.
- [138] Hepler, P. K. & Gunning, B. E.: Confocal fluorescence microscopy of plant cells. *Protoplasma* **201** (1998), 121–157.
- [139] Hernlund, E.; Svedbom, A.; Ivergård, M.; Compston, J.; Cooper, C.; Stenmark, J.; McCloskey, E. V.; Jönsson, B. & Kanis, J. A.: Osteoporosis in the european union: medical management, epidemiology and economic burden. *Arch. Osteoporos.* **8** (2013), 136.
- [140] Hoffmann, C.; Moes, D.; Dieterle, M.; Neumann, K.; Moreau, F.; Furtado, A. T.; Dumas, D.; Steinmetz, A. & Thomas, C.: Live cell imaging reveals actin-cytoskeleton-induced self-association of the actin-bundling protein wlim1. *J Cell Sci* **127** (2014), 583–598.
- [141] Hohe, A.; Decker, E.; Gorr, G.; Schween, G. & Reski, R.: Tight control of growth and cell differ. in photoautotrophically growing moss (*Physcomitrella patens*) bioreactor cultures. *Plant Cell Rep.* **20** (2002), 1135–1140.
- [142] Hohe, A.; Egener, T.; Lucht, J. M.; Holtorf, H.; Reinhard, C.; Schween, G. & Reski, R.: An improved and highly standardised transformation procedure allows efficient production of single and multiple targeted gene-knockouts in a moss, *Physcomitrella patens*. *Curr. Genet.* **44** (2004), 339–347.
- [143] Hohe, A. & Reski, R.: Optimisation of a bioreactor culture of the moss *Physcomitrella patens* for mass production of protoplasts. *Plant Science* **163** (2002), 69–74.
- [144] Holden, S. J.; Pengo, T.; Meibom, K. L.; Fernandez Fernandez, C.; Collier, J. & Manley, S.: High throughput 3D super-resolution microscopy reveals *Caulobacter crescentus* In Vivo Z-ring organization. *Proceedings of the National Academy of Sciences* **111** (2014), 4566–4571, ISSN 1091-6490.
- [145] Holguin, N.; Brodt, M. D.; Sanchez, M. E.; Kotiya, A. A. & Silva, M. J.: Adaptation of tibial structure and strength to axial compression depends on loading history in both c57bl/6 and balb/c mice. *Calcif. Tissue Int.* **93** (2013), 211–221.
- [146] Holmes, K. C.; Popp, D.; Gebhard, W. & Kabsch, W.: Atomic model of the actin filament. *Nature* **347** (1990), 44.
- [147] Holzapfel, G. A. & Ogden, R. W.: On the bending and stretching elasticity of biopolymer filaments. *Journal of elasticity* **104** (2011), 319–342.
- [148] Hörger, I.; Velasco, E.; Mingorance, J.; Rivas, G.; Tarazona, P. & Vélez, M.: Langevin computer simulations of bacterial protein filaments and the force-generating mechanism during cell division. *Physical Review E* **77** (2008), 011902.

- [149] Hörger, I.; Velasco, E.; Rivas, G.; Vélez, M. & Tarazona, P.: Ftsz bacterial cytoskeletal polymers on curved surfaces: the importance of lateral interactions. *Biophysical journal* **94** (2008), L81–L83.
- [150] Hua, K.-L.; Hsu, C.-H.; Hidayati, S. C.; Cheng, W.-H. & Chen, Y.-J.: Computer-aided classification of lung nodules on computed tomography images via deep learning technique. *OncoTargets and therapy* **8** (2015).
- [151] Huang, B.; Bates, M. & Zhuang, X.: Super resolution fluorescence microscopy. *Annu. Rev. Biochem.* **78** (2010), 993–1016, ISSN 1545-4509.
- [152] Huiskes, R. & Van Rietbergen, B.: Biomechanics of bone. *Basic orthopaedic biomechanics and mechano-biology* **3** (2005), 123–179.
- [153] Ihmels, J.; Friedlander, G.; Bergmann, S.; Sarig, O.; Ziv, Y. & Barkai, N.: Revealing modular organization in the yeast transcriptional network. *Nature genetics* **31** (2002), 370.
- [154] Ingber, D. E.: Cellular tensegrity: defining new rules of biological design that govern the cytoskeleton. *J. Cell Sci.* **104** (1993), 613–627.
- [155] Ingber, D. E.: Tensegrity: the architectural basis of cellular mechanotransduction. *Annu. Rev. Physiol.* **59** (1997), 575–599, ISSN 0066-4278.
- [156] Ingber, D. E.: Tensegrity: the architectural basis of cellular mechanotransduction. *Annual review of physiology* **59** (1997), 575–599.
- [157] Iwai, M.; Yokono, M.; Kurokawa, K.; Ichihara, A. & Nakano, A.: Live-cell visualization of excitation energy dynamics in chloroplast thylakoid structures. *Scientific reports* **6** (2016), 29940.
- [158] Jacob, F.: Evolution and tinkering. *Science* **196** (1977), 1161–1166.
- [159] Janmey, P. A.; Euteneuer, U.; Traub, P. & Schliwa, M.: Viscoelastic properties of vimentin compared with other filamentous biopolymer networks. *The Journal of cell biology* **113** (1991), 155–160.
- [160] Janmey, P. A.; Hvidt, S.; Käs, J.; Lerche, D.; Maggs, A.; Sackmann, E.; Schliwa, M. & Stossel, T. P.: The mechanical properties of actin gels. elastic modulus and filament motions. *Journal of Biological Chemistry* **269** (1994), 32503–32513.
- [161] Janmey, P. A. & McCulloch, C. A.: Cell mechanics: integrating cell responses to mechanical stimuli. *Annual review of Biomed. Eng.* **9** (2007), 1–34, ISSN 1523-9829.
- [162] Jasnin, M.; Ecke, M.; Baumeister, W. & Gerisch, G.: Actin organization in cells responding to a perforated surface, revealed by live imaging and cryo-electron tomography. *Structure* **24** (2016), 1031–1043.
- [163] Jiang, P.; Wu, H.; Wang, W.; Ma, W.; Sun, X. & Lu, Z.: Mipred: classification of real and pseudo microrna precursors using random forest prediction model with combined features. *Nucleic acids research* **35** (2007), W339–W344.

- [164] Jilka, R. L.: The relevance of mouse models for investigating age-related bone loss in humans. *Journals of Gerontology Series A: Biomed. Sci.s and Medical Sciences* **68** (2013), 1209–1217.
- [165] Jordan, M. A. & Wilson, L.: Microtubules as a target for anticancer drugs. *Nature Reviews Cancer* **4** (2004), 253.
- [166] Jordan, M. I. & Mitchell, T. M.: Machine learning: Trends, perspectives, and prospects. *Science* **349** (2015), 255–260.
- [167] Kan, A.: Machine learning applications in cell image analysis. *Immunology and cell biology* **95** (2017), 525–530.
- [168] Kanis, J.; Burlet, N.; Cooper, C.; Delmas, P.; Reginster, J.-Y.; Borgstrom, F. & Rizzoli, R.: European guidance for the diagnosis and management of osteoporosis in postmenopausal women. *Osteoporos. Int.* **19** (2008), 399–428.
- [169] Kanis, J.; Johnell, O.; Odén, A.; Johansson, H. & McCloskey, E.: Frax™ and the assessment of fracture probability in men and women from the uk. *Osteoporosis international* **19** (2008), 385–397.
- [170] Kanis, J.; Johnell, O.; Oden, A.; Sernbo, I.; Redlund-Johnell, I.; Dawson, A.; De Laet, C. & Jonsson, B.: Long-term risk of osteoporotic fracture in malmö. *Osteoporosis international* **11** (2000), 669–674.
- [171] Kanis, J. A.: Diagnosis of osteoporosis and assessment of fracture risk. *The Lancet* **359** (2002), 1929–1936.
- [172] Katti, D. R. & Katti, K. S.: Cancer cell mechanics with altered cytoskeletal behavior and substrate effects: A 3d finite element modeling study. *Journal of the mechanical behavior of biomedical materials* **76** (2017), 125–134.
- [173] Keller, P. J.; Schmidt, A. D.; Wittbrodt, J. & Stelzer, E. H.: Reconstruction of zebrafish early embryonic development by scanned light sheet microscopy. *science* **322** (2008), 1065–1069.
- [174] Kerr, D.; Morton, A.; Dick, I. & Prince, R.: Exercise effects on bone mass in postmenopausal women are site-specific and load-dependent. *Journal of Bone and Mineral Research* **11** (1996), 218–225.
- [175] Ketene, A. N.; Schmelz, E. M.; Roberts, P. C. & Agah, M.: The effects of cancer progression on the viscoelasticity of ovarian cell cytoskeleton structures. *Nanomedicine: Nanotechnology, Biology and Medicine* **8** (2012), 93–102.
- [176] Kiessling, J.; Kruse, S.; Rensing, S. A.; Harter, K.; Decker, E. L. & Reski, R.: Visualization of a cytoskeleton-like ftsz network in chloroplasts. *The Journal of cell biology* **151** (2000), 945–950.
- [177] Kim, M.; Madden, M. & Warner, T. A.: Forest type mapping using object-specific texture measures from multispectral ikonos imagery. *Photogrammetric Engineering & Remote Sensing* **75** (2009), 819–829.

- [178] Kim, T.; Hwang, W. & Kamm, R. D.: Dynamic role of cross-linking proteins in actin rheology. *Biophysical journal* **101** (2011), 1597–1603.
- [179] Kingma, D. P. & Ba, J.: Adam: A method for stochastic optimization. *arXiv preprint* (2014), arXiv:1412.6980.
- [180] Kircher, S.; Wellmer, F.; Nick, P.; Rügner, A.; Schäfer, E. & Harter, K.: Nuclear import of the parsley bzip transcription factor cprf2 is regulated by phytochrome photoreceptors. *The J. Cell Biol.* **144** (1999), 201–211.
- [181] Ko, C.-Y.; Seo, D. H. & Kim, H. S.: Deterioration of bone quality in the tibia and fibula in growing mice during skeletal unloading: gender-related differences. *J. Biomech. Eng.* **133** (2011), 111003.
- [182] Kocijan, R.; Muschitz, C.; Haschka, J.; Hans, D.; Nia, A.; Geroldinger, A.; Ardel, M.; Wakolbinger, R. & Resch, H.: Bone structure assessed by hr-pqct, tbs and dxl in adult patients with different types of osteogenesis imperfecta. *Osteoporosis International* **26** (2015), 2431–2440.
- [183] Koehne, T.; Vettorazzi, E.; Küsters, N.; Lüneburg, R.; Kahl-Nieke, B.; Püschel, K.; Amling, M. & Busse, B.: Trends in trabecular architecture and bone mineral density distribution in 152 individuals aged 30–90years. *Bone* **66** (2014), 31–38.
- [184] Kojima, H.; Ishijima, A. & Yanagida, T.: Direct measurement of stiffness of single actin filaments with and without tropomyosin by in vitro nanomanipulation. *Proceedings of the National Academy of Sciences* **91** (1994), 12962–12966.
- [185] Kotsiantis, S. B.; Zaharakis, I. & Pintelas, P.: Supervised machine learning: A review of classification techniques. *Emerging artificial intelligence applications in computer engineering* **160** (2007), 3–24.
- [186] Kraus, O. Z.; Grys, B. T.; Ba, J.; Chong, Y.; Frey, B. J.; Boone, C. & Andrews, B. J.: Automated analysis of high-content microscopy data with deep learning. *Molecular Syst. Biol.* **13** (2017), 924.
- [187] Krizhevsky, A.; Sutskever, I. & Hinton, G. E.: Imagenet classification with deep convolutional neural networks. In *Adv. Neural. Inf. Process. Syst.*, 2012, pp. 1097–1105.
- [188] Krug, R.; Burghardt, A. J.; Majumdar, S. & Link, T. M.: High-resolution imaging techniques for the assessment of osteoporosis. *Radiologic Clinics* **48** (2010), 601–621.
- [189] Kubitschke, H.; Schnauss, J.; Nnetu, K. D.; Warmt, E.; Stange, R. & Kaes, J.: Actin and microtubule networks contribute differently to cell response for small and large strains. *New Journal of Physics* **19** (2017), 093003.
- [190] Kumar, S. & Weaver, V. M.: Mechanics, malignancy, and metastasis: the force journey of a tumor cell. *Cancer Metastasis Rev.* **28** (2009), 113–127.

- [191] Kuroiwa, T.; Misumi, O.; Nishida, K.; Yagisawa, F.; Yoshida, Y.; Fujiwara, T. & Kuroiwa, H.: Vesicle, mitochondrial, and plastid division machineries with emphasis on dynamin and electron-dense rings. *International review of cell and molecular biology* **271** (2008), 97–152.
- [192] Laib, A.; Häuselmann, H. J. & Rügsegger, P.: In vivo high resolution 3d-qct of the human forearm. *Technology and health care* **6** (1998), 329–337.
- [193] Lambers, F. M.; Kuhn, G.; Weigt, C.; Koch, K. M.; Schulte, F. A. & Müller, R.: Bone adaptation to cyclic loading in murine caudal vertebrae is maintained with age and directly correlated to the local micromechanical environment. *J. Biomech.* **48** (2015), 1179–1187.
- [194] Landau, L. D.; Lifshitz, E. M.; Berestetskii, V. & Pitaevskii, L.: *Course of Theoretical Physics: Theory of Elasticity*. Pergamon Press, Oxford 1995.
- [195] Landis, W.; Song, M.; Leith, A.; McEwen, L. & McEwen, B.: Mineral and organic matrix interaction in normally calcifying tendon visualized in three dimensions by high-voltage electron microscopic tomography and graphic image reconstruction. *Journal of structural biology* **110** (1993), 39–54.
- [196] Landis, W. J. & Silver, F. H.: Mineral deposition in the extracellular matrices of vertebrate tissues: identification of possible apatite nucleation sites on type I collagen. *Cells Tissues Organs* **189** (2009), 20–24.
- [197] Lang, T.; LeBlanc, A.; Evans, H.; Lu, Y.; Genant, H. & Yu, A.: Cortical and trabecular bone mineral loss from the spine and hip in long-duration spaceflight. *Journal of bone and mineral research* **19** (2004), 1006–1012.
- [198] LeCun, Y.; Bengio, Y. & Hinton, G.: Deep learning. *nature* **521** (2015), 436.
- [199] LeCun, Y.; Bottou, L.; Bengio, Y.; Haffner, P. et al.: Gradient-based learning applied to document recognition. *Proceedings of the IEEE* **86** (1998), 2278–2324.
- [200] Lee, H.; Tajmir, S.; Lee, J.; Zissen, M.; Yeshiwas, B. A.; Alkasab, T. K.; Choy, G. & Do, S.: Fully automated deep learning system for bone age assessment. *J. Digit. Imaging* **30** (2017), 427–441.
- [201] Lee, H.; Tajmir, S.; Lee, J.; Zissen, M.; Yeshiwas, B. A.; Alkasab, T. K.; Choy, G. & Do, S.: Fully Automated Deep Learning System for Bone Age Assessment. *J. Digit. Imaging* **30** (2017), 427–441, ISSN 1618727X.
- [202] Lee, K.; Jessop, H.; Suswillo, R.; Zaman, G. & Lanyon, L.: Endocrinology: bone adaptation requires oestrogen receptor- α . *Nature* **424** (2003), 389.
- [203] Leslie, C.; Eskin, E. & Noble, W. S.: The spectrum kernel: A string kernel for svm protein classification. In *Biocomputing 2002*. World Scientific 2001, pp. 564–575.
- [204] Lewis, J. & Dickson, D. W.: Propagation of tau pathology: hypotheses, discoveries, and yet unresolved questions from experimental and human brain studies. *Acta Neuropathol. (Berl.)* **131** (2016), 27–48.

- [205] Li, J.; Lykotrafitis, G.; Dao, M. & Suresh, S.: Cytoskeletal dynamics of human erythrocyte. *Proceedings of the National Academy of Sciences* **104** (2007), 4937–4942.
- [206] Li, M.; Xi, N.; Wang, Y. & Liu, L.: Advances in atomic force microscopy for single-cell analysis. *Nano Research* **12** (2019), 703–718.
- [207] Li, X.; Cui, R.; Sun, L.; Aifantis, K. E.; Fan, Y.; Feng, Q.; Cui, F. & Watari, F.: 3d-printed biopolymers for tissue engineering application. *International Journal of Polymer Science* **2014** (2014).
- [208] Lin, Y.-C.; Koenderink, G. H.; MacKintosh, F. C. & Weitz, D. A.: Viscoelastic properties of microtubule networks. *Macromolecules* **40** (2007), 7714–7720.
- [209] Lindsay, R.; Nieves, J.; Formica, C.; Henneman, E.; Woelfert, L.; Shen, V.; Dempster, D. & Cosman, F.: Randomised controlled study of effect of parathyroid hormone on vertebral-bone mass and fracture incidence among postmenopausal women on oestrogen with osteoporosis. *The Lancet* **350** (1997), 550–555.
- [210] Lindsay, R. & Tohme, J. F.: Estrogen treatment of patients with established postmenopausal osteoporosis. *Obstetrics and Gynecology* **76** (1990), 290–295.
- [211] Litjens, G.; Kooi, T.; Bejnordi, B. E.; Setio, A. A. A.; Ciompi, F.; Ghafoorian, M.; Van Der Laak, J. A.; Van Ginneken, B. & Sánchez, C. I.: A survey on deep learning in med. image anal. *Med. Image Anal.* **42** (2017), 60–88.
- [212] Liu, J.; Wang, Y.; Goh, W. I.; Goh, H.; Baird, M. A.; Ruehland, S.; Teo, S.; Bate, N.; Critchley, D. R.; Davidson, M. W. & Kanchanawong, P.: Talin determines the nanoscale architecture of focal adhesions. *Proceedings of the National Academy of Sciences* **112** (2015), E4864–E4873.
- [213] Liu, X.; Yuk, H.; Lin, S.; Parada, G. A.; Tang, T.-C.; Tham, E.; de la Fuente-Nunez, C.; Lu, T. K. & Zhao, X.: 3d printing of living responsive materials and devices. *Advanced Materials* **30** (2018), 1704821.
- [214] Lloyd, C.; Shaw, P.; Warn, R. & Yuan, M.: Gibberellic-acid-induced reorientation of cortical microtubules in living plant cells. *Journal of Microscopy* **181** (1996), 140–144.
- [215] Lo, S.-C.; Lou, S.-L.; Lin, J.-S.; Freedman, M. T.; Chien, M. V. & Mun, S. K.: Artificial convolution neural network techniques and applications for lung nodule detection. *IEEE Transactions on Medical Imaging* **14** (1995), 711–718.
- [216] Louveaux, M.; Rochette, S.; Beauzamy, L.; Boudaoud, A. & Hamant, O.: The impact of mechanical compression on cortical microtubules in arabidopsis: a quantitative pipeline. *The Plant Journal* **88** (2016), 328–342.
- [217] L.P., B.: Bloomberg data collection report (1999), URL <http://www.bloomberg.com/europe>.

- [218] Lu, C.; Reedy, M. & Erickson, H. P.: Straight and curved conformations of ftsz are regulated by gtp hydrolysis. *Journal of bacteriology* **182** (2000), 164–170.
- [219] Lukas, C.; Ruffoni, D.; Lambers, F. M.; Schulte, F. A.; Kuhn, G.; Kollmannsberger, P.; Weinkamer, R. & Müller, R.: Mineralization kinetics in murine trabecular bone quantified by time-lapsed in vivo micro-computed tomography. *Bone* **56** (2013), 55–60.
- [220] Lukinavičius, G.; Reymond, L.; D'este, E.; Masharina, A.; Göttfert, F.; Ta, H.; Güther, A.; Fournier, M.; Rizzo, S.; Waldmann, H. et al.: Fluorogenic probes for live-cell imaging of the cytoskeleton. *Nature methods* **11** (2014), 731.
- [221] Luo, T.; Mohan, K.; Iglesias, P. A. & Robinson, D. N.: Molecular mechanisms of cellular mechanosensing. *Nature materials* **12** (2013), 1064.
- [222] Lynch, M. E.; Main, R. P.; Xu, Q.; Schmicker, T. L.; Schaffler, M. B.; Wright, T. M. & van der Meulen, M. C.: Tibial compression is anabolic in the adult mouse skeleton despite reduced responsiveness with aging. *Bone* **49** (2011), 439–446.
- [223] Lynch, M. E.; Main, R. P.; Xu, Q.; Walsh, D. J.; Schaffler, M. B.; Wright, T. M. & van der Meulen, M. C.: Cancellous bone adaptation to tibial compression is not sex dependent in growing mice. *Journal of applied physiology* **109** (2010), 685–691.
- [224] Macdonald, H. M.; Nishiyama, K. K.; Kang, J.; Hanley, D. A. & Boyd, S. K.: Age-related patterns of trabecular and cortical bone loss differ between sexes and skeletal sites: a population-based hr-pqct study. *J. Bone Miner. Res.* **26** (2011), 50–62.
- [225] Machesky, L. M.; Mullins, R. D.; Higgs, H. N.; Kaiser, D. A.; Blanchoin, L.; May, R. C.; Hall, M. E. & Pollard, T. D.: Scar, a wasp-related protein, activates nucleation of actin filaments by the arp2/3 complex. *Proceedings of the National Academy of Sciences* **96** (1999), 3739–3744.
- [226] Mader, K. S.; Schneider, P.; Müller, R. & Stampanoni, M.: A quantitative framework for the 3d characterization of the osteocyte lacunar system. *Bone* **57** (2013), 142–154.
- [227] Marini, J. C.; Forlino, A.; Bächinger, H. P.; Bishop, N. J.; Byers, P. H.; De Paepe, A.; Fassier, F.; Fratzl-Zelman, N.; Kozloff, K. M.; Krakow, D. et al.: Osteogenesis imperfecta. *Nature reviews Disease primers* **3** (2017), 17052.
- [228] Martin, A.; Lang, D.; Hanke, S. T.; Mueller, S. J.; Sarnighausen, E.; Vervliet-Scheebaum, M. & Reski, R.: Targeted gene knockouts reveal overlapping functions of the five *physcomitrella patens* ftsz isoforms in chloroplast division, chloroplast shaping, cell patterning, plant development, and gravity sensing. *Molecular plant* **2** (2009), 1359–1372.
- [229] Martin, A.; Lang, D.; Hanke, S. T.; Mueller, S. J. X.; Sarnighausen, E.; Vervliet-Scheebaum, M. & Reski, R.: Targeted gene knockouts reveal overlapping functions of the five *physcomitrella patens* ftsz isoforms in chloroplast division, chloroplast

- shaping, cell patterning, plant development, and gravity sensing. *Molecular Plant* **2** (2009), 1359–1372, ISSN 16742052.
- [230] Martin, A.; Lang, D.; Hanke, S. T.; Mueller, S. J. X.; Sarnighausen, E.; Vervliet-Scheebaum, M. & Reski, R.: Targeted gene knockouts reveal overlapping functions of the five *Physcomitrella patens* ftsz isoforms in chloroplast division, chloroplast shaping, cell patterning, plant development, and gravity sensing. *Molecular Plant* **2** (2009), 1359–1372, ISSN 16742052.
- [231] Masso, M. & Vaisman, I. I.: Accurate prediction of stability changes in protein mutants by combining machine learning with structure based computational mutagenesis. *Bioinformatics* **24** (2008), 2002–2009.
- [232] McCreadie, B. R.; Hollister, S. J.; Schaffler, M. B. & Goldstein, S. A.: Osteocyte lacuna size and shape in women with and without osteoporotic fracture. *J. Biomech.* **37** (2004), 563–572.
- [233] McNeil, C. J.; Raymer, G. H.; Doherty, T. J.; Marsh, G. D. & Rice, C. L.: Geometry of a weight-bearing and non-weight-bearing bone in the legs of young, old, and very old men. *Calcif. Tissue Int.* **85** (2009), 22–30.
- [234] van der Meulen, M. C.; Yang, X.; Morgan, T. G. & Bostrom, M. P.: The effects of loading on cancellous bone in the rabbit. *Clinical Orthopaedics and Related Research* **467** (2009), 2000–2006.
- [235] Milner, J. S.; Grol, M. W.; Beaucage, K. L.; Dixon, S. J. & Holdsworth, D. W.: Finite-element modeling of viscoelastic cells during high-frequency cyclic strain. *Journal of functional biomaterials* **3** (2012), 209–224.
- [236] Miyagishima, S.-y.; Kuwayama, H.; Urushihara, H. & Nakanishi, H.: Evolutionary linkage between eukaryotic cytokinesis and chloroplast division by dynamin proteins. *Proceedings of the National Academy of Sciences* **105** (2008), 15202–15207.
- [237] Morgan, E. F.; Barnes, G. L. & Einhorn, T. A.: The bone organ system: form and function. In *Osteoporosis*. Elsevier 2013, pp. 3–20.
- [238] Mosekilde, L.: Age-related changes in vertebral trabecular bone architecture—assessed by a new method. *Bone* **9** (1988), 247–250.
- [239] Moustafa, A.; Sugiyama, T.; Saxon, L. K.; Zaman, G.; Sunters, A.; Armstrong, V. J.; Javaheri, B.; Lanyon, L. E. & Price, J. S.: The mouse fibula as a suitable bone for the study of functional adaptation to mechanical loading. *Bone* **44** (2009), 930–935.
- [240] Mukherjee, A. & Lutkenhaus, J.: Guanine nucleotide-dependent assembly of ftsz into filaments. *J. Bacteriol.* **176** (1994), 2754–2758.
- [241] Narayanaswamy, A.; Dwarakapuram, S.; Bjornsson, C. S.; Cutler, B. M.; Shain, W. & Roysam, B.: Robust adaptive 3-d segmentation of vessel laminae from fluorescence confocal microscope images and parallel gpu implementation. *IEEE transactions on medical imaging* **29** (2010), 583–597.

- [242] Navajas, P. L.; Rivas, G.; Mingorance, J.; Mateos-Gil, P.; Hörger, I.; Velasco, E.; Tarazona, P. & Vélez, M.: In vitro reconstitution of the initial stages of the bacterial cell division machinery. *Journal of biological physics* **34** (2008), 237–247.
- [243] Neer, R. M.; Arnaud, C. D.; Zanchetta, J. R.; Prince, R.; Gaich, G. A.; Reginster, J.-Y.; Hodsmann, A. B.; Eriksen, E. F.; Ish-Shalom, S.; Genant, H. K. et al.: Effect of parathyroid hormone (1-34) on fractures and bone mineral density in postmenopausal women with osteoporosis. *New England journal of medicine* **344** (2001), 1434–1441.
- [244] Nijhuis, W.; Eastwood, D.; Allgrove, J.; Hvid, I.; Weinans, H.; Bank, R. & Sakkers, R.: Current concepts in osteogenesis imperfecta: bone structure, biomechanics and medical management. *Journal of children's orthopaedics* **13** (2019), 1–11.
- [245] Nishiyama, K. K. & Shane, E.: Clinical imaging of bone microarchitecture with hr-pqct. *Current osteoporosis reports* **11** (2013), 147–155.
- [246] Notbohm, H.; Nokelainen, M.; Myllyharju, J.; Fietzek, P. P.; Müller, P. K. & Kivirikko, K. I.: Recombinant human type ii collagens with low and high levels of hydroxylysine and its glycosylated forms show marked differences in fibrillogenesis in vitro. *Journal of Biological Chemistry* **274** (1999), 8988–8992.
- [247] O'connor, J.; Lanyon, L. & MacFie, H.: The influence of strain rate on adaptive bone remodelling. *Journal of biomechanics* **15** (1982), 767–781.
- [248] Ofek, G.; Wiltz, D. C. & Athanasiou, K. A.: Contribution of the cytoskeleton to the compressive properties and recovery behavior of single cells. *Biophysical journal* **97** (2009), 1873–1882.
- [249] Osterhoff, G.; Morgan, E. F.; Shefelbine, S. J.; Karim, L.; McNamara, L. M. & Augat, P.: Bone mechanical properties and changes with osteoporosis. *Injury* **47** (2016), S11–S20.
- [250] Osteryoung, K. W.: Conserved cell and organelle division. *Nature* **376** (1995), 473–474.
- [251] Osteryoung, K. W. & Pyke, K. A.: Division and dynamic morphology of plastids. *Annual Review of Plant Biology* **65** (2014), 443–472.
- [252] Osteryoung, K. W.; Stokes, K. D.; Rutherford, S. M.; Percival, A. L. & Lee, W. Y.: Chloroplast division in higher plants requires members of two functionally divergent gene families with homology to bacterial ftsz. *The Plant Cell* **10** (1998), 1991–2004.
- [253] Ota, S.; Hisano, Y.; Ikawa, Y. & Kawahara, A.: Multiple genome modifications by the crispr/cas9 system in zebrafish. *Genes to Cells* **19** (2014), 555–564.
- [254] Otsu, N.: A threshold selection method from gray-level histograms. *Automatica* **11** (1975), 23–27.

- [255] Özdemir, B.; Asgharzadeh, P.; Birkhold, A. I.; Mueller, S. J.; Röhrle, O. & Reski, R.: Cytological analysis and structural quantification of ftsz1-2 and ftsz2-1 network characteristics in *Physcomitrella patens*. *Scientific reports* **8** (2018), 11165.
- [256] Pal, M.: Random forest classifier for remote sensing classification. *International Journal of Remote Sensing* **26** (2005), 217–222.
- [257] Parent, C. A.: Making all the right moves: chemotaxis in neutrophils and dictyostelium. *Current opinion in cell biology* **16** (2004), 4–13.
- [258] Parfitt, A. M.: Skeletal heterogeneity and the purposes of bone remodeling: implications for the understanding of osteoporosis. In *Osteoporosis (Second Edition)*. Elsevier 2001, pp. 433–447.
- [259] Parfitt, A. M.: Misconceptions (2): turnover is always higher in cancellous than in cortical bone. *Bone (NY)* **30** (2002), 807–809.
- [260] Pärnamaa, T. & Parts, L.: Accurate classification of protein subcellular localization from high-throughput microscopy images using deep learning. *G3: Genes, Genomes, Genetics* **7** (2017), 1385–1392.
- [261] Pauchard, Y.; Liphardt, A.-M.; Macdonald, H. M.; Hanley, D. A. & Boyd, S. K.: Quality control for bone quality parameters affected by subject motion in high-resolution peripheral quantitative computed tomography. *Bone* **50** (2012), 1304–1310.
- [262] Pedregosa, F.; Varoquaux, G.; Gramfort, A.; Michel, V.; Thirion, B.; Grisel, O.; Blondel, M.; Prettenhofer, P.; Weiss, R.; Dubourg, V.; Vanderplas, J.; Passos, A.; Cournapeau, D.; Brucher, M.; Perrot, M. & Duchesnay, E.: Scikit-learn: Machine Learning in Python . *Journal of Machine Learning Research* **12** (2011), 2825–2830.
- [263] Peng, H.; Ruan, Z.; Long, F.; Simpson, J. H. & Myers, E. W.: V3d enables real-time 3d visualization and quantitative analysis of large-scale biological image data sets. *Nat. Biotechnol.* **28** (2010), 348–353.
- [264] Pflanz, D.; Birkhold, A. I.; Albiol, L.; Thiele, T.; Julien, C.; Seliger, A.; Thomson, E.; Kramer, I.; Kneissel, M.; Duda, G. N.; Kornak, U.; Checa, S. & Willie M., B.: Sost deficiency led to a greater cortical bone formation response to mechanical loading and altered gene expr. *Sci. Rep.* **7** (2017), 9435.
- [265] Pialat, J.; Burghardt, A.; Sode, M.; Link, T. & Majumdar, S.: Visual grading of motion induced image degradation in high resolution peripheral computed tomography: impact of image quality on measures of bone density and micro-architecture. *Bone* **50** (2012), 111–118.
- [266] Pistoia, W.; Van Rietbergen, B.; Lochmüller, E.-M.; Lill, C.; Eckstein, F. & Rüeggsegger, P.: Estimation of distal radius failure load with micro-finite element analysis models based on three-dimensional peripheral quantitative computed tomography images. *Bone* **30** (2002), 842–848.

- [267] Pivkin, I. V.; Peng, Z.; Karniadakis, G. E.; Buffet, P. A.; Dao, M. & Suresh, S.: Biomechanics of red blood cells in human spleen and consequences for physiology and disease. *Proceedings of the National Academy of Sciences* **113** (2016), 7804–7809.
- [268] Pivkin, I. V.; Peng, Z.; Karniadakis, G. E.; Buffet, P. A.; Dao, M. & Suresh, S.: Biomechanics of red blood cells in human spleen and consequences for physiology and disease. *Proceedings of the National Academy of Sciences* **113** (2016), 7804–7809.
- [269] Pollard, T. D. & Borisy, G. G.: Cellular motility driven by assembly and disassembly of actin filaments. *Cell* **112** (2003), 453–465.
- [270] Popp, K. L.; McDermott, W.; Hughes, J. M.; Baxter, S. A.; Stovitz, S. D. & Petit, M. A.: Bone strength estimates relative to vertical ground reaction force discriminates women runners with stress fracture history. *Bone* **94** (2017), 22–28.
- [271] Powers, R. E.; Wang, S.; Liu, T. Y. & Rapoport, T. A.: Reconstitution of the tubular endoplasmic reticulum network with purified components. *Nature* **543** (2017), 257–260, ISSN 0028-0836.
- [272] Pritchard, R. H.; Huang, Y. Y. S. & Terentjev, E. M.: Mechanics of biological networks: from the cell cytoskeleton to connective tissue. *Soft Matter* **10** (2014), 1864–84, ISSN 1744-6848.
- [273] Püspöki, Z.; Storath, M.; Sage, D. & Unser, M.: Transforms and operators for directional bioimage analysis: a survey. In *Focus on Bio-Image Informatics*. Springer 2016, pp. 69–93.
- [274] Raghunath, M.; Bruckner, P. & Steinmann, B.: Delayed triple helix formation of mutant collagen from patient with osteogenesis imperfecta. *Journal of molecular biology* **236** (1994), 940–949.
- [275] Rajagopal, V.; Holmes, W. R. & Lee, P. V. S.: Computational modeling of single-cell mechanics and cytoskeletal mechanobiology. *Wiley Interdisciplinary Reviews: Systems Biology and Medicine* **10** (2018), e1407.
- [276] Rauch, F.; Travers, R.; Parfitt, A. & Glorieux, F.: Static and dynamic bone histomorphometry in children with osteogenesis imperfecta. *Bone* **26** (2000), 581–589.
- [277] Reski, R.: Rings and networks: The amazing complexity of FtsZ in chloroplasts. *Trends Plant Sci.* **7** (2002), 103–105, ISSN 13601385.
- [278] Reski, R.: Rings and networks: the amazing complexity of ftsz in chloroplasts. *Trends Plant Sci.* **7** (2002), 103–105.
- [279] Reski, R.: Challenges to our current view on chloroplasts. *Biol. Chem.* **390** (2009), 731–738, ISSN 14316730.

- [280] Riggs, B. L.; Khosla, S. & Melton, L. J.: The assembly of the adult skeleton during growth and maturation: implications for senile osteoporosis. *The Journal of clinical investigation* **104** (1999), 671–672.
- [281] Riggs, B. L. & Melton, L. J.: Bone turnover matters: the raloxifene treatment paradox of dramatic decreases in vertebral fractures without commensurate increases in bone density. *J. Bone Miner. Res.* **17** (2002), 11–14.
- [282] Riggs, B. L.; Melton, L. J.; Robb, R. A.; Camp, J. J.; Atkinson, E. J.; McDaniel, L.; Amin, S.; Rouleau, P. A. & Khosla, S.: A population-based assessment of rates of bone loss at multiple skeletal sites: evidence for substantial trabecular bone loss in young adult women and men. *J. Bone Miner. Res.* **23** (2008), 205–214.
- [283] Rodriguez, E. A.; Campbell, R. E.; Lin, J. Y.; Lin, M. Z.; Miyawaki, A.; Palmer, A. E.; Shu, X.; Zhang, J. & Tsien, R. Y.: The growing and glowing toolbox of fluorescent and photoactive proteins. *Trends in biochemical sciences* **42** (2017), 111–129.
- [284] Rolvien, T.; Stürznickel, J.; Schmidt, F. N.; Butscheidt, S.; Schmidt, T.; Busse, B.; Mundlos, S.; Schinke, T.; Kornak, U.; Amling, M. et al.: Comparison of bone microarchitecture between adult osteogenesis imperfecta and early-onset osteoporosis. *Calcified tissue international* **103** (2018), 512–521.
- [285] Roschger, P.; Paschalis, E.; Fratzl, P. & Klaushofer, K.: Bone mineralization density distribution in health and disease. *Bone* **42** (2008), 456–466.
- [286] Roux, W.: *Der kampf der theile im organismus*. W. Engelmann 1881.
- [287] Roweis, S. T. & Saul, L. K.: Nonlinear dimensionality reduction by locally linear embedding. *science* **290** (2000), 2323–2326.
- [288] Rubin, C. T. & Lanyon, L. E.: Regulation of bone mass by mechanical strain magnitude. *Calcified tissue international* **37** (1985), 411–417.
- [289] Rügsegger, P.; Elsasser, U.; Anliker, M.; Gnehm, H.; Kind, H. & Prader, A.: Quantification of bone mineralization using computed tomography. *Radiology* **121** (1976), 93–97.
- [290] Rugar, D. & Hansma, P.: Atomic force microscopy. *Physics today* **43** (1990), 23–30.
- [291] Safavian, S. R. & Landgrebe, D.: A survey of decision tree classifier methodology. *IEEE transactions on systems, man, and cybernetics* **21** (1991), 660–674.
- [292] Samelson, E. J.; Broe, K. E.; Xu, H.; Yang, L.; Boyd, S.; Biver, E.; Szulc, P.; Adachi, J.; Amin, S.; Atkinson, E.; Berger, C.; Burt, L.; Chapurlat, R.; Chevalley, T.; Ferrari, S.; Goltzman, D.; Hanley, D. A.; Hannan, M. T.; Khosla, S.; Liu, C.; Lorentzon, M.; Mellstrom, D.; Merle, B.; Nethander, M.; Rizzoli, R.; Sornay-Rendu, E.; Van Rietbergen, B.; Sundh, D.; Kin On Wong, A.; Ohlsson, C.; Demissie, S.; Kiel, D. P. & Bouxsein, M. L.: Cortical and trabecular bone microarchitecture as an independent predictor of incident fracture risk in older women and men in

- the bone microarchitecture international consortium (bomic): a prospective study. *Lancet Diabetes Endocrinol.* **7** (2019), 34–43.
- [293] Schaap, I. A.; Carrasco, C.; de Pablo, P. J.; MacKintosh, F. C. & Schmidt, C. F.: Elastic response, buckling, and instability of microtubules under radial indentation. *Biophysical journal* **91** (2006), 1521–1531.
- [294] Scheffers, D.-J. & Driessen, A. J.: The polymerization mechanism of the bacterial cell division protein ftsz. *FEBS letters* **506** (2001), 6–10.
- [295] Schein, C. H. & Noteborn, M. H.: Formation of soluble recombinant proteins in escherichia coli is favored by lower growth temperature. *Bio/technology* **6** (1988), 291–294.
- [296] Schneider, P.; Meier, M.; Wepf, R. & Müller, R.: Serial fib/sem imaging for quantitative 3d assessment of the osteocyte lacuno-canalicular network. *Bone* **49** (2011), 304–311.
- [297] Schoumacher, M.; Goldman, R. D.; Louvard, D. & Vignjevic, D. M.: Actin, microtubules, and vimentin intermediate filaments cooperate for elongation of invadopodia. *The Journal of cell biology* **189** (2010), 541–556.
- [298] Schuit, S.; Van der Klift, M.; Weel, A.; De Laet, C.; Burger, H.; Seeman, E.; Hofman, A.; Uitterlinden, A.; Van Leeuwen, J. & Pols, H.: Fracture incidence and association with bone mineral density in elderly men and women: the rotterdam study. *Bone* **34** (2004), 195–202.
- [299] Seok, J.; Warren, H. S.; Cuenca, A. G.; Mindrinos, M. N.; Baker, H. V.; Xu, W.; Richards, D. R.; McDonald-Smith, G. P.; Gao, H.; Hennessy, L. et al.: Genomic responses in mouse models poorly mimic human inflammatory diseases. *Proceedings of the National Academy of Sciences* **110** (2013), 3507–3512.
- [300] Shao, L.; Kner, P.; Rego, E. H. & Gustafsson, M. G. L.: Super-resolution 3D microscopy of live whole cells using structured illumination. *Nat. Methods* **8** (2011), 1044–1046, ISSN 1548-7105.
- [301] Sharma, G. B.; Robertson, D. D.; Laney, D. A.; Gambello, M. J. & Terk, M.: Machine learning based analytics of micro-MRI trabecular bone microarchitecture and texture in type 1 Gaucher disease. *J. Biomech.* **49** (2016), 1961–1968, ISSN 18732380.
- [302] Shen, D.; Wu, G. & Suk, H.-I.: Deep learning in med. image anal. *Annual review of Biomed. Eng.* **19** (2017), 221–248.
- [303] Shen, H.-S.: Nonlocal shear deformable shell model for bending buckling of microtubules embedded in an elastic medium. *Physics Letters A* **374** (2010), 4030–4039.
- [304] Shore, J. & Johnson, R.: Axiomatic derivation of the principle of maximum entropy and the principle of minimum cross-entropy. *IEEE Transactions on information theory* **26** (1980), 26–37.

- [305] Sillence, D.; Senn, A. & Danks, D.: Genetic heterogeneity in osteogenesis imperfecta. *Journal of medical genetics* **16** (1979), 101–116.
- [306] Simard, M.; Saatchi, S. S. & De Grandi, G.: The use of decision tree and multiscale texture for classification of jers-1 sar data over tropical forest. *IEEE Transactions on Geoscience and Remote Sensing* **38** (2000), 2310–2321.
- [307] Simard, P. Y.; Steinkraus, D. & Platt, J. C.: Best practices for convolutional neural networks applied to visual document analysis. In *null*, IEEE 2003, p. 958.
- [308] Simonyan, K.; Vedaldi, A. & Zisserman, A.: Deep inside convolutional networks: Visualising image classification models and saliency maps. *arXiv preprint* (2013), arXiv:1312.6034.
- [309] Singh, A.; Dutta, M. K.; Jennane, R. & Lespessailles, E.: Classification of the trabecular bone structure of osteoporotic patients using machine vision. *Comput. Biol. Med.* **91** (2017), 148–158, ISSN 18790534.
- [310] Smilkov, D.; Thorat, N.; Kim, B.; Viégas, F. & Wattenberg, M.: Smoothgrad: removing noise by adding noise. *arXiv preprint arXiv:1706.03825* (2017).
- [311] Smith, M. B.; Li, H.; Shen, T.; Huang, X.; Yusuf, E. & Vavylonis, D.: Segmentation and tracking of cytoskeletal filaments using open active contours. *Cytoskeleton* **67** (2010), 693–705.
- [312] Somerville, J.; Aspden, R. M.; Armour, K.; Armour, K. & Reid, D. M.: Growth of c57bl/6 mice and the material and mechanical properties of cortical bone from the tibia. *Calcif. Tissue Int.* **74** (2004), 469–475.
- [313] Spampinato, C.; Palazzo, S.; Giordano, D.; Aldinucci, M. & Leonardi, R.: Deep learning for automated skeletal bone age assessment in x-ray images. *Med. Image Anal.* **36** (2017), 41–51.
- [314] Stein, A. M.; Vader, D. A.; Jawerth, L. M.; Weitz, D. A. & Sander, L. M.: An algorithm for extracting the network geometry of three-dimensional collagen gels. *J. Microsc.* **232** (2008), 463–475.
- [315] Stevenson, A.: *Oxford dictionary of English*. Oxford University Press, USA 2010.
- [316] Strauss, M. P.; Liew, A. T.; Turnbull, L.; Whitchurch, C. B.; Monahan, L. G. & Harry, E. J.: 3d-sim super resolution microscopy reveals a bead-like arrangement for ftsz and the division machinery: implications for triggering cytokinesis. *PLoS Biol.* **10** (2012), e1001389.
- [317] Strychalski, W.; Copos, C. A.; Lewis, O. L. & Guy, R. D.: A poroelastic immersed boundary method with applications to cell biology. *Journal of Computational Physics* **282** (2015), 77–97.
- [318] Subach, F. V.; Patterson, G. H.; Renz, M.; Lippincott-schwartz, J. & Verkhusha, V. V.: for Two-Color Super-Resolution sptPALM of Live Cells. *Cell* (2010), 12651–12656.

- [319] Sugiyama, T.; Meakin, L. B.; Galea, G. L.; Jackson, B. F.; Lanyon, L. E.; Ebetino, F. H.; Russell, R. G. G. & Price, J. S.: Risedronate does not reduce mechanical loading-related increases in cortical and trabecular bone mass in mice. *Bone* **49** (2011), 133–139.
- [320] Sugiyama, T.; Price, J. S. & Lanyon, L. E.: Functional adaptation to mechanical loading in both cortical and cancellous bone is controlled locally and is confined to the loaded bones. *Bone* **46** (2010), 314–321.
- [321] Suk, H.-I.; Lee, S.-W.; Shen, D.; Initiative, A. D. N. et al.: Hierarchical feature representation and multimodal fusion with deep learning for ad/mci diagnosis. *NeuroImage* **101** (2014), 569–582.
- [322] Sun, D.; Brodt, M. D.; Zannit, H. M.; Holguin, N. & Silva, M. J.: Evaluation of loading parameters for murine axial tibial loading: Stimulating cortical bone formation while reducing loading duration. *J. Orthop. Res.* **36** (2018), 682–691.
- [323] Suresh, S.: Mechanical response of human red blood cells in health and disease: some structure-property-function relationships. *Journal of materials research* **21** (2006), 1871–1877.
- [324] Suresh, S.; Spatz, J.; Mills, J.; Micoulet, A.; Dao, M.; Lim, C.; Beil, M. & Seufferlein, T.: Connections between single-cell biomechanics and human disease states: gastrointestinal cancer and malaria. *Acta biomaterialia* **1** (2005), 15–30.
- [325] Svedbom, A.; Ivergård, M.; Hernlund, E.; Rizzoli, R. & Kanis, J. A.: Epidemiology and economic burden of osteoporosis in switzerland. *Arch. Osteoporos.* **9** (2014), 187.
- [326] Szulc, P.; Seeman, E.; Duboeuf, F.; Sornay-Rendu, E. & Delmas, P. D.: Bone fragility: failure of periosteal apposition to compensate for increased endocortical resorption in postmenopausal women. *J. Bone Miner. Res.* **21** (2006), 1856–1863.
- [327] Taber, L.; Shi, Y.; Yang, L. & Bayly, P.: A poroelastic model for cell crawling including mechanical coupling between cytoskeletal contraction and actin polymerization. *Journal of mechanics of materials and structures* **6** (2011), 569–589.
- [328] Tao, D.; Tang, X. & Li, X.: Which components are important for interactive image searching? *IEEE Transactions on Circuits and Systems for Video Technology* **18** (2008), 3–11.
- [329] Tao, D.; Tang, X.; Li, X. & Wu, X.: Asymmetric bagging and random subspace for support vector machines-based relevance feedback in image retrieval. *IEEE Transactions on Pattern Analysis & Machine Intelligence* (2006), 1088–1099.
- [330] Tartibi, M.; Liu, Y.; Liu, G.-Y. & Komvopoulos, K.: Single-cell mechanics—an experimental–computational method for quantifying the membrane–cytoskeleton elasticity of cells. *Acta biomaterialia* **27** (2015), 224–235.

- [331] TerBush, A. D.; MacCready, J. S.; Chen, C.; Ducat, D. C. & Osteryoung, K. W.: Conserved dynamics of chloroplast cytoskeletal ftsz proteins across photosynthetic lineages. *Plant physiology* **176** (2018), 295–306.
- [332] TerBush, A. D. & Osteryoung, K. W.: Distinct functions of chloroplast ftsz1 and ftsz2 in z-ring structure and remodeling. *J Cell Biol* **199** (2012), 623–637.
- [333] TerBush, A. D.; Yoshida, Y. & Osteryoung, K. W.: Ftsz in chloroplast division: structure, function and evolution. *Current Opinion in Cell Biology* **25** (2013), 461–470.
- [334] Théry, M. & Bornens, M.: Cell shape and cell division. *Curr. Opin. Cell Biol.* **18** (2006), 648–657.
- [335] Tian, X.; Jee, W. S.; Li, X.; Paszty, C. & Ke, H. Z.: Sclerostin antibody increases bone mass by stimulating bone formation and inhibiting bone resorption in a hindlimb-immobilization rat model. *Bone* **48** (2011), 197–201.
- [336] Tong, S. & Chang, E.: Support vector machine active learning for image retrieval. In *Proceedings of the ninth ACM international conference on Multimedia*, ACM 2001, pp. 107–118.
- [337] Torres, F.; Bravo, M. A.; Salinas, E.; Triana, G. & Arbeláez, P.: Bone age detection via carpogram analysis using convolutional neural networks. In *13th International Conference on Medical Information Processing and Analysis*, International Society for Optics and Photonics 2017, vol. 10572, p. 1057217.
- [338] Trepatt, X.; Deng, L.; An, S. S.; Navajas, D.; Tschumperlin, D. J.; Gerthoffer, W. T.; Butler, J. P. & Fredberg, J. J.: Universal physical responses to stretch in the living cell. *Nature* **447** (2007), 592–5, ISSN 1476-4687.
- [339] Tsai, J. N.; Uihlein, A. V.; Burnett-Bowie, S.-A. M.; Neer, R. M.; Zhu, Y.; Derrico, N.; Lee, H.; Bouxsein, M. L. & Leder, B. Z.: Comparative effects of teriparatide, denosumab, and combination therapy on peripheral compartmental bone density, microarchitecture, and estimated strength: the data-hrpqct study. *J. Bone Miner. Res.* **30** (2015), 39–45.
- [340] Turner, D. J.; Portman, I.; Dafforn, T. R.; Rodger, A.; Roper, D. I.; Smith, C. J. & Turner, M. S.: The mechanics of ftsz fibers. *Biophysical journal* **102** (2012), 731–738.
- [341] Unterberger, M. J.; Schmoller, K. M.; Bausch, A. R. & Holzapfel, G. A.: A new approach to model cross-linked actin networks: multi-scale continuum formulation and computational analysis. *Journal of the mechanical behavior of biomedical materials* **22** (2013), 95–114.
- [342] Urban, N. T.; Willig, K. I.; Hell, S. W. & Nägerl, U. V.: Sted nanoscopy of actin dynamics in synapses deep inside living brain slices. *Biophys. J.* **101** (2011), 1277–1284.

- [343] Vahabikashi, A.; Park, C. Y.; Perkumas, K.; Zhang, Z.; Deurloo, E. K.; Wu, H.; Weitz, D. A.; Stamer, W. D.; Goldman, R. D.; Fredberg, J. J. et al.: Probe sensitivity to cortical versus intracellular cytoskeletal network stiffness. *Biophysical journal* **116** (2019), 518–529.
- [344] Van Dijk, F. & Sillence, D.: Osteogenesis imperfecta: clinical diagnosis, nomenclature and severity assessment. *American journal of medical genetics Part A* **164** (2014), 1470–1481.
- [345] Van Opbroek, A.; Ikram, M. A.; Vernooij, M. W. & De Bruijne, M.: Transfer learning improves supervised image segmentation across imaging protocols. *IEEE Trans. Med. Imaging* **34** (2015), 1018–1030.
- [346] Van Ruijven, L.; Giesen, E.; Mulder, L.; Farella, M. & Van Eijden, T.: The effect of bone loss on rod-like and plate-like trabeculae in the cancellous bone of the mandibular condyle. *Bone* **36** (2005), 1078–1085.
- [347] Versaevel, M.; Braquenier, J.-B.; Riaz, M.; Grevesse, T.; Lantoine, J. & Gabriele, S.: Super-resolution microscopy reveals LINC complex recruitment at nuclear indentation sites. *Sci. Rep.* **4** (2014), 7362, ISSN 2045-2322.
- [348] Vicidomini, G.; Moneron, G.; Han, K. Y.; Westphal, V.; Ta, H.; Reuss, M.; Engelhardt, J.; Eggeling, C. & Hell, S. W.: Sharper low-power STED nanoscopy by time gating. *Nat. Methods* **8** (2011), 571–573, ISSN 1548-7091.
- [349] Vico, L.; Zouch, M.; Amirouche, A.; Frère, D.; Laroche, N.; Koller, B.; Laib, A.; Thomas, T. & Alexandre, C.: High-resolution pqt analysis at the distal radius and tibia discriminates patients with recent wrist and femoral neck fractures. *Journal of Bone and Mineral Research* **23** (2008), 1741–1750.
- [350] Vining, K. H. & Mooney, D. J.: Mechanical forces direct stem cell behaviour in development and regeneration. *Nature Reviews Molecular Cell Biology* **18** (2017), 728.
- [351] Wang, Y. & Qian, J.: Buckling of filamentous actin bundles in filopodial protrusions. *Acta Mechanica Sinica* (2019), 1–11.
- [352] Weber, B.; Greenan, G.; Prohaska, S.; Baum, D.; Hege, H.-C.; Müller-Reichert, T.; Hyman, A. A. & Verbavatz, J.-M.: Automated tracing of microtubules in electron tomograms of plastic embedded samples of *Caenorhabditis elegans* embryos. *J. Struct. Biol.* **178** (2012), 129–138.
- [353] Weeks, B. K.; Young, C. M. & Beck, B. R.: Eight months of regular in-school jumping improves indices of bone strength in adolescent boys and girls: the power pe study. *Journal of Bone and Mineral Research* **23** (2008), 1002–1011.
- [354] Wegel, E.; Göhler, A.; Lagerholm, B. C.; Wainman, A.; Uphoff, S.; Kaufmann, R. & Dobbie, I. M.: ImAging Cellular structures in super-resolution with SIM, STED and Localisation Microscopy: A practical comparison. *Sci. Rep.* **6** (2016), 27290, ISSN 2045-2322.

- [355] Weiner, O. D.; Marganski, W. A.; Wu, L. F.; Altschuler, S. J. & Kirschner, M. W.: An actin-based wave generator organizes Cell Motil. *PLoS Biol.* **5** (2007), 2053–2063, ISSN 15449173.
- [356] Wernick, M. N.; Yang, Y.; Brankov, J. G.; Yourganov, G. & Strother, S. C.: Machine learning in medical imaging. *IEEE signal processing magazine* **27** (2010), 25–38.
- [357] White, J.; Amos, W. & Fordham, M.: An evaluation of confocal versus conventional imaging of biological structures by fluorescence light microscopy. *The Journal of cell biology* **105** (1987), 41–48.
- [358] Wiche, G.: Role of plectin in cytoskeleton organization and dynamics. *Journal of cell science* **111** (1998), 2477–2486.
- [359] Wick, S. M.; Seagull, R. W.; Osborn, M.; Weber, K. & Gunning, B.: Immunofluorescence microscopy of organized microtubule arrays in structurally stabilized meristematic plant cells. *The Journal of cell biology* **89** (1981), 685–690.
- [360] Williamson, R. E.: Orientation of cortical microtubules in interphase plant cells. In *International review of cytology*. Elsevier 1991, vol. 129, pp. 135–206.
- [361] Willie, B. M.; Birkhold, A. I.; Razi, H.; Thiele, T.; Aido, M.; Kruck, B.; Schill, A.; Checa, S.; Main, R. P. & Duda, G. N.: Diminished response to in vivo mechanical loading in trabecular and not cortical bone in adulthood of female c57bl/6 mice coincides with a reduction in deformation to load. *Bone* **55** (2013), 335–346.
- [362] Willig, K. I. & Barrantes, F. J.: Recent applications of superresolution microscopy in neurobiology. *Curr. Opin. Chem. Biol.* **20** (2014), 16–21, ISSN 18790402.
- [363] Wirshing, A. C. & Cram, E. J.: Myosin activity drives actomyosin bundle formation and organization in contractile cells of the caenorhabditis elegans spermatheca. *Molecular biology of the cell* **28** (2017), 1937–1949.
- [364] Wolff, J.: Das gesetz der transformation der knochen. *DMW-Deutsche Medizinische Wochenschrift* **19** (1893), 1222–1224.
- [365] Wulf, E.; Deboben, A.; Bautz, F.; Faulstich, H. & Wieland, T.: Fluorescent phallotoxin, a tool for the visualization of cellular actin. *Proceedings of the national academy of sciences* **76** (1979), 4498–4502.
- [366] Xiao, X.; Geyer, V. F.; Bowne-Anderson, H.; Howard, J. & Sbalzarini, I. F.: Automatic optimal filament segmentation with sub-pixel accuracy using generalized linear models and b-spline level-sets. *Med. Image Anal.* **32** (2016), 157–172.
- [367] Xu, G.-K.; Li, B.; Feng, X.-Q. & Gao, H.: A tensegrity model of cell reorientation on cyclically stretched substrates. *Biophysical journal* **111** (2016), 1478–1486.
- [368] Xu, K.; Zhong, G. & Zhuang, X.: Actin, spectrin, and associated proteins form a periodic cytoskeletal structure in axons. *Science* **339** (2013), 452–456.

- [369] Xu, T.; Vavylonis, D. & Huang, X.: 3d actin network centerline extraction with multiple active contours. *Med. Image Anal.* **18** (2014), 272–284.
- [370] Xu, T.; Vavylonis, D.; Tsai, F.-C.; Koenderink, G. H.; Nie, W.; Yusuf, E.; Lee, I.-J.; Wu, J.-Q. & Huang, X.: Soax: a software for quantification of 3d biopolymer networks. *Sci. Rep.* **5** (2015), 9081.
- [371] Xuan, B.; Ghosh, D.; Cheney, E. M.; Clifton, E. M. & Dawson, M. R.: Dysregulation in actin cytoskeletal organization drives increased stiffness and migratory persistence in polyploid giant cancer cells. *Scientific reports* **8** (2018), 11935.
- [372] Yang, A. D.; Fan, F.; Camp, E. R.; van Buren, G.; Liu, W.; Somcio, R.; Gray, M. J.; Cheng, H.; Hoff, P. M. & Ellis, L. M.: Chronic oxaliplatin resistance induces epithelial-to-mesenchymal transition in colorectal cancer cell lines. *Clin. Cancer Res.* **12** (2006), 4147–4153.
- [373] Yang, H.; Albiol, L.; Chan, W.-L.; Wulsten, D.; Seliger, A.; Thelen, M.; Thiele, T.; Spevak, L.; Boskey, A.; Kornak, U.; Checa, S. & Willie M., B.: Examining tissue composition, whole-bone morphology and mechanical behavior of *gorabprx1* mice tibiae: A mouse model of premature aging. *J. Biomech.* **65** (2017), 145–153.
- [374] Yang, H.; Embry, R. E. & Main, R. P.: Effects of loading duration and short rest insertion on cancellous and cortical bone adaptation in the mouse tibia. *PloS one* **12** (2017), e0169519.
- [375] Yang, T. T.; Hampilos, P. J.; Nathwani, B.; Miller, C. H.; Sutaria, N. D. & Liao, J. C.: Superresolution STED microscopy reveals differential localization in primary cilia. *Cytoskeleton* **70** (2013), 54–65, ISSN 19493584.
- [376] Yang, W.; Battineni, M. L. & Brodsky, B.: Amino acid sequence environment modulates the disruption by osteogenesis imperfecta glycine substitutions in collagen-like peptides. *Biochemistry* **36** (1997), 6930–6935.
- [377] Yang, X.; Sun, L.-W.; Du, C.-F.; Wu, X.-T. & Fan, Y.-B.: Finite element analysis of osteocytes mechanosensitivity under simulated microgravity. *Microgravity Science and Technology* (2018), 1–13.
- [378] Yang, Y.; Bai, M.; Klug, W. S.; Levine, A. J. & Valentine, M. T.: Microrheology of highly crosslinked microtubule networks is dominated by force-induced crosslinker unbinding. *Soft matter* **9** (2013), 383–393.
- [379] Yevick, H. G. & Martin, A. C.: Quantitative analysis of cell shape and the cytoskeleton in developmental biology. *Wiley Interdisciplinary Reviews: Developmental Biology* **7** (2018), e333.
- [380] Zhang, Q.; Ragnauth, C. D.; Skepper, J. N.; Worth, N. F.; Warren, D. T.; Roberts, R. G.; Weissberg, P. L.; Ellis, J. A. & Shanahan, C. M.: Nesprin-2 is a multi-isoformic protein that binds lamin and emerin at the nuclear envelope and forms a subcellular network in skeletal muscle. *J. Cell Sci.* **118** (2005), 673–687.

-
- [381] Zhang, Z.; Nishimura, Y. & Kanchanawong, P.: Extracting microtubule networks from superresolution single-molecule localization microscopy data. *Mol. Biol. Cell* **28** (2017), 333–345.
- [382] Zienkiewicz, O. C. & Taylor, R. L.: *The finite element method for solid and structural mechanics*. Elsevier 2005.
- [383] Zilske, M.; Lamecker, H. & Zachow, S.: Adaptive remeshing of non-manifold surfaces. *Proc. EUROGRAPHICS* **27** (2008).
- [384] Zysset, P. K.; Dall’Ara, E.; Varga, P. & Pahr, D. H.: Finite element analysis for prediction of bone strength. *Bonekey Rep.* **2** (2013), 386.



This thesis lies at the interface of biophysics, computer science, and mechanical engineering. This work is devoted to development, application, and validation of methods for an automatic analysis of the structure-function relationship on two different scales of biological environments naming protein networks on the nano scale and metaphyseal bone on the micro and macro scale. The methodologies are developed in the frameworks of machine learning and continuum mechanics to carry out an image-based, data-driven assessment of this relationship.



Pouyan Asgharzadeh

ISBN 978-3-946412-05-2

CBM-06 (2020)

Data-driven Analysis of Biological Network Structures

P. Asgharzadeh

Image-based Analysis of Biological Network Structures using Machine Learning and Continuum Mechanics

Pouyan Asgharzadeh

vorgelegt an der

